Modelling the Microstructure–Charge Transport Relationship in Organic Semiconductors

Jack Felix Coker

Department of Physics,

Imperial College London

Submitted in fulfilment of the requirements for the degree of Doctor of Philosophy

January 2025

Statement of Originality

This thesis describes work undertaken by myself between March 2020 and September 2024, under the supervision of Professor Jenny Nelson and Dr Jarvist Frost. Results based on the work of my collaborators have been explicitly highlighted. All other results are the product of my own work.

Copyright Statement

The copyright of this thesis rests with the author. Unless otherwise indicated, its contents are licensed under a Creative Commons Attribution-NonCommercial 4.0 International Licence (CC BY-NC). Under this licence, you may copy and redistribute the material in any medium or format. You may also create and distribute modified versions of the work. This is on the condition that: you credit the author and do not use it, or any derivative works, for a commercial purpose. When reusing or sharing this work, ensure you make the licence terms clear to others by naming the licence and linking to the licence text. Where a work has been adapted, you should indicate that the work has been changed and describe those changes. Please seek permission from the copyright holder for uses of this work that are not included in this licence or permitted under UK Copyright Law.

Abstract

Organic semiconductor materials can offer major advantages over commonly-used inorganic alternatives when integrated into electronic devices. However, they tend to suffer from low charge carrier mobilities, which can limit device performance. Microstructural disorder plays a key – but sometimes poorly understood – role in determining the mobility of organic materials.

This thesis describes a series of computational investigations aimed at improving our understanding of the relationships between chemical structure, microstructure, and charge transport in organic semiconductors. A multiscale modelling approach, employing density functional theory, molecular dynamics, and charge transport simulations, is applied to capture these relationships as they emerge from processes occurring across a range of time- and length-scales.

First, the development of two transport modelling codes is described, with their utility being verified in two case studies. The first study focuses on the influence of electron density and mobility in an interfacial photocatalytic system for hydrogen production, while the second focuses on the influence of molecular symmetry and crystalline packing on the mobility of bis-adduct isomers of PCBM. A significant portion of this thesis centres on rationalising the high mobility of the disordered polymer C16-IDTBT. Its microstructure is shown to feature an unusual packing motif involving perpendicularly crossing backbones. Combined with rigid chains, this promotes a highly interconnected transport network, greatly benefiting mobility. This investigation is extended to evaluate four heteroatom-substituted analogues of C16-IDTBT. A final investigation reveals that charge transport in thin films of the non-fullerene acceptor O-IDTBR is limited by intermolecular electrostatic contributions to energetic disorder, which in turn emerges from the conformational and packing disorder of molecules.

This work reaffirms the importance of understanding the role of microstructure – and microstructural disorder in particular – in determining the charge transport properties of organic semiconductors, and demonstrates how computational techniques may be applied to deepen this understanding.

Acknowledgements

This PhD would not have been possible without the guidance and support of my colleagues, friends, and family. My heartfelt thanks go out to you all. Among many others, I would like to thank:

Jenny Nelson, for being an inspiration, for always finding the time for your students, and for the amazing extent of your knowledge and curiosity. Finally, for sharing my enthusiasm for research that is directly focussed on addressing the needs of people and society.

Jarvist Frost, for the depth and clarity of your knowledge on computational techniques, and for always knowing why my simulations weren't working.

My collaborators, including Stefania Moro, Giovanni Costantini, Ljiljana Stojanović, Jochen Blumberger, Weimin Zhang, Iain McCulloch, Matthew J. Bird, Yucheng Xu, Xingyuan Shi, and Jun Yan, for all of your hard work, and for the insightful discussions.

Hanbo and Jolanda, for the provinces, for encouraging me to push through the pain, and for being part of the best corner in Huxley.

Everyone in H1101 and the Nelson group, for the friendship, camaraderie, and snacks.

Anders, Martin, James, and Joe, for doing all the hard parts first.

Carolyn, Juraci, and Beth, for your patience and helpfulness, and for keeping me in pay.

The HPC team, for the computing power, which I always tried, and mostly succeeded, in using wisely.

Everyone at the Colwith Road house, for creating a warm and welcoming home over almost four years, and Charlotte, who was there at the beginning of it all.

Smriti, for the time shared together, and for your boundless affection.

Mum, Dad, and Joe, for all of your care, love, and support.

Contents

1 Introduction **17**

1.1 Motivation and Challenges . . . 17

1.2 Modelling . . . 20

1.2.1 Why Simulate? . . . 20

1.2.2 Multiscale Modelling . . . 21

1.3 Overview . . . 22

2 Background **24**

2.1 Microstructure of Organic Solids . . . 24

2.1.1 Intermolecular Forces . . . 24

2.1.2 Microstructural Forms and Features . . . 25

2.2 Electronic Structure of Conjugated Molecules . . . 26

2.2.1 Conjugation . . . 26

2.2.2 Potential Energy Surfaces . . . 28

2.3 Charge Transfer . . . 29

2.3.1 Transitions between Potential Energy Surfaces . . . 29

2.3.2 Hopping Rates . . . 31

2.3.3 Electronic Structure Parameters . . . 33

2.4 Charge Transport . . . 34

2.4.1 Hopping Transport . . . 34

2.4.2 Transport Beyond the Hopping Regime . . . 36

2.4.3 Charge Transport Models . . . 37

2.5 Donor-Acceptor Polymers . . . 42

2.5.1 Before Donor-Acceptor Polymers . . . 42

2.5.2 C16-IDTBT: History and Applications . . . 43

2.5.3 C16-IDTBT: Microstructure and Transport . . . 44

2.6 Scope of this Thesis . . . 45

3 Methods **47**

3.1 Electronic Structure Calculation . . . 47

3.1.1 Density Functional Theory . . . 49

3.1.2 Exchange-Correlation Functionals . . . 51

3.1.3 Dispersion Corrections . . . 52

3.1.4 Basis Sets . . . 52

3.1.5 Electronic Coupling Calculations . . . 53

3.2 Microstructure Prediction . . . 55

3.2.1 Molecular Dynamics . . . 56

3.2.2 Molecules and Dimers (Small Systems) . . . 58

3.2.3 Atomistic Molecular Dynamics (Medium Systems) . . . 58

3.2.4 Coarse-Grained Molecular Dynamics (Large Systems) . . . 59

3.3 Charge Transport Simulations . . . 60

3.3.1 Kinetic Monte Carlo . . . 61

3.3.2 Master Equation . . . 64

4 Transport Model Development **66**

4.1 Introduction . . . 66

4.2 Simulation Setup . . . 67

4.3 Updates to ToFeT . . . 68

4.4 MESol . . . 72

4.5 Case Studies . . . 74

4.5.1 Polymer Photocatalysts for Sacrificial Hydrogen Evolution . . . 74

4.5.2 Crystalline Packing Arrangements and their Impact on Mobility . . . 82

4.6 Conclusions . . . 87

5 Microstructure of C16-IDTBT **88**

5.1 Introduction . . . 88

5.2 Methods and Results . . . 91

5.2.1 Chains on Surfaces . . . 91

5.2.2 Backmapping Coarse-Grained Structures . . . 98

5.2.3 General Microstructural Trends . . . 99

5.2.4 Interchain Contact Selection . . . 101

5.2.5 Interchain Contact Geometry . . . 104

5.2.6 Interconnectivity . . . 108

5.3 Conclusions . . . 111

6 Transport in C16-IDTBT **113**

6.1 Introduction . . . 113

6.2 Methods and Results . . . 115

6.2.1 Contact Interaction Maps . . . 115

6.2.2 Electronic Coupling at Contacts . . . 121

6.2.3 Charge Transport Simulations . . . 123

6.3 Conclusions . . . 129

6.3.1 Design Rules . . . 130

7 Variants of C16-IDTBT **133**

7.1 Introduction . . . 133

7.2 Methods and Results . . . 135

7.2.1 Frontier Orbitals . . . 135

7.2.2 Torsional Potentials . . . 136

7.2.3 Contact Interaction Maps . . . 138

7.2.4 Thermal Distributions of Contact Arrangements . . . 141

7.3 Conclusions . . . 143

8 Disorder and Transport in O-IDTBR **146**

8.1 Introduction . . . 146

8.2 Method . . . 148

8.3 Results . . . 151

8.3.1 Effect of Microstructure on Transport . . . 151

8.3.2 Impact of Energetic Disorder on Transport . . . 152

8.4 Conclusions . . . 154

9 Conclusions and Outlook **156**

9.1 Chemical Structure, Microstructure, and Charge Transport . . . 156

9.2 Future Work . . . 159

9.2.1 Experimental Assessment of the Geometry and Density of Interchain Contact Points by Solid-State Nuclear Magnetic Resonance . . . 159

9.2.2 Further Analysis of Contact Locking . . . 160

9.2.3 Analysis of Contact Formation (Aggregation) during the Solution State-Solid State Transition . . . 161

9.2.4 Network Analysis of Conjugated Polymer Microstructures . . . 161

9.2.5 Further Analysis of IDTxBx Variants . . . 162

9.2.6 Light-Matter Interactions in IDTBT . . . 162

A Microstructure **184**

A.1 IDTBT Chains on Substrate: S and T stacks 184

A.2 Backmapping Details 187

A.3 Chain Orientation in C16-IDTBT Microstructural Models 189

B Contact Geometry and Electronic Coupling **190**

B.1 Extended Moiety Contact Maps 190

B.2 Interaction Maps with y-Shift 191

B.3 Variants B and C Interaction maps 194

B.4 LUMO-LUMO Coupling 195

C Temperature and Field Dependence of Mobility. **198**

D Parameter Exploration for Polymer Photocatalyst Model **200**

List of Tables

4.1 Hopping rates in the interfacial photocatalysis model system. 77
4.2 Information about representative bis-PCBM isomers. 83

D.1 Default parameters for polymer photocatalyst model. 200

List of Figures

1.1 Benzene. . . . 17
1.2 Modelling as elephants. . . . 20
1.3 Multiscale modelling. . . . 21

2.1 Formation of a molecular π-orbital in benzene. . . . 27
2.2 Potential energy surface of a diatomic molecule. . . . 28
2.3 Charge transfer reaction between molecules. . . . 29
2.4 Potential energy diagram for a coupled system of two diatomic molecule. . . . 30
2.5 Potential energy diagram for charge transfer reaction. . . . 32

3.1 First reaction method flowchart. . . . 61
3.2 Time progression of first reaction method with multiple charges. . . . 63

4.1 System size and field dependence of mobility in `ToFeT`. . . . 70
4.2 Transient-absorption spectroscopy of FS-Hex film. . . . 75
4.3 Interfacial photocatalysis model system. . . . 76
4.4 Interfacial photocatalysis electron population decay curves. . . . 78
4.5 Interfacial photocatalysis half lives. . . . 79
4.6 Bis-PCBM isomer structures. . . . 83
4.7 Bis-PCBM crystal supercells. . . . 84
4.8 Bis-PCBM simulated mobilities. . . . 86

5.1 C16-IDTBT. . . . 88
5.2 C16-IDTBT chains packed edgewise on substrate. . . . 93
5.3 C16-IDTBT chains crossing on substrate. . . . 95
5.4 Chains on substrate crossing angles. . . . 96
5.5 Backmapping of a coarse-grained IDTBT monomer. . . . 98
5.6 Verification of backmapped structures. . . . 99
5.7 Structural order displayed by backmapped models 100
5.8 Interchain contact selection pitfalls 102

5.9 Identification of interchain contacts . . . 104
5.10 Interchain contact geometry trends . . . 106
5.11 Interchain contact moieties in C16-IDTBT . . . 107
5.12 Interchain contact occurrence statistics . . . 108
5.13 Interconnectivity visualisation . . . 109
5.14 Perpendicular and parallel contacts. . . . 110

6.1 Explanation of contact interaction maps. . . . 116
6.2 Contact interaction maps for IDTBT and P3HT . . . 118
6.3 Distance dependence of coupling strength. . . . 121
6.4 Crossing angle dependence of coupling strength . . . 122
6.5 Converting atoms to sites. . . . 124
6.6 Hole mobilities from transport simulations. . . . 126
6.7 Hole mobilities from transport simulations, with modified coupling strengths. . . . 128
6.8 Hypothetical contact arrangement. . . . 130

7.1 Heteroatom-substituted variants of IDTBT. . . . 134
7.2 HOMO and LUMO of IDTBT and variants. . . . 136
7.3 Torsional potential between donor and acceptor units of IDTBT and variants. . . . 137
7.4 Geometry optimised monomers of IDTBT and variant *D*. . . . 137
7.5 Contact interaction maps for variants *A* and *D* of IDTBT. . . . 139
7.6 Contacting segments of IDTBT and variant D in antiparallel arrangements. . . . 140
7.7 Maps of thermal distribution of contact geometries for IDTBT and variants *A* and *D*. . 142
7.8 Thermal distribution of electronic coupling strengths for IDTBT and variants. . . . 143

8.1 Chemical structure of O-IDTBR. . . . 147
8.2 Crystal structure of O-IDTBR. . . . 149
8.3 Timescales of hopping and intramolecular reorganisation modes in O-IDTBR . . . 150
8.4 O-IDTBR mobilities. . . . 151

A.1 Relative orientation between IDTBT backbone planes for chains on substrate. . . . 185
A.2 Interaction energy trends for pairs of IDTBT chains on substrate. . . . 186
A.3 Orientation of C16-IDTBT chains in microstructural model . . . 189

B.1 Extended contact interaction maps. . . . 190
B.2 Interaction energy maps for IDTBT with y-shifts. . . . 191
B.3 HOMO-HOMO coupling maps for IDTBT with y-shifts (linear scale). . . . 192
B.4 HOMO-HOMO coupling maps for IDTBT with y-shifts (logarithmic scale). . . . 193

B.5 Contact interaction maps for variants B and C of IDTBT. 194
B.6 LUMO-LUMO coupling maps for IDTBT and P3HT. 195
B.7 Comparison of HOMO-HOMO and LUMO-LUMO coupling at MD contacts. 196
B.8 LUMO-LUMO coupling maps for variants of IDTBT. 197
B.9 Thermal distribution of LUMO-LUMO coupling strengths for IDTBT and variants. . . 197

C.1 Simulated temperature- and field-dependence of mobility for C16-IDTBT and P3HT. . 199

D.1 Photocatalysis model: Default parameters 201
D.2 Photocatalysis model: Varying N_{metal}. 201
D.3 Photocatalysis model: Varying J_{polymer}. 202
D.4 Photocatalysis model: Varying J_{polymer} and J_{metal}. 202
D.5 Photocatalysis model: Varying J_{metal}. 203
D.6 Photocatalysis model: Varying $J_{\text{reduction}}$. 203
D.7 Photocatalysis model: Disordered coupling and site energy distributions. 204
D.8 Photocatalysis model: Varying ξ. 205
D.9 Photocatalysis model: Varying β_{polymer}. 205
D.10 Photocatalysis model: Varying β_{metal}. 206
D.11 Photocatalysis model: Varying $\beta_{\text{reduction}}$. 206
D.12 Photocatalysis model: Transient population fluctuations. 207

Abbreviations

OSC organic semiconductor

OPV organic photovoltaic

OLED organic light-emitting diode

NFA non-fullerene acceptor

PES potential energy surface

MO molecular orbital

HOMO highest occupied molecular orbital

LUMO lowest unoccupied molecular orbital

DoS density of states

LJ Lennard-Jones

BO Born-Oppenheimer

MLJ Marcus-Levich-Jortner

CoG centre-of-geometry

NN nearest neighbour

DoF degree-of-freedom

PBC periodic boundary condition

SVD singular value decomposition

HF Hartree-Fock

DFT density functional theory

LDA local density approximation

GGA general gradient approximation

MD molecular dynamics

CG coarse-grained

KMC kinetic Monte Carlo

FRM first reaction method

ME master equation

NAMD non-adiabatic molecular dynamics

FSSH fewest switches surface hopping

PR-TRMC pulse radiolysis time-resolved microwave conductivity

ToF time-of-flight

FET field effect transistor

SCLC space-charge limited current

HRTEM high-resolution transmission electron microscopy

AFM atomic force microscopy

XRD X-ray diffraction

GIXD grazing incidence X-ray diffraction

GIWAXS grazing-incidence wide-angle X-ray scattering

SANS small-angle neutron scattering

STM scanning tunnelling microscopy

ESD vacuum-electrospray deposition

SS-NMR solid-state nuclear magnetic resonance

TAS transient-absorption spectroscopy

Chemical Units, Molecules, and Polymers

Note that, for brevity, abbreviations in this list will not be expanded in the text.

IDT indacenodithiophene

BT benzothiadiazole

DTBT dithiophenebenzothiadiazole

IDTBT indacenodithiophene-co-benzothiadiazole

IDTzBT indacenodithiazole-co-benzothiadiazole

IDTTBT indacenodithieno[3,2-b]thiophene-co-benzothiadiazole

TIFBT dithiopheneindenofluorene-co-benzothiadiazole

TBIDTBT thiophenebenzo[b]indacenodithiophene-co-benzothiadiazole

PCPDTBT poly[2,6-(4,4-bis-(2-ethylhexyl)-4H-cyclopenta[2,1-b;3,4-b0]-dithiophene)-alt-4,7-(2,1,3-benzothiadiazole)]

P3HT regioregular poly-3-hexilthiophene

PBTTT poly(2,5-bis(3-alkylthiophen-2-yl)thieno[3,2-b]thiophene)

PffBT4T-2OD poly[(5,6-difluoro-2,1,3-benzothiadiazol-4,7-diyl)-alt-(3,3”’-di(2-octyldodecyl)-2,2’;5’,2”;5”,2”’-quaterthiophen-5,5”’-diyl)]

PCBM (1-[3-(methoxycarbonyl)propyl]-1-phenyl)-[6,6]C62

bis-PCBM bis-(1-[3-(methoxycarbonyl)propyl]-1-phenyl)-[6,6]C62

FS 9,9-di-*R*-2,7-diyl-co-dibenzo[b,d]thiophene 5,5-dioxide

O-IDTBR 5,5’-[(4,9-dihydro-4,4,9,9-tetraoctyl-s-indaceno[1,2-b:5,6-b’]-dithiophene2,7-diyl)-bis-(2,1,3-benzothiadiazole-7,4-diylmethylidyne)]-bis-[3-ethyl-2-thioxo-4-thiazolidinone

Commonly Used Symbols

e	charge of an electron (elementary charge)
k_{B}	Boltzmann constant
$\hbar$	Planck constant
J	electronic coupling
ϵ	site energy
$\Delta\epsilon$	difference in site energies
λ	reorganisation energy
Γ	charge transfer rate (hopping rate)
μ	charge carrier mobility
F	external (applied) field strength
T	temperature

Chapter 1

Introduction

1.1 Motivation and Challenges

New electronic materials could play a part in addressing many of the societal and technological issues we face today. Issues of sustainability, including the climate crisis and chemical pollution of the natural environment, pose a looming threat to Earth's self-regulatory systems, and therefore to human well-being [1–3]. Compared to other issues, however, efforts to improve the sustainability of modern society may, at least in part, be aided by new material technologies.

Organic semiconductors (OSCs) represent a class of materials that are intrinsically well suited to aiding in these efforts, while also enabling other new and exciting technologies. They combine the optoelectronic properties of semiconductors with the processability, chemical tunability, low-toxicity, and versatile mechanical properties of plastics [4, 5].

OSC materials are molecular solids composed of largely carbon-based small molecules or polymers, bound together by weak non-bonding intermolecular forces. Their semiconducting character arises from a conjugated chemical structure that is able to support mobile charge carriers.[1] The benzene ring is one of the simplest conjugated structures. Its skeletal structure, displayed in Figure 1.1, shows the alternating single and double bonds that characterise conjugation.

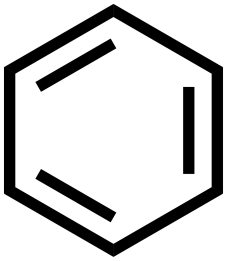


Figure 1.1: Benzene.

In the context of sustainability, devices based on OSCs can offer advantages in terms of low-energy intensive, high-volume device fabrication (which additionally reduces their financial cost), while also being constructed from non-toxic, and oftentimes recyclable materials. In the specific case of organic photovoltaic (OPV) devices [6], the low financial and energy costs are particularly important, given the need to rapidly transition away from our current fossil-fuel based energy infrastructure. As well as OPVs, electronically-active organic materials could enable new technological developments in the fields

[1] Strictly speaking, the term 'conjugation' can include chemical structural forms other than the π-conjugated form that gives rise to semiconducting properties (e.g., σ-conjugation). However, here and throughout this thesis, I retain the typical use of 'conjugation' as referring to chemical systems featuring delocalised π-orbitals (see Section 2.2.1).

of batteries, transistors, displays, photonics, sensors, and biocompatible devices, to name a few [5].

With the above advantages and applications in mind, current OSC materials face several disadvantages compared to industry-standard inorganic alternatives, such as silicon. Chief among these is their relatively poor electronic properties, which typically lead to worse device performance metrics. This has limited the widespread adoption of OSC-based devices, outside of specific technologies such as organic light-emitting diodes (OLEDs) [5].

One crucial property, often used as a figure-of-merit to assess the suitability of a given semiconducting material for use in device applications, is its *charge mobility* (or, simply, *mobility*). It is typically given in units of $\mathrm{cm}^2/\mathrm{Vs}$. We can factor this into $\mathrm{cm\,s}^{-1}$ per $\mathrm{V\,cm}^{-1}$, which clarifies the physical origin of the property; it is a measure of the speed at which mobile charges move through a material under the influence of an applied electric field. Mobility is a measure of the *charge transport* capability of a material. There are a number of reasons why, in most applications, higher mobilities lead to better device performance. In general, fast moving charges can improve the current densities established for a given applied voltage. Reducing the time taken for charges to be transported to device contacts will also decrease the likelihood of charge recombination, and therefore decrease voltage losses across devices. Among other things, mobility is an important factor in determining the switching speed and gain of transistors, the sensitivity of photodetectors, and the efficiency of photovoltaic devices [7].[2] For context, the electron mobility of crystalline silicon is typically $\sim$1000 $\mathrm{cm}^2/\mathrm{Vs}$, whereas only the best OSCs tend to achieve mobilities $>1\,\mathrm{cm}^2/\mathrm{Vs}$. While this represents a drastic improvement from the mobilities measured in early organic devices, such as $1\times10^{-6}\,\mathrm{cm}^2/\mathrm{Vs}$ to $1\times10^{-5}\,\mathrm{cm}^2/\mathrm{Vs}$ for field effect transistor (FET) devices in the 1980s [11, 12], it also highlights the work that remains to be done.

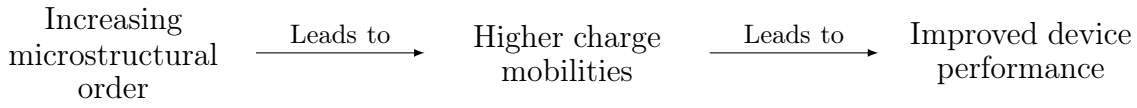
Improving the mobilities of OSCs in a systematic way will require new insights and a deeper understanding of how the bulk electronic properties of semiconducting materials are governed by the structure and assembly of their constituent molecules. Several factors, emerging across multiple length-scales, are responsible for the mobility exhibited by a given OSC material. One of the most important is the material's microstructure – that is, the packing arrangements of molecules in the solid state. This can be demonstrated by a comparison between the typically high mobilities displayed by crystalline molecular solids, and the typically low mobilities of more disordered materials. The microstructure itself is chiefly controlled by the chemical structure of the constituent molecules, although a significant degree of control is also provided by choices of processing conditions (e.g., solvent, substrate, temperature, and pressure) applied during the fabrication stage.

Most commonly, information about a material's microstructure is sourced from X-ray diffraction (XRD) experiments [13–16]. These experiments image the diffraction patterns produced by X-rays

[2] OLED devices are a notable exception to this rule, since their performance is critically dependent on achieving balanced hole and electron mobilities, which is generally easier at low-to-moderate mobilities [8–10]. However, this thesis focuses on materials suited to unipolar transport.

scattering off of periodic arrangements of molecules, and are therefore very effective at characterising the crystalline regions of a material. Since, as stated, there is typically a correlation between a high degree of crystalline order and a high charge mobility, the microstructural features that can most easily be detected and characterised are often, conveniently, also those that can be used to explain a given material's mobility.

Across most OSC materials, and in most applications, the typical relationship between microstructural order, charge transport, and device performance, can be laid out in the following simple form:



Drawing upon this relationship has been, and continues to be, extremely useful for researchers seeking to develop new materials for better performing devices. It provides a broad guideline that can be followed when synthesising new molecules and fabricating devices. Furthermore, it provides a framework for rationalising the performance of existing materials by pointing towards their microstructural characteristics. However, in this regard, as in life, the most valuable lessons are learnt when we fail – or, our current understanding fails, as the case may be. It is important, therefore, to recognise and study those material cases where this trend no longer holds. Understanding the relationships between microstructure, transport, and performance in such 'outliers' can provide us with a more nuanced (and, hopefully, more accurate) understanding of OSC materials and their properties, and may reveal alternative avenues towards improving device performance that might otherwise be rejected.

This thesis details investigations into several material systems for which the above framework appears to breaks down (or, in the final case, has not been previously confirmed). These include:

- The conjugated polymer C16-IDTBT, which displays the apparently incongruous characteristics of high mobility and low microstructural order (see Section 2.5 and Chapters 5, 6, and 7).
- Photocatalytic sulfone polymers, which perform unusually well in hydrogen production applications, despite poor mobilities (see Section 4.5.1).
- Bis-adduct isomers of the fullerene acceptor PCBM, for which experiments have shown a roughly inverse relationship between crystallinity and mobility (see Section 4.5.2).
- The non-fullerene acceptor (NFA) O-IDTBR, for which recently developed theories may provide a good description of transport in crystalline arrangements (see Section 2.4.2), but it is unknown how well this description carries over to transport in the disordered regions, which tend to dominate the microstructure (see Chapter 8).

For all of these materials, a high degree of microstructural disorder appears to play a key – but poorly understood – role in informing their transport behaviour and performance in relevant applications.

Notably, when seeking to address these gaps in our understanding, a challenge is presented by the fact that we cannot gain as much information about the microscopic features of disordered materials by conventional experimental means. In this regard, computational tools can serve a vital role.

1.2 Modelling

1.2.1 Why Simulate?

Alongside experiments and theoretical developments, computational methods can serve as powerful tools for improving our understanding of the origins of material properties, such as the relationship between microstructure and mobility. It may be useful to briefly outline why such methods are used at all, given that they do not provide information about the real, physical systems that we ultimately care about.

Individual experimental methods tend to provide a somewhat narrow window into the behaviour of physical systems. The picture can be filled out by employing multiple different methods, like shining light on different parts of an unknown object, but this may not always be enough to fully understand the system. A simulated model can stand in for the unknown object, and help unify information provided by each experiment into a single coherent picture, as illustrated in Figure 1.2. Thus, simulations can help guide our choice of experiment, and test underlying assumptions about how a system operates [17].

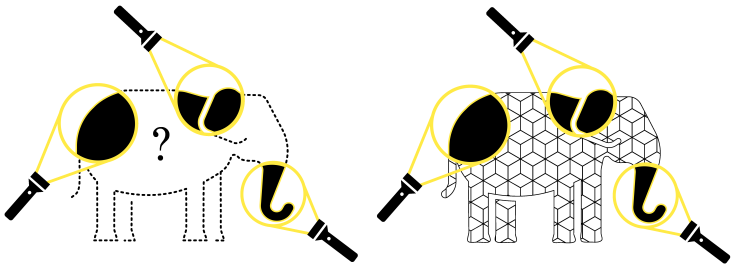


Figure 1.2: "What is it?" "Oh, that makes sense!"

Simulations can also provide insight into behaviours that are difficult to access from our macroscopic world [18]. In the context of OSCs, we can use simulated models to view the packing arrangements of molecules at the atomic level, or to track the paths of mobile charges as they travels through a material.

Furthermore, simulations can allow us to evaluate counterfactuals. By tweaking parameters, even deliberating choosing unphysical values, we can answer questions not just about what *is*, but about what *matters*.

One ultimate goal of developing new simulation methods is to enable the *in silico* prediction of hypothetical material properties prior to synthesis. Developing reliable ways to achieve this would greatly enhance our ability to systematically determine the best candidate materials from the vast chemical space of OSCs, allowing us to do away with the largely trial-and-error approach that has thus far been the main way by which new materials are discovered. Although this 'holy grail' remains largely on the horizon for now, improvements in simulation accuracy, computational power, and machine learning algorithms provide some hope that such an approach may someday become feasible [18–22].

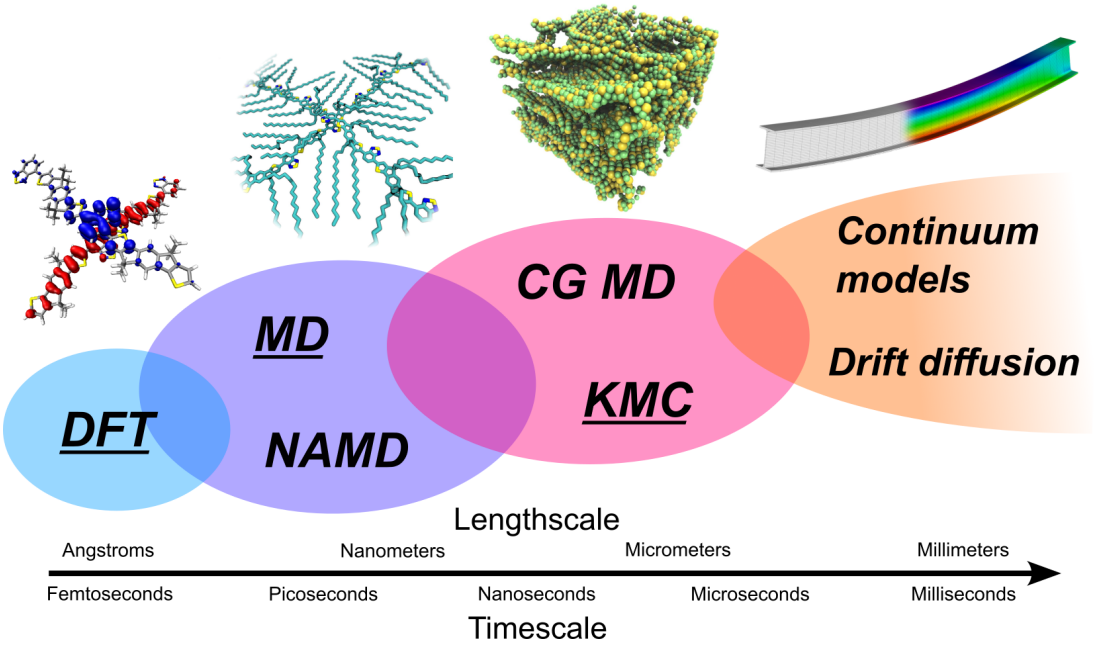


Figure 1.3: A diagram indicating the various length- and time-scales that must be considered when investigating material systems. Examples of computational methods that may be applied at different scales are named. The top row lists methods used for structure prediction, while the bottom row lists methods used for charge transport simulation. Except for continuum models, all other methods indicated here have been applied by myself (underlined) or my collaborators during the investigations described in this thesis. Methods details are provided in Chapter 3. For an overview of charge transport simulation methods, see Section 2.4.3.

1.2.2 Multiscale Modelling

When it comes to understanding the relationship between microstructure and charge transport, a major obstacle is thrown up by the fact that both areas involve processes that occur over disparate time- and length-scales. This is challenging from a simulation perspective because we have two opposed goals that require balancing with only limited computational resources. These goals are 1) achieving physical accuracy at small scales, and 2) capturing large enough scales to be relevant to the macroscopic properties we are trying to understand. We can, however, partially circumvent this problem by employing different computational approaches to simulate a system at various scales - equivalent to viewing it at various different resolutions - and linking these scales together to build a single coherent picture [23].

In many cases, the processes that govern behaviour at different scales are approximately separable. For instance, because electrons tend to exhibit much faster motion than nuclei, we can approximate electron dynamics as occurring on a fixed 'background' of static nuclei (see Section 2.2.2). Based on this, and similar insights, it is often possible to adopt a sequential modelling strategy when investigating the relationship between microstructure and transport for a given system. This may involve first predicting a microstructural model of the system (see Section 3.2), then evaluating the electronic structure of the model (see Section 3.1), before finally simulating charge transport using information

about the electronic structure and microstructure (see Section 3.3). Information from each of the scales can be interpreted individually, as well as correlated together, to gain an understanding of the system.

In cases where the scales are not easily separated, for instance when the electron dynamics have a significant influence on the nuclei dynamics, we generally need to adopt simulation methods that can model both subsystems concurrently, and account for their interplay. Sophisticated methods have been developed for performing such simulations, although they are intrinsically more computationally demanding than techniques applied in the separable case (see Section 2.4.3). This generally limits the maximum length- and time-scales that can be modelled, so extra care must be taken to ensure that evaluated properties (e.g. mobility) are still representative of the macroscopic properties we are ultimately interested in.

For the work described in this thesis, I employed a sequential approach to multiscale modelling (i.e., assuming separable scales). This provides a good balance between reaching appropriately large scales to be relevant to macroscopic properties, and representing the underlying chemical and physical processes with reasonable accuracy.

1.3 Overview

In this thesis I describe a series of computational investigations into the relationship between chemical structure, microstructure, and charge transport in OSC materials, with a particular focus on the effects of microstructural disorder.

Chapter 2 provides a review of relevant background information provided by prior studies. This includes general information about the electronic structure and microstructure of OSCs, the mechanisms and factors governing charge transport, and a section dedicated to reviewing previous works investigating the high-mobility conjugated polymer C16-IDTBT.

Chapter 3 describes the theoretical underpinnings of the computational methods I have employed. This includes methods for evaluating the electronic structure and microstructure of OSCs, and methods for simulating charge transport.

Chapter 4 describes the development of two charge transport codes I used during my investigations. It also describes two case studies demonstrating the application of these codes in systems of bis-PCBM and photocatalytic sulfone polymers, respectively.

Chapter 5 describes an investigation into the microstructural characteristics of C16-IDTBT, and how these are related to its chemical structure.

Chapter 6 describes the continued investigation of C16-IDTBT. Here, I focus on understanding how the microstructural features identified in Chapter 5 govern the charge transport properties of the polymer. This chapter concludes with a discussion of potential avenues towards the development of higher mobility polymer materials, based on my findings in Chapters 5 and 6.

Chapter 7 describes an investigation of four variants of C16-IDTBT that feature heteroatoms substituted onto the the donor unit of the backbone. In light of my results in Chapters 5 and 6, I analyse factors found to be crucial for governing transport in C16-IDTBT, and explore how these factors are likely to be affected by the modified backbones of the variants.

Chapter 8 describes an investigation into the relationship between microstructure and charge transport for the small acceptor molecule O-IDTBR.

Finally, in Chapter 9, I summarise the findings of these investigations, and suggest a number of avenues for future research.

Chapter 2

Background

2.1 Microstructure of Organic Solids

2.1.1 Intermolecular Forces

OSCs are considered 'soft' materials due to the weak intermolecular forces that bind molecules and polymers together in the solid state. The most prevalent attractive force between molecules stems from *van der Waals* interactions [5]. These are purely electrostatic interactions that do not involve the sharing of electrons between molecules. They originate from three main sources, each relating to different types of dipoles that may be present:

- *Keesom interactions* occur between the permanent dipoles of polar molecules, and are highly dependent on the relative orientation of molecules.
- *Debye interactions* arise when a permanent dipole on one molecule induces a temporary dipole in a neighbouring molecule.
- *London* or *dispersive interactions* arise when instantaneous fluctuations in the electron density of one molecule establish a dipole that then induces an oppositely-directed instantaneous dipole on a neighbouring molecule.

Of the three components, dispersive interactions are the most universal, since they occur between all atoms and molecules, regardless of whether they are polar or non-polar.

The packing of molecules in the solid state is also dependent on the nature of repulsive interactions. These primarily arise from the Pauli exclusion principle, which prevents two fermions (electrons in this case) from occupying the same quantum state, and thus the same location in space (assuming the same spin configuration). This constraint leads to repulsive exchange interactions between electrons at short interatomic distances. In a chemical context involving atoms and molecules, these repulsive forces are typically referred to as *steric interactions*.

Conveniently for the modelling of molecular materials, both the long-range attractive interactions and short-range repulsive interactions can be accurately represented by simple distance-dependent analytical functions (see Section 3.2). The *Lennard-Jones potential* is the the archetypal example of such a function [24].

2.1.2 Microstructural Forms and Features

Because of the diversity in shape and size that organic molecules and polymers present, and the weak forces between them, OSCs display a wide variety of different microstructural forms in the solid state [4]. This has consequences for the charge transport behaviour of the materials [11, 25]. The most common microstructural forms may be classified as follows:

- *Amorphous molecular films* are composed of small molecules with disordered packing arrangements. They may be fabricated by low energy-intensive methods, but typically suffer from low charge mobilities.

- *Molecular crystals* are composed of small molecules arranged in an ordered lattice. Many OSC materials display both crystalline and amorphous regions within a single heterogeneous microstructure, with a higher crystalline volume fraction generally being beneficial to charge transport. In this regard, pure single crystals typically present the highest mobilities among OSCs, but require energy-intensive fabrication and processing conditions to encourage their formation.

- *Semicrystalline polymer films* are composed of polymer chains and feature both crystalline and amorphous regions. The high solubility of many polymers (especially with side chains attached) means that they are generally energetically cheap to fabricate. Historically, semicrystalline microstructures were assumed to enable the highest mobilities among polymers [12].

- *Disordered polymer films* are composed of polymer chains and lack experimentally-detectable signs of long-range microstructural order. They are similarly energetically cheap to fabricate. Although the low mobilities presented by early amorphous polymers were overtaken by semicrystalline polymers, more recently, several high-mobility disordered polymers have been developed (see Section 2.5 for further details). These display mobilities matching or exceeding the best semicrystalline polymers [26–28]. This is typically understood to be enabled by transport-beneficial backbone conformations and the presence of 'short-range' order in their packing structures [12, 29–32].

Most conjugated polymers, and many semiconducting small molecules, contain side chains. These are generally attached in order to increase solubility, and thus enable the use of solution-based processing and fabrication techniques [33, 34]. Alkyl side chains are used most commonly. Due to their lack of conjugation (see Section 2.2.1), these side chains are electronically insulating, and thus do not directly

affect the electronic characteristics of the molecular cores or polymer backbones they are attached to. However, they can still significantly affect the bulk electronic properties of materials, due to the steric influence they have on solid-state packing arrangements [35].

Two important characteristics influencing the microstructures and charge transport properties of semiconducting polymer films are the *contour length* and *persistence length* of the individual polymer chains [36, 37]. The contour length is equivalent to the physical length of the chain backbone, that is, the length of the backbone when stretched out to its maximum 1D extent. It is related to the molecular weight of the polymer chain, since this determines the number of repeat units.[1]

The persistence length describes the stiffness of a given polymer. Polymer chains with a persistence length longer than their contour length will behave like rigid rods, whereas chains with a persistence length shorter than their contour length can bend, or even fold.[2] Although persistence length is usually measured for chains dispersed in solution, being an intrinsic property of the chains, it also affects their conformation and packing in the solid state. The monomers, or sub-monomer units, of semiconducting polymers are generally rigid, due to their conjugated chemical structures (see Section 2.2.1). However, these are typically linked by bonds that allow for dihedral rotations between the units. The stiffness (and planarity) of conjugated polymers is therefore largely determined by the torsional potentials controlling these dihedral angles [41].

2.2 Electronic Structure of Conjugated Molecules

2.2.1 Conjugation

The molecules and polymers that make up OSC materials are distinguished from other organic compounds by a π-conjugated chemical structure that facilitates the conduction of electricity.[3] Carbon atoms with three compatible neighbours undergo sp^2-hybridisation, forming three in-plane σ-bonds and leaving an out-of-plane p_z-orbital. The overlapping p_z-orbitals of the atoms combine into molecular π-orbitals (MOs), which are delocalised across the interconnected π-system. This process is visualised for benzene in Figure 2.1. Energy level splitting from the mixing of p_z-orbitals produces a density-of-states analogous to the band-structure of inorganic semiconductors, where the highest occupied molecular orbital (HOMO) replaces the valence band-edge and the lowest unoccupied molecular orbital (LUMO) replaces the conduction band-edge. The HOMO and LUMO of a molecule are referred to collectively as the *frontier orbitals*.

[1] Physical samples of polymers typically present a distribution of molecular weights. The width of this distribution may be quantified by the sample's polydispersity index, calculated from the ratio of average molecular weight to number-averaged molecular mass.

[2] There is evidence that the crystalline domains of some flexible polymer films may be significantly composed of repeatedly-folded chains, which is likely to impact charge transport pathways [38–40].

[3] As noted in Section 1.1 footnote 1, throughout this thesis I use the unqualified term 'conjugation' to refer specifically to 'π-conjugation' as it is described in this section. Other forms of conjugation exist (e.g., σ-conjugation), but do not generally facilitate charge transport.

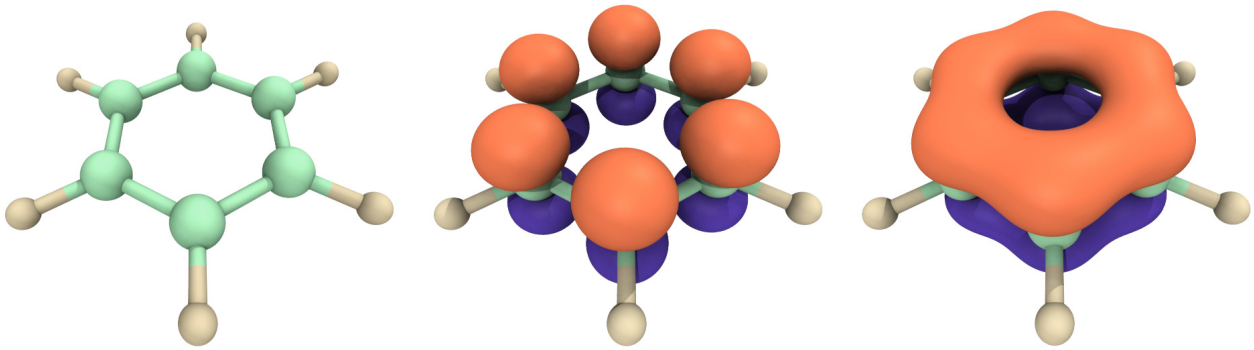


Figure 2.1: The carbon atoms of a benzene molecule (left) feature p_z atomic orbitals (centre). The overlap of these atomic orbitals gives rise to delocalised molecular π-orbitals (right). Note that, to show this process in a visually simple manner, I have chosen to depict the lowest energy π-orbital (out of six), which is formed when all the atomic orbitals combine constructively. This lies at a lower energy than the (degenerate) HOMO, and as such is labelled the HOMO-1.

The HOMO and LUMO energies associated with a particular molecule or sub-molecular unit are largely governed by the chemical structure of the conjugated system (with some influence due to intermolecular interactions). Synthetic chemistry techniques can be employed to modify the conjugated system, thus providing control over the frontier orbitals and, consequently, control over the electronic and optical properties of OSC materials. This can involve, for example, substituting heteroatoms (i.e., atoms that are not carbon or hydrogen) into the conjugated system, or linking together sub-molecular units which themselves feature differences in the frontier orbital energy levels (i.e., donors and acceptors). This latter method is particularly useful in OPV applications, since it allows the optical band gap[4] to be tuned through the visible and near-infrared spectral bands. Linking together donor and acceptor units in this way has led to the development of a multitude of high-performing small molecules – referred to as *non-fullerene acceptors* (NFAs) – and donor-acceptor polymers (see Section 2.5).

The delocalised nature of the frontier orbitals means that holes occupying the HOMO, or electrons occupying the LUMO, are highly mobile. Collectively, these mobile holes and electrons may be refereed to as *charge carriers*, *excess charges*, or *mobile charges*. These charge carriers will respond to the application of an external field, thus allowing for the intramolecular conduction of electricity.

An unbroken π-system allows charge carriers to move around single molecules or polymer chains. However, for transport to occur on device length-scales, charges must be able to traverse between molecules as well. Electronic coupling, associated with the overlap of MOs on different molecules, can allow charge carriers to *transfer* onto neighbouring molecules, opening up intermolecular pathways for charges to make their way through materials. The rate of these transfer reactions is naturally one of the governing factors determining the mobility of an OSC material. However, charge transfer reactions in molecular materials are heavily linked to the motion of nuclei, so it is important to understand

[4]The optical band gap is linked to – but not identical to – the energy gap between the HOMO and LUMO. However, a detailed description of the differences between these two types of band gap is beyond the scope of this thesis.

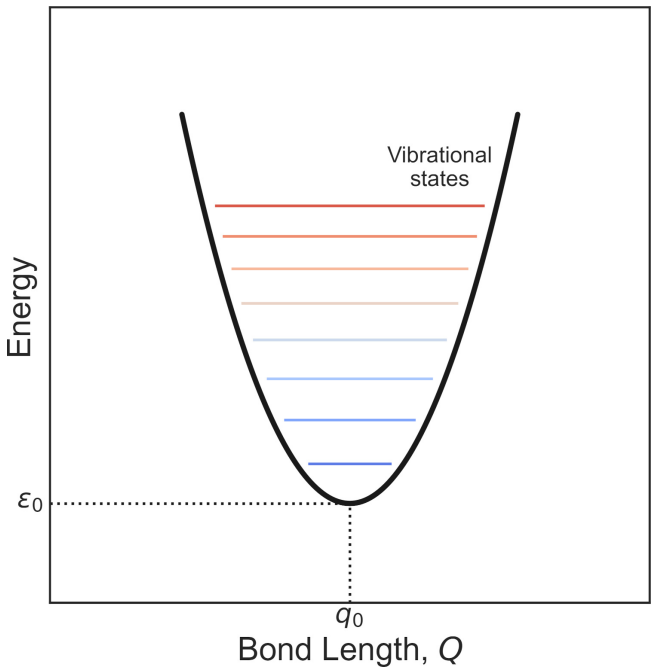


Figure 2.2: A PES for a diatomic molecule. This system can be described by a single aggregate nuclear coordinate Q, since the bond length is the only degree-of-freedom that contributes to the potential.

the relationship between electronic and nuclear dynamics before moving on to exploring the factors influencing transfer rates, which will be covered in Section 2.3.

2.2.2 Potential Energy Surfaces

For a given molecular system, a *potential energy surface* (PES) describes the energetic landscape that nuclear dynamics are subject to.[5] Specifically, the PES describes how the total energy of the system, minus nuclear kinetic energy, varies with nuclear coordinates.

Perhaps surprisingly, given the quantum nature of the particles involved, such surfaces are fairly simple mathematical objects. Their construction is made possible by a vital empirical observation; that the total energy of a molecular system, E_{total}, can usually be closely approximated by a linear sum of contributions from its electronic and nuclear subsystems. In quantum mechanical terms, the wavefunction of the system in state $|\Psi\rangle$ may be treated as separable:

$$|\Psi\rangle \approx |\Phi\rangle|\chi\rangle, \tag{2.1}$$

where $|\Phi\rangle$ and $|\chi\rangle$ are the states of the electronic and nuclear subsystems respectively. This behaviour is explained by the low mass of electrons compared to nuclei, which leads to an orders-of-magnitude separation in the timescales of their motion. From the perspective of the electrons, the nuclei appear effectively fixed in space at any one time. The influence of the nuclei is therefore felt as a static potential landscape. Congruently, the electrons can usually be treated as perfectly responsive to the 'gradual'

[5] Although rigorously the term 'surface' only refers to 2D mathematical objects, it is commonly used independent of the number of dimensions.

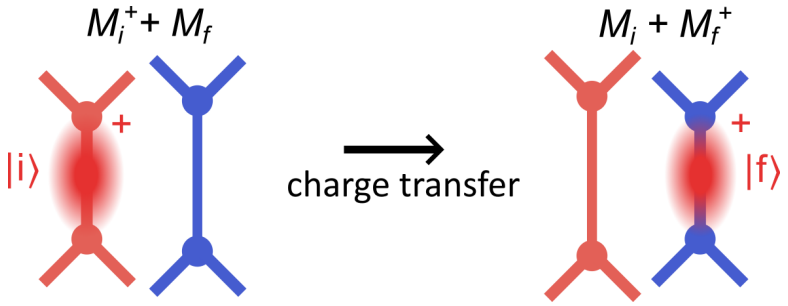


Figure 2.3: Charge transfer reaction between two molecules. Note the changing equilibrium lengths of the molecules, depending on whether they are charged or uncharged. This system may be reduced to a single nuclear coordinate; the difference between the two bond lengths.

motion of the nuclei. Emphasis on this last point is the foundation of the *adiabatic representation*.

Describing a system using Equation 2.1 is known as the *Born-Oppenheimer* (BO) *approximation*. It is based in the adiabatic representation, but further assumes that the adiabatic electronic states are energetically well-separated. The evolution of the nuclei is then described by the following form of the Schrödinger equation:

$$\left(\hat{T}_n + U_i(\vec{R})\right)|\chi\rangle_i = E_{\text{total}}|\chi\rangle_i, \tag{2.2}$$

where $\hat{T}_n$ is the nuclear kinetic operator and i designates an adiabatic electronic state. The function $U_i(\vec{R})$, which takes the nuclear coordinates as input, is the PES. It sums the energy contributions from the kinetic energy of the electrons, plus electron-electron, electron-nuclear, and nuclear-nuclear interactions. Each PES represents the system as it would be if electrons were restricted to occupying a single energetic eigenstate, albeit one continuously evolving with changing nuclear coordinates.

2.3 Charge Transfer

A *charge transfer reaction* involves the transfer of an excess charge from the frontier orbital of one molecule, to the unoccupied frontier orbital of a neighbouring molecule. At the moment of transfer, these reactions occur without a change in energy, as evidenced by the fact that they can proceed in the dark, and do not emit photons.

2.3.1 Transitions between Potential Energy Surfaces

Following the same logic as the BO approximation, the *Franck-Condon principle* asserts that electronic transitions are fast enough to be effectively instant on the timescales of nuclear motion. Transitions between PESs associated with different electronic states must therefore be 'vertical' in the sense that they may involve a change in energy but no change in nuclear coordinates. Satisfying these two conditions (no change in energy and no change in nuclear coordinates) therefore requires a vertical transition of zero 'height'. In other words, charge transfer reactions may only occur at the crossing point between two PESs.

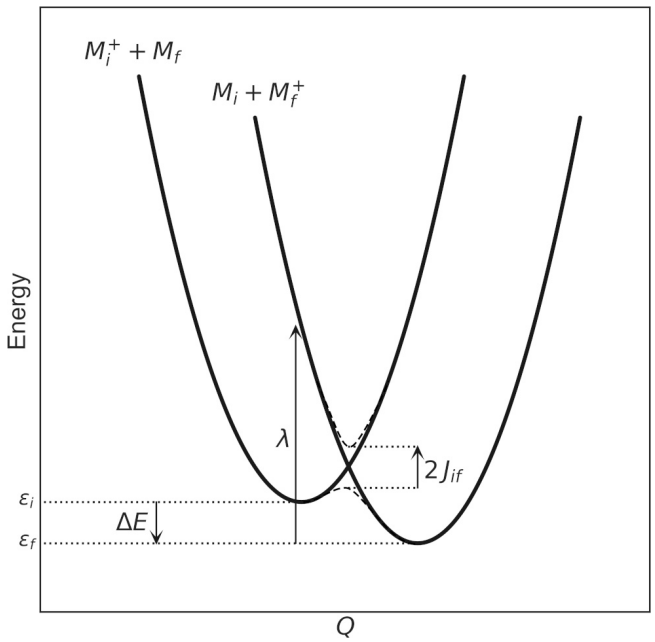


Figure 2.4: Potential energy surfaces for a system of two diatomic molecules with an excess hole occupying either M_i or M_f. The coordinate Q is the difference in bond length between the two molecules. The solid lines are the diabatic surfaces, whilst the dotted lines show the adiabatic surfaces in the vicinity of the avoided crossing, established when coupling of strength J is present between the frontier orbitals. ϵ_i and ϵ_f denote the equilibrium energies of the initial and final states, while λ denotes the reorganisation energy.

To complicate matters, the existence of *avoided crossings* between energetic eigenvalues means that such intersections will not strictly occur in systems reducible to one nuclear coordinate (such as bond length in a diatomic molecule). Avoided crossings arise in the adiabatic representation because the nuclear kinetic operator is off-diagonal in the system Hamiltonian. This prevents the complete separation of the electronic and nuclear subsystems when there are multiple electronic states interacting. The BO approximation may still hold for most nuclear configurations, but will break down where the energies of the adiabatic electronic states converge, i.e., in the vicinity of the 'intended' crossing.

At this point, it may seem that charge transfer reactions have been rendered impossible. To understand why they still occur, consider a system of two molecules and a single excess charge, as depicted in Figure 2.3. Both molecules host a localised electronic state (the frontier orbitals) that the charge may occupy. At first considered independently, two approximately parabolic PESs can be drawn, representing the molecular coordinates of the system when the charge is occupying one or the other state. When coupling between the states is introduced, an avoided crossing is established on the potential energy diagram. The charge's ability to partially occupy both states simultaneously means that the eigenstates of the system no longer match the eigenstates of the isolated molecules, but will instead be some mixture of them. The energy of the system is then described by two new curves, whose correspondence to the original parabolas depends on the strength of electronic coupling (J) between the local states.

In molecular systems, the coupling between MOs is often small. For nearly all nuclear configu-

rations, the system wavefunction will be almost entirely weighted towards one local state at a time, meaning they can be used as a good approximation for the state of the system. To still include the effects of electronic coupling we adopt the *diabatic representation*. This involves describing the system using a basis set of electronic states chosen such that they do not respond to changes in the nuclear coordinates. Since the coupling between diabatic states does not occur through the nuclear dynamics, avoided crossings no longer appear on the potential energy diagram. This picture allows us to recover the description of charge transfer as a distinct event, a transition between states, which will be examined further in the next section. For the system shown in Figure 2.3, the PESs associated with diabatic and adiabatic states may be seen in Figure 2.4.

2.3.2 Hopping Rates

To investigate transport, we are principally concerned with how fast charges move from molecular site to molecular site. Treating the electronic coupling as a perturbation acting on the diabatic states, a rate of charge transfer ($\Gamma_{i\to f}$) can be deduced, starting from *Fermi's golden rule*:

$$\Gamma_{i\to f} = \frac{2\pi}{\hbar}|\langle\Psi_i|H'|\Psi_h\rangle|^2\delta(E_i - E_f), \tag{2.3}$$

where $\langle\Psi_i|H'|\Psi_h\rangle$ is the matrix element describing the coupling between initial (i) and final (f) states. The Dirac delta function $\delta(E_i - E_f)$ enforces energy conservation by allowing transitions only between states when they have the same energy. We can apply the Franck-Condon principle to simplify the transition matrix factor, separating it into an electronic coupling term (J_{if}), and a nuclear overlap term ($\langle\chi_i|\chi_f\rangle$):

$$\langle\Psi_i|H'|\Psi_h\rangle = \langle\Phi_i|H'|\Phi_f\rangle\langle\chi_i|\chi_f\rangle = J_{if}\langle\chi_i|\chi_f\rangle. \tag{2.4}$$

Since we are interested in any transition that takes us between initial and final electronic states, we sum over all the combinations of nuclear vibrational states that could enable this transition, resulting in a transition rate of

$$\Gamma_{i\to f} = \frac{2\pi}{\hbar}\sum_{\upsilon}\sum_{\upsilon'}\left[Z^{-1}\exp\left(\frac{-E_\upsilon}{k_\mathrm{B}T}\right)|\langle\chi_\upsilon|\chi_{\upsilon'}\rangle|^2\delta(E_i - E_f)\right], \tag{2.5}$$

where υ and υ' denote the initial and final nuclear vibrational states. The initial phonon occupation probabilities follow a Boltzmann distribution, $Z^{-1}\exp(-E_\upsilon/k_\mathrm{B}T)$, where Z is the partition function.

Figure 2.5 illustrates how excitations of certain nuclear vibrational modes can enable the transition by bringing the system into a nuclear configuration accessible to both reactants and products. The restoring forces associated with each mode will give them a characteristic frequency ω which results in a spacing between vibrational energy levels of $\hbar\omega$. At high temperatures, the energetic spacing for all modes will be small compared to $k_\mathrm{B}T$. Vibrational energies can then be treated as a continuum,

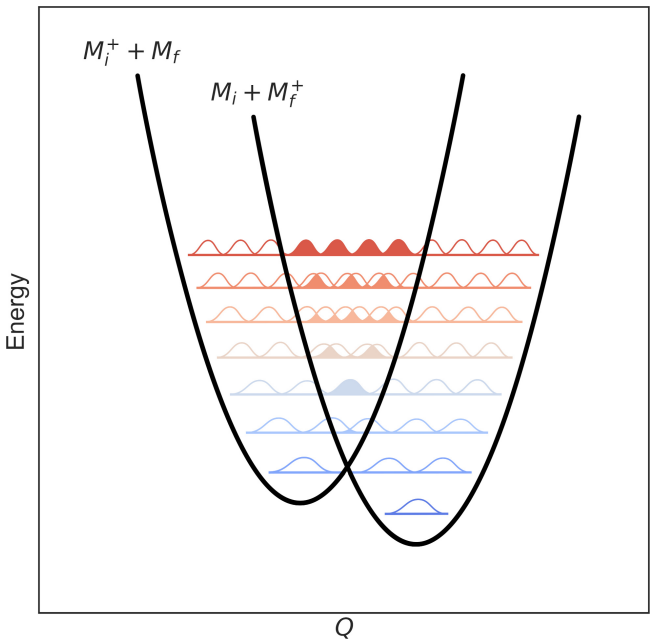


Figure 2.5: Potential energy diagram for a charge transfer reaction. The horizontal lines indicate different energy states of a single vibrational mode. The humps illustrated on each line represent the squared wavefunction of each vibrational state. In other words, they indicate the probability of finding the system at different nuclear configurations. The filled regions demonstrate how certain nuclear vibronic excitations can enable the reaction by bringing the system into a configuration that is allowed for both reactants and products.

meaning that quantum effects are negligible, and all nuclear dynamics may be approximated as classical. If the initial and final PESs are also approximated as parabolic, then the *semi-classical* or *high-temperature Marcus rate* for electron transfer [42–45] may be derived from Equation 2.5, taking the form

$$\Gamma_{i\to f}^{\text{Marcus}} = \frac{|J_{if}|^2}{\hbar}\sqrt{\frac{\pi}{\lambda k_{\text{B}}T}}\exp\left(-\frac{(\Delta\epsilon_{if}+\lambda)^2}{4\lambda k_{\text{B}}T}\right) \tag{2.6}$$

where we have introduced the *reorganisation energy* λ, and the difference in equilibrium energies between the two surfaces $\Delta\epsilon_{if}$. These are shown graphically in Figure 2.4, and will be discussed in more detail in the following section.

At intermediate temperatures, there may be high-frequency intramolecular modes contributing to λ for which the spacing between vibrational (phonon) energy levels is no longer large compared to $k_{\text{B}}T$. In this situation, accounting for quantum effects may be important for accurate calculations of charge transfer rates. *Marcus-Levich-Jortner* (MLJ) theory is an extension of Marcus theory which accounts for electron-phonon coupling associated with a single high-frequency vibrational mode [46]. This is typically chosen to be the C=C stretching mode, since this tends to be significantly involved in intramolecular reorganisation. MLJ theory provides a more accurate description of the charge transfer reaction, at the expense of requiring more knowledge about the molecules involved. However, the largest deviations between Marcus theory and MLJ occur only in the inverted regime, when $-\Delta\epsilon_{if} > \lambda$. For the investigations described in this thesis, λ was generally large enough that we were not likely to

encounter the inverted regime. Based on this, Marcus theory was assumed to strike a reasonable balance between predictive power, and a generality of application derived from its simplicity.

2.3.3 Electronic Structure Parameters

Here I discuss the physical origins of the electronic structure parameters in the Marcus rate equation (J_{if}, λ, $\Delta\epsilon_{if}$), and briefly introduce approaches for calculating their values.

Electronic Coupling

The electronic coupling, J_{if}, also known as the *transfer integral*, is approximately proportional to the degree of overlap between the frontier MOs of the two molecules involved in the charge transfer reaction [47, 48]. It quantifies the strength of the interaction between the initial and final states of the excess charge.

Methods for calculating J_{if} are described in detail in Section 3.1.5. For now, it is worth mentioning that, since the magnitude of the MOs feature an approximately exponentially decreasing distance-dependent part, the overlap between MOs will also tend to decrease approximately exponentially with increasing separation distance between the molecules.

Reorganisation Energy

The reorganisation energy, λ, is an energy cost that arises because the equilibrium conformations of both reacting molecules, plus the local environment, are different before and after the charge transfer reaction takes place. λ can be separated into inner-sphere (conformational changes of the reacting pair) and outer-sphere (conformational changes of the surrounding molecules[6]) contributions, denoted by λ_{inner} and λ_{outer}, respectively.

Typically, the two contributions are expected to be of a similar order of magnitude. However, λ_{outer} is difficult to evaluate and is often neglected. In some cases, it may be evaluated empirically from the *activation energy* (E_{A}) observed in temperature-dependent experimental measurements of charge transfer reactions. E_{A} will also contain contributions from λ_{inner} and $\Delta\epsilon_{if}$, although these may be calculated independently (see next subsection), allowing one to estimate λ_{outer}.

λ_{inner} can be calculated by considering the difference between the energy of the reactants when they are held in the nuclear configuration of the products, the energy of the products when they are held in the nuclear configuration of the reactants, and the energies of their equilibrium configurations. This constitutes the *four-point method* [49].

Both contributions are likely to remain approximately constant for charge transfer reactions within a single-component material system, although there may be different λ associated with intrachain and interchain transfer in conjugated polymer systems.

[6] plus positional and orientational changes in the case of small solvent molecules.

Difference in Equilibrium Energies

$\Delta\epsilon_{if}$ is the difference in the energy of the relaxed system before and after the charge transfer reaction. The largest contribution to variations of the system energy generally originates from differences in the energy levels of frontier MOs between the reacting molecules. These energy levels are determined by the strength of interactions experienced by an excess charge when it is localised on each of the molecules in the material, with shifts between different molecular energy levels arising from conformational differences between molecules, as well as electrostatic interactions and induction interactions involving the charged molecule and its environment [50].

In principle, conformational contributions to the frontier MO energies of all molecules in a modelled system can be computed from electronic structure calculations (see Section 3.1). The environmental contributions may also be computed using, for instance, microelectrostatics calculations [51] (see Chapter 8). However, these approaches may be computationally unfeasible for large systems, so the MO energies are often drawn from an approximate distribution. In many OSCs, the frontier MO energies tend to follow a density of states (DoSs) with a characteristic Gaussian shape, which can be observed experimentally, for instance using energy resolved electrochemical impedance spectroscopy [52]. Based on this, it is common practice to model energetic disorder in the solid state using energies randomly drawn from a Gaussian distribution [53]. The width of the Gaussian DoS may be approximated from experimental probes of the DoS, or it may be set with reference to E_{A}.

2.4 Charge Transport

2.4.1 Hopping Transport

The charge transfer rates derived above are applicable in the low-coupling regime, where $J_{if} \ll \lambda$. This condition applies to many OSC materials, and denotes the fact that their soft microstructures will shift in response to the presence of an excess charge. This induces a degree of polarisation centred on the charge, which acts to localise and energetically trap it at each given molecular location. The combination of the excess charge and the local distortion of molecules may be described by a pseudo-particle called a *polaron*. The consequence of this self-trapping effect is that charge carriers are subject to potential barriers that must be overcome for each transfer onto a new molecule. Transfer events must be *thermally activated* to overcome these barriers, with the result being that transfer rates will increase with increasing system temperatures. This is accounted for by the temperature-dependent exponential factor in Equation 2.6.

In this regime, charge transport is simply the cumulative effect of a series of uncorrelated charge transfer events, which are commonly referred to as *hops*. Since the individual hopping events are thermally activated, the overall mobility of materials with hopping-based transport will also increase

with temperature. This characteristic temperature-dependence of mobility can be observed in transport experiments [25].

Mobility in an Ordered 1D System

For a charge carrier in an ordered 1-dimensional system, such as in a molecular crystal, it is possible to derive an expression for the mobility (μ) based on the Marcus rate equation (Equation 2.6). Consider a system comprising a linear chain of sites (representing HOMOs) with equal energies, separated by an inter-site distance a. Each site is coupled to its immediate neighbours with strength J. Under the influence of an applied electric field with strength F, a hole placed on one of these sites can hop forward (+) or backwards (−) along the chain, with respect to the field direction. Using Equation 2.6, the forward and backwards hopping rates are given by

$$\Gamma_{\pm} = \frac{|J|^2}{\hbar}\sqrt{\frac{\pi}{\lambda k_{\mathrm{B}} T}}\exp\left(-\frac{(\lambda \pm \mathrm{e}aF)^2}{4\lambda k_{\mathrm{B}} T}\right), \tag{2.7}$$

where the effect of the field has been included as a change in system energy associated with hopping forwards or backwards. In the limit of low field strength, this may be approximated by

$$\Gamma_{\pm} = \frac{|J|^2}{\hbar}\sqrt{\frac{\pi}{\lambda k_{\mathrm{B}} T}}\exp\left(\frac{-\lambda}{4k_{\mathrm{B}} T}\right)\left(1 \pm \frac{\mathrm{e}aF}{2k_{\mathrm{B}} T}\right). \tag{2.8}$$

The net velocity of holes v is related to the forward and backwards hopping rates by

$$v = a(\Gamma_{+} - \Gamma_{-}) = \frac{|J|^2}{\hbar}\sqrt{\frac{\pi}{\lambda k_{\mathrm{B}} T}}\exp\left(\frac{-\lambda}{4k_{\mathrm{B}} T}\right)\frac{\mathrm{e}a^2 F}{2k_{\mathrm{B}} T}, \tag{2.9}$$

from which we can find the mobility of the system, by dividing by the field strength:

$$\mu = \frac{|J|^2}{\hbar}\sqrt{\frac{\pi}{\lambda k_{\mathrm{B}} T}}\exp\left(\frac{-\lambda}{4k_{\mathrm{B}} T}\right)\frac{\mathrm{e}a^2}{2k_{\mathrm{B}} T}. \tag{2.10}$$

This expression may be applied to predict the low field limit of mobility for transport through an ordered system, such as a molecular crystal, or between chains in the ordered regions of a semicrystalline polymer. It is valid so long as the electronic structure of the system can be treated as comprising a series of localised and weakly coupled frontier orbitals. The expression is less physically valid for modelling intrachain transport in conjugated polymers, which is likely to involved strong electronic coupling. In this situation, a hopping mechanism may not be an appropriate description of transport along the backbone. This has potential ramifications for one of the investigations described in this thesis, and will be discussed further in Section 6.2.3.

2.4.2 Transport Beyond the Hopping Regime

Hopping is not always an appropriate description of the charge transport mechanism in OSCs. In fact, by focusing on the requirement that the timescales of hopping must be longer than the timescales of thermal relaxation, Alessandro Troisi was able to make a succinct argument that mobilities $\gtrsim 0.1\,\mathrm{cm}^2/\mathrm{Vs}$ cannot be due to a hopping mechanism alone [54]. In this section I will briefly outline some of the alternative transport mechanisms that may occur in OSCs.

In the limit of very high coupling ($J \gg \lambda$) and low energetic and structural disorder, as is typical for metals or crystalline inorganic semiconductors, transport may be described well by *band theory*. In this picture, charge carriers move through the solid as delocalised Bloch waves. This mechanism imparts a high mobility on materials that characteristically decreases with increasing temperature, due to the increased phonon scattering interrupting otherwise ballistic transport. Although relatively rare compared to more dispersive transport mechanisms, band-like transport has been detected in some highly pure and structurally ordered organic crystalline materials [55, 56].

Between the limits of low- and high-coupling, where hopping or band-like models may be applied respectively, lies the intermediate regime ($J \simeq \lambda$). To describe transport under these conditions, which are particularly applicable to crystalline OSCs, the more recent theory of *transient localisation* has been developed [11, 57]. This theory is used to describe a situation where electronic and intermolecular nuclear motion are highly interlinked. The electronic coupling between frontier orbitals is large enough to support delocalisation of charges across multiple molecular sites, but this is continuously disrupted by dynamic coupling disorder induced by thermal vibrations. This leads to a mechanism of transport in which charges typically occupy delocalised states, where they can exhibit band-like characteristics, but are transiently localised on timescales shorter than typical molecular motion. Despite the localising effect of molecular motion, mobilities still follow a decreasing relationship with temperature, reminiscent of band transport.

An alternative picture of transport in the intermediate regime, that reproduces experimentally-verified mobility predictions from transient localisation theory, has been proposed based on simulations of charge dynamics in molecular crystals at ambient temperatures [58–60]. In this picture, charges are typically localised onto a small number of molecular sites, but may be transported by short bursts of delocalisation (again, induced by nuclear motion) before re-localising in a different position. Transport therefore occurs through a series of diffusive hops, although these tend to be between spatially-separated molecular sites rather than immediate neighbours, as in the traditional hopping regime. Under these circumstances, the label transient *de*localisation has been proposed as a better descriptor of charge transport behaviour.

Although it is important to recognise the different transport behaviours that can occur in OSC materials, in this thesis my focus is on structurally disordered materials, where we can expect electronic

coupling to be relatively weak. Thus, we can expect the hopping model of transport to be generally applicable.

2.4.3 Charge Transport Models

Since overall charge transport represents the cumulative effect of large numbers of charge transfer events, gaining a picture of the transport behaviour in a given OSC system generally requires the application of computational models. Such models allow us to 'average over' the individual events to evaluate the (ideally) macroscopic transport behaviour of the system. There exist a number of models that can be applied to perform this averaging [17, 61]. Each comes with its own set of assumptions and approximations, so the choice of model can have a significant impact on the accuracy of results. This choice must be made with respect to a prior estimation of which system characteristics are important for controlling transport, as well as what information we would like to obtain from the application of the model.

Here, I briefly outline some of the commonly applied transport models used for understanding OSC materials. I aim to provide enough detail to justify my selection of methods for the investigations described in this thesis, although most theoretical and implementation details will be left to Chapters 3 and 4, and restricted to only those models which I applied.

Drift-Diffusion

Drift-diffusion models may be used to simulate charge transport from a device-level (macroscopic) perspective [17]. The basic drift-diffusion model originates from a simplification of the *Boltzmann transport equation*, used to describe the statistical behaviour of a non-equilibrium thermodynamic system. Integrating over momentum space to find the moments of the Boltzmann transport equation, we find that the current density through a system ($\mathcal{J}$) is given by

$$\mathcal{J} = \mathcal{J}_{\text{drift}} + \mathcal{J}_{\text{diffusion}}. \tag{2.11}$$

The terms are given by

$$\mathcal{J}_{\text{drift}} = \mathrm{e}n\mu F \quad \text{and} \quad \mathcal{J}_{\text{diffusion}} = \mathrm{e}D\nabla n, \tag{2.12}$$

where e is the charge of an electron, n is the carrier density, μ is the mobility of the system, and F is the strength of the applied electric field. The diffusion coefficient D is related to μ and the system temperature (T) via the Einstein relation

$$D = \frac{k_{\mathrm{B}}T}{\mathrm{e}}\mu. \tag{2.13}$$

As seen from the above equations, all material-specific information is wrapped up in the mobility parameter. This somewhat limits the use of drift-diffusion models when we would like to understand which material characteristics are important for determining μ. In this case, we must adopt further models to relate μ to material features such as the microstructure or energetic landscape (e.g., the density of trap states), which will carry their own sets of approximations and assumptions. As such, drift-diffusion models are decidedly not *ab initio*, and must be heavily parameterised on an empirical basis. Because of this, they can generally be used to *correlate* simulations to experimental evidence, but are limited in their utility for assigning *causation* to specific chemical- or micro-structural origins.

With this in mind, the advantage of drift-diffusion models lies in the fact that they can facilitate direct comparisons with experiments, since they solve for the macroscopic current density flowing through devices. Comparison is also made easier by the fact that, relative to other (microscopic) models, the additional computational cost of simulating high charge densities is small, which is valuable given the high charge density regime that many experiments are conducted in. A drift-diffusion model was used by my collaborators to fit μ values to experimental space-charge limited current (SCLC) measurements in the study described in Chapter 8.

In contrast to the above, the models described in the following subsections all take into account microscopic information about the molecules, and the interactions between them, within the OSC system of interest. This reduces the number of assumptions that must be made, but carries larger computational costs, which can only be accommodated for by reducing the scale of modelled systems. The result is that we can no longer simulate device-scale systems, but must instead consider transport through a small volume of the solid state. Therefore, care must be taken to ensure that the modelled region represents an appropriate sample of the full device microstructure.

Master Equation

Rather than dealing with explicit charges (as in the following two models), the *master equation* (ME) model describes the dynamics of charge carriers in terms of time-averaged site occupation probabilities [62–64]. The system is modelled as a set of simultaneous differential equations describing the continuous 'flow' of occupation probabilities through a static network representing the molecules and their interactions. These equations are referred to collectively as the master equation of the system. It is worth clarifying that the occupation probabilities do not represent charge delocalisation or a quantum superposition, since, in most cases, the model assumes a localised hopping mechanism for charge transfer. Rather, the probabilities express where spatial charge density is likely to build up or dissipate from in the system.

Solving the ME may be performed using linear algebra methods. Under the typical assumption of low charge density, this has the advantage of being fast and computationally inexpensive for small systems. The computational cost and speed of solving the ME is largely independent of the charge

transfer rates in the system, meaning that this approach is well-suited to modelling systems with large variance in the magnitude of rates, such as those featuring energetic traps. Solving the ME returns the occupation probability density of the system, which is useful in itself for understanding charge behaviour, but may also be used to compute μ from an additional matrix multiplication step. When a solution is found, it is guaranteed to describe the steady state of the system, which means it can be related directly to the time-independent characteristics of the material, such as μ. The solution is further guaranteed to be unbiased by statistical errors that may be introduced by stochastic models (see next subsection).

As for the disadvantages of applying an ME model, I have already mentioned how a hopping mechanism for charge transfer is typically assumed. The assumption of a steady state also prevents transient effects from being explored. Furthermore, the computational cost of solving the ME increases rapidly with the number of molecules in the system. This generally restricts the ME model to evaluating relatively small systems. If multiple charges are included in the model, then the resulting charge correlation requires an ME composed of non-linear equations. These may be difficult or impossible to solve, which further restricts ME models to evaluating systems of very low charge density, where such correlations can be neglected. Finally, no information at all is returned until the full system has been solved, which may take an undetermined amount of computational time.

Further details about the methodological underpinnings of ME models may be found in Section 3.3.2. Details about the development and implementation of a particular ME model may be found in Section 4.4, with results from its application provided in Section 4.5.2.

Kinetic Monte Carlo

A *kinetic Monte Carlo* (KMC) model can be used to simulate transport in a manner that mimics the physical time-evolution of explicit charges moving through a material [65, 66]. Many features are similar to those adopted by the ME model, so these two approaches are often compared [61]. In particular, both models assume a hopping mechanism for charge transfer events, and simulate transport through a static network representing the molecules and their interactions. Unlike the ME model however, the KMC model is solved by a stochastic method that operates by randomly selecting charge transfer events based on their probabilities. Across multiple runs with long enough simulation times, the charges will explore the system of interest. Information about the system, such as μ, can then be calculated by averaging over the charge motion exhibited during each run, with multiple runs being averaged together until μ converges to a stable value.

Potentially the biggest advantage over ME models is that, in principle, systems of arbitrary size can be modelled, with simulations always providing at least an approximate result for μ. Although the accuracy of this approximation is likely to be low at first, increased accuracy can always be straightforwardly achieved by allowing for longer simulation times or more repeat runs. This makes

KMC models well suited for evaluating large, complex systems. A related benefit is that KMC models can output preliminary estimates for μ during run-time, which can be useful for checking the progress of simulations, and quickly identifying and fixing potential issues if required. In terms of the scope of included effects, KMC models have the advantage of being able to probe both transient and steady state effects. This is useful for comparison with transient experiments such as *time-of-flight* mobility measurements. Charge correlation effects can also easily be included, allowing for multiple charge carrier simulations, although long-range Coulombic interactions can significantly reduce the efficiency of the time-propagation algorithm (see Section 3.3.1).

As for the disadvantages of KMC models, similar to ME models, they also typically assume a hopping mechanism for transport, although recently a delocalised-KMC model has been demonstrated [67]. Compared to ME models, the numerical efficiency of KMC models is reduced significantly by large variances in the charge transfer rates, which can slow down convergence (the origin of this issue is explained in Section 3.3.1). A more fundamental issue may result from the stochastic nature of the model. As with all Monte Carlo methods, there is always a risk of *false convergence* events. This involves the 'accidental' fulfilling of convergence criteria, halting simulations early, and returning an erroneous value for μ. These potential issues highlight the fact that, when setting up a KMC simulation, parameters such as the number of repeat runs, simulation time, and convergence criteria, must all be decided by the user, which can introduce statistical bias.

Further details about the methodological underpinnings of KMC models may be found in Section 3.3.1. Details about the development and implementation of a particular KMC model may be found in Section 4.3, with results from its application provided in Sections 4.5.1 and 6.2.3.

Non-adiabatic Molecular Dynamics

A notable drawback of the ME and KMC models is that they neglect nuclear motion. This can have a significant impact in the intermediate-coupling regime, where dynamic coupling disorder linked to nuclear motion has been shown to be an important factor influencing charge transport [57, 68, 69]. This touches on a further drawback of hopping-based models, namely that they treat electronic coupling between localised states perturbatively. This rests on the assumption that the coupling is relatively weak, which by definition is not applicable to the intermediate-coupling regime.

A number of *non-adiabatic molecular dynamics* (NAMD) models have been developed to account for the effects of intermediate coupling and nuclear motion [70, 71]. Here, I briefly outline one of the more commonly applied models from this class, namely *fewest switches surface hopping* (FSSH) molecular dynamics (MD), which combines classical molecular dynamics (see Section 3.2) with electronic transitions [72, 73]. For simplicity, I will describe the operation of this model for a system containing a single mobile electron.

The term 'non-adiabatic' refers to the fact that we are dealing with a situation where the BO

approximation is allowed to partially break down. Rather than being fully separated, the electronic and nuclear motion are coupled, meaning that nuclear motion can induce non-adiabatic state changes for the electron. Notably however, the model assumes that the states the mobile electron can occupy *at any one time* are adiabatic. This is why the breakdown of the BO is only partial, an assumption that must be made to allow for a classical treatment of the nuclear dynamics. The non-adiabatic part then comes in by the fact that the adiabatic states have non-vanishing non-adiabatic coupling between them. This coupling is influenced by the nuclear motion, and is utilised to allow the mobile charge to transfer into different adiabatic states.

During operation, the FSSH MD model propagates a superposition of adiabatic electronic states using the time-dependent electronic Schrödinger equation. Meanwhile, the nuclei evolve classically on the PES established by the currently occupied adiabatic electronic state. The motion of the nuclei influence the time-evolution of the adiabatic electronic states, and the non-adiabatic coupling between them. The reciprocal influence of the mobile electron on the nuclear motion is incorporated by allowing the electron to stochastically transfer between different adiabatic states ('switching' the nuclear motion onto a different PES, hence the name *surface hopping MD*). The probabilities for switching between different PESs are controlled by the non-adiabatic coupling between the adiabatic electronic states. An algorithm is included in the model which minimises the number of PES transitions, while maintaining the correct average population of each adiabatic state. This improves the efficiency of simulations, and gives the model its name *fewest switches* [72, 74].

Compared to the KMC and ME models, NAMD models are decidedly 'more *ab initio*'. Fewer assumptions are made about the nature of charge transport, and in particular the mechanism of charge transfer. This means that NAMD models can be applied to a broader range of systems, including systems in the intermediate-coupling regime, while maintaining convergence with hopping-based models in the low-coupling regime [75]. Furthermore, it means that such models can be used to interrogate a broader range of factors that may influence transport behaviour, including the effects of dynamic coupling disorder, and the nature of the charge transfer mechanism itself.

The main trade-off is the high computational cost of applying a NAMD model, which can limit the size and complexity of systems that can be evaluated. In systems where a hopping-mechanism can be safely assumed, this cost comes without any significant improvement in the accuracy of results, compared to ME or KMC models. A significant contribution to the high computational cost of the model arises from the need to calculate the coupling between electronic states on-the-fly during simulations. This typically requires the adoption of a fairly simple model to perform quick coupling calculations, which may not be accurate under all circumstances. A further drawback is that systems cannot generally be parametrised using information not already included in the NAMD model, such as non-local electrostatic effects, which would be too expensive to calculate on-the-fly during operation [60].

Results from the use of a FSSH MD model by my collaborators are provided in Section 8.3.1, where

they are compared against a KMC approach.

2.5 Donor-Acceptor Polymers

In Section 1.1, I laid out the typical correspondence observed between increased microstructural order, higher mobilities, and improved device performance, and stressed the importance of studying those material cases where this correspondence breaks down. Donor-acceptor polymers represent a class of materials which often deviate from this pattern, commonly displaying high hole mobilities but relatively disordered microstructures compared to well-known semicrystalline polymers [26–32]. For this reason, a significant portion of this thesis centres on the investigation of a notable example from this class, C16-IDTBT (see Chapters 5 and 6. Chemical structure is shown in Figure 5.1). Here, I summarise information from past studies relevant to donor-acceptor polymers in general, and C16-IDTBT in particular, to provide context for my investigation.

2.5.1 Before Donor-Acceptor Polymers

Although now challenged by the discovery of a new class of high-mobility polymers displaying unusual levels of structural disorder, traditionally the best transport behaviour in polymers was associated with a semicrystalline morphology, as displayed by the archetypal P3HT. In line with the relatively clear guidelines established for small molecule OSCs – a high degree of crystallinity, with close π-π stacking, preferably in multiple directions, all minimally disrupted by defects and thermal vibrations [12] – it was believed that a microstructure containing well-ordered crystal domains was ideal for transport in polymers.

Since the relatively fast motion of charge carriers along individual chains may be enabled by strong electronic coupling along conjugated backbones, the limiting factor for macroscopic transport is generally assumed to involve the slower hops between chains [76]. Based on this, the purpose of the crystalline domains is to facilitate fast rates of intermolecular charge transfer, by ensuring significant overlap between the MOs of closely packed chain segments. In fact, once this heterogeneous microstructure is established, there is evidence that the amorphous fraction does not participate in transport at all, resulting in percolation-type behaviour. For instance, FET measurements of P3HT reveal a significant jump in mobility as the crystalline volume fraction increases from 5% to 20%, assigned to the attainment of a critical percolation threshold [77]. This is suggested to occur because the amorphous regions feature a widened band gap – the result of contorted chains with shorter conjugation lengths – making it energetically favourable for charge carriers to remain within the crystalline domains only. The presence of 'tie-chains' with segments belonging to multiple ordered domains are thus required for charge carriers to cross the amorphous regions between domains [78–80].

Within the semicrystalline paradigm, the most essential target for achieving good bulk transport

relies on using a combination of 1) a large crystalline volume fraction, and 2) high molecular weight (for long tie-chains), to ensure a sufficiently connected percolation network. Further improvements may then be sought by increasing the regularity of the crystallites. A standout success of these guidelines was the discovery of PBTTT, which, by way of interdigitating side chains, has a crystalline structure that effectively extends into an additional dimension compared to P3HT.[7] The typical mobilities of $\sim$0.01 cm^2/Vs for P3HT were thus surpassed, with $\sim$0.5 cm^2/Vs being typical for PBTTT [12, 77, 81].

However, not all polymers appear to follow the principle, charted by the switch from P3HT to PBTTT, of better transport performance being tied to increasing crystallinity and crystalline order. More recently developed donor-acceptor copolymers are regularly reported to exhibit high mobilities, despite often lacking signs of long-range order. One example that has sustained interest since its discovery is C16-IDTBT, which was first reported with a mobility of 1 cm^2/Vs [82, 83], increasing to 3.6 cm^2/Vs a few years later [29].

2.5.2 C16-IDTBT: History and Applications

C16-IDTBT was one member of the new class of donor-acceptor copolymers whose apparently incongruous characteristics of high mobility and low structural order disrupted the traditional consensus that the best mobilities would be found by semicrystalline polymers with ever-increasing degrees of crystalline order and crystalline volume fraction.

Donor-acceptor copolymers were originally developed for OPV applications, since their alternating backbone structure enables the optical band gap to be tuned through the visible and near-infrared spectral bands [12, 26, 84]. However, it was found that the smaller intrachain bandwidth induced by the donor-acceptor structure also made transport more resilient to conformational disorder, which may otherwise induce energetic traps [11, 85, 86].

Early on, IDTBT, with various side chains, was put forward as a possible material for use in transistors [82] and OPV devices [83, 87, 88]. However, its consideration as a donor in OPV devices was not long lasting, because the long C16 side chains that (unusually) provide the best mobilities, also prevent good intermixing with acceptor molecules, resulting in low device efficiencies of 0.66%, as reported by Bronstein et al. [83]. On the other hand, OPV devices using IDTBT with shorter branched side chains have been shown to reach moderate efficiencies, up to 5.5% [87], despite the lower mobilities of these variants.

Because of its high mobility, and useful mechanical properties, such as high ductility and stretchability, C16-IDTBT has maintained interest for possible integration into flexible, wearable and biocompatible electronics [89–91], as well as representing an interesting case study for furthering our understanding of the microstructure-transport link in conjugated polymers.

[7] i.e., π-stacking direction, backbone direction, and side chain direction for PBTTT (3D), compared to just the π-stacking and backbone directions for P3HT (2D).

2.5.3 C16-IDTBT: Microstructure and Transport

The disordered microstructure of C16-IDTBT limits the amount of information that can be gained from experimental diffraction methods [29]. However some microstructural details have been previously reported. From these, and chemical-structural considerations, we can gain some understanding of the origins of C16-IDTBT's high mobility.

The bonds linking the IDT and BT units are collinear, and torsional rotation between them is restricted by a relatively high potential barrier [86, 87]. This indicates support for fast intrachain charge transport, with simulations suggesting intrachain mobilities of $\sim 3\,\mathrm{cm}^2/\mathrm{Vs}$ at room temperature [92]. This is larger than most experimental measurements of bulk mobility, suggesting that the transfer of charges between backbones acts as a limiting bottleneck to transport. This view is supported by evidence that the mobility increases with chain length, only levelling off for ultra-high molar mass samples of $500\,\mathrm{kg\,mol}^{-1}$ and beyond [91]. Notably, the increase of mobility with chain length is gradual; there is no step change that would indicate the crossing of a percolation threshold, such as occurs in semicrystalline polymers.

Diffraction experiments conducted by Zhang et al. demonstrated that the conjugated planes of chain backbones are almost universally oriented face-on with respect to the substrate and upper interface [29]. Furthermore, these experiments indicated a spacing of 3.8 Å between backbones in the π-stacking direction. Although the number of chains participating in these stacks is very low in C16-IDTBT, this spacing is comparable to the interchain spacing in highly crystalline polymers. Despite lacking the signs of long-range interchain order that would indicate the presence of crystallites [29, 82], recent works by Cendra et al. and Dobryden et al. have pointed towards other signs of unconventional ordering at the mesoscale that may impact interchain charge transfer. In particular, domains of aligned backbones have been observed via low-dose high-resolution transmission electron microscopy (HRTEM) [93] and atomic force microscopy (AFM) [94]. On its own, however, packing within these domains is unlikely to be responsible for the efficient transfer of charges, since adjacent backbones are separated by a relatively large spacing of 1.6 nm [94]. Furthermore, the space between the edge-wise packed backbones is occupied by insulating side chains. Importantly however, analysis of the HRTEM measurements also showed a degree of ordering *between* domains, with backbones preferentially crossing at 20° and 90° in regions of domain overlap [93].

Although we know comparatively less about the nanoscale picture in C16-IDTBT – i.e., the local scales most relevant to interchain contact and charge transfer rates [95, 96] – it is generally believed that backbone contacts involve the BT unit of the monomer. This was suggested by Thomas et al. based on the fact that the attachment locations of the four bulky side chains are likely to sterically inhibit contact between IDT units [97, 98]. This is supported by solid-state nuclear magnetic resonance measurements of another BT containing copolymer, which indicated that BT-BT contacts dominate

interchain interactions [99]. The suggestion of BT contact is also present in a microstructural organisation for C16-IDTBT, proposed in a work by Makki et al., involving a mesh-like arrangement of parallel and perpendicular chains contacting via BT units [100]. This arrangement bares similarities to the cross-hatched crystallite structures described in some semicrystalline polymers [101, 102].

With the above in mind, several questions remain about the microstructure-transport link in C16-IDTBT (see Sections 5.1 and 6.1). For this reason, an investigation into this material forms a large portion of this thesis (see Chapters 5 and 6).

2.6 Scope of this Thesis

In this thesis, I describe a series of computational investigations into the relationship between microstructure and charge transport in OSC materials, with a particular focus on the role of microstructural disorder. For each of the material cases studied, there appears to be a breakdown in the typical correspondence, laid out in Section 1.1, between increased microstructural order, higher charge mobilities, and better device performance. This raises the question of how these materials are able to present the charge transport and/or performance metrics they do, in spite of their typically high degrees of microstructural disorder. Is it the case that other factors compensate for the lack of crystalline order? If so, what are these factors? Alternatively, does the microstructure, while appearing from experiments to be disordered, in fact feature a non-traditional form of order which can explain the observed transport behaviour and performance?

I employ a multiscale modelling approach that includes the use of molecular dynamics (MD), density functional theory (DFT) and charge transport simulation methods. These methods are applied to various small molecule and conjugated polymer systems, with results compared against experimental and computational work performed by my collaborators. From this, I show how chemical structure determines molecular packing arrangements, how this impacts the strength of electronic coupling and broader microstructural trends, and how these factors govern the bulk transport properties of OSC materials and, where relevant, their performance in device applications.

A significant portion of this thesis is centred on rationalising the high mobility of the disordered polymer C16-IDTBT (Chapters 5 and 6), as well as exploring the potential effect on transport of modifying the IDTBT backbone (Chapter 7). Other parts of the thesis explore charge transport in the non-fullerene acceptor O-IDTBR (Chapter 8), bis-adducts of PCBM (Section 4.5.2), and interfacial photocatalytic polymer systems (Section 4.5.1), plus the development of charge transport codes (Chapter 4).

The specific research questions I seek to answer may be summarised as follows:

- What factors are responsible for the high hole mobilities displayed by C16-IDTBT? Specifically, how does its chemical structure influence its microstructure and electronic properties, and how do the features presented across multiple length-scales combine to explain its transport behaviour?
- In light of the factors governing transport in C16-IDTBT, how is transport likely to be affected by substituting heteroatoms onto the donor unit of the C16-IDTBT backbone?
- How does structural and energetic disorder govern the mechanism and speed of electron transport in O-IDTBR?
- How does molecular symmetry influence crystalline packing in bis-PCBM isotopes, and why do more crystalline isotopes tend to display lower electron mobilities?
- How does electron mobility impact the performance of polymer photocatalysts for hydrogen production? Specifically, why do low-mobility polymers often display the highest efficiencies in this application?
- Finally, how useful is a localised hopping model for describing transport in a range of OSC materials? In what situations is it appropriate? And when does it fail?

Chapter 3

Methods

3.1 Electronic Structure Calculation

The chemical structure of molecules, and the interactions between them, are governed by the quantum mechanical behaviour of electrons. This is described mathematically by the *Schrödinger equation*. The hydrogen atom has the distinction of being the only chemical system for which the Schrödinger equation may be solved analytically, since it is the only two-body system within chemistry. All other atoms, molecules, and groups of molecules constitute many-body systems, which must be solved numerically. Although important for the functioning of many OSC devices, the work covered in this thesis does not involve the study of optical excitations. For this reason, in the following derivations, I focus on methods for understanding the *ground state electronic structure* of a given system with neutral charge.[1] Because we are generally interested in understanding steady state behaviour, we begin our derivations from the time-independent Schrödinger equation.[2]

To understand the behaviour of electrons in molecular systems, we start by applying the *Born-Oppenheimer* (BO) approximation, treating the nuclei as a fixed background (i.e., 'external') potential. The time-independent Schrödinger equation is then given by

$$\hat{H}_{\mathrm{e}}|\Phi\rangle = E|\Phi\rangle, \tag{3.1}$$

where $\hat{H}_{\mathrm{e}}$ is the Hamiltonian of the electronic system, E is the electronic system energy, and Φ is the wavefunction of the electrons. I note that here, and throughout this section, I have adopted atomic units ($\hbar = \mathrm{e} = a_0 = m_{\mathrm{e}} = 1$). The Hamiltonian can be separated into three terms:

$$\hat{H}_{\mathrm{e}} = \hat{T} + \hat{V}_{\mathrm{ee}} + \hat{V}_{\mathrm{ext}}, \tag{3.2}$$

[1] In the context of charge transport – for which excess charges are present by definition – the use of neutral molecules in calculations of electronic coupling is justified by my adoption of the *frozen orbital approximation* (see Section 3.1.5).

[2] The summarised derivations of Hartree-Fock theory and density functional theory provided over the following sections are based on those in [103]. Helpful clarifications were also provided by [104] and [105].

where $\hat{T}$ is the kinetic energy operator and $\hat{V}_{\text{ee}}$ is the electron-electron interaction operator. The external potential operator $\hat{V}_{\text{ext}}$ describes the interactions between the electrons and the fixed nuclear background. For an arbitrary wavefunction Φ (which does not necessarily need to be an eigenfunction of Equation 3.1), the average total energy of the electronic system is given by the expectation value of $\hat{H}_{\text{e}}$:

$$E[\Phi] = \langle \Phi | \hat{H}_{\text{e}} | \Phi \rangle. \tag{3.3}$$

The notation $E[\Phi]$ is used to demonstrate that the electronic system energy is a *functional*, which takes a wavefunction as a parameter. Since, by definition, the ground state energy (E_0) of the electronic system defines a lower bound for all possible energies ($E[\Phi] \geq E_0$) we can find E_0 by employing the *variational method*. This involves searching through all possible Φ, to find the one that minimises $E[\Phi]$. The Φ that produces E_0 will then describe the ground state (Φ_0) of the system.

Hartree-Fock Theory

Of course, it is not computationally feasible to search through an infinite range of both physical and non-physical Φ. Instead, an approximate ansatz for the electron wavefunction (ϕ) may be inserted in place of Φ. ϕ can then be iteratively updated to try and minimise the expectation value of $\hat{H}_{\text{e}}$, until an approximate ground state energy is found. The most common approach following this procedure is described by *Hartree-Fock theory*. This involves using a form of ϕ that is the product of single-electron wavefunctions. To account for the fermionic nature of electrons and the Pauli exclusion principle, ϕ is enforced to be antisymmetric with respect to the exchange of any two electrons. A wavefunction with these characteristics is described as a *Slater determinant*.

After inserting ϕ into Equation 3.1, the Schrödinger equation can be separated into a system of single-electron equations, termed the *Hartree-Fock equations*. Each equation describes the behaviour of a single electron under the influence of the average Coulombic potential of all other electrons, plus a non-local *exchange potential* that arises from the constraint that all single electron states (i.e., orbitals) must be orthonormal.

The main drawback of the Hartree-Fock (HF) method is that, by adopting a mean-field approximation for Coulombic interactions, it neglects the effects of *Coulomb correlation*. In simple terms, this means that it neglects the instantaneous reciprocal adjustments made by the electrons in response to each others movements. These adjustments occur even in the ground state of the system, due to the quantum nature of the particles. Because the mean field doesn't allow the electrons to respond to each other as effectively as in reality, this leads to an overestimation of the electron-electron repulsion energy.[3] For this reason, the ground state energy predicted by the HF method is consistently higher than experimental values.

[3] as well as a failure to capture effects such as London dispersion interactions.

The Coulomb correlation error inherent to the HF method can be accounted for by extensions of the theory, which typically relax the assumptions associated with the mean field approximation and use of a single Slater determinant to represent the electron wavefunction. This has led to a number of *post-HF* methods that can more accurately approximate the electronic structure and ground state energy. However, the computational cost of these methods is very high, and scales rapidly with the number of electrons, which makes them unfeasible for simulating many molecular systems.

3.1.1 Density Functional Theory

Density functional theory (DFT) represents an alternative approach to evaluating the electronic structure of a many-electron system. The central insight that enabled the development of the DFT method was that there exists a one-to-one correlation between the ground state electron density and the external potential representing the system of interest. Therefore, rather than solving for the many-body electron wavefunction, one only needs to find a function describing the spatial variation of the charge density ($\rho(\vec{r})$). Since the correlation is one-to-one, finding $\rho(\vec{r})$ allows for the unique determination of $\hat{H}_\mathrm{e}$, and from this, the full electron wavefunction Φ (including both exchange and Coulomb correlation), and all properties of the molecule. Thus, for a system of N electrons, the dimensionality of the problem is reduced from $3N$ in the HF approach, to only 3 in the DFT approach. This insight is equivalent to stating that the system energy is a functional of the charge density: $E[\rho(\vec{r})]$. Since each $\rho(\vec{r})$ corresponds to a single $\hat{H}_\mathrm{e}$, and therefore Φ, we can apply the variational method introduced above:

$$E[\rho(\vec{r})] \geq E_0. \tag{3.4}$$

This holds so long as we restrict $\rho(\vec{r})$ to only those charge density functions that reproduce the same number of electrons as the physical system of interest, after integrating over all space:

$$\int \rho(\vec{r})\,\mathrm{d}\vec{r} = N. \tag{3.5}$$

Thus, starting from a suitable functional form of $E[\rho(\vec{r})]$, the ground state electronic structure can be determined by iteratively adjusting $\rho(\vec{r})$ until the energy of the system is minimised.

In the *Kohn-Sham* approach, the charge density is represented by a set of N fictitious non-interacting orthonormal single-electron orbitals:

$$\rho(\vec{r}) = \sum_i^N |\phi_i(\vec{r})|^2. \tag{3.6}$$

Using this representation, the energy functional can be separated into the following terms:

$$E[\rho] = T_s[\rho] + V_\mathrm{ext}[\rho] + V_\mathrm{H}[\rho] + E_\mathrm{xc}[\rho], \tag{3.7}$$

where $T_s[\rho]$ is the kinetic energy functional for the non-interacting orbitals, given by

$$T_s[\rho] = -\frac{1}{2}\sum_i^N \langle\phi_i|\nabla|\phi_i\rangle. \tag{3.8}$$

$V_{\text{ext}}[\rho]$ is the external potential functional, given by

$$V_{\text{ext}}[\rho] = \int \hat{V}_{\text{ext}}\rho(\vec{r})\,\mathrm{d}\vec{r}, \quad \text{with} \quad \hat{V}_{\text{ext}} = -\sum_\alpha^{N_\alpha} \frac{Z_\alpha}{\vec{r}_i - \vec{R}_\alpha}, \tag{3.9}$$

for N_α nuclei, each with nuclear charge Z_α, located at coordinates $\vec{R}_\alpha$. $V_{\text{H}}[\rho]$ is the classical Coulomb potential functional, i.e. the *Hartree energy*, given by

$$V_{\text{H}}[\rho] = \frac{1}{2}\int \frac{\rho(\vec{r}_1)\rho(\vec{r}_2)}{|\vec{r}_1 - \vec{r}_2|}\,\mathrm{d}\vec{r}_1\,\mathrm{d}\vec{r}_2, \tag{3.10}$$

and $E_{\text{xc}}[\rho]$ is the *exchange-correlation functional*, which accounts for the error made by assuming non-correlated orbitals in the previous terms. It is given by the difference between the true, correlated, kinetic energy ($T[\rho]$) and electron-electron interaction functionals ($V_{\text{ee}}[\rho]$), and the uncorrelated functionals:

$$E_{\text{xc}}[\rho] = (T[\rho] - T_s[\rho]) + (V_{\text{ee}}[\rho] - V_{\text{H}}[\rho]). \tag{3.11}$$

Writing Equation 3.7 in terms of the density constructed from non-interacting orbitals (Equation 3.6), and applying the variational principle, we find the following set of equations

$$\left(-\frac{1}{2}\nabla^2 + v_{\text{ext}}(\vec{r}) + \int \frac{\rho(\vec{r}\,')}{|\vec{r} - \vec{r}\,'|}\,\mathrm{d}\vec{r}\,' + v_{\text{xc}}(\vec{r})\right)\phi_i(\vec{r}) = \epsilon_i\phi_i(\vec{r}), \tag{3.12}$$

which are known as the *Kohn-Sham equations* [106]. The local potentials from external interactions and exchange-correlation interactions are given by

$$v_{\text{ext}}(\vec{r}) = \frac{\delta V_{\text{ext}}[\rho]}{\delta\rho} \quad \text{and} \quad v_{\text{xc}}(\vec{r}) = \frac{\delta E_{\text{xc}}[\rho]}{\delta\rho}. \tag{3.13}$$

Because we have, in theory, accounted for the Coulomb correlation errors neglected in the HF approach, if we can find the exact local potentials in Equation 3.13, this approach will give us the exact $\rho(\vec{r})$ and ground state energy. Notably, this is possible despite the fact that the Kohn-Sham equations describe a system of non-interacting fictitious electrons in an effective local potential. While formally true, determining the local potentials depends on knowledge of the exchange-correlation functional, $E_{\text{xc}}[\rho]$, which in practice must be approximated.

3.1.2 Exchange-Correlation Functionals

Here, I describe a series of approximate exchange-correlation functionals in order of increasing chemical accuracy, and increasing computational cost [103].

- The *local density approximation* (LDA) defines a form of $E_{\mathrm{xc}}[\rho]$ corresponding to a homogeneous electron gas with the same charge density as the system of interest, given by

$$E_{\mathrm{xc}}^{\mathrm{LDA}}[\rho] = \int \rho(\vec{r})\epsilon_{\mathrm{xc}}(\rho(\vec{r}))\,\mathrm{d}\vec{r}, \tag{3.14}$$

  where $\epsilon_{\mathrm{xc}}(\rho(\vec{r}))$ is a simple function of the local density at $\vec{r}$. This approximation is relatively poor in molecular systems, where the gradients of $\rho(\vec{r})$ can be steep, with a consquent effect on the energy of the system.

- The *general gradient approximation* (GGA) accounts for the local gradient of $\rho(\vec{r})$ at $\vec{r}$, yielding

$$E_{\mathrm{xc}}^{\mathrm{GGA}}[\rho] = \int \rho(\vec{r})\epsilon_{\mathrm{xc}}(\rho(\vec{r}), \nabla\rho(\vec{r}))\,\mathrm{d}\vec{r}. \tag{3.15}$$

- Hybrid exchange-correlation functionals include terms from the LDA and GGA, plus contributions from the exact exchange potential calculated by the HF approach.

For the investigations described in this thesis, I generally used the `cam-b3lyp` hybrid functional for DFT calculations [107]. This is based on the `b3lyp` functional [108, 109], which has the form

$$E_{\mathrm{xc}}^{\mathrm{B3LYP}} = E_{\mathrm{x}}^{\mathrm{LDA}} + a_0(E_{\mathrm{x}}^{\mathrm{HF}} - E_{\mathrm{x}}^{\mathrm{LDA}}) + a_{\mathrm{x}}(E_{\mathrm{x}}^{\mathrm{GGA}} - E_{\mathrm{x}}^{\mathrm{LDA}}) + E_{\mathrm{c}}^{\mathrm{LDA}} + a_{\mathrm{c}}(E_{\mathrm{c}}^{\mathrm{GGA}} - E_{\mathrm{c}}^{\mathrm{LDA}}), \tag{3.16}$$

where the exchange-correlation terms from each of the substituent functionals have been separated into exchange (E_{x}) and Coulomb correlation (E_{c}) contributions. The parameters $a_0 = 0.20$, $a_{\mathrm{x}} = 0.72$ and $a_{\mathrm{c}} = 0.81$ were set empirically by the functional's developers, by comparing DFT calculations with experiments. The `cam-b3lyp` functional improves the accuracy of calculations when long-range interactions are significant. This is achieved by partitioning the electron-electron repulsion operator into short- and long-range components. The `cam-b3lyp` functional smoothly transitions between these using a two-electron operator ($\frac{1}{r_{12}}$, where $r_{12} = |\vec{r}_1 - \vec{r}_2|$) with the form

$$\frac{1}{r_{12}} = \frac{(\alpha + \mathrm{erf}(\gamma r_{12})\beta)}{r_{12}} + \frac{1 - (\alpha + \mathrm{erf}(\gamma r_{12})\beta)}{r_{12}}, \tag{3.17}$$

where erf is the standard error function. The empirical parameter $\gamma = 0.33$ describes how quickly the included fraction of exact HF exchange potential is activated, from $\alpha = 0.19$ at short range to $\alpha + \beta = 0.65$ at long range [110].

3.1.3 Dispersion Corrections

Although the long-range corrections present in functionals such as `cam-b3lyp` can improve the accuracy of calculations by treating repulsive exchange interactions, none of the standard DFT approaches account for the long-range Coulomb correlations which are the physical basis for dispersion interactions. Dispersion forces play a significant role in dictating the conformations and packing arrangements present in molecular solids. Thus, it is important to accurately model them when predicting or rationalising microstructural features of OSCs. For the investigations described in this thesis, Grimme's D3 dispersion correction was included in DFT calculations [111]. This adds a semi-empirical dispersion term (E_{disp}) to energy calculations,

$$E_{\text{DFT-D3}} = E_{\text{DFT}} - E_{\text{disp}}, \tag{3.18}$$

where E_{disp} is separated into two terms,

$$E_{\text{disp}} = E^{(2)} - E^{(3)}, \tag{3.19}$$

which account for two- and three-body corrections respectively. The two-body term is most important, typically accounting for 90% - 95% of the dispersion correction. It is given by

$$E^{(2)} = \sum_{AB} \sum_{n=6,8,10,\ldots} s_n \frac{C_n^{AB}}{{r_{AB}}^n} f_{d,n}(r_{AB}), \tag{3.20}$$

which sums over atom pairings AB, separated by distance r_{AB}. The coefficients C_n^{AB} are derived *ab initio* from accurate time-dependent DFT calculations, while the scaling factor s_n is set empirically and varies with respect to the choice of exchange-correlation functional. The damping functions $f_{d,n}(r_{AB})$ are used to determine the range of the dispersion corrections, which helps to avoid singularities at small r_{AB}, and double counting of correlation effects at mid-range r_{AB} [112].

3.1.4 Basis Sets

The electronic wavefunction, and thus $\rho[\vec{r}]$, is represented by a linear combination of simple mathematical functions. These *basis functions* approximate the states (orbitals) that electrons can occupy. The form of the basis functions can affect the accuracy of the calculated $\rho[\vec{r}]$ and E_0, so it is important to choose a basis set that corresponds well with the system of interest. Furthermore, the accuracy of calculations can be affected by the size of the chosen basis set, with larger sets typically providing more accurate results, at the cost of higher computational expense. For the investigations described in this thesis, I employed a basis set consisting of Gaussian-type orbitals, which are appropriate for representing the atom-centred orbitals in molecular systems. In particular, I generally applied the `cc-pVDZ` basis

set. This includes polarisation functions and two sets of functions for describing each valence orbital. These features allow the `cc-pVDZ` basis set to accurately represent bonding in molecular systems, and thus the molecular π-orbitals important for charge transport considerations [113].

3.1.5 Electronic Coupling Calculations

Here, I provide a description of the *projective method*, used for calculating the strength of electronic coupling between a pair of molecules [114, 115]. To simplify the derivation, I assume we are dealing with a hole-transporting material, for which the HOMOs are the frontier orbitals of interest. We assume that the HOMO of the dimer (i.e. the molecule pair, labelled AB) can be approximated as originating from interaction between the HOMOs of the individual molecules (labelled A and B, with frontier orbitals ϕ_A and ϕ_B, respectively). This corresponds to the *frozen orbital approximation*, which can also be described as assuming that the only difference in the wavefunction before and after charge transfer is the difference in occupation of the HOMOs of the respective molecules.

For a Hamiltonian of the form

$$\hat{H} = \begin{pmatrix} \epsilon_A & J_{AB} \\ J_{AB} & \epsilon_B \end{pmatrix}, \tag{3.21}$$

with ϵ_A and ϵ_B representing the HOMO energies for A and B, the coupling is given by

$$J_{AB} = \langle \phi_A | \hat{H} | \phi_B \rangle. \tag{3.22}$$

Because $\hat{H}$ is not diagonal, we see that ϕ_A and ϕ_B are not eigenfunctions of $\hat{H}$. Instead, the eigenfunctions are the set of dimer orbitals $\{\phi_i^{AB}\}$. Using these, we can define the identity operator

$$\hat{1} = \sum_i |\phi_i^{AB}\rangle\langle\phi_i^{AB}|. \tag{3.23}$$

Inserting the identity operator twice into Equation 3.22, we find

$$J_{AB} = \sum_i \sum_j \langle \phi_A | \phi_i^{AB} \rangle \langle \phi_i^{AB} | \hat{H} | \phi_j^{AB} \rangle \langle \phi_j^{AB} | \phi_B \rangle. \tag{3.24}$$

Since $\{\phi_i^{AB}\}$ are the eigenfunctions of $\hat{H}$,

$$\langle \phi_i^{AB} | \hat{H} | \phi_j^{AB} \rangle = \begin{cases} \epsilon_i^{AB}, & \text{for} \quad i = j \\ 0, & \text{for} \quad i \neq j \end{cases}, \tag{3.25}$$

where $\{\epsilon_i^{AB}\}$ are the energies of the dimer orbitals, the summation simplifies to

$$J_{AB} = \sum_i \langle \phi_A | \phi_i^{AB} \rangle \epsilon_i^{AB} \langle \phi_i^{AB} | \phi_B \rangle. \tag{3.26}$$

$\langle\phi_A|\phi_i^{AB}\rangle$ and $\langle\phi_B|\phi_i^{AB}\rangle$, are *projections* of the isolated molecule HOMOs onto the MOs of the dimer. The projections can be determined by representing $|\phi_A\rangle$, $|\phi_B\rangle$, and $|\phi_i^{AB}\rangle$ in a common atom-centred basis set, yielding expansion coefficients $\{\zeta_\alpha^A\}$, $\{\zeta_\alpha^B\}$, and $\{\zeta_\alpha^{AB}\}$. Then, taking $\langle\phi_A|\phi_i^{AB}\rangle$ as an example, we find

$$\begin{aligned}\langle\phi_A|\phi_i^{AB}\rangle &= \sum_\alpha \sum_\beta \zeta_\alpha^A S_{AB} \zeta_\alpha^{AB} \\ &= \boldsymbol{\zeta}^A \boldsymbol{S} \boldsymbol{\zeta}^{AB},\end{aligned} \tag{3.27}$$

where $\boldsymbol{\zeta}^A$ and $\boldsymbol{\zeta}^{AB}$ are vectors containing the expansion coefficients in the atom-centred basis set, and $\boldsymbol{S}$ is the overlap matrix of the atomic orbitals.

In summary, J_{AB} may be computed from the expansion coefficients $\{\zeta_\alpha^A\}$, $\{\zeta_\alpha^B\}$, and $\{\zeta_\alpha^{AB}\}$, the overlap matrix $\boldsymbol{S}$, and the energies of the dimer MOs, $\{\epsilon_i^{AB}\}$. Practically, these may be found by performing three DFT calculations, one each on the isolated molecules, and one on the dimer. To retrieve the expansion coefficients in the shared basis set, virtual atoms (with zero nuclear charge) must be placed into the systems of the isolated molecules, at locations corresponding to the atoms of the other molecule. Then, calculations are performed on

- Molecule A (with virtual atoms for molecule B), yielding $\{\zeta_\alpha^A\}$.
- Molecule B (with virtual atoms for molecule A), yielding $\{\zeta_\alpha^B\}$.
- Dimer AB, yielding $\{\zeta_\alpha^{AB}\}$, $\boldsymbol{S}$ and $\{\epsilon_i^{AB}\}$.

I note that the derivation given above is a slight simplification, since I have treated $|\phi_A\rangle$ and $|\phi_B\rangle$ as orthogonal. In situations where this is not the case, the coupling strength can be corrected using

$$J_{AB}^{\text{eff}} = \frac{J_{AB} - \frac{1}{2}(\epsilon_A + \epsilon_B)\langle\phi_A|\phi_B\rangle}{1 - \langle\phi_A|\phi_B\rangle^2}. \tag{3.28}$$

This method was used to calculate electronic coupling strengths between polymer chain segments for the investigations described in Chapters 6 and 7.

The projective method is applicable across all length scales of separation between molecules. Adopting an *ab initio* method such as this is particularly important for computing J_{AB} when the separation distance is small. In this case, the interactions between molecules can alter the shape of the respective MOs (hence the need to include a DFT evaluation of the dimer in the above method). At larger separation distances, not only is the effect on the isolated MOs negligible, but, in addition, the conformation and relative orientation of the molecules will also have a reduced effect on the coupling. This is even more so the case when the molecules are relatively rigid and/or symmetrical.

Under these conditions, the strength of coupling can be estimated using a simple distance-dependent

expression of the form [65, 116, 117]:

$$J_{AB}(R_{AB}) = \alpha \exp\left(-\frac{R_{AB}}{\beta}\right), \quad \text{where} \quad R_{AB} = |\vec{R}_A - \vec{R}_B|. \tag{3.29}$$

For most OSC molecules, it is reasonable to use the molecular centres-of-geometry (CoGs) for the positions $\vec{R}_A$ and $\vec{R}_B$.[4] The parameters α and β may be set by fitting the expression to a small number of *ab initio* calculations, performed on dimers covering a range of R_{AB}. Since, in the context of charge transfer, rates are dependent on $|J_{AB}{}^2|$, the sign of the expression is inconsequential.

The functional form of Equation 3.29 can be understood from reference to the fact that the MOs can typically be approximated as a linear combination of atomic orbitals, which by definition will feature an exponentially decaying radial factor. Because the electronic coupling is proportional to the integrated overlap between the MOs, as the orbitals decay exponentially with distance, so will their overlap, and thus the strength of coupling.

Equation 3.29 was used to estimate electronic coupling strengths between fullerene derivatives for the investigation described in Section 4.5.2.

3.2 Microstructure Prediction

As well as an understanding of the microscopic quantum mechanical processes involved, rationalising the charge transport behaviour of materials requires an accurate description of the microstructural environment in which these processes play out. The soft chemical structure and weak intermolecular forces between OSCs molecules mean that they are prone to conformational and microstructural disorder. Even in materials featuring crystalline regions, transport is often limited by the non-crystalline regions. In some materials, a more comprehensive crystalline structure can be promoted by certain fabrication techniques and processing conditions, such as high annealing temperatures. However, these can be time-consuming and costly, and run somewhat counter to one of the main appeals of OSCs; their processability and consequent suitability for high-volume, low-cost device manufacturing. On this basis, a method is required that can generate representative structures of amorphous or otherwise non-crystalline materials. This may be achieved using *molecular dynamics* (MD) simulations.

The key challenge to be overcome is the simulation of enough molecules to represent the solid state of a material. For understanding transport in disordered structures, this includes producing a large enough sample of nanoscale molecular arrangements that, when 'averaged-over' by transport simulations (see Section 3.3), mobility predictions can apply in a general sense to the material under study.

A full quantum treatment of any such system is generally computationally infeasible. Luckily, in

[4] There is some evidence, from calculations performed on biological systems, that for large molecules (e.g. proteins), it is more appropriate to use an *edge-to-edge* distance for R_{AB}, defined as the separation between the closest π-conjugated atoms on each molecule [118, 119].

most circumstances it is reasonable to apply the BO approximation and to treat nuclear motion classically. Based on this approximation[5], nuclear dynamics can then be propagated using Newton's laws of classical mechanics. As discussed in Section 2.2.2, this propagation occurs along a PES largely defined by the behaviour of the electrons. To avoid a full suite of electronic structure calculations covering all possible molecular conformations and arrangements, the PES is approximated using empirically derived potentials known as *force fields*. Using data from experimental measurements and selected electronic structure calculations, these are constructed to represent chemical bonds and intermolecular forces using simple functional forms. For example, the most well known function for approximating intermolecular interactions is the *Lennard-Jones* (LJ) potential [24]. A force field representing a given molecule may include a number of LJ potentials, with parameters tuned to give a best approximation for how atoms belonging to that molecule should interact with other atoms in the system.

3.2.1 Molecular Dynamics

With force fields in place, MD can be used to simulate the time-evolution of a model system using the following procedure [120, 121]. For a system of N interacting particles (typically corresponding to individual atoms) the motion of particle i, with mass m_i, is described by Newton's second law of motion:

$$m_i \frac{\mathrm{d}^2 \vec{r}_i}{\mathrm{d}t^2} = \vec{F}_i, \tag{3.30}$$

where $\vec{r}_i$ is the position of particle i, and $\vec{F}_i$ is the force acting upon it. $\vec{F}_i$ is calculated from the negative gradient of the PES, taken with respect to $\vec{r}_i$:

$$\vec{F}_i = -\frac{\partial U(\vec{R})}{\partial \vec{r}_i}, \tag{3.31}$$

where $\vec{R}$ includes the positions of all particles. Combining the above two equations gives the equation of motion for particle i:

$$-\frac{\partial U(\vec{R})}{\partial \vec{r}_i} = m_i \frac{\mathrm{d}^2 \vec{r}_i}{\mathrm{d}t^2}. \tag{3.32}$$

The motion of the system as a whole is then described by a set of simultaneous differential equations, one for each particle in the system. The MD method propagates this set of equations numerically to produce a *trajectory*; a time series of coordinates $\vec{R}$, each separated by a small timestep (Δt), that describes the evolution of the system.

There are several algorithms that can be applied to propagate the equations of motion. For the MD simulations described in this thesis, I applied a *leap-frog integrator* algorithm [120, 122]. This algorithm calculates the next positions and velocities of particles at separate timesteps, shifted by a

[5] With relativistic effects also neglected.

half step ($\frac{1}{2}\Delta t$). Positions and velocities are updated using the relations

$$\vec{v}_i(t + \frac{1}{2}\Delta t) = \vec{v}_i(t - \frac{1}{2}\Delta t) + \frac{\Delta t}{m_i}\vec{F}_i(t), \tag{3.33}$$

$$\vec{r}_i(t + \Delta t) = \vec{r}_i(t) + \vec{v}_i(t + \frac{1}{2}\Delta t)\Delta t. \tag{3.34}$$

The benefit of this algorithm over alternatives is that it only requires one expensive calculation of $\vec{F}_i(t)$ per timestep, at the cost of a small memory overhead from needing to store the velocities from the previous timestep.

To reduce the computational cost of evaluating $\vec{F}_i(t)$, forces are only calculated between particles when they are within an *interaction cutoff* distance. Forces between particles beyond this cutoff are assumed to be negligible. A potential-shift scheme is typically applied to ensure that the forces between particles smoothly transition to zero at the cutoff distance, to avoid discontinuities which may impact the energy of the system. The MD algorithm keeps track of which particle pairs are interacting by generating a *neighbour list*. This is periodically updated to account for the movement of particles. However, updates do not need to be done as frequently as the integrator timesteps, since, in most circumstances, particles move slow enough that the neighbour list remains representative for several Δt.[6] For the MD simulations described in this thesis, a *Verlet cutoff scheme* was used to generate neighbour lists. This constructs a neighbour list that includes all particle pairs within the interaction cutoff distance, plus a short buffer distance. The buffer reduces the likelihood that interactions are erroneously neglected when particles move within the interaction cutoff distance. The Verlet scheme groups particles into spatially-defined clusters of 4 or 8 before the neighbour search is performed, which improves its efficiency.

Since the dynamics of the systems we are interested in are temperature-dependent, thermal coupling to an external bath is used to control the temperature of the systems. This ensures that simulated models represent an NVT ensemble. I applied a *velocity-rescaling thermostat* to control system temperature. This is an extension of the Berendsen thermostat, which works by rescaling all velocities, once every n_{TC} timesteps, by a factor of

$$\gamma(t) = \sqrt{1 + \frac{n_{\mathrm{TC}}\Delta t}{\tau}\left(\frac{T_0}{T(t - \frac{1}{2}\Delta t)} - 1\right)} \tag{3.35}$$

where T_0 is the target temperature, and τ is the temperature coupling time constant.[7] The velocity-rescaling thermostat includes an additional stochastic term that ensures a correct kinetic energy dis-

[6] Systems simulated at very high temperatures represent one notable exception. In this case the neighbour list should be updated more frequently.

[7] Strictly speaking, τ is related to, but only approximately equal to the 'true' temperature coupling time constant. It is not exactly equal because the kinetic energy change caused by scaling the velocities is partly redistributed between kinetic and potential energy [120].

tribution corresponding to the NVT ensemble.

In the following subsections I will describe some practical details about the application of the DFT and MD methods for generating molecular structures.

3.2.2 Molecules and Dimers (Small Systems)

We can use DFT to accurately predict the structures of small systems, such as short polymer segments, single molecules, or pairs of molecules. The size of systems evaluated in this way is limited by the high computational cost of DFT, which scales rapidly with increasing numbers of atoms. On this basis, we are typically limited to simulations of up to ∼100 atoms. Although DFT may be used to simulate the time evolution of systems, in practice I used it only for optimisation, i.e., to locate lower energy conformations and arrangements.

As discussed in Section 2.3, charge transport is dependent on the electronic coupling between molecules. If we want to evaluate the coupling between molecule pairs extracted from larger-scale MD models, it is usually necessary to first perform a degree of DFT optimisation on the structures. This is because there will be small differences between the structure predicted by the empirical force fields of MD, and the *ab initio* calculations of DFT. The more approximate structures predicted by MD are therefore likely to be somewhat unrealistic when evaluated by the more accurate method, which could lead to erroneous coupling values if we evaluated them without some degree of optimisation to 'fix' bond lengths and other structural features. However, we generally want to limit the number of DFT optimisation steps to a small number (typically 3 in the investigations described in this thesis). This is partly to reduce the computational expense, since we are often evaluating large samples of such structures, but it is also important to ensure that we do not lose too much of the structural information predicted by MD. This is because DFT calculations are generally performed in vacuum, while we would like the structures to remain informed by the solid state environment from which they were extracted. Furthermore, for conjugated polymers, we would like the structures of polymer segments evaluated by DFT to remain informed by the extended polymer chains from which they were extracted. Side chains are generally replaced with methyl groups prior to DFT calculations, to reduce computational expense. It is reasonable to do this because the side chains (especially alkyl side chains) generally have little influence on the electronic structure of the π-conjugated backbone which is most relevant to transport.

The application of DFT for predicting the structures of polymer chain segments is described in Sections 6.2.2 and 7.2.2.

3.2.3 Atomistic Molecular Dynamics (Medium Systems)

For mid-sized systems, such as small volumes of solid-state microstructure, we can generate structures using atomistic MD. In these simulations, each particle represents a single atom. As with all time-evolution simulation methods, there is a trade off between the time- and length-scales of the modelled

system. Typically, we are limited to simulating systems of up to ∼100,000 atoms for tens of ns. These scales can be increased by choosing longer Δt for the numerical integrator, but in this aspect we are limited by the timescales of motion for the fastest moving atoms in the system. For a full atomistic representation, this will generally be the vibrational frequency of hydrogen atoms, which limits us to a maximum Δt of ∼10 fs.

The application of atomistic MD for predicting the packing structures of polymer chains is described in Section 5.2.1.

3.2.4 Coarse-Grained Molecular Dynamics (Large Systems)

In real OSC materials, the microstructure is informed by the self-assembly process that occurs during the transition from the solution state to the solid state [38, 40, 123–125]. This process occurs over much longer timescales than are computationally accessible by atomistic MD simulations. The use of a *coarse-grained* (CG) representation can address this. In CG MD approaches, the particles propagated by the MD algorithm are referred to as *beads*, with each bead representing a group of atoms. The investigations described in this thesis involved the use of the `Martini 3` force field package [126]. Under the `Martini` scheme, each bead represents ∼4 heavy atoms, plus their bonded hydrogen atoms. This corresponds to a somewhat finer scale representation than other CG schemes, which typically group whole molecules or large sub-molecular units (i.e., moieties) into single beads.

The interactions between beads specified by the CG force field represent the average interactions of the grouped atoms. CG force fields are typically parameterised by comparison with verified atomistic force fields, with further information being provided by experiments and electronic structure calculations, when desired.

Naturally, grouping atoms together in this way greatly reduces the number of degrees of freedom in the model, which improves the efficiency of simulations. It also carriers a further benefit, since the use of partially-averaged interactions leads to a much smoother PES. This means we can select longer Δt for the numerical integrator without running into errors. For these reasons, the time- and length-scales achievable by a CG approach are much increased compared to the full-resolution atomistic approach, at the cost of losing atomic-scale detail. We can therefore simulate systems of up to a few million atoms, for timescales of up to a few µs. It should be noted that, because of the smoother PES, the relationship between simulated time and real time is less robust in CG MD compared to atomistic MD. In the `Martini` model, a standard conversion factor of 4 is typically applied, meaning that the µs time scales of the simulations represent times ∼4× longer in physical systems [127]. The large time- and length-scales reachable in this approach enable simulations of microstructure formation starting from the solution state, which may be used to generate realistic microstructural models of OSC thin films. Such simulations were employed by my collaborators to enable the gathering of results presented in Chapters 5, 6, and 8.

Once we have generated a CG microstructural model, it is often useful to recover atomistic detail. This can be achieved by a procedure known as *backmapping*. If desired, structures extracted from the now atomistic models may then be passed back to DFT, to evaluate their electronic structures. For further details about the backmapping procedure, including examples of its implementation, see Section 5.2.2 and Appendix A.2.

Taking Sections 3.2.2, 3.2.3, and this section together, we can understand the essence of the sequential multiscale modelling approach implemented for the investigations in this thesis. I have described how information can be gathered across multiple time- and length-scales, and how information can be passed between scales, for instance by using DFT to parameterise MD forcefields (passing information 'up the chain'), or by extracting molecular pair arrangements from backmapped CG models to input into DFT calculations (passing information 'down the chain'). For the purposes of understanding charge transport in OSC materials, the electronic and microstructural information gathered by these techniques can be tied together by the use of *charge transport simulations*. These will be described in the following section.

3.3 Charge Transport Simulations

With knowledge of an OSC material's electronic structure (Section 3.1) and microstructure (Section 3.2) at hand, it becomes possible to probe the behaviour of mobile charge carriers using charge transport simulations. In the hopping transport regime, a material can be modelled by a 3-dimensional *transport network*, analogous to a mathematical graph. Since nodes (vertices) have explicit coordinates, they are typically referred to as *sites*. These sites correspond to the molecular π-orbitals which charge carriers can occupy. Edges are included between sites with non-negligible electronic coupling, and are each weighted by a hopping rate, typically calculated using the Marcus equation (Equation 2.6). Equation 2.6 takes as inputs the electronic structure parameters J_{ij}, λ and $\Delta\epsilon_{ij}$. Section 2.3.2 contains a discussion of how values for these parameters can be determined based on their physical origins.

The influence of an external electric field may be factored in by modifying $\Delta\epsilon_{ij}$ during rate calculations, using

$$\Delta\epsilon_{ij} = \epsilon_j - \epsilon_i \pm \mathrm{e}\vec{F} \cdot \vec{r}_{ij} \tag{3.36}$$

where e is the standard charge, $\vec{F}$ is the external electric field and $\vec{r}_{ij}$ is the displacement between sites i and j. The sign of the field term depends on whether we are studying hole or electron transport. In combination with energetic disorder in the system, the presence of the field term will generally mean that $\Delta\epsilon_{ij} \neq \Delta\epsilon_{ji}$. Thus, different forward and backward hopping rates are established between sites.

When charge densities are high, long-range Coulombic interactions between charge carriers may significantly impact transport. These can be accounted for by introducing an additional term into Equation 3.36. However, for the investigations detailed in this thesis, low enough charge densities were

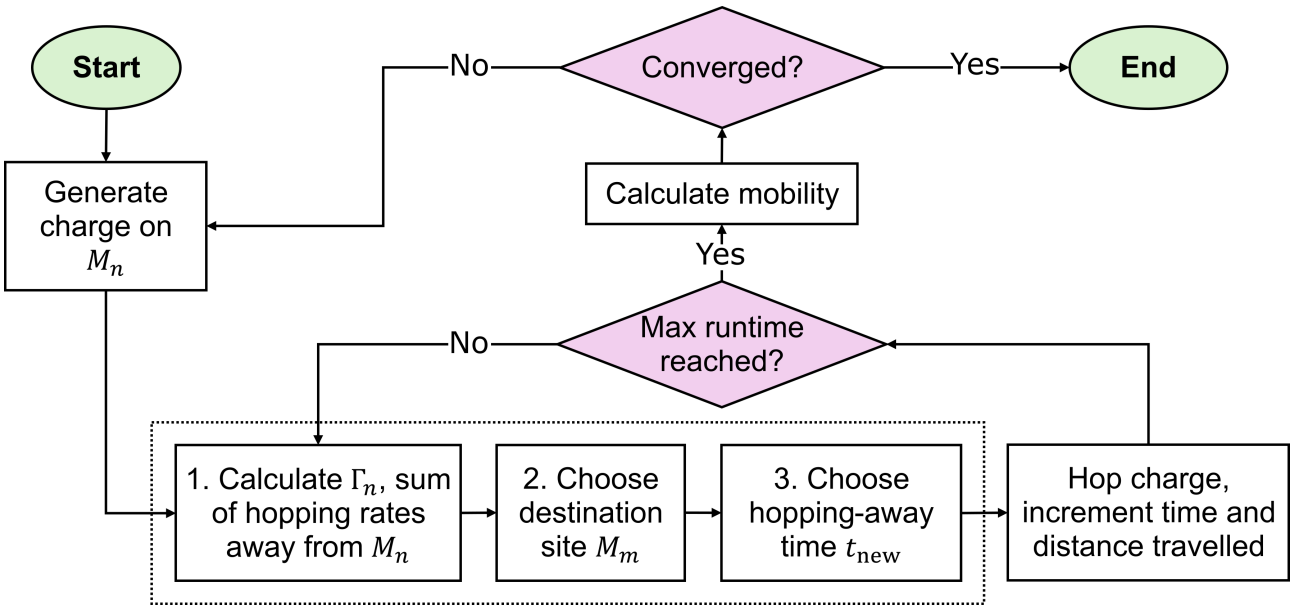


Figure 3.1: Flowchart depicting the first reaction method (FRM) algorithm for a single charge carrier.

assumed for this term to be neglected. Although long-range interactions are neglected, local Coulombic repulsion is typically still accounted for by imposing a single-occupancy constraint on sites.

Once a transport network has been set up, several methods may be employed to simulate charge carrier motion. The choice of method depends on the nature of the problem, including the complexity of the network, conditions that may be assumed, and which aspects of transport behaviour it may be useful to reproduce. That said, evaluating the charge mobility of a system is typically a goal shared by all. Two methods, employed during investigations described in this thesis, are outlined below.

3.3.1 Kinetic Monte Carlo

The *kinetic Monte Carlo* (KMC) method (introduced in Section 2.4.3) can be used to simulate transport in a manner that mimics the physical time-evolution of charges moving through a material. This is achieved by treating time as an explicit, non-abstract variable, which is repeatedly incremented until a halting condition is met. Taking hole transport as an example, the average velocity of holes in the external electric field direction ($\langle v_F \rangle$), is then calculated from $\langle \vec{d} \rangle \cdot \hat{F}/t_{\text{sim}}$, where $\langle \vec{d} \rangle$ is the average displacement of holes from their initial locations and t_{sim} is the final simulation time. From this, we can find the charge carrier mobility (μ) using

$$\mu = \frac{v_F}{F}, \tag{3.37}$$

where $F = |\vec{F}|$ is the strength of the external field.

Several algorithms fall under the KMC banner. One that is computationally well-suited to simulating transport behaviour is the *first reaction method* (FRM). This implementation is described below, first for the case of a single charge carrier, followed by the extension to multiple carriers [104].

Single Charge Carrier

Figure 3.1 depicts the FRM algorithm as a flowchart. During operation, hopping events are selected for execution based on whichever is most likely to occur first. It may therefore appear unusual that the choice of destination site is made *before* hopping times are calculated. This choice may be explained by considering the steps surrounded by a dashed box in detail:

1. A charge carrier located on site n will have a probability flux of hopping to site m given by

$$H_{n\to m}(t) = \Gamma_{n\to m} P_n(t). \tag{3.38}$$

   This depends on the rate constant $\Gamma_{n\to m}$, and $P_n(t)$, the occupation status of site n. The occupation status can only take values of 0 or 1, but is time-dependent, since the charge carrier may hop to a different destination site before it hops to m. If we introduce t_{old} as the time that the charge carrier first landed on site n, and assert that $P_n(t_{\text{old}}) = 1$, then

$$P_n(t) = \exp(-\Gamma_n(t - t_{\text{old}})), \tag{3.39}$$

   where the *total hopping away* rate (Γ_n) is given by

$$\Gamma_n = \sum_m \Gamma_{n\to m}. \tag{3.40}$$

   The flux can then be expressed as

$$H_{n\to m}(t) = \Gamma_{n\to m} \exp(-\Gamma_n(t - t_{\text{old}})) \tag{3.41}$$

2. If we enforce that the next hop must occur at a specific time t_{new}, then a destination can be randomly chosen from among the possible destination sites by weighting each with a probability $\Gamma_{n\to m}/\Gamma_n$. Then, we see that

$$H_{n\to m}(t_{\text{new}}) = \frac{\Gamma_{n\to m}}{\Gamma_n} H_{n\to\text{any}}(t_{\text{new}}). \tag{3.42}$$

   Inserting Equation 3.41 into Equation 3.42, and rearranging for the probability flux towards any site, we get

$$H_{n\to\text{any}}(t_{\text{new}}) = \Gamma_n \exp(-\Gamma_n(t_{\text{new}} - t_{\text{old}})), \tag{3.43}$$

   which depends only on Γ_n, and not the hopping rate towards any specific destination site.

3. We can use $H_{n\to\text{any}}$ as a distribution to generate *first hop away* times. This is considerably more efficient than finding and comparing hopping times to each possible destination. The form of

Equation 3.43 corresponds to a Poisson distribution for occurrences of a single event. Introducing X, a uniform random number between 0 and 1, we can select hopping times using the formula

$$t_{\text{new}} = t_{\text{old}} - \frac{\ln(X)}{\Gamma_n}. \tag{3.44}$$

In Section 2.4.3, I mentioned that the numerical efficiency of the KMC method is reduced significantly by large variances in the charge transfer rates. This is linked to the fact that the computational expense of the above steps is mostly independent of the magnitude of rates involved. To clarify the origin of this issue, it is useful to consider a toy system in which fast forwards and backwards transfer rates are established between two sites (which I label A and B), while all other site pairings are linked by slow rates. This may, for instance, describe a system of many molecules in which only two molecules are coupled strongly. A charge carrier that hops onto A will have a high probability of next hopping onto B, and vice versa. The charge will tend to continue hopping back and forth between only these two sites, without exploring the rest of the system. Therefore, the computational efficiency of the algorithm is reduced, since a large number of calculations (and therefore real time) are spent evaluating only a small region of the system.[8]

Multiple Charge Carriers

To handle multiple charge carriers in the FRM, we assign a hopping time and destination to all carriers at the start of the simulation, and then move each carrier in the order that events occur. This is demonstrated by the schematic in Figure 3.2. When neglecting Coulombic interactions between charges, new hopping times and destinations only need to be calculated for each charge after it has been moved.

To prevent multiple occupancy, it would be inefficient to check whether each neighbouring site is occupied before deciding whether to add its hopping rate to Γ_n. A better method is as follows:

[8] While I have described the issue with reference to a single charge carrier, it is just as significant for simulations of multiple carriers.

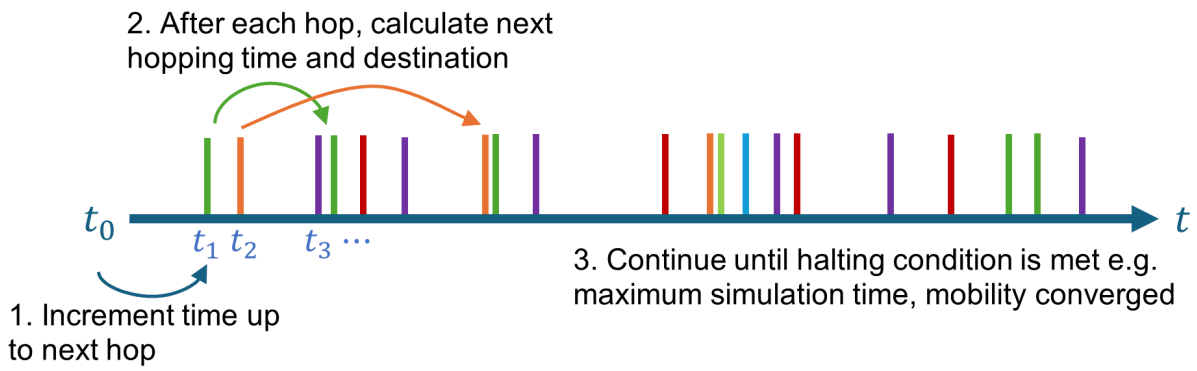


Figure 3.2: Schematic depicting time progression of the FRM algorithm with multiple charge carriers.

1. At the start of the simulation, or immediately after a charge carrier has been moved, calculate the next destination and hopping time for that charge carrier as if all neighbours are unoccupied.

2. Immediately before a charge carrier is about to be moved, check if its destination is occupied.

3. If so, don't perform the hop, but still increment the simulation time.

4. Recalculate Γ_n for this charge, now excluding the rate to the known occupied neighbour.

5. Using this new total rate, select a new destination and hopping time.

The probability of hopping to an unoccupied site at the recalculated time is the same as if the rate of hopping to the occupied neighbour had been excluded from the start. This method limits the number of occupation status checks to only those sites chosen as destinations, rather than all possible neighbours.

When long-range Coulombic interactions are included, the hopping rates to any destination will vary depending on the current distribution of charges. It therefore becomes necessary to recalculate rates, destinations, and hopping times for all charges after any one is moved.

The development and implementation of an FRM KMC code is described in Sections 4.1 and 4.3. Results stemming from the use of this code are provided in Sections 4.5.1, 6.2.3, and 8.3.

3.3.2 Master Equation

In contrast to KMC, the *master equation* (ME) approach (introduced in Section 2.4.3) does not simulate the time-evolution of explicit charge carriers. Instead, it begins by analysing the transport network as a linear algebra problem, to determine the occupation probabilities of each site. The system is modelled as a set of simultaneous differential equations describing the 'flow' of occupation probabilities through the network. These equations are referred to collectively as the master equation of the system.

In some circumstances, calculated rates will need to account for the occupation status of destination sites, in order to prevent charges hopping into already occupied sites, which should be blocked by strong local Coulombic repulsion. The resulting non-linear ME may be difficult or impossible to solve. This generally restricts the ME approach to application in the very low charge carrier regime, where all interactions between charge carriers can be neglected.

The ME approach is outlined as follows [64, 117]. For site n, the rate of change in occupation probability depends on the probability itself ($P_n(t)$), and that of any coupled sites ($P_m(t)$), plus the rate constants for hopping to and from each neighbour m, designated $\Gamma_{n\to m}$ and $\Gamma_{m\to n}$, respectively. Thus, we find

$$\frac{\mathrm{d}}{\mathrm{d}t}P_n(t) = \sum_{m\neq n}(\Gamma_{m\to n}P_m(t) - \Gamma_{n\to m}P_n(t)). \tag{3.45}$$

The full system of equations can be expressed in matrix form as

$$\mathbf{A}\vec{P} = \dot{\vec{P}}, \quad \text{with} \quad A_{mn} = \begin{cases} \Gamma_{m\to n}, & m \neq n \\ -\sum_{m\neq n} \Gamma_{n\to m}, & m = n \end{cases}. \tag{3.46}$$

From an initial probability distribution, the time-evolution of the system may be modelled by iteratively calculating $\vec{P}$ for small time increments of δt. However, we are generally interested in the steady-state mobility, and can therefore set

$$\mathbf{A}\vec{P} = \vec{0}, \tag{3.47}$$

from which we can find a solution for $\vec{P}$, subject to the additional conditions

$$\sum_n P_n = 1, \quad \text{and} \quad 0 < P_n < 1 \quad \forall \quad n. \tag{3.48}$$

Finding $\vec{P}$ then becomes an eigendecomposition problem, which may be solved by one of several algorithms. For instance, *singular value decomposition* is used to compute $\vec{P}$ in the ME implementation described in Section 4.4. For a system with periodic boundaries in the field direction, a non-zero drift velocity (v_F) can be found using

$$v_F = \sum_{m\neq n} A_{mn} P_n \vec{r}_{mn} \cdot \hat{F}, \tag{3.49}$$

where $\vec{r}_{mn}$ is the displacement between sites m and n. From v_F, the mobility may be calculated using Equation 3.37.

The development and implementation of an ME code is described in Sections 4.4. Results stemming from the use of this code are provided in Sections 4.5.2.

Chapter 4

Transport Model Development

I describe the development and implementation of two charge transport models, `ToFeT` *and* `MESol`*, which employ the KMC and ME approaches respectively. In the latter half of the chapter, I demonstrate the utility of the codes via their application in two case studies. In the first, I use* `ToFeT` *to probe the effects of charge density and mobility on the performance of an interfacial photocatalytic polymer system for hydrogen production. By correlating with experimental results, we find that, under operating conditions, performance may not always benefit from higher mobility materials. In the second case study, I use* `MESol` *to evaluate charge transport in different crystalline packing arrangements of fullerene-derived acceptor molecules, finding that the dimensionality of transport is important for rationalising experimental measurements of mobility. These investigations contribute to a study* in preparation *[128] and a study published in* Chemistry of Materials *[129].*

4.1 Introduction

In this chapter, I describe the development and implementation of two programs that model charge transport in the hopping regime. The first program, `ToFeT`, employs the KMC approach introduced in Section 2.4.3 and described further in Section 3.3.1. The second program, `MESol`, employs the ME approach introduced in Section 2.4.3 and described further in Section 3.3.2. The source code for both programs is written in `C++`. The codes may be found at [130] (`ToFeT`) and [131] (`MESol`).

At its inception, `ToFeT` was based on another KMC code developed in the Nelson group [132]. Development of this code into what became `ToFeT` was largely undertaken by Joe J. Kwiatkowski [65], with assistance from James Kirkpatrick. The core functionality of `ToFeT` consists of an FRM-KMC algorithm. A theoretical description of this algorithm has been provided in Section 3.3.1. To briefly reiterate, the algorithm simulates the time evolution of explicit mobile charge carriers moving through a system representing the microstructure of (typically) an OSC material. Information about the electronic- and micro-structure of the material is contained in a transport network, which is equivalent to a mathematical graph. In the transport network, molecules (or polymer segments) are represented

by sites, while the electronic coupling between molecules is represented by edges. A hopping mechanism is assumed for charge transport, with the hopping rates calculated using the Marcus rate equation (see Section 2.3.2).

As discussed in Section 2.4.3, the KMC approach is useful for simulating transport in large systems and/or probing transient processes, but it has some disadvantages. Compared to the ME approach, it is less suited to studying systems with large variations in hopping rates (see Section 3.3.1), and for studying steady state properties. For this reason, I developed the ME code `MESol`. A theoretical description of the procedure underlining the ME approach has been provided in Section 3.3.2. To ensure comparability between the codes, I designed `MESol` to accept the same input files as `ToFeT`, which it uses to build a transport network in the same manner as `ToFeT` (see Section 4.2). Following the initial steps described in Section 3.3.2, the transport network is transformed into a rate matrix ($\mathbf{A}$). This rate matrix undergoes some pre-treatment steps, which are the focus of Section 4.4, before the ME of the system is solved as an eigendecomposition problem, and the mobility calculated, following the rest of the procedure outlined in Section 3.3.2.

For the remainder of this chapter, I begin by providing some information about how simulations are set up in both the programs (Section 4.2). This is useful for contextualising the updates and modifications I made to `ToFeT`, which are described after (Section 4.3). This is followed by details about the implementation of `MESol` (Section 4.4). Finally, the latter half of the chapter covers two case studies, which I use to demonstrate the utility of the codes for understanding charge transport, and other processes, in systems based on OSC materials (Sections 4.5.1 and 4.5.2).

4.2 Simulation Setup

To define the transport network representing a particular system, as well as other simulation parameters, three input files are provided to the codes:[1]

- A site file (`.xyz`) which lists the molecular sites, one per row. This file has five columns, with the first three holding the x-, y- and z-coordinates of the sites. The fourth column is used to specify the type of site, which may be one of `generator`, `transport` or `collector`. This describes where charge carriers can be initialised in the system, and where they can be removed from the simulation.[2] In a typical model system, a layer of `generator` sites is included close to one boundary and a layer of `collector` sites is included close to the opposite boundary, while those in between are left as `transport` sites. The final column holds the site energies (ϵ), in eV.

- An edge file (`.edge`) which describes the interactions between sites. This file has three columns.

[1] As they relate to `ToFeT`, the details provided in this section describe the *unmodified* version of the code, before my updates.

[2] Only applies to `ToFeT`. The contents of this column are ignored by `MESol`.

The first two hold the indices of interacting sites (ordered by their position in the site file), while the third specifies the electronic coupling (J) between them, in eV.

- A parameter file (`.sim`) which lists system-wide parameters, such as temperature (T) and applied electric field strength (F). The reorganisation energy (λ) is also set here, on a system-wide basis. This file is also used to specify options for controlling the simulation, such as the maximum simulation time of each run in `ToFeT`.

`ToFeT` simulations are performed in one of three *modes* (now four, see Section 4.3), named `tof`, `fet` and `regenerate`. These are selected between using an option in the `.sim` file.

`tof` mode is used to perform transient simulations of charge transport. Typically, site types are set such that charge carriers are generated close to one boundary, travel through the system, and are collected close to the opposite boundary. The simulation run halts when all charges have been collected. As its name implies, this mode is designed to replicate the behaviour of charge carriers in time-of-flight (ToF) experiments. Comparison with experiments is aided by the computing of transient photocurrents during the simulation.

Both `fet` and `regenerate` modes are used to perform steady state simulations of charge transport. Charge carriers that hop onto a `collector` are re-initiated back on a `generator` site, allowing them to loop over the system multiple times during each run. Simulation runs are halted when a user-defined maximum simulation time is reached. By default, `fet` mode includes long-range Coulombic interactions between charge carriers. This increases the accuracy of simulations at high charge densities, facilitating comparison with FET experiments.

In both the `ToFeT` and `MESol` programs, the direction of the external electric field is fixed in the z-direction of the input system.

Information in the input files listed above is used to initialise the transport network. The codes then proceed to model transport in the system following the steps outlined in Sections 3.3.1 and 3.3.2.

4.3 Updates to ToFeT

The major updates and modifications made to `ToFeT` are described in the following subsections. Here, I briefly state some of the other minor changes I made, which focus on improvements to the 'quality of life' for users of the code.

Firstly, I implemented capabilities for handling crashes and other sources of early termination. In particular, `ToFeT` now flushes its output more often during runtime, to provide the user with more feedback as to how calculations are proceeding. It also attempts to perform and output preliminary mobility results after receiving a `TERM` signal during operation. This capability made it possible for me to implement a timeout feature (controlled via an optional `timeout` keyword in the `.sim` file), which attempts to halt the simulation early if/when the amount of real time that has passed since the program

initialised passes a user-defined threshold. Secondly, I implemented an option to switch hopping rate calculations from the Marcus model to the Miller-Abrahams model if desired.[3] Finally I carried out general refactoring of the code. This involved removing redundancies and otherwise simplifying the code, without change to its functionality.

Periodic Boundaries Conditions

During my early experimentation with `ToFeT`, I noticed the introduction of systematic errors in the predicted mobility (μ) under certain conditions. These errors manifested as a dependence of μ on the z-dimension size of modelled systems (i.e., size in the field direction), and on F. Specifically, μ would increase in systems with either a small z-size or small F. This affected calculations performed in all of the original modes (`tof`, `fet` and `regenerate`). Evidence for the error is shown by the `regeneration` mode results in Figure 4.1. Although the scale of the systematic error could be reduced by decreasing either of these parameters, this would reduce the range of systems that we could confidently apply `ToFeT` to. The system-size dependence was a particular issue, because one of the major use-cases for `ToFeT` relies on its ability to model transport through realistic material microstructures. Microstructural models are typically generated using techniques such as MD, meaning that the size of the systems is predefined, prior to transport modelling.

I identified the origin of the systematic error as arising due to boundary effects. In order to sample the bulk of a system during transport simulations, charges are typically generated close to the lower z-boundary and collected close to the upper z-boundary. Newly generated charges are thus blocked from making 'backwards' hops i.e., hops against the field direction (assuming, for clarity, that we are simulating hole transport). This is the equivalent of establishing an infinite potential wall at one boundary of the system, which results in charges experiencing an initial 'boost' in the field direction. Figure 4.1 shows the significant influence this can have on μ, depending on the simulation setup.

Before moving on to my implemented solution, it is worth briefly discussing the physical validity of this effect. In ToF experiments, a thin sheet of charges, of both polarities, are generated by a laser pulse at one edge of the device. By selecting a wavelength corresponding to a high absorption coefficient of the material, the charges can be excited close to one contact (typically $<$100 nm [134, 135]). The contact quickly collects charge carriers of one polarity, while blocking the other carrier type. This initial blocking of charge carriers is reminiscent of the 'erroneous' boundary effect I identified in `ToFeT` simulations. However, although the process is equivalent in both cases, the impact it has on the measured μ is distinct. This is for two reasons. Firstly, only a small fraction of the charges generated in ToF experiments are located close enough to the contact to be blocked by it. Secondly, the films

[3] Since the Miller-Abrahams model was not applied in any of the investigations in this thesis, I have neglected to include a theoretical description of this model in Chapter 2. To very briefly summarise, it is similar to the Marcus model, except that only hops to higher energy sites are thermally activated, while all hops to lower energy sites occur with a constant rate. For a comparison of the Miller-Abrahams and Marcus models in transport simulations, see [133].

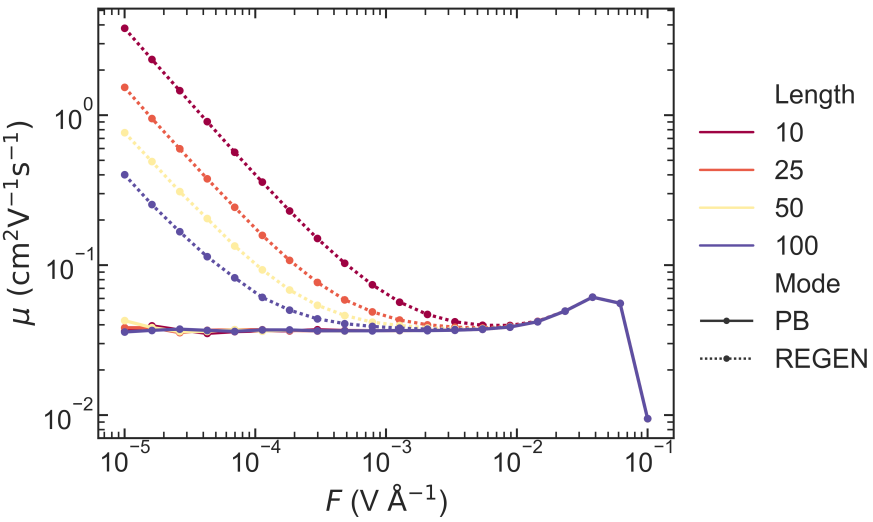


Figure 4.1: System size and field dependence of mobility (μ) in `ToFeT`. μ is evaluated from simulations of charge transport through a cubic lattice, with the number of site layers in the z-direction given by the parameter *Length*. The sudden drop-off of μ at high field strength ($F > 4 \times 10^{-2}\,\mathrm{V\,Å^{-1}}$) is expected, due to the inverted-Marcus regime. The field strength and system size dependence of μ in `regenerate` (*REGEN*) mode is due to an erroneous boundary effect. This error is eliminated in `pb` (*PB*) mode.

used in a ToF device architecture are much thicker than the systems we can model within reasonable computational limits. As shown in Figure 4.1, the influence of the initial 'boost' decreases as the system becomes larger in the field direction. The contact-blocking effect is therefore negligible in experiments, but may be significant in simulations. Furthermore, with our simulations (and ideally in experiments) we are generally interested in assessing the inherent characteristics of the material of interest, rather than any contingent effects of the the device architecture.

To address this issue, I implemented the handling of periodic boundary conditions (PBCs) into `ToFeT`. By allowing backwards hops near the system boundaries, this eliminated the z-size and F dependence of μ, as shown by the `pb` results in Figure 4.1.

Since, depending on the system we are modelling, it may be preferable to keep the old functionality, I implemented this as a new simulation mode. This may be selected by setting `mode pb` in the `.sim` parameter file. Selecting `pb` mode requires the user to set a value for a new parameter, `sizez`, which controls the position of the upper z-boundary. The lower z-boundary is assumed to be at $z = 0$. Note that this requires the modelled system boundaries to form a prism, since the z-boundaries are assumed to constitute xy-planes. Using these boundary positions, the separation between sites in the z-direction is calculated based on the minimum image convention [136], when accounting for the applied field in hopping rate calculations. The new `pb` mode was used to collect the results presented in Section 6.2.3 and Chapter 8.

Coulombic interactions between multiple charge carriers separated across periodic boundaries can also be handled in `pb` mode, if the locations of the x- and y-boundaries are also defined using `sizex`

and `sizey`. This assumes the modelled system is orthorhombic.[4] The self-interaction of charges across periodic boundaries is neglected.

Modifications for Modelling Conjugated Polymer Systems

Much of my work involved investigating charge transport in solid-state conjugated polymer systems (see Section 6.2.3), where we can expect different electronic structure parameters to be present between intrachain and interchain transport pathways. Originally, `ToFeT` was able to handle different J and $\Delta\epsilon$ values involved in these in these pathways. However, the program assumed that only one value for λ would apply for all charge transfer reactions in a given system. Therefore, I decided to update `ToFeT` to allow multiple λ values to be specified.

As before, λ is declared in the `.sim` parameter file, however it is now possible to provide a list of values. To select between these, an extra column may be placed in the `.edge` file. This column is populated by indices specifying the *edge type* (e.g., intrachain or interchain), with each edge type associated with one of the listed λ values.[5]

Differentiating edge types in this way carries an the additional utility. Namely, it can be used to record the total number of hops along each edge type. This can be useful, for instance, for gaining insight into the high mobility pathways in molecular crystal structures. For my purposes, tracking the number of hops across different edge types was particularly useful when interrogating charge transport results for conjugated polymer systems. As well as providing information about the proportion of transfer events occurring via different pathways under normal working conditions, it was useful for detecting a common issue in transport simulations of polymer systems. Typically, hops associated with intrachain transport would proceed at faster rates than interchain hops. If the system was poorly parametrised (from a computational standpoint), the rate of intrachain hops could be considerably faster, to the extent that interchain hops almost never occurred during simulations. This would lead to erroneously small, even negative, predictions for μ. It was therefore useful to be able to quickly detect and, where possible, eliminate this issue by reconsidering the chosen simulation parameters. The multiple edge type functionality was used when collecting the results presented in Section 6.2.3.

Modifications for Modelling Interfacial Processes

The final modification I describe allowed `ToFeT` to track the transient population of charges located on either `generator` or `transport` sites, as well as the number of charges collected. This was useful for understanding the behaviour of charges in systems with distinct regions, such as interfacial systems, where we would like to probe the transient population of charges moving between the regions.

[4] In an orthorhombic system with Coulombic interactions disabled, PBCs in x and y could already be handled by the original `ToFeT` code, since hopping rates are only affected by the separation between sites in the z-direction.

[5] Note that, because of an overlap in how multiple λ values are provided, at the time of writing this functionality is not compatible with the `ToFeT` wrapper `tft_run_batch.py`.

To implement this, I adapted much of the code infrastructure originally included to track transient photocurrents in `tof` mode, without change to that functionality. The tracking of transient charge populations can be enabled by specifying `trackpop 1` in the `.sim` parameter file.

Note that, some care is required to get robust results from this functionality, because of the way populations are recorded, and the way time is handled by the FRM algorithm. Currently, the transient population outputted at the end of the full simulation represents a simple summation of the transient populations recorded by each run. Ordinarily, this can simply be divided by the number of runs to find the average populations between the runs. However, in the FRM algorithm, time is only propagated when a charge transfer event (hop) occurs (see Section 3.3.1). This means that the current state of the system is also only updated when a hop occurs. Therefore, when attempting to log the charge populations at a given time snapshot, the relevant information will only have been updated in the program's memory if at least one hop took place since the previous snapshot. Since the total charge population statistics are typically accumulated over multiple runs, this can lead to erroneous fluctuations in the populations (see Figure D.12), because only those runs that featured a hop during the relevant time bin will add to the total number of recorded charges in the different regions.[6]

Because of this effect, when using `trackpop 1`, it is best to 1) include multiple charge carriers in the simulation, and 2) set the `deltaTime` and `alpha` parameters such that the width of the time-bins is much larger than the timescales of hopping. Results gathered using the transient population tracking functionality may be seen in Section 4.5.1.

4.4 MESol

In Section 3.3.2, I introduced the ME approach for estimating the mobility of a system, and compared it with KMC. Some of the systems I investigated were better suited to evaluation with a ME approach. In particular, I am referring to molecular crystal systems, which tend to be fully defined by a low numbers of sites, and can occasionally show large variations in charge transfer rates. Hence, I developed the program `MESol` to evaluate charge transport in these crystalline systems.

As stated, `MESol` was designed to accept the same input files as `ToFeT` and calculates charge transfer rates using the Marcus equation. Because of these choices, the two transport codes converge to the same steady-state results (μ and average site occupation) for the same input system, which was useful for testing purposes.

In some systems, for instance those containing deep trap sites, the calculated hopping rates can vary by several orders-of-magnitude. While this does not slow down or prevent convergence to the same extent as in KMC, it can still lead to slower calculations and the inaccurate estimations of the

[6] It may be possible to account for this by also keeping track of how many runs contributed to the populations recorded for each time bin, and by returning average charge population (i.e., dividing by the number of contributing runs) rather then total charge populations. However this has not been implemented at present.

charge carrier probability density ($\vec{P}$) and mobility (μ). Similarly, issues can arise if some, or all, of the rate-values are extremely large or small in an absolute sense.[7] These low calculation speeds and inaccuracies arise from a combination of floating-point errors and an ill-conditioned rate matrix ($\mathbf{A}$).

To handle this, `MESol` optionally applies two preconditioning steps to $\mathbf{A}$ before the eigendecomposition step. The first, which I term the *compression* step, is used to reduce the numerical distance between the fastest and slowest rates, which improves the conditioning of $\mathbf{A}$. The second, which I term the *scaling* step, is used to scale all rates equally, such that they are distributed close to 1, since this is where floating point arithmetic is most robust.

For the compression step, I found reasonable results were achieved by dividing each row by the element in that row which is diagonal in $\mathbf{A}$. In other words, we divide all rates for hops into site i by the sum of rates into i. To later recover the properly treated $\vec{P}$ after eigendecomposition, an additional step must be undertaken to reverse the preconditioning applied to $\mathbf{A}$. This involves iterating over the probability elements (P_i) in $\vec{P}$ and rescaling each element by the sum of rates into i. The compression step can help in dealing with systems that include energetic traps, but does not necessarily lead to a well-conditioned $\mathbf{A}$ in all cases.[8]

For the scaling step, `MESol` multiplies all hopping rates by $10^{-\kappa}$, where κ is the base-10 exponent of the largest hopping rate in the system. Since all rates are affected equally, there is no need to reverse this treatment when recovering the correct P_i values.

After preconditioning $\mathbf{A}$, and constructing the set simultaneous differential equations defining the ME, `MESol` performs eigendecomposition using singular value decomposition (SVD), to find the treated (i.e. 'compressed') $\vec{P}$. This is carried out using the function `gsl_linalg_SV_decomp`, provided by the GNU Scientific Library, which applies the Golub-Reinsch SVD algorithm [137]. The compression step is then reversed, as described above, to recover the true $\vec{P}$. The remaining steps taken by `MESol` to calculate a mobility from $\vec{P}$ have been detailed in Section 3.3.2. The code can optionally carry out one final step, in which it uses $\mathbf{A}$ to propagates $\vec{P}$ in time. This serves as a final check on the calculations, since, if no issues have been encountered, the system should be in a steady state, and no change should occur to $\vec{P}$ following time-propagation.

[7] Practically, they will be large, if rates are in units of s^{-1}.

[8] Furthermore, it can make things worse if the trap is deep enough that hops *into* the trap are slow, due to the Marcus inverted regime. However, dealing with this issue is beyond the scope of this thesis.

4.5 Case Studies

4.5.1 Polymer Photocatalysts for Sacrificial Hydrogen Evolution

Introduction

Metal-decorated conjugated polymers can be used as photocatalysts for hydrogen production from water. Many of the highest performing systems for this application combine sulfone polymers (featuring an aryl-SO2-aryl unit as part of the backbone) with a palladium co-catalyst. However, sulfone polymers are known to display poor charge transport, large particle sizes in suspension, and mediocre exciton diffusion lengths, which typically could be expected to limit the efficiency of these systems [138, 139]. This raises the question of how these systems still show such high performance, and highlights a lack of understanding about the nature of charge transport in these systems, particularly in relation to the effects of water permeation.

To address this, Sam A. J. Hillman and my other collaborators on [128] studied films and dispersions of the sulfone polymers FS-Hex and FS-TEG. These comprise the same backbone, but feature hydrophobic alkyl and hydrophilic glycol side chains respectively. Importantly, the hydrophilicity of the glycol side chains encourages much higher levels of water permeation [140], affecting the microstructures of the nanoparticles and films, and the dielectric environment of the polymers.

My collaborators used transient-absorption spectroscopy (TAS) to measure the kinetics of excited states and charges (electrons) in FS-Hex and FS-TEG. They found that, for similar electron densities, the lifetime of electrons in FS-TEG were significantly longer than in FS-Hex. Notably, when exposed to higher fluence, both materials displayed an unusual trend of longer electron lifetimes with increasing density of generated electrons, as may be seen in Figure 4.2. This runs counter to the more common observation of higher charge densities reducing lifetimes, due to bimolecular recombination processes [141–143]. The mechanism behind these longer lifetimes was understood as originating from a 'queuing' effect involving an unintentionally introduced palladium co-catalyst that remains in the polymer from synthesis. The current hypothesis is that the palladium catalytic sites can become fully occupied by electrons. These electrons must be used up in slow proton reduction reactions before any more can transfer onto the palladium.[9] Therefore, some electrons must 'wait' (i.e. queue) in the polymer region before they can be extracted. Assuming the same density of catalytic sites, the queuing time becomes longer for higher electron densities, resulting in the fluence-dependent decay rates observed by TAS.

For my contribution to the study, I carried out charge transport simulations using `ToFeT` to explore

[9] More precisely this step involves several processes, including the migration and then binding of protons onto the palladium, the charge transfer reaction, further reactions involving the hydrogen intermediates bound to the palladium surface, and finally the unbinding and migrating away of hydrogen molecules. This sequence of steps results in a slow overall process [144, 145].

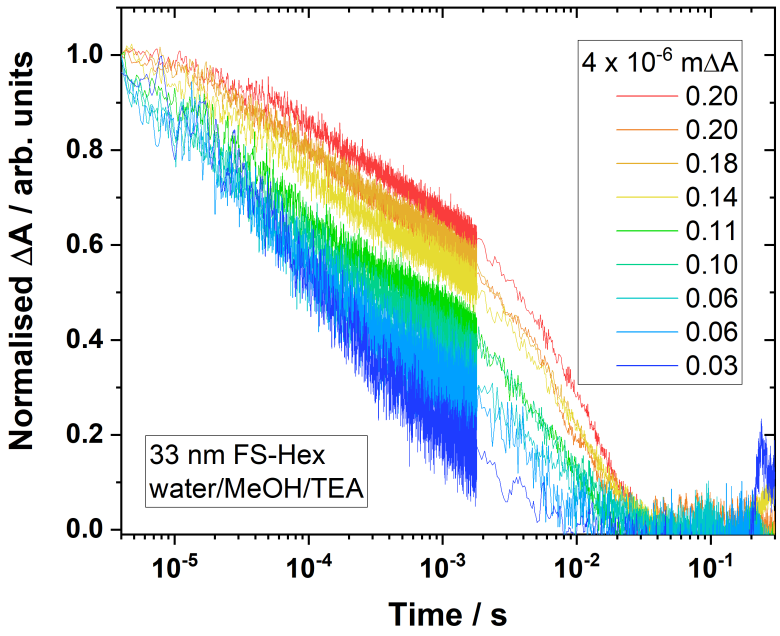


Figure 4.2: Electron kinetics from transient-absorption spectroscopy of FS-Hex film, at various fluence levels [128]. Included with permission from Sam A. J. Hillman.

the behaviour of electrons in these interfacial systems, specifically focusing on the lifetime of electrons in the polymer region. My goal was to identify the conditions under which the simulations could recreate the unusual electron-density dependent decay rates, to ensure we had a model showing good correspondence with the TAS experiments. With a suitable baseline model in place, I could then modify its parameters to explore the various factors influencing the behaviour of electrons. Analysis of the simulation results could then allow us to rationalise the experimental observations of FS-Hex and FS-TEG, and draw out insights to improve our understanding of photocatalytic polymer systems.

Method

A visualisation of the interfacial photocatalysis model system may be seen in Figure 4.3. The system is divided into three regions, representing the polymer, the metal co-catalyst occupation sites, and the proton reduction step. The polymer region consists of a $9 \times 9 \times 9$ cubic grid of generator-type sites (coloured green in Figure 4.3), with a lattice constant of 5 Å. Edges were placed between all nearest neighbours (NNs), including those separated by periodic boundaries in the x- and y-directions. The metal occupation sites were represented by a small number of transport-type sites (grey in Figure 4.3), placed in a plane 5 Å from the upper z-layer of the polymer grid. Different numbers of metal sites (N_{metal}) were tested (see Figure D.2), however six metal sites were used to produce the results presented here, since this provided the best match with the TAS data. Physically, this may represent clusters of palladium atoms that are likely to be present in experimental devices, as opposed to single-atom sites.

Edges were placed to connect one polymer site in the upper z-layer to all the metal sites. All the metal sites were connected by edges to one collection site (red in Figure 4.3). The transfer of electrons

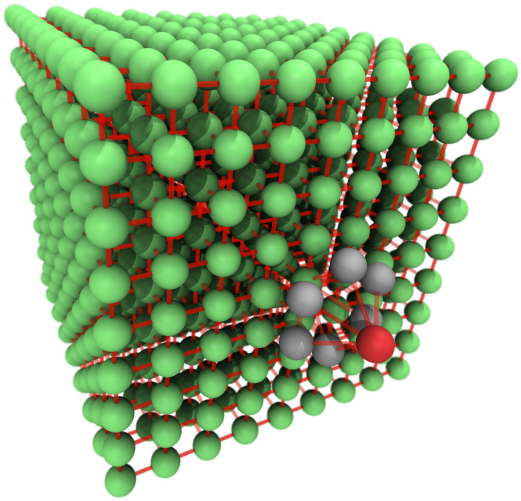


Figure 4.3: A visualisation of the interfacial photocatalysis model system used in charge transport simulations. Green sites represent the polymer region of the system. Grey sites represent the metal co-catalyst occupation sites. The red site is a collection site. Electronic coupling between nearby sites is indicated by red lines. Electron transfer between the metal sites and the collection site represents the proton reduction reaction.

from the metal sites to the collection site represented the proton reduction reaction.

The electronic coupling between polymer sites (J_{polymer}) was set to 0.6 meV, a somewhat low value relative to typical polymer-polymer coupling strengths in the solid-state (see Section 6.2.2). I considered this appropriate given the disruption to the polymer microstructure imparted by water permeation. Coupling between the polymer site and metal sites (J_{metal}) was set to 0.1 meV (equal to a lower value used for J_{polymer} when representing a situation of higher water permeation). I chose a similar (or equal) value to J_{polymer} to represent the intermixing of polymer and metal sites in the experimental devices, leading to similar separation distances between polymer-to-polymer and polymer-to-metal. Finally, coupling between the metal and collection sites ($J_{\text{reduction}}$) was set to 3×10^{-4} meV. Here, a much lower value than J_{polymer} or J_{metal} was used, to represent the slow rate of the final hydrogen-production step.

A degree of energetic disorder was included in the polymer region, to produce dispersive transport behaviour corresponding with the TAS measurements (see Figure 4.2). Polymer site energies ($\epsilon_{\text{polymer}}$) were drawn from an exponential distribution with the probability density function

$$f(\epsilon_{\text{polymer}};\xi) = \begin{cases} \frac{1}{\xi}\exp\left(\epsilon_{\text{polymer}}/\xi\right), & \epsilon_{\text{polymer}} \leq 0 \\ 0, & \epsilon_{\text{polymer}} > 0 \end{cases}, \tag{4.1}$$

where the scaling parameter (ξ) was set to 0.036 eV to give a good correspondence with the TAS data (the effect of energetic disorder on the simulated kinetic will be discussed further in the results section).

To increase the rate of transfer from the polymer site to metal sites, and decrease the rate of back transfer, the site energy of the metal sites (ϵ_{metal}) was set to -300 meV. The site energy of the

From	To	Rate
Polymer	Polymer	6×10^8
Polymer	Metal	3×10^8
Metal	Polymer	3×10^3
Metal	Collection	2×10^2

Table 4.1: Hopping rates in the interfacial photocatalysis model system. Rates are provided in s^{-1}, and are calculated for a system temperature of 300 K. All rates involving polymer sites were calculated assuming $J_{\text{polymer}} = 0.6\,\text{meV}$ (representing FS-Hex) and $\epsilon_{\text{polymer}} = 0$. Note that the relatively small effect of the external field was neglected for these calculations.

collection site ($\epsilon_{\text{reduction}}$) was similarly set to $-300\,\text{meV}$. The reorganisation energy (λ) was set to 300 meV for all hops. With these electronic structure parameters in place, the various hopping rates within the system may be calculated. These are provided in Table 4.1.

The consequence of this system topology and parameter values was that transfer between the different regions was notably and deliberately asymmetric. Electrons could relatively easily travel through the polymer region and be transferred onto one of the unoccupied metal sites. These electrons would then be trapped on the metal site for some time, being slowly transferred onto the collection site, and with only a small chance of being transferred back into the polymer region. The probability of back transfer into the polymer region is further decreased by the occupation of the polymer site connected to the metal sites by queuing electrons. This artificial bottleneck was designed to recreate the queuing effect observed in the TAS data (Figure 4.2).

Simulations were run in `tof` mode, meaning electrons were not regenerated after collection, and were not able to loop back through the system via a periodic boundary in the z-direction. Using the new `ToFeT` functionality described in Section 4.3, the transient electron populations in each region were recorded during simulations by setting `trackpop 1`. An external electric field, with strength $-1 \times 10^4\ \text{V cm}^{-1}$ was applied in the z-direction, to encouraged electrons to move towards the metal and collection sites. The system temperature was set to 300 K. To recreate the electron-density dependent decay rates observed by TAS, a series of simulations were run with variable numbers of electrons (N_{e}) initially generated at random locations in the polymer region. For each simulation in the series, the number of runs (N_{run}) was adjusted, such that

$$N_{\text{e}} \times N_{\text{run}} \approx 10{,}000. \tag{4.2}$$

This[10] was done to automatically normalise the transient electron population data between simulations, and provide better statistics, since the population values represent a summation over all runs. Each run is halted once all electrons have been collected, and the full simulation halts once all runs have been completed.

[10] 'Approximately equal', since N_{e} and N_{run} are integers.

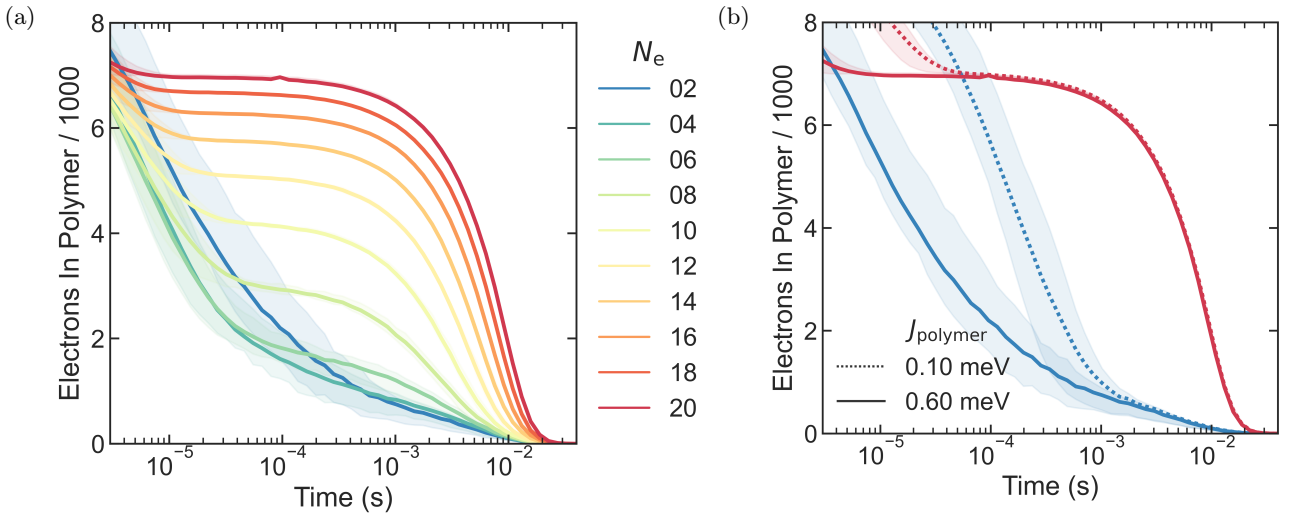


Figure 4.4: Decay of electron populations in the polymer region of an interfacial photocatalytic system. Lifetimes are shown to vary with the initial number of electrons (N_e). (a) Time-evolution of electron population in the polymer region, for $J_{polymer} = 0.6\,meV$ (representing FS-Hex). (b) Time-evolution of electrons in the polymer region, comparing $J_{polymer} = 0.1\,meV$ and $0.6\,meV$, representing FS-TEG and FS-Hex, respectively. Only $N_e = 20$ and $N_e = 2$ curves are shown, for clarity. Typically, the kinetics show two distinct phases. The first phase (before $\sim 3 \times 10^{-6}\,s$) represents the period where metal sites are becoming occupied but are not yet filled. Since the queuing effect has not yet begun to influence the population transients, all N_e-curves follow a similar exponentially-decaying trend. Only the second phase is shown, which begins once all metal sites have been occupied, and kinetics become dominated by the queuing effect.

Results

Results of the `ToFeT` simulations are shown in Figure 4.4. Figure 4.4a shows the time evolution of electrons in the polymer region of the baseline model, representing the FS-Hex system. The model was able to recreate the qualitative dependence of the population decay rates on the initial population of generated electrons, as observed by TAS (Figure 4.2); For a high N_e, the simulations results show a slower decay in the electron population compared to low N_e.

The kinetics tend to show two distinct phases, which relate to the times before and after the metal sites have become fully occupied (at $\sim 3 \times 10^{-6}\,s$), and thus will start to block the exit of other electrons from the polymer region. Corollary to this, when $N_e \leq N_{metal}$ the kinetics feature only a single phase, which is the cause of the much faster decay of the electron populations at low N_e.

In addition to the presence of one or both phases, the kinetics for different N_e are further differentiated by the length of a plateauing period, which initiates at the point in time when the metal sites have just been filled (i.e., representing the start of the second phase). This corresponds to the time at which the population remaining in the polymer region (n) first reaches a threshold of

$$\begin{aligned} n &\approx N_{run} \times (N_e - N_{metal}) \\ &\approx 10{,}000 \times (1 - N_{metal}/N_e)\,. \end{aligned} \tag{4.3}$$

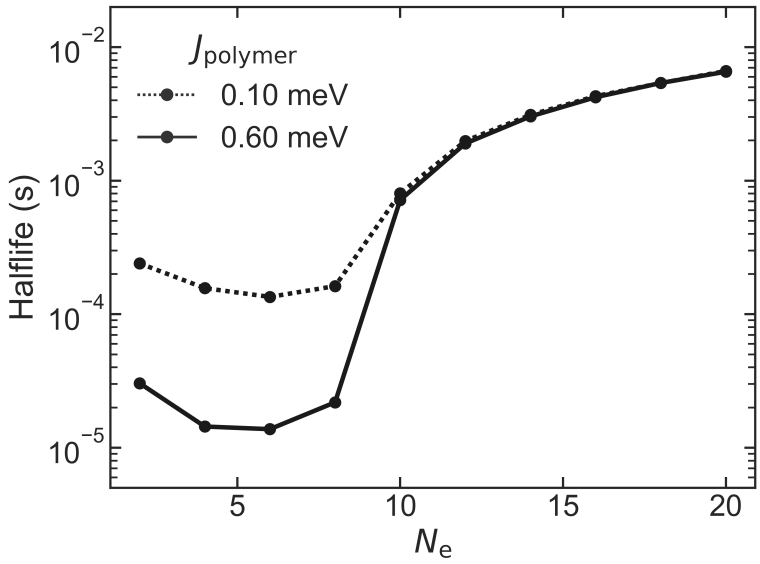


Figure 4.5: Half lives (τ) of electrons in the polymer region, calculated from when the electron population in the polymer region decreases below 3500. This corresponds to a 50% decrease from 7000, which is the remaining electron population after the first phase in the electron decay kinetics has concluded (and the population curves start to diverge due to the queuing effect). Half lives are calculated for $J_{\text{polymer}} = 0.1\,\text{meV}$ and $J_{\text{polymer}} = 0.6\,\text{meV}$, representing FS-TEG and FS-Hex respectively.

Figure 4.4b compares the transient populations in FS-Hex and FS-TEG using the extreme N_e values. In this case, FS-TEG is differentiated from the FS-Hex baseline by reducing J_{polymer} from 0.6 meV to 0.1 meV, representing the higher degree of water permeation in FS-TEG pushing polymer backbones apart. The rate of population decay is similar between the two systems when N_{e} is large, due to the dominance of the queuing effect. However, the decay curves are distinct when N_{e} is small. In this case, the electron population in FS-Hex decays significantly faster rate than FS-TEG.

This discrepancy is borne out in the calculated half lives (τ) shown by Figure 4.5. In order to represent the half-lives of only the second (queuing) phase, I located τ with reference to the electron population remaining when the N_{e}-curves start to diverge. This approximately corresponds to the earliest onset of a plateau in any of the population kinetics. From Equation 4.3, this occurs when the $N_{\text{e}}^{\text{max}} = 20$ population approaches 7000. Therefore, we can find τ from the point in time when each of the transient populations first decreases below 3500.

We observe that the τ of FS-Hex at $N_{\text{e}} \leq 10$ are significantly shorter than the τ of FS-TEG. A kink can be observed in the τ trends of both systems after $N_{\text{e}} \simeq 8$, due to the increasing dominance of the queuing effect.[11] Therefore, by $N_{\text{e}} \simeq 10$, the polymer-region populations in both systems show similar τ.

The simulations described above were conducted using a selection of model parameters that resulted in a reasonable correspondence with the experimental data. However, a much broader range

[11] For increasing N_{e}, we can expect a jump in τ to occur when the threshold population at which the kinetics plateau (Equation 4.3) becomes larger than the population we used to locate τ (3500). This occurs when $N_{\text{e}} > 2N_{\text{m}}N_{\text{e}}^{\text{max}}/(N_{\text{m}} + N_{\text{e}}^{\text{max}})$, which gives $N_{\text{e}} > 9.2$.

of parameter values was also explored. The results of this exploration were useful for clarifying in which ways different parameters governed the behaviour of the system, and in some cases allowed us to rule out certain phenomena as playing a major role in the behaviour of the experimental devices (see below). A large selection of the parameter exploration results are provided in Appendix D, along with discussion of the effect of varying different parameters. Here, I limit my discussion to the results that are most informative about the behaviour of the physical devices.

As stated, introducing a degree of energetic disorder led to a better correspondence between the simulated and experimental TAS results. In particular, higher values of ξ increased the time at which the slowest electrons were collected, due to the effect of energetic trapping on transport in the polymer region. As is commonly observed in systems featuring energetic traps, the filling of traps at high charge densities (high N_e) meant that increasing ξ had a larger impact when N_e was low.[12] Therefore, by tuning ξ, I was able to replicate a particular characteristic of the TAS data. Namely, that the point in time at which all electrons had exited the polymer was approximately the same ($\sim$10 ms), independent of the initial charge density.

Continuing to increase ξ led to increased competition between the queuing effect (which slows down population decay at high N_e) and charge trapping (which slows down population decay at low N_e). Eventually, charge trapping effects become dominant, producing a reversal in the trend of the kinetics for different N_e. As may be seen in Figure D.8, at high ξ the low N_e curves decay slower than the high N_e curves.

The observation of this trend reversal in the simulations may provide insight into the mechanism by which increased water permeation slows down electron transport in FS-TEG relative to FS-Hex. In particular, the fact that the reversed trend was not observed in the experimental data implies that a mechanism based on water-induced energetic traps may be ruled out as playing a dominant role. Zuo et al. identified that a typical trap depth of 0.3 eV to 0.4 eV would arise from such a mechanism [146]. This may be compared with the distributions of site energies in Figure D.7a, and the corresponding effect of including these site energies on the kinetics of the transient populations, in Figure D.8. From these, we observe that, at typical trap densities $\ll$0.3 eV, the kinetics have already begun to display the aforementioned reversal in order that separates them from the TAS kinetics. Therefore, rather than energetic traps, the dominant mechanism causing increased water permeation to slow down transport in FS-TEG, relative to FS-Hex, appears to be from increased disruption of the FS-TEG microstructure, which in this study was modelled by reducing J_{polymer} for this polymer (Figure 4.4b).

While introducing a limited degree of energetic disorder enhanced the dispersive behaviour of the transient population kinetics at low N_e, at high N_e the kinetics maintained a characteristic exponential

[12] This is particularly evident in the $N_e = 2$ kinetics, which are slowed down to a greater extent those of $N_e = 4$ and $N_e = 6$, while otherwise showing similar behaviour i.e., having no second (queuing) phase.

shape. This is distinct from the TAS data (Figure 4.2), in which the kinetics are dispersive across all the tested fluence levels, implying that the final proton reduction reaction may occur with a distribution of rates. In the model system, I attempted to replicate this by introducing disorder in $J_{\text{reduction}}$ (see Figure D.11). At the highest levels of disorder that I evaluated, the kinetics at all values of N_{e} did show marginally more dispersive behaviour, which slightly improves the qualitative correspondence with the experimental data. Potentially, this could be improved further by continuing to explore different levels of $J_{\text{reduction}}$ disorder and/or by adopting alternative distribution shapes (see Table D.1 caption). However, determining the physical origin of – and therefore appropriate method for modelling – dispersive rates in the hydrogen evolution process is beyond the scope of the work covered in this thesis. I have therefore chosen to present results based on a single (non-disordered) value for $J_{\text{reduction}}$ throughout this section.

The following implications can be drawn from the simulation data, in combination with data from TAS and other experiments in [128]. For commercial devices, we typically want to operate with high fluence, to generate a high density of electrons, which in turn results in the highest rate of hydrogen production. In other words, devices will generally be operating in the regime dominated by the identified electron queuing effect. Because of this, device performance gains little benefit from transporting electrons faster through the polymer to the metal co-catalytic sites. On the contrary, a higher mobility in the the polymer can harm performance by increasing the likelihood of recombination events; By allowing the 'waiting' electrons to move around the polymer faster, they can more quickly locate holes and/or recombination sites, causing them to decay before they can be used in the hydrogen production process. Based on this premise, you may be able to achieve longer charge lifetimes in the polymer region, and better device performance, by *slowing down* transport in the polymer.

Between the two polymers examined in this study, FS-TEG showed significantly higher populations of long-lived electrons in experiments, and superior device performance. We surmised that this was because the increased water permeation in FS-TEG reduced the electronic coupling between polymer chains, and thus reduced its mobility compared to FS-Hex. Thus, based on our analysis of the simulation and TAS data, we were able to rationalise the high performance of sulfone polymers in this application, in light of their low mobilities compared to other polymers [128, 138].

In conclusion, this case study demonstrates the utility of `ToFeT` for recreating and analysing charge transport in systems containing OSC materials. Furthermore, it demonstrates the versatility of `ToFeT`, which has been enhanced by the modifications and updates described in Section 4.3. With careful consideration of the model system setup, `ToFeT` can be used to gain insights into the functioning of devices other than those associated with mobility measurements (e.g., ToF and FET devices), such as interfacial photocatalytic systems for hydrogen production.

4.5.2 Crystalline Packing Arrangements and their Impact on Mobility

Introduction

Fullerenes and fullerene derivatives constitute one of the most widely used classes of acceptor materials in OPV devices. The electronic structure of these molecules, and the microstructure of the solid state, can be modified by attaching single or multiple functional groups to the fullerene cage. bis-PCBM features two phenyl-butyric acid methyl ester groups attached to the C60 cage. The attachment locations of the functional groups can influence the packing arrangements of the molecules, which in turn affects the electronic properties of the solid.

Ordinarily, understanding the impact of functional group location on the characteristics of materials is hindered by the fact that samples of bis-PCBM are typically synthesised containing a mixture of different isomers. In a previous work by Shi et al., this was overcome by applying a combination of advanced synthesis and purification techniques, to obtain ∼99.9% pure samples of the different bis-isomers [147]. These samples were then associated with the 19 different functional group attachment locations in a work by Liu et al. [148]. The structures of the 19 isomers are shown in Figure 4.6.

In this work [129], my collaborator Xueyan Hou carried out a number of experimental characterisation techniques on thin films fabricated from samples of the various purified isomers. The microstructures of the isomers were characterised based on thermal analysis of the films, while FET experiments were performed to measure their electron mobilities. Xueyan found correlations between these solid-state properties and the degree of symmetry exhibited by the isolated molecular structures. In particular, she observed that molecules with higher symmetry generally showed higher crystallinity, but worse experimental mobilities.

The symmetry of the molecules is itself determined by the attachment positions of the functional groups. By considering the distance around the fullerene cage that one group is attached relative to the other, the 19 different isomers can be classified into groups exhibiting similar symmetries. My collaborators solved the crystal structures of one representative isomer from each of the three main molecular geometry groups, referred to as the *trans*, *e* (for equatorial), and *cis* groups. These group descriptors refer to the location of the second functional group, assuming the first functional group is located at the pole position of the fullerene cage. The specific representative isomers taken from these groups are referred to by the numeric labels *2.3*, *3.3.2* and *7*. A summary of information about these isomers, including the point group symmetries they exhibit, and the degree of crystallinity this is predicted to lead to, is shown in Table 4.2.

In terms of their transport properties, isomer *3.3.2* was measured to have the highest mobility ($\sim 0.03\,\mathrm{cm}^2/\mathrm{Vs}$) of the three. Isomer *2.3* showed a similar, but slightly lower mobility ($\sim 0.02\,\mathrm{cm}^2/\mathrm{Vs}$), while isomer *7* showed the lowest mobility ($< 8 \times 10^{-4}\,\mathrm{cm}^2/\mathrm{Vs}$), demonstrating overall poor transport.

For my contribution to this study, I carried out a series of charge transport simulations using

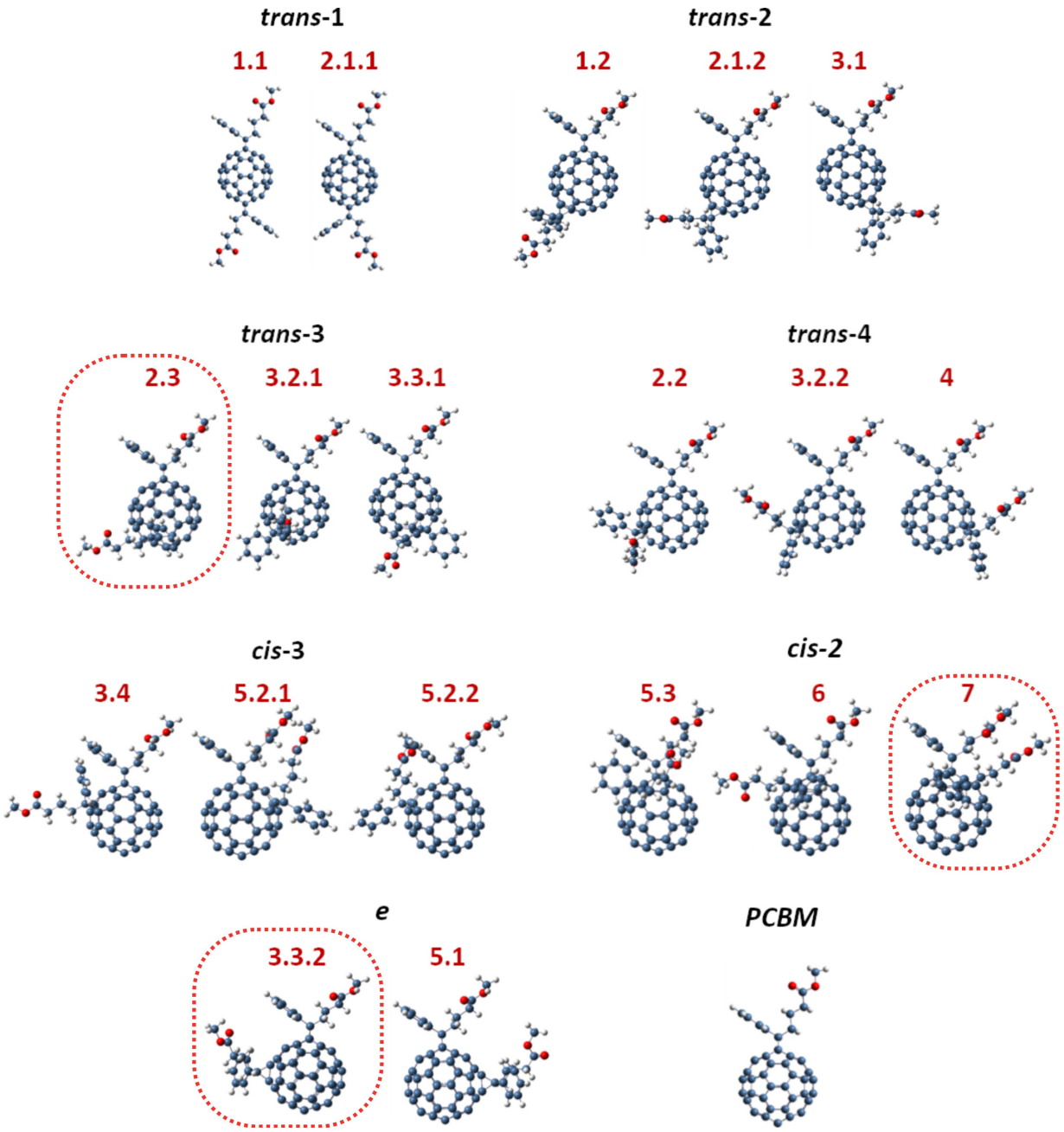


Figure 4.6: Chemical structures of the 19 bis-PCBM isomers and PCBM. The representative isomers explored in this study have been circled in red. With permission from Xueyan Hou, this image has been adapted from [129].

Isomer	**Functional group location**	**Point group symmetry**	**Expected crystallinity**
2.3	*trans*-3	C_2	Moderate
3.3.2	*e*	C_1, C_1	Low
7	*cis*-2	C_s, C_1, C_s	High (poor solubility*)

Table 4.2: Information about representative bis-PCBM isomers evaluated by transport simulations. Comparison with transport simulations reveals that the isomers display decreasing dimensionality of transport as we move down the table.

* High molecular symmetry decreases the polarity of molecules, which can reduce solubility [129].

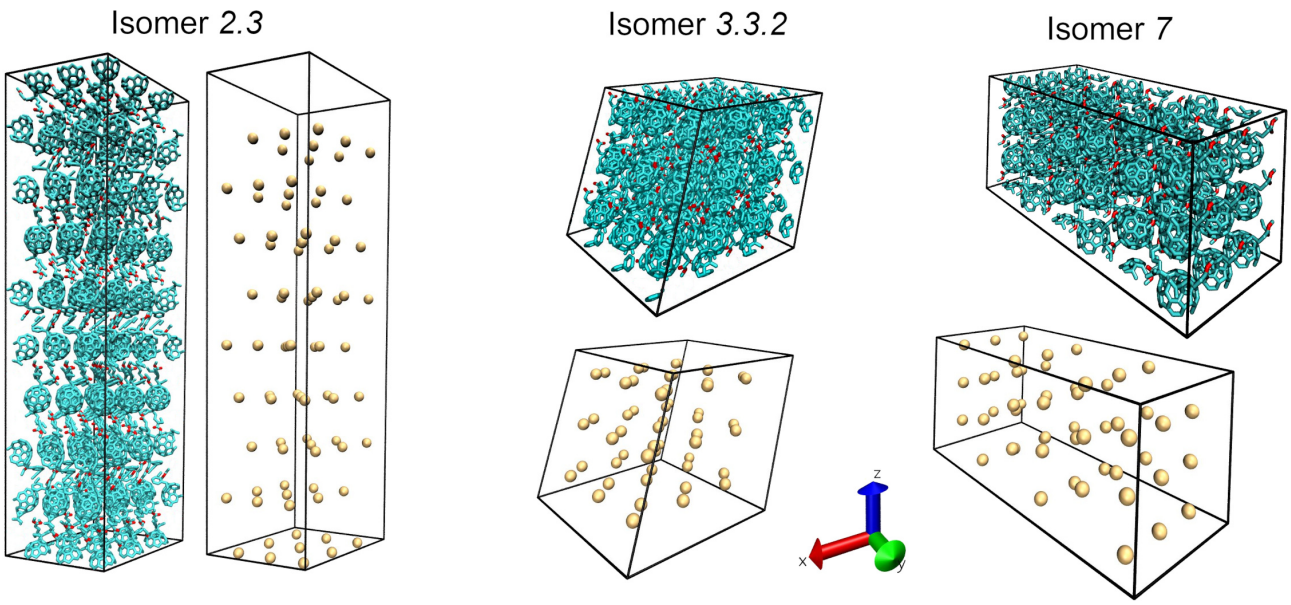


Figure 4.7: bis-PCBM supercells, for the three example isomers. The molecule structures are shown, with hydrogen atoms hidden for clarity, alongside fullerene CoG positions. Simulation PBCs are shown as black boxes.

the different crystal structures associated with the isomers listed in Table 4.2. By comparing the simulation results against the FET measurements mentioned above, we were able to rationalise the impact of crystal structure packing arrangements on the transport behaviour of the different bis-PCBM isomers. This analysis revealed the effect of functional group attachment location on the transport properties of devices, via its impact on crystalline packing arrangements.

Method

To carry out transport simulations, I first needed to convert the crystal structures of the three isomers into a suitable graph representation. Since the LUMO is delocalised over the fullerene cage, we can treat each cage as a single electron site [116]. I therefore placed sites at the CoGs of the fullerene cages, taking care to find the correct locations when cages were split across cell boundaries. The site coordinates were then translated to create $3 \times 3 \times 3$ supercells, which are shown in Figure 4.7. This was done in order to avoid placing edges that connected sites back to themselves (i.e. loops). To parameterise the edges of the transport network, I began by finding the distance (r) between all NN and next-NN sites, employing the minimum image convention to find r between sites separated by the PBCs. I used Equation 3.28 and r to estimate the LUMO-LUMO coupling between molecules (J), adopting the function

$$J(r) = \alpha \exp\left(-\frac{r}{\beta}\right),$$

where the parameters α and β were set to values of 15 meV and 0.5 Å, respectively. These values were chosen based off calculations performed by Steiner et al. [116]. I used a value of 200 meV for the reorganisation energy (λ) based on an approximate average of the inner-sphere λ for bis-PCBM, also

reported in [116].[13] The Marcus equation was used to calculate the hopping rates between sites (see Section 2.3.2). I considered it justified to assume a hopping mechanism for transport, since $J \ll \lambda$ even for the closest packed molecules (due to the low degree of contact surface between fullerene cages [149]). Site energies (ϵ) were set to zero for all sites, representing a situation of negligible energetic disorder, as appropriate for crystalline structure with little difference between the conformation of molecules.

Since both the transport programs described in this chapter fix the direction of the external electric field in the z-direction of inputted systems, evaluating the electron mobility (μ) in different directions required the system coordinates to be rotating prior to input. However, with the exception of isomer *7*, the crystal cells were not orthorhombic. Because the plane of the periodic boundary in the transport direction must be orthogonal with the field direction, it was not always possible to evaluate mobilities in directions aligned with the crystal lattice vectors ($\hat{a}$, $\hat{b}$, and $\hat{c}$). Instead, I rotated the systems to assess transport in the $\hat{b} \times \hat{c}$, $\hat{c} \times \hat{a}$, and $\hat{a} \times \hat{b}$ directions, corresponding approximately to $\hat{a}$, $\hat{b}$, and $\hat{c}$, respectively (or sometimes corresponding exactly, depending on the angle between lattice vectors).

I initially ran transport simulations using `ToFeT`. However, because of the wide range in hopping rates, mobilities in the slowest transport direction of isomer *2.3* did not converge, even with long simulation times. I therefore repeated the simulations using `MESol`. During all simulations, the system temperature was set to 300 K, and the strength of the external field was set to 1×10^4 V cm^{-1}. Results of the simulations, and comparison with experiments, are discussed below.

Results

Figure 4.8 shows the mobilities evaluated by `MESol` for the bis-PCBM isomers *2.3*, *3.3.2* and *7*, in the directions $\hat{b} \times \hat{c}$, $\hat{c} \times \hat{a}$, and $\hat{a} \times \hat{b}$. Transport is predicted to be highly anisotropic in all cases, with all isomers found to be effectively non-transporting ($\mu < 10^{-4}$cm^2/Vs) in one of the evaluated directions. However, there remains differences in the degree of transport dimensionality shown. Isomer *2.3* displays the highest dimensionality of transport, with two high mobility pathways in the $\hat{b}\times\hat{c}$ and $\hat{c}\times\hat{a}$ directions. Isomer *3.3.2* shows similar, but slightly lower dimensionality, with a high mobility pathway in the $\hat{c} \times \hat{a}$ direction, and marginally slower mobility in $\hat{b} \times \hat{c}$. In contrast, transport in isomer *7* is mostly 1-dimensional, featuring one high mobility pathway in the $\hat{b} \times \hat{c}$ direction, and ∼10× lower mobility in $\hat{a} \times \hat{b}$.

Neglecting the non-transporting directions, isomer *2.3* shows the highest average mobility, while average mobilities for isomers *3.3.2* and *7* are lower and approximately equal. It is important to note that, because values for the electronic structure parameters were chosen on an informed, but semi-arbitrary basis, we did not expect the simulated mobilities to align quantitatively with experiments. This is compounded by the fact that the complimentary FET experiments described in [129] were not

[13] Simulations were also performed with a λ of 500 meV, as an estimate for the combined inner- and outer-sphere λ. However, only the $\lambda = 200$ meV results are reported here, since there was little difference between the trends in μ shown in each case.

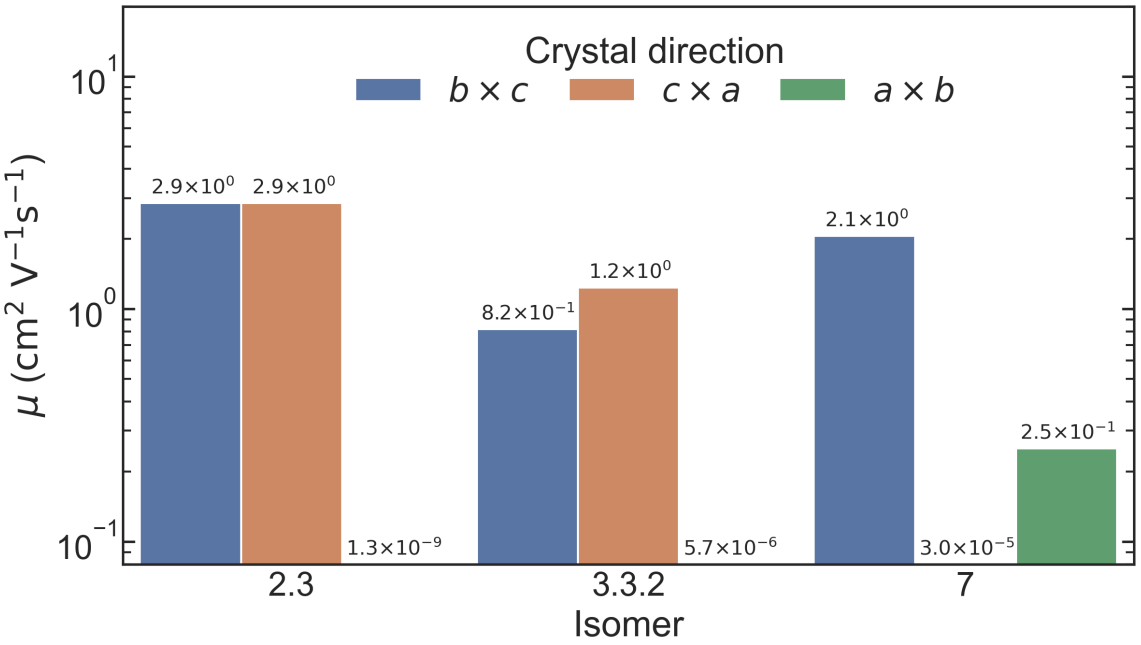


Figure 4.8: Simulated mobilities of representative bis-PCBM isomers.

performed on single crystals. Nevertheless, the qualitative trends in the simulation results were still useful for rationalising the experimental data characterising transport in thin films fabricated from the different isomers.

The FET experiments showed isomer *3.3.2* as having the highest mobility ($\sim$0.03 cm^2/Vs) of the three example isomers. Isomer *2.3* showed a similar, but slightly lower mobility ($\sim$0.02 cm^2/Vs), while isomer *7* showed the lowest mobility ($< 8 \times 10^{-4} cm^2$/Vs), demonstrating overall poor transport. The trend in experimental mobility values aligned approximately with the trend in the dimensionality of simulated transport, with isomers *2.3* and *3.3.2* being approximately equal, and both superior to isomer *7*. These results demonstrate the utility of analysing the dimensionality of transport in crystal structures of the different isomers for rationalising the experimental transport measurements: higher dimensionality is likely to lead to higher bulk mobility by increasing the availability of percolating transport pathways.

At this point, it is of interest to explore the slight discrepancy between the trends in simulated dimensionality and experimental mobility for the two higher performing isomers. In this regard, further insight can be gained by considering the molecular symmetry and experimental microstructures of the isomers. Isomer *2.3* featured moderate molecular symmetry, and produced crystalline films. Isomer *3.3.2* featured low symmetry, and produced amorphous films. Isomer *7* featured very high symmetry, which was predicted to lead to highly crystalline films. However the high degree of symmetry reduces the polarity of the molecules, leading to low solubility, and the fabrication of poor film microstructures. Therefore, the highest experimental mobilities were measured for the least symmetrical, most amorphous isomer (*3.3.2*). An amorphous microstructure implies that there is less

preference between the different packing arrangements of molecules, and that transport will be effectively 3-dimensional. Therefore, in experimental microstructures, transport is effectively 3D for the amorphous isomer *3.3.2*, 2D for the crystalline isomer *2.3*, and 0D in the poor microstructure of isomer *7*. Hence, this may explain the slight discrepancy observed between the simulated transport dimensionalities ($2.3 \gtrsim 3.3.2 \gg 7$) and the experimental mobilities ($3.3.2 \gtrsim 2.3 \gg 7$).

The results and analysis presented in this section demonstrate the utility of `MESol` for rationalising the transport behaviour of OSC materials.

4.6 Conclusions

In this chapter, I described my development of two charge transport simulation programs, `ToFeT` and `MESol`, and their respective application in two case studies. The first study investigated the two sulfone photocatalytic polymers FS-Hex and FS-TEG, while the second looked at bis-isomers of PCBM.

In Section 4.3 I described several updates and modifications made to the KMC code `ToFeT`, originally created by Joe J. Kwiatkowski [65]. These changes improved the accuracy of the charge mobilities evaluated by `ToFeT` (see Chapters 6 and 8), and its versatility (see Section 4.5.1). The utility of this code has been demonstrated by its application in the studies [150], [128], and [60]. For the case study detailed in Section 4.5.1, `ToFeT` was employed to provide evidence rationalising the high performance of sulfone polymers in hydrogen production applications, in light of their low mobilities. By combining with TAS experiments, we showed that hydrogen production efficiencies were ultimately limited by the slow proton reduction step involving electrons on palladium co-catalytic sites. Due to an identified 'queuing' effect, little benefit was gained from transporting electrons more quickly through the polymer region of devices. The simulation results were also useful for demonstrating that the main mechanism by which water permeation was likely to slow down transport was via disruption to the polymer microstructure, and not via an alternative mechanism involving water-induced energetic traps.

In Section 4.4 I described the development of the ME code `MESol`, including the implementation of a rate matrix preconditioning functionality designed to speed up calculations and ensure the accuracy of evaluated charge mobilities. The utility of this code has been demonstrated by its application in the study [129]. Relevant portions of this study were detailed in Section 4.5.2. Here, I described how `MESol` was utilised to help rationalise an unexpected trend in experimental results in which those isomers showing the highest crystallinity also tended to show the lowest mobilities. This trend was understood by considering the dimensionality of transport established by the different crystalline structures and degrees of crystallinity exhibited by the isomers. In particular, the most amorphous isomers were surmised to benefit from mostly 3D transport, while an increasing propensity to crystallise first reduced the transport dimensionality to 2D, before ultimately reducing it to 0D due to low solubility and thus poor film formation.

Chapter 5

Microstructure of C16-IDTBT

This chapter, and the following, describe an investigation into the high-mobility, non-crystalline polymer C16-IDTBT. Here, I detail insights about the microstructure of C16-IDTBT gained from analysis of MD models and comparisons with experiments. I identify an unusual packing motif involving polymer backbones crossing at near-perpendicular angles, which encourages the backbones to form a highly interconnected network-like structure. The resulting effect on transport is explored further in Chapter 6. The majority of the work described here has been published in Proceedings of the National Academy of Sciences *[150].*

5.1 Introduction

The high-mobility conjugated polymer C16-IDTBT was introduced in the background chapter (Section 2.5). In this chapter I describe my investigation into the microstructure of C16-IDTBT, focusing on those microstructural features which can help rationalise the transport behaviour of the polymer.

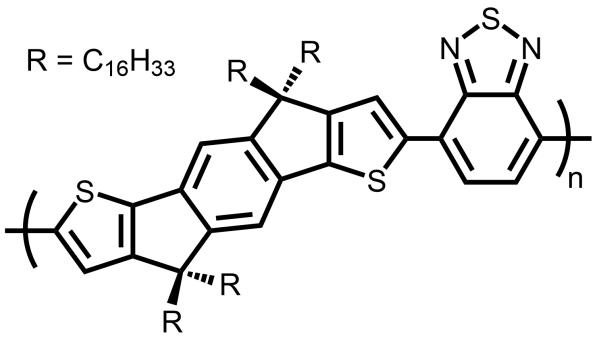


Figure 5.1: Chemical structure of C16-IDTBT.

Here, I briefly summarise insights from past work relevant to this investigation. These were presented in an expanded form in Section 2.5.3. The C16-IDTBT backbone is linear and planar, indicating support for fast intrachain transport [86]. There are four bulky side chains attached to the IDT unit of the backbone, which do not appear to inhibit electronic transport properties [83]. In thin films, chains are oriented largely in-plane, i.e. with backbones parallel to the substrate and with their π-conjugated planes face-on to the substrate [29]. Despite the microstructure being mostly disordered, there is evidence for domains of aligned backbones [93, 94]. There is a preference for 20° and 90° angles between the backbones of intersecting domains [93]. Finally, despite relatively little ordering in the π-stacking direction, backbones appear to form close π-stacked contacts [29].

With these observations in mind, there remains a number of questions about the microstructure of C16-IDTBT, which I list here:

- What is the persistence length of C16-IDTBT?
- How does the chemical structure of C16-IDTBT influence the geometry of contacts? Does this explain how interchain packing is close, in spite of the long side chains and lack of crystallinity?
- How does the geometry of contacts influence their propensity to form, and thus the density of contacts in thin films?
- In combination with other microstructural features (such as backbone rigidity), how is the geometry and density of contacts likely to influence charge transport?
- Do the above features and behaviours differ between C16-IDTBT and other conjugated polymers?

To address these questions, I carried out a series of computational investigations. However, it is important to acknowledge that much of my work was done in collaboration with my coauthors on [150]. A brief summary of their contributions is provided here.

C16-IDTBT samples were synthesised by Weimin Zhang and Iain McCulloch. To characterise the conformation of individual C16-IDTBT chains, small-angle neutron scattering (SANS) measurements were performed by Chad R. Snyder and Lee J. Richter. These were carried out on samples of different molar masses and concentrations in solution. They analysed the scattering data under a flexible cylinder model, finding that the persistence length (P) of the polymer lies in the range 6.8 nm to 39 nm, therefore confirming the rigid structure of the backbone [150].

To complement these measurements, P was also evaluated computationally by Anders S. Gertsen. He performed CG MD simulations of chains in chloroform. His analysis of the simulation trajectories provided a value of 27.0 ± 6.7 nm [150].

For the following accounts, I only describe the methods employed by my collaborators. Results are provided later in the chapter, at the point where they are most relevant to my investigations.

To understand the behaviour of C16-IDTBT chains adhered to substrates, Giovanni Costantini and Stefania Moro used vacuum-electrospray deposition (ESD) to deposit monolayer films of C16-IDTBT on atomically flat Au(111) substrates. They then captured images of the structures formed using scanning tunnelling microscopy (STM). When imaged in this manner, conjugated polymer chains adopt a uniformly face-on orientation to the substrate. Because this is also the case throughout C16-IDTBT thin films with thicknesses up to several tens of nm [29], we can presume that the STM images provide a good representation of the initial stages of thin film formation [150].

Much of my MD work was enabled by building on top of work carried out by Anders S. Gertsen during his PhD at the Technical University of Denmark, especially the painstaking task of parameterising forcefields for C16-IDTBT and other materials. Because we were interested in modelling large

volumes of the solid, and long time scales associated with microstructure formation, Anders developed CG forcefields for a set of conjugated polymers [151], as well as a procedure for simulating the solution-evaporation deposition of thin films [121, 152]. The procedure was designed to replicate the slot-die coating fabrication technique for thin films. Using this, Anders generated CG models of C16-IDTBT thin film microstructures, and other conjugated polymers for comparison [150].

My contributions to the investigation of C16-IDTBT are described in the remainder of this chapter. Here, I briefly outline the various methods I employed, and how these were used to address the research questions listed above:

- In Section 5.2.1 I describe MD simulations of chains deposited onto a 2D plane, representing a substrate (see Section 3.2.1 for theoretical background of MD). Analysis of the resulting structures provided information about the aggregation of chains during the initial stages of thin film formation and how this behaviour is directed by the chemical structure of C16-IDTBT.

- In Section 5.2.2 I describe the backmapping of CG microstructural models of C16-IDTBT, P3HT, and PffBT4T-2OD. This allowed me to gain atomic-scale detail about the microstructures, which was particularly useful for gathering information about the geometry of contacts in thin films.

- In Section 5.2.4 I describe the identification and selection of interchain contact locations. This enabled the analysis of contact geometries and the occurrence of contacts in the following sections.

- In Section 5.2.5 I describe the analysis of contact geometries. The results provide insight into the different packing structures present in the different materials, how these are promoted by the chemical structure of the polymers, and how they are likely to influence the strength of electronic coupling between chains.

- In Section 5.2.6 I describe analysis of the occurrence of contacts, differentiating between cases where multiple contacts are shared between the same paired chains, and where contacts couple distinct chains. The results provide insight into how the different contact geometries exhibited in each of the materials impact broader microstructural trends, and the implications for charge transport.

Based on analysis of these results, I aim to provide a coherent picture of interchain contact, and other broader microstructural trends in C16-IDTBT. This picture should align with, and link together, evidence provided by previous experiments. Furthermore, it should aid in rationalising the high μ of C16-IDTBT, while providing insight into potential pathways to even higher mobility materials. Although the analysis provided in this chapter should stand on its own, much of it feeds into further investigations of the transport behaviour of C16-IDTBT, which are described in Chapter 6.

5.2 Methods and Results

For the microstructural investigations described here, I relied heavily on the use of MD simulations. All the MD simulations described in this section were performed using atomistic and CG forcefields originally developed by Anders. However, some small adaptations were made in the following cases to create models suited for my purposes. Unless otherwise stated, I generally reused Anders' forcefield parameters without change. My modifications included:

1. Creating new models for polymers of different backbone lengths. This sometimes required making small tweaks to the atomic charges, to keep the total charge of each monomer neutral.

2. Creating new models with different alkyl side chain lengths. This also sometimes required making small tweaks to the atomic charges, to keep the total charge of each side chain neutral.

3. Indexed fragments of the models into different charge groups. This is a legacy feature of `Gromacs`, and has no effect on the simulations. However it is required to enable a trick used during the `backwards` procedure to temporarily make parts of the system non-interacting (see Section 5.2.2).

Unless otherwise stated, many simulation parameters were left as their default values for the MD simulations described in the following subsections. For brevity, these parameters are listed here. Atomistic simulations were run in an NVT ensemble, with system temperatures coupled to a thermal bath using a velocity-rescaling thermostat with a time constant of 0.1 ps. Usually, simulations were initiated with at a high temperature (∼600 K) to simulate annealing, and included a period of gradual cooling to 300 K. Non-bonded interactions were treated using the potential-shift Verlet scheme, with a cut-off of 1.5 nm. The default leap-frog integrator was used, with a simulation time step of 1 fs. PBCs were typically used for the x- and y-directions. The boundary types used for the z-direction depended on the features of the system being modelled.

5.2.1 Chains on Surfaces

The STM images captured by Giovanni Costantini and Stefania Moro presented a number of interesting structural features. In particular, they observed an unusual structural motif involving chain backbones crossing at perpendicular angles, formed whenever two backbones were in contact [150]. This aligned with a similar motif we had identified in 3D microstructural models of C16-IDTBT predicted by CG MD (see Section 5.2.5). We decided to replicate the experiments using MD simulations to further explore the behaviour of these structures in 2D and draw lessons about interchain contact, as well as test our MD forcefields. As argued previously, the STM images should provide a good representation of the initial stages of thin film formation. Based on this, and the face-on orientation of chains in C16-IDTBT thin films, we can infer that similar structural features to those observed by STM and MD are also likely to form in thin films.

In this section, I describe the setup and analysis of two sets of simulations. The first set involved several chains deposited side-by-side to form 'mats' (Section 5.2.1). The second set involved pairs of chains deposited one on top of the other, recreating the circumstances under which backbone contact was observed in the STM experiments (Section 5.2.1).

For the simulations described in this section, I used a simulation box with a specially treated z-boundary designed to replicate the surface of a substrate. Since the behaviour I was studying was not dependent on achieving very large length- or time-scales, an atomistic model of a C16-IDTBT was used. The following changes were made in the `.mdp` simulation parameter file. I implemented the modelled substrate using the `walls` function in `Gromacs`, setting `nwall = 2` to include walls at the top and bottom z-boundaries of the simulation box, while `pbc = xy` was used to specify PBCs only in the x- and y-directions. Walls were placed at both boundaries to enable the use of semi-isotropic pressure coupling if required, although it was not used for gathering the results described here. To ensure that chains only interacted with one wall, they were initially placed in a face-on arrangement close to the lower z-boundary and the z-dimension of the box was set to 50 nm. I gave every atom a small initial velocity of $1\,\mathrm{m\,s^{-1}}$ directed towards the substrate, to ensure chains would make contact.

Since we wanted to compare the simulated structures to STM images of C16-IDTBT chains deposited on Au(111) substrate, I parameterise the wall using the following settings in the `.mdp` file. I set `wall-density = 60` to match the number density of gold atoms, in $\mathrm{nm^{-3}}$. `wall-type = 9-3` was used to set to shape of the effective potential for interactions with the wall, treating it as a solid medium below the plane of the lower z-boundary.

During the process of ESD, the solvent from the prepared polymer solution is evaporated during the dispersal and transit of the solution towards the substrate target. However, it is probable that some remnants of solvent remain upon reaching the substrate, and therefore that the polymer chains are initially immersed in small droplets of solvent. These solvent remnants also quickly evaporate (they are not observed by STM), but it is possible that they have some impact on the formation of polymer structures observed [153].

For the simulations described here, I chose not to include solvent molecules. This is because we cannot be sure whether solvent is still present during the initial stages of polymer-substrate interaction, or whether its presence has a significant influence on the formation of chains that persists after the solvent has evaporated. Furthermore, simulating evaporation is not a straightforward task, although it has been done [152], including for some work relevant to other sections of this thesis (see Section 5.2.2).

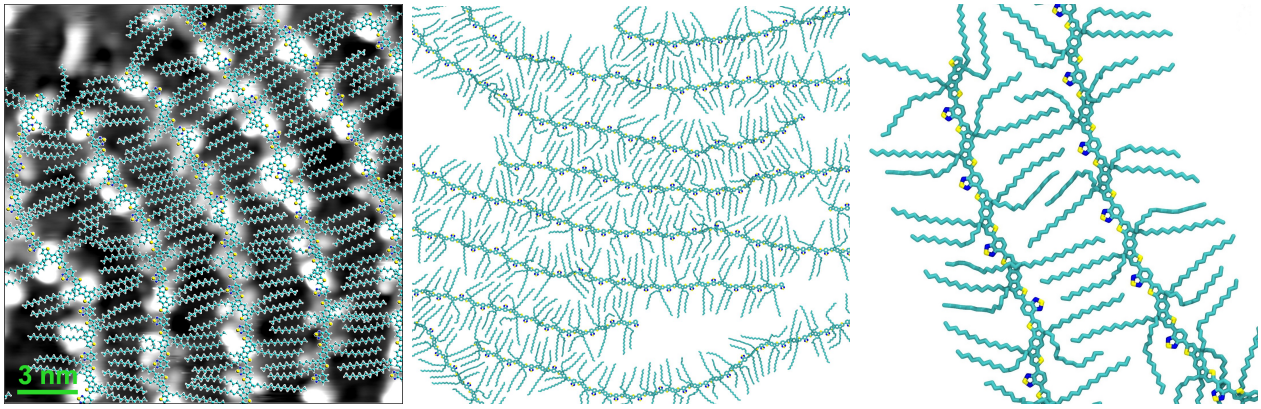
Without solvent molecules, interactions between chains, or between different sections of the same chain, are no longer shielded by a solvation shell. For this reason, and to ensure that the substrate interactions are felt by the chains in their initial positions slightly above the substrate, I increased the cutoff distance for interactions to 2.5 nm, by including the following parameters in the `.mdp` file: `vdwtype = cut-off`, `rvdw = 2.5`, and `rlist = 2.7`.

Mats

Most chains in the monolayer imaged by STM are packed edgewise, with backbones aligned in parallel, and side chains occupying the space in-between [150]. I decided to simulate 'mats' of chains adhered to substrate, to explore their lateral packing behaviour. I employed two simulation setups. In the first, nine 24mer chains of C16-IDTBT were initiated at the same z-height (2.5 nm from the lower boundary), with their backbones aligned in the x-direction, and evenly spaced by 5 nm in the y-direction. The x- and y-dimensions of the box were set to 50 nm, longer than the length of a stretched 24mer chain, but small enough to confine the chains and encourage them to pack. PBCs were in place in the x- and y-directions. The simulation was run at a system temperature of 600 K for 2.5 ns, before being cooled to 300 K over 2 ns, followed by 0.5 ns at 300 K (totalling 5 ns).

The second simulation setup was used to explore the effect of longer simulation times on the structures formed. In this case, only two 24mer chains were simulated, and the y-dimension of the box was reduced to 15 nm. With fewer chains, the simulation time could be increased to 50 ns. The same system temperatures were applied, but with all time periods now $\times 10$ longer.

Images of edgewise-packed C16-IDTBT chains are shown in Figure 5.2. Structures imaged by STM are shown in Figure 5.2a, while those predicted by MD simulations are shown in Figures 5.2b and 5.2c. Overall, the simulated structures show good correspondence with those imaged by STM. Interdigitated structures of the side chains were present in both simulation models, although interdigitation was more ordered in the two-chain model due to the longer simulation time. The backbones in the two-chain model were separated by 2.5 nm, calculated from the spacing between the CoGs of the two closest π-system rings. In the nine-chain model, the average closest spacing between neighbouring chains was 2.2 nm.



(a) (b) (c)

Figure 5.2: C16-IDTBT chains packed edge-wise on substrate. (a) An STM image is shown in the background, with structural models of C16-IDTBT chains overlaid. (b) Structure predicted by MD simulation of nine chains. (c) Zoomed-in image of structure predicted by long MD simulation of two chains.

The spacing between backbones in the simulated structures was comparable with that observed by STM [150] (2.7 nm. Note that this is an average spacing, whereas I provided closest spacing for the simulated structures), and larger than the periodicity observed in the top layer of films in AFM images (1.6 nm) [94]. The difference with the AFM-observed periodicity is likely due to the 2D nature of the simulation setup. The substrate confines both the backbones and side chains to the same monolayer, meaning that the space between backbones must be wide enough to fit the full length of the side chains. At the upper interface, and in the bulk, of a thin film, the side chains can be positioned above or below the plane of the backbones, allowing the backbones to pack more closely.

These results confirm the relatively wide spacing between aligned, edge-wise packed backbones observed by experiments. For transport considerations, this implies that the edgewise-packing observed in domains of parallel backbones is unlikely to be particularly relevant to the high mobilities displayed by C16-IDTBT, since the spacing between neighbouring backbones is too large to support reasonable rates of intermolecular charge transfer.

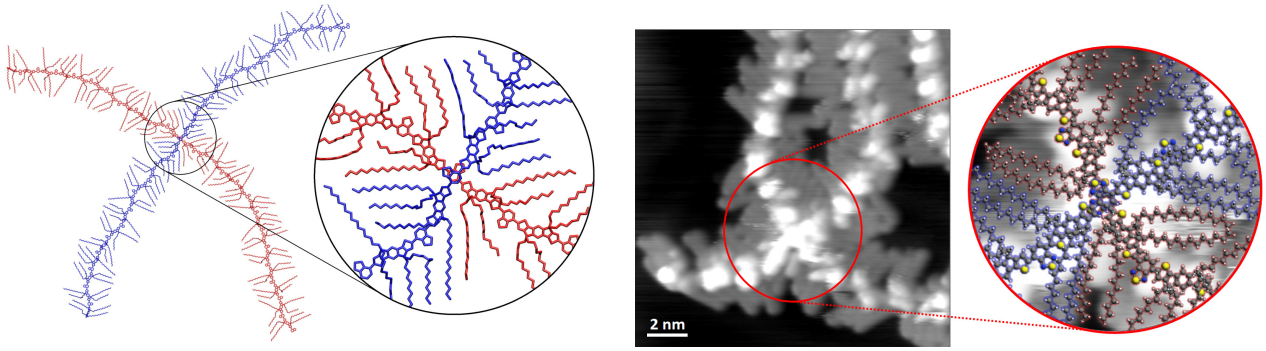
Pairs of contacting chains

We are particularly interested in exploring structural features involving backbone contact, because such contact is required to facilitate interchain charge transfer. The spacing and arrangement of the backbones impacts the strength of coupling and therefore the rate of interchain charge transfer.

In the STM images, contact was achieved when chains were deposited one on top of the other. To replicate this in simulation, pairs of chains were initiated in the following manner. The backbone of the first chain was placed 2 nm above the substrate, orientated along x-direction. The second chain was placed with its backbone 6 nm from the substrate. The upper chain was rotated around its central BT unit, to point along a random direction in the xy-plane, and then translated in the x-direction by a random distance between ± 3 nm. 200 repeats were run, with different rotations and x-shifts. The system temperature was varied over the course of each simulation to encourage the chains to adopt an optimal, low-energy arrangement. This was implemented by coupling the system temperature to a thermal bath at 600 K for 5 ns, which was then cooled to 300 K over 4 ns. After this, the simulation continued at 300 K for a further 1 ns.

An example of a contact structure predicted by MD can be seen in Figure 5.3a. Comparing this with Figure 5.3b reveals the remarkable agreement between our simulated structures and those observed by STM. From these images, we can observe that, around the contact locations, the closest side chains tend to splay out in a neat, dovetailed pattern. Somewhat akin to interdigitation, this pattern is likely the result of side chains optimising intermolecular interactions within the constrained geometry of the contact structure.

Because the observed contacts featured an unusual perpendicular arrangement of the backbones, I analysed the MD-produced structures by evaluating the crossing angle (θ) between chain backbones.



(a) (b)

Figure 5.3: A pair of contacting C16-IDTBT chains in a crossing formation. (a) Contact structure predicted by an MD simulation. The chains have been coloured red and blue respectively, to help distinguish them. (b) A contact imaged by STM. Structural models of C16-IDTBT chains are overlaid on the zoomed-in portion of the image. These have been outlined in red and blue respectively, to help distinguish them.

We can expect θ to influence the strength of interchain coupling, since varying θ will vary the amount of contact surface between the chains, and thus the degree of MO overlap. For each structure θ was calculated by first locating the closest 6-member π-system rings on the two chains, which I term the 'contact rings' (yellow beads in Figure 5.4a). A pair of vectors, $\vec{v}_A$ and $\vec{v}_B$, are then found, defining the local orientation of the backbones at the point of contact. These vectors are drawn between the centres of the two units (IDT or BT) on either side of the central contact ring (green beads in Figure 5.4a). θ is then calculated as the angle between $\vec{v}_A$ and $\vec{v}_B$.

Figure 5.4b shows the distribution of θ adopted by the simulated chain pairs. We can see that θ is clustered in a narrow distribution centred on the perpendicular. 95% of the simulated structures have θ in the range $90° \pm 30°$.

I ran a further set of simulations to assess the impact of side chain length on the arrangement of contacts. Pairs of chains with side chain lengths of one (C1), four (C4), eight (C8), and twelve (C12) alkyl units were simulated in the same manner as for the C16 case. 20 repeated simulations were run for each side chain length. The effect on the distribution of θ can be seen in Figure 5.4c. From these results we can deduce that medium-to-long side chains (C8, C12, C16) tend to promote a much tighter distribution of angles around the perpendicular compared to short side chains (C1, C4).

Figure 5.4d shows the proportions of moieties present at the point of closest contact between the chain backbones. These results are from the simulations with C16 side chains. 77% of contacts involve the BT unit of at least one chain, with BT-BT contact being most common (37%), followed by BT-Th (33%) (where Th is used to denote the thiophene rings at either end of the IDT unit). Although BT-BT stacks seemed to be generally adopted in all contacts observed by STM [150], the simulation results suggest that chains in a crossing formation may have a small amount of freedom to 'slip' along their backbone direction, such that the point of closest contact involves a thiophene. This discrepancy may relate to 1) the presence of solvent during ESD but not in simulation, 2) the inability to locate

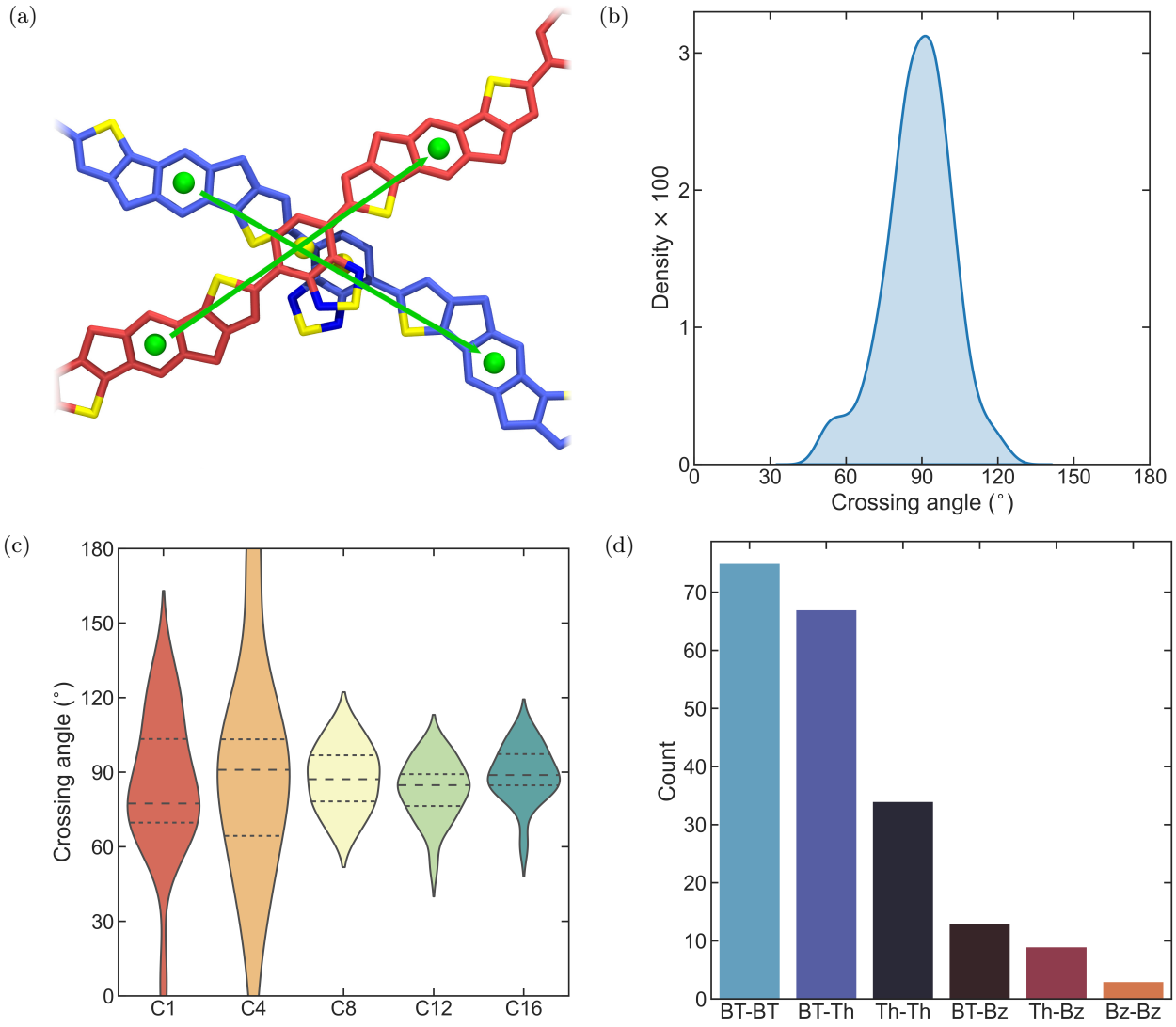


Figure 5.4: (a) Calculation of crossing angle. The diagram illustrates the origin of vectors (green arrows) used to evaluate crossing angle between two polymer backbones, in modelled systems. (b) Distribution of crossing angles, from C16 simulations. (c) Distribution of crossing angles, from simulations with varying side chains lengths. (d) Moieties in contact, from C16 simulations.

global minima due to limited simulation times, 3) inaccuracies in the forcefield of C16-IDTBT, or treatment of the substrate, or 4) the limited sampling of contacts in STM images. However, it may also be the case that the slightly broader range of structures observed from the simulations is relevant to the contact structures we might expect to form in the solid state, where contacts are likely to be less 'ideal' than those observed by STM.

With annealing in place, the chain closest to the substrate would adopt a fully face-on orientation. However, the upper chain would sometimes twist, fully or partially, into an edge-on orientation as it crossed over the lower chain. Since this type of arrangement was not observed by STM [150], it is difficult to verify if they are physically legitimate. An exploration of the reasons why these contact arrangements formed, and remained stable, in simulation is provided in Appendix A.1.

Alongside confirming the strong tendency of C16-IDTBT to form perpendicular contacts, the results presented in this section provide an indication of the chemical-structural reasons why a crossing arrangement is preferred. This arrangement appears to be a consequence of the size and attachment locations of the side chains. The side chains sterically block the IDT units on opposing chains from approaching one another during the aggregation process. This guides the backbones towards a BT-BT stacked arrangement, due to the relative 'nakedness' of the BT unit (Figure 5.4d). With BT units in contact, the side chains can optimise their interactions by rotating the backbones into a perpendicular formation. An ideal manifestation of this is shown by the neatly spaced side chains in the dovetailed arrangements shown in Figure 5.3a and Figure 5.3b. The fact that longer side chains lead to a narrowing of the distribution of θ (Figure 5.4c) further confirms the crucial role of the side chains in encouraging the crossing motif. Although side chains have traditionally been considered a 'necessary evil' for improving the the solution-processability of conjugated polymers, these results indicate a noteworthy case in which the side chains can play a positive role in promoting potentially useful contact arrangements (the utility of the crossing motif for transport in the bulk is explored further in Section 5.2.6 and Chapter 6).

For transport considerations, we might expect that, compared to a parallel, face-on contact arrangement, perpendicular contacts will lead to weaker electronic coupling and therefore lower interchain charge transfer rates. However, an interesting question is raised by the narrow distribution of θ for long side chains. This result demonstrates that side chain interactions help to stabilise contacts in a narrow range of geometries, which is likely to reduce the scale of time-dependent fluctuations in the contact geometry (i.e. interchain vibrational modes). Since coupling is extremely sensitive to the contact geometry, and since dynamic disorder in coupling has been identified as a key influence on transport [11, 57, 68, 69], it is possible that the crossing motif could lead to benefits for interchain transport by sterically 'locking' the backbone positions. Further results relevant to this effect are presented in Section 7.2.4.

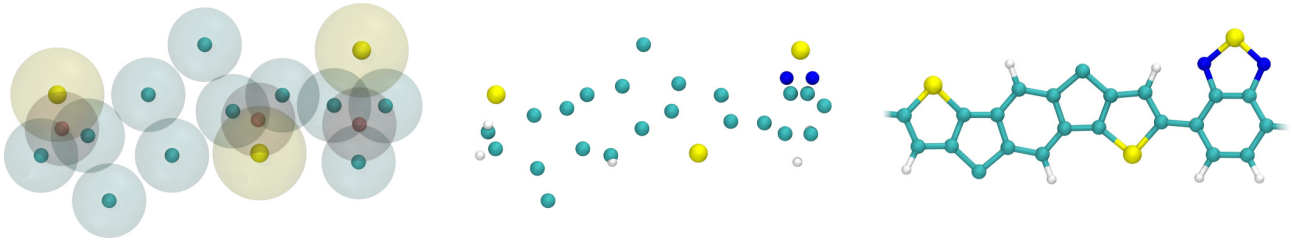


Figure 5.5: Backmapping of a CG IDTBT monomer. From left to right are shown: The CG representation, the initial projection of atoms, and the final backmapped structure after subsequent optimisation and propagation steps. Only backbone atoms are shown (side chains are hidden).

5.2.2 Backmapping Coarse-Grained Structures

To explore the solid-state microstructure of C16-IDTBT, we employed CG MD to generate models of thin films of C16-IDTBT in 3D, and other conjugated polymers for comparison. The use of CG forcefields allowed us to simulate larger system sizes and timescales than had been achieved by previous works. Thus, we were able to generate microstructural models composed of high numbers of chains with physically representative chain lengths. The largest model included 300 chains of 24mer C16-IDTBT.[1] The initial work of producing these models was done by Anders S. Gertsen. Using his evaporation simulation procedure (summarised in Section 6.1, see also [121, 152]), Anders generated models of C16-IDTBT 24mers, C16-IDTBT 12mers, P3HT 48mers, and PffBT4T-2OD 12mers. Summarised information about the models may be found in Table S2 of [150].

Because I was interested in the fine-grained details of the packing structures present in these models, I employed a *backmapping* procedure to convert the models from a CG representation to an atomistic representation. This retains the general orientation and conformation of chains predicted by the CG simulations, while providing access to atomic-scale detail. The backmapping of an IDTBT monomer is shown in Figure 5.5.

My implementation of the backmapping technique was based on the procedure `backwards`, developed by Tsjerk Wassenaar [154]. A notable feature of `backwards` is the inclusion of an initial projection step, which produces a rough estimate for the positions of atoms based on a mapping scheme applied to the CG beads. The projection step is followed by a series of optimisation and short time-propagation steps, to gradually encourage the atoms into a realistic configuration. To improve its performance on the models in this investigation, I made some modifications to the original `backwards` procedure. These included the implementation of an additional collision avoidance step, which locates overlapping atoms and pushes them apart. This step helped to avoid the occurrence of extremely large forces (and subsequent crashes in the MD algorithm) when backmapping large and dense solid-state models. Further details about the backmapping procedure, including an overview of the mapping schemes I created

[1] This may be compared with the 8mer and 10mer oligomer models previously reported by Thomas et al. [97] and Venkateshvaran et al. [86], respectively. Makki et al. reported models of 20mers, although system sizes were limited to 25 chains [100].

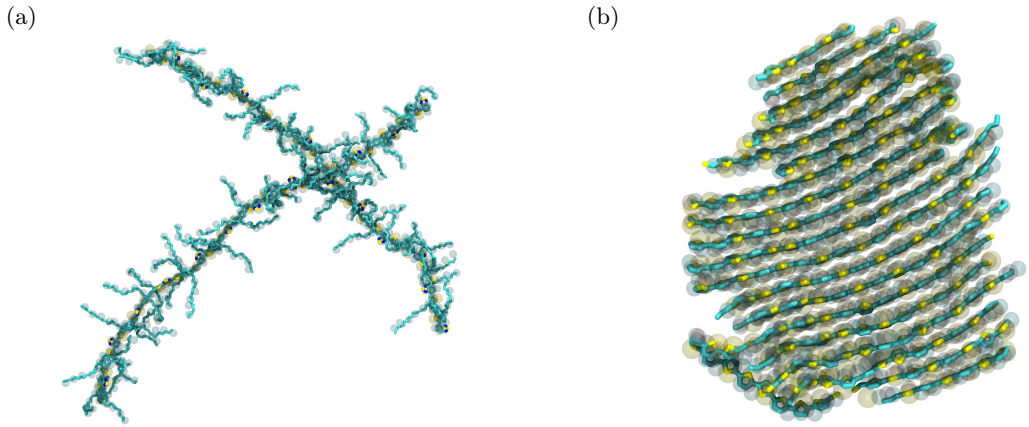


Figure 5.6: Verification of the backmapping procedure, by comparing overlaid CG and backmapped models, and confirming that chain conformations are similar. CG beads are shown as semitransparent spheres. Hydrogen atoms are hidden in the atomistic structures for clarity. (a) A pair of C16-IDTBT chains in contact. (b) A crystalline region of a P3HT microstructural model, with side chains hidden for clarity.

for the polymers in this study, and other modifications to `backwards`, are provided in Appendix A.2.

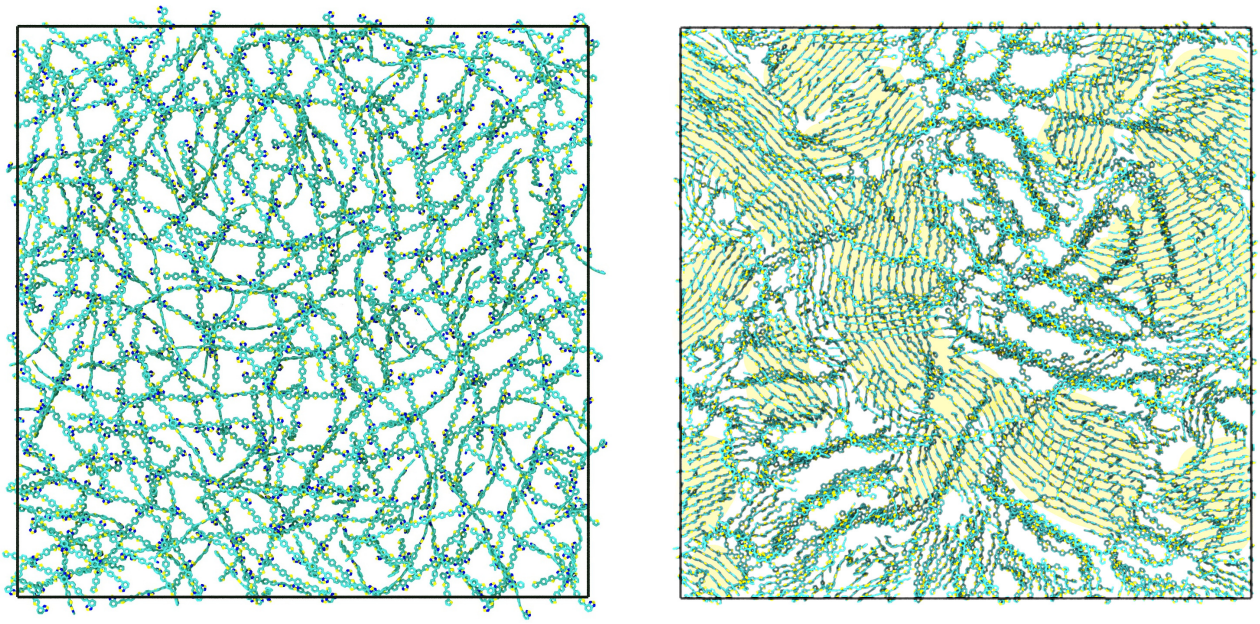
I verified the backmapped thin film models against the original CG structures by visual inspection. The models as a whole were compared, as were samples of individual chains and locations of chain contact, by visualising overlaid CG and backmapped models, as seen in Figure 5.6.

In the following sections, I describe my analysis of the microstructures presented by the backmapped thin film models. From this analysis I draw conclusions about the influence of the different microstructures on the charge transport behaviour of the conjugated polymers.

5.2.3 General Microstructural Trends

I begin my analysis with some observations about the mesoscale features displayed by the models. For all the polymers, the backbone axes of chains are generally orientated in-plane i.e with most segments of the backbone directed in the xy-plane. This corresponds with experimental measurements of backbone orientations in C16-IDTBT [29], and likely arises due to the anisotropic shrinking of the simulation box (i.e. only in the z-direction) during the drying stages of the CG MD procedure. In polymers with fast intrachain transport, such as C16-IDTBT, this is likely to benefit in-plane mobility, i.e. the mobility measured by FET experiments. This was corroborated by transport simulation results, which showed higher mobilities in the xy-plane compared to the z-direction for the C16-IDTBT 24mer system. However, chain backbones in the C16-IDTBT 12mer models tended to show a wider distribution of orientations with respect to the the out-of-plane z-direction, compared to the 24mer model (see Figure A.3a). This led to higher mobilities in the z-direction than in the xy-plane for the 12mer systems (See Section 6.2.3 for method details and Appendix C for results).

In the C16-IDTBT models, there was a slight preference for the π-conjugated backbone planes to be orientated in the z-direction of the models (i.e, face-on, see Figure A.3b). This partially corresponds



(a) (b)

Figure 5.7: A top-down view of the bottom 30 Å slice of backmapped thin film models composed of (a) C16-IDTBT 12mers, and (b) P3HT 48mers. Only atoms that form part of the π-conjugated system are shown for clarity. Some examples of ordered domains have been highlighted in yellow for P3HT. Simulation bounding boxes are shown in black. Box side lengths are 25 nm for both systems.

with experiments, which show a very strong preference for face-on orientations in C16-IDTBT thin films [29]. The partial discrepancy is likely related to the lack of explicit substrate included in the MD simulations. In a different study, employing the same evaporation procedure but using atomistic forcefields and an explicit substrate, a stronger orientational preference was measured for a small molecule OSC [152]. Another contributing factor is likely to be the limited timescales that can be simulated by MD, which invariably lead to less ordered structures than those observed in experiments.

Figure 5.7 shows slices of the C16-IDTBT and P3HT models, from which we can observe the different degrees of structural order. The P3HT system shows semicrystalline features, including domains of repeated stacks of parallel-packed backbones, alongside more amorphous regions. Similar mesoscale ordering was also observed in the PffBT4T-2OD system, which makes sense given their shared classification as semicrystalline polymers. As expected, based on experimental evidence, the C16-IDTBT systems are far less structurally ordered. Although there is some evidence of domains of aligned backbones shown in the top layer of C16-IDTBT films by AFM [94], these kinds of structure are not present in the models. The reason that aligned structures form in the P3HT models but not in the C16-IDTBT models is most likely due to a combination of difference in flexibility of the polymer backbones, the different length and attachment of side chains that allow P3HT chains to align in a parallel sense more easily, and the timescales reachable by MD (including CG MD). However, I do not consider the absent regions of aligned backbones important for explaining the transport behaviour of C16-IDTBT. Unlike in semicrystalline polymers, experimentally-observed domains of aligned chains

in C16-IDTBT are made of edgewise-packed backbones. The spacing between aligned backbones is therefore large (∼1.6 nm [94]), and occupied by insulating side chains, meaning that these domains are not likely to be responsible for facilitating fast interchain transport.

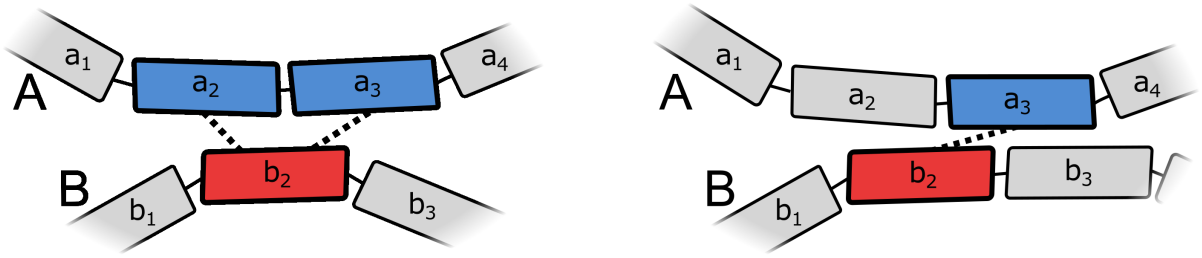
The structural order present in P3HT and PffBT4T-2OD leads to extended lengths of backbone contact between neighbouring chains (see Section 5.2.6). For transport considerations, these structures are likely to improve interchain electronic coupling and therefore mobility, in agreement with the traditional explanation for why semicrystalline polymers tend to outperform older amorphous conjugated polymers [12]. Of course, this explanation does not apply to C16-IDTBT, which links back to the original source of puzzlement about the transport behaviour of this polymer, presented in Section 2.5. Since this behaviour cannot be rationalised from a mesoscale view alone, in the following sections I 'zoom in' to present analysis of fine-scale features associated with precise locations of contact between backbones.

5.2.4 Interchain Contact Selection

To understand interchain charge transport in C16-IDTBT and other polymers, we need to understand how polymer backbones make contact in the solid state. It is relatively straightforward to detect which chain backbones are in contact in the backmapped models using a simple cutoff scheme. To do this, I searched through the models to identified all pairs of chains with an interchain separation between π-system atoms $\leq$8 Å (using a function from the python package `MDAnalysis` [155, 156]), thus producing a list of pairs of contacting chains. For further analysis, it is useful to not only detect contacting chains, but to also assess the *degree* of contact between chains. This step is made less straightforward by the fact that, as we will see later, the arrangement of backbones in contact can be radically different between different conjugated polymer systems.

At this point, there are a number of approaches we could adopt to assess the degree of contact. Since, for our consideration, the importance of interchain contact lies in the fact that it facilitates electronic coupling, one approach would be to use a continuous function that takes in the separation between π-system atoms (or moieties) and calculates a value that acts as a proxy for the electronic coupling. For instance, by using the exponential relationship between separation distance and coupling strength (see Section 3.1.5).

Instead of this, however, I found it useful to locate discrete points of contact between chains, and then to infer the implications for transport from statistics about the occurrence of these contact locations. The benefit of detecting discrete contact location, over adopting a definition of 'degree of contact' as a continuous property, is that each contact location is associated with a distinct arrangement of backbones in the microstructural models. The geometry of these arrangements can then be analysed (see Section 5.2.5), along with the contact occurrence statistics (see Section 5.2.6), to gain insight into the relationship between microstructure and transport. An additional practical benefits of locating



(a) (b)

Figure 5.8: Interchain contact selection pitfalls. (a) Double-counting. This can occur when a segment on one chain is located within the cutoff distance of multiple segments on another. In this case segment b_2 is coupled to both a_2 and a_3. (b) Under-counting. Segments a_3 and b_2 have been paired up (e.g. because this pairing was detected first, or because the shortest interchain separation is between these monomers), but this means segments a_2 and b_3 are left unpaired despite being close to the other chain. A more representative choice of pairings might be to pair up a_2:b_2 and a_3:b_3. However the offset between segments is likely to lead to a relatively small total coupling between the backbones, after coupling calculations are performed (see Section 6.2.2).

contacts in this way, is that it allows for the streamlined application of DFT and KMC methods to our systems (see Chapter 6).

A drawback of this approach is that there is some ambiguity in how we select contact locations. For example, chains of P3HT will often be packed such that the backbones of neighbour chains run alongside each other for significant portions of their length. To delineate specific contact locations, we must decide how far along the length of the backbones is appropriate for the spacing between each subsequent contact.

I used a backbone segment length of approximately 3.2 nm as the basis for detecting discrete contact locations between backbones. Specifically, this corresponded to two monomers in C16-IDTBT and PffBT4T-2OD, and eight monomers in P3HT. As well as the distance between contacts, this defined the segment lengths of backbones that would later be used to evaluate the geometry of contacts (see Section 5.2.5), and to perform quantum chemical calculations (see Section 6.2.2). Based on this, segment lengths of approximately 3.2 nm were considered appropriate, as the maximum length of backbone for which thousands of DFT calculations could be performed within reasonable computational expense. In addition, I considered it desirable to use an IDTBT segment length greater than one monomer, as there is evidence that holes delocalise across multiple monomers in the IDTBT backbone [82, 86].

The method I developed to detect contacts between chain backbones ended up being fairly complex. A naïve approach would involve simply dividing up each backbone into sequential segments, starting from the first group of two or eight monomers and moving down the backbone. One could then locate contacts between any two chains by detecting whether pairs of segments were separated by less than some cutoff distance. However, arbitrarily dividing up the backbone in this way can lead to some pitfalls when segments on paired chains are not ideally positioned. These are depicted visually in Figure 5.8. The first issue, shown by Figure 5.8a, is the double-counting of contacts. Since we are

using the number of contacts between chains as a rough proxy for how strongly coupled they are, this situation would exaggerate the degree of coupling between the chains. We could circumvent this problem by only allowing each segment on chain A to pair with a maximum of one segment on chain B and vice-versa. However, as depicted by Figure 5.8b, this can commonly lead to the second issue of under-counting contacts, again due to non-ideal positioning of the segments.

To avoid these issues I developed a 'dynamic' contact selection method. The main improvement over the approach outlined above is that the chains are divided into segments only *after* evaluating the best way of dividing backbones into segments and assigning segments to contact pairs. This method is implemented as an algorithm that carries out the following steps:

1. Create a 'coupling matrix' with dimensions equal to the number of monomers in each of the two chains (which we label A and B). This matrix is populated using a function that estimates the electronic coupling between each monomer on A, with each monomer on B. The function sums the exponentially-weighted separation distances ($\sim \exp(-r/\beta)$) between CoG of ring structures in each monomers, and returns zero beyond a cutoff distance of 1 nm.

2. The coupling matrix is divided into submatrices by slicing along any rows or columns that are filled with zeros. Submatrices containing only zeros are discarded. Each of the remaining submatrices represents a location where there are monomers in contact between the two chains, which are from here referred to as *islands*. Different islands represent different positions along the two chains that are separated by consecutive non-interacting monomers (e.g., contact 3 in the C16-IDTBT image in Figure 5.9, which is separated from contacts 1 and 2).

3. For each island, several different possible segment pair choices are compared, by summing up the total estimated coupling each choice would provide. This is equivalent to sliding the choice of segments back and forth on each chain backbone, in increments of one monomer, and in each position calculating the total estimated coupling between the segments on each chain.

4. The choice of segment pairs that maximises the total estimated coupling between chains is selected and outputted. Examples of the results of this selection process may be seen in Figure 5.9.

Running the algorithm on the list of the chain pairs found for each backmapped system, I identified 5787 contact locations in the C16-IDTBT 24mer model, 2821 in the C16-IDTBT 12mer model, 6062 in the P3HT model, and 4512 in the PffBT4T-2OD model. On their own, these numbers might give the impression that the P3HT model features a much higher degree of backbone contact than the C16-IDTBT 12mer model. However it is important to remember that the former model contains more chains (420 versus 250, see Table S2 of [150]).

For the analyses presented below, I considered only a subset of the identified contact locations, which I refer to as *close contacts*. These locations are the most likely to support large interchain

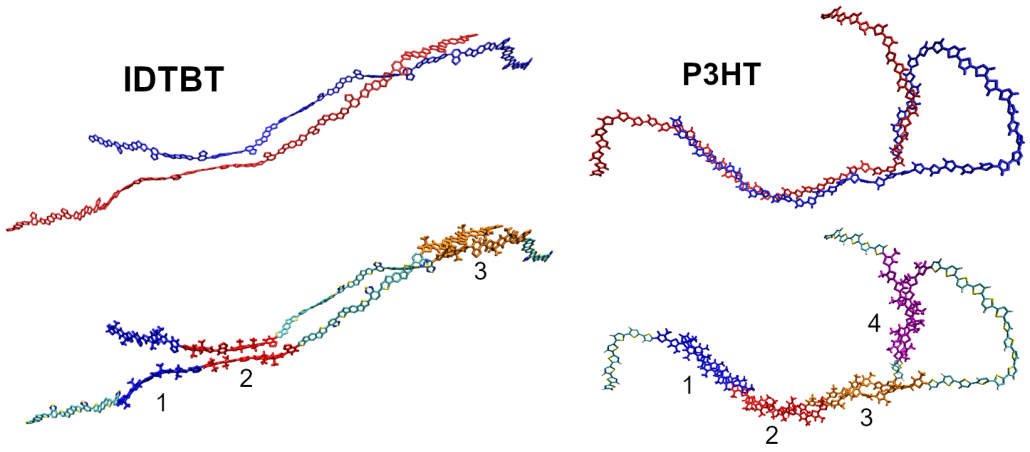


Figure 5.9: Diagram shows how multiple contact points are located between pairs of chains. In the top two images, the two chains are coloured red and blue respectively. In the bottom two images, the unused (non-interacting) sections of the two chains are coloured according to their atom types (e.g., carbon atoms are cyan). The solid-coloured segments are those associated with contact structures, which have been numbered.

couplings, and are thus the most relevant to charge transport. The criteria for close contacts was that the paired segments contain at least one pair of rings for which the interchain separation between CoGs was $\leq$6 Å. These may also be thought of as 1st NN contacts (see Figure 5.10a). I identified 3365 close contacts in the C16-IDTBT 24mer model, 1661 in the C16-IDTBT 12mer model, 2551 in the P3HT model, and 1967 in the PffBT4T-2OD model.

5.2.5 Interchain Contact Geometry

To understand what interchain packing looks like in the different polymer materials, I considered the different arrangements that chain segments tend to make at contact locations i.e. the *contact geometries*.

To generate contact geometries from contact locations, I first extracted the relevant chain pairs from the thin film model. I then trimmed the backbones down to the approximately 3.2 nm segments identified by the contact locating algorithm. This involved removing any excess monomers and capping the remaining segments with terminal hydrogen atoms. All side chains were similarly shortened to methyl groups. In some cases, chain segments participating in a contact were separated across PBCs, so it was necessary to shift one of the segments by the appropriate box dimension to place them next to each other before further analysis.

Strictly speaking, the number of degrees-of-freedom (DoFs) defining a contact is 3 $\times$ the number of atoms in the two participating chain segments. To simplify my analysis, and draw insights, I sought to greatly reduce this number by identifying collective variables that could meaningfully describe the contact geometries. One way to do this would involve treating the backbone segments as rigid bodies and considering the six DoFs that describe the translation and rotation of one segment with respect to

the other (neglecting conformation differences between the segments). However, in preliminary testing, I found that this still represented too many variables to enable a straightforward analysis.[2]

Instead of six DoFs, I settled on using two collective variables to describe the contact geometries. These were the interchain separation distance (r) and the crossing angle between backbones (θ). The r for a given contact was defined using the distance between the CoGs of the closest rings belonging to each segment (meaning that shorter r could be more easily achieved by a cofacial arrangement of rings). r is known to correlate with electronic coupling, especially at larger distances. Following theoretical arguments summarised in Section 3.1.5, it can be shown that the strength of coupling should decrease exponentially as r increases. The definition of θ, and my motivation for using this variable, have been discussed in Section 5.2.1.

Figure 5.10 shows the results of my evaluation of r and θ for the conjugated polymer models. Figure 5.10a shows a distribution of r for all contacts identified in the systems. It features two sharp, well-defined peaks for the semicrystalline polymers, corresponding to 1st and 2nd NN packing structures. The 1st NN peaks are centred on modal distances of 3.8 Å and 3.7 Å for P3HT and PffBT4T-2OD respectively. The 2nd NN peaks are centred on distances of 7.3 Å and 7.1 Å for P3HT and PffBT4T-2OD respectively. These are both very close to twice the distance of the 1st NN contacts. Taken together, these features reveal the presence of repeated packing structures within these two systems, which is appropriate given the semicrystalline nature of the modelled polymers.

In contrast, the C16-IDTBT systems each show one prominent 1st NN peak, while the 2nd NN peaks are present but diminished compared to the semicrystalline polymers. Both peaks are also much broader. The 1st NN peaks occur at a separation distance of 3.9 Å in the two C16-IDTBT models. This value corresponds well with the π-stacking distance of 3.8 Å extracted from grazing-incidence wide-angle X-ray scattering (GIWAXS) experiments by Zhang et al. [29]. The 2nd NN peaks occur at 8.3 Å, slightly longer than twice the distance of the 1st NN peaks. These features suggest a lack of repeat packing structures in the C16-IDTBT models, which aligns with the lack of experimental observations of long-range order in C16-IDTBT thin-films.

Figure 5.10b reveals the very different behaviour of contacts within the C16-IDTBT and semicrystalline polymer models, when θ is evaluated. In agreement with the 2D results (Section 5.2.1), the C16-IDTBT models show a clear preference for chains to cross at near-perpendicular angles. 62% of close contacts featured a crossing angle in the $90° \pm 30°$ range. By contrast, the P3HT and PffBT4T-2OD models show a preference for more parallel contacts. Only 10% of P3HT and 9% of PffBT4T-2OD close contacts feature crossing angles in the near-perpendicular range. The preference for perpendicular contacts in the C16-IDTBT models aligns with the preference for 90° angles between neighbouring domains observed by HRTEM experiments [93]. This may indicate that, in

[2] A machine learning approach could potentially be useful in this effort, provided that enough training data can be provided.

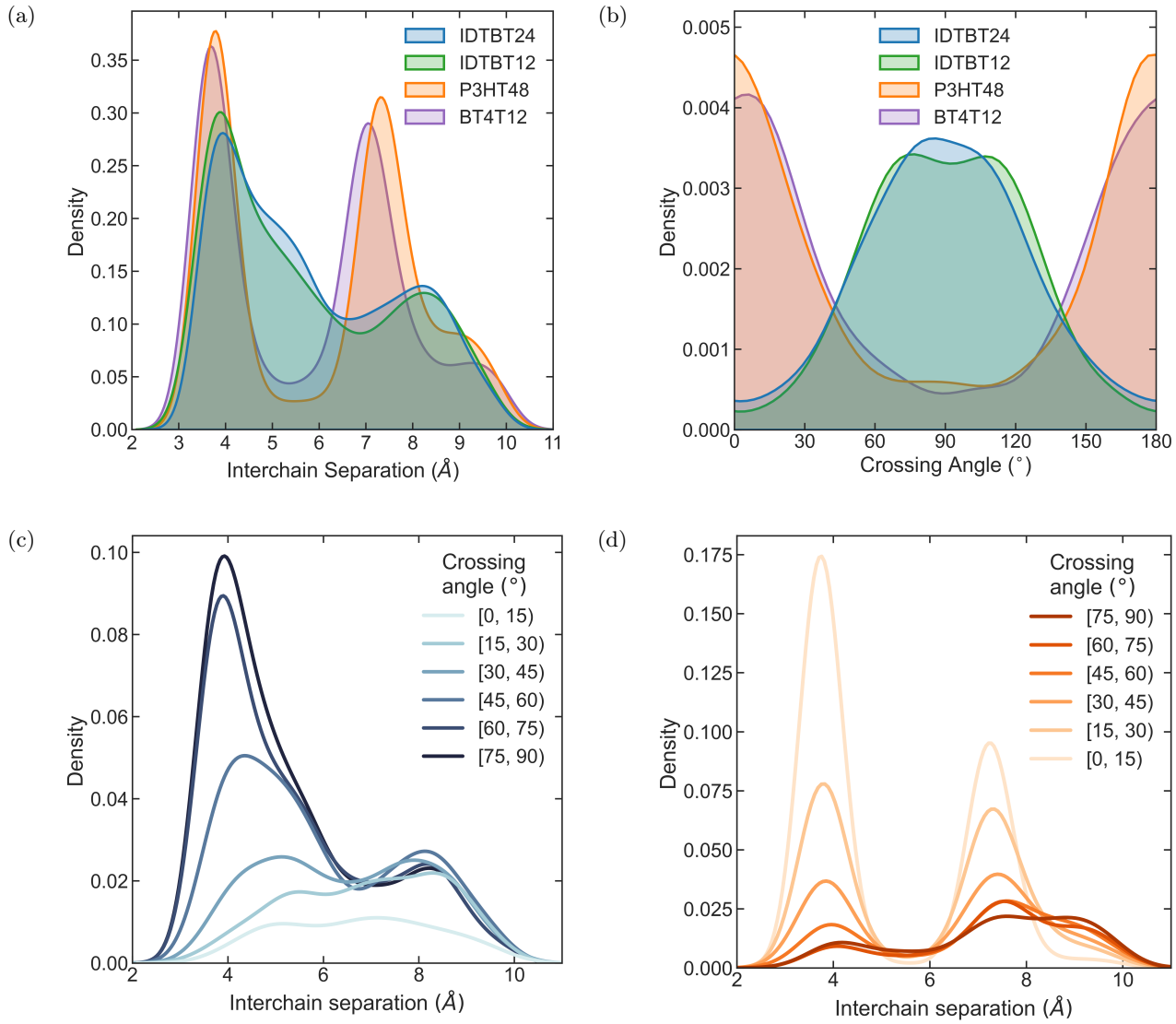


Figure 5.10: (a) Distributions of interchain separation distances. (b) Distribution of crossing angles at close contacts. (c) Distribution of interchain separation distances for contacts in the C16-IDTBT 24mer system. (d) Distribution of interchain separation distances for contacts in the P3HT system. In (c) and (d), the distributions are separated into bins according to the crossing angle of the contacts, symmetrised around 90°. Darker shaded distributions represent more perpendicular crossing angles. Note that the distributions corresponding to larger crossing angles are drawn at the back for (c), but in front for (d).

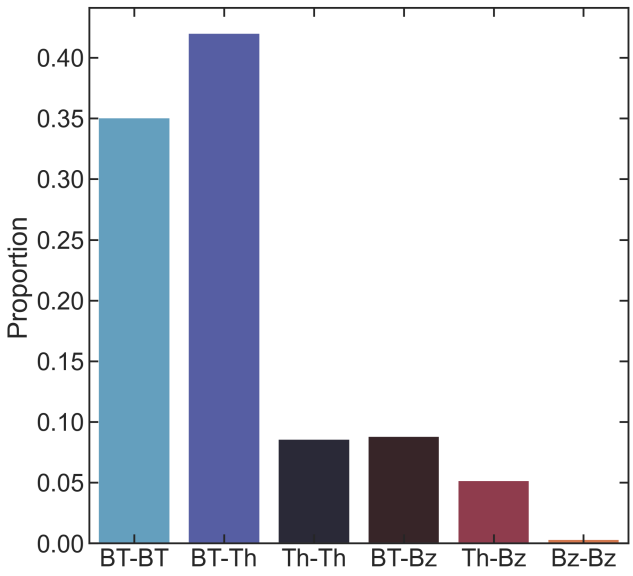
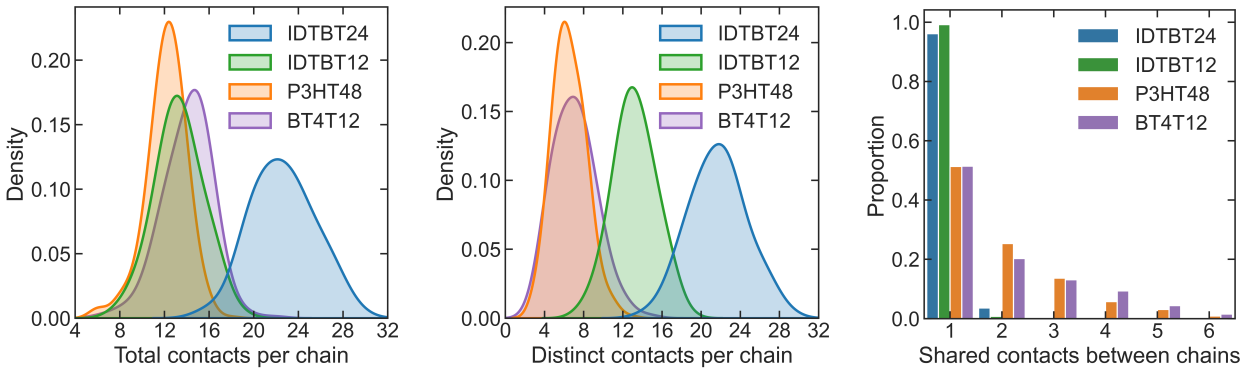


Figure 5.11: Proportion of close contacts involving different moiety pairings. Data is from contacts in the C16-IDTBT 24mer system.

physical films, where chains belonging to the same domain are more likely to be arranged in parallel, most backbone contacts might occur in regions of domain overlap rather than within domains.

Figures 5.10c and 5.10d reveal the different relationships between r and θ at contact locations in the C16-IDTBT 24mer and P3HT systems. In C16-IDTBT, we see that contacts tend to be packed most tightly when crossing angles are large; the 1^{st} NN peaks of the $[60, 75)$ and $[75, 90)$ crossing angle bins are at a shorter distance than the peaks for smaller angle contacts. In P3HT the opposite trend is seen, with the closest contacts being much more associated with smaller crossing angles. Furthermore, both the sharp peaks, associated with 1^{st} and 2^{nd} NNs, are largely made up of parallel contacts. The fact that very few perpendicular contacts contribute to the peaks indicates that they are not part of the ordered packing scheme favoured by the chemical structure of P3HT. This confirms the expected picture of the semicrystalline system microstructures as containing large numbers of repeated stacks of parallel contacts. For C16-IDTBT, these results strongly imply that there is a fundamental incompatibility between the formation of perpendicular contacts and repeated packing structures; The microstructure of C16-IDTBT does not present long-range order exactly because the C16-IDTBT chains so strongly prefer to arrange themselves in a perpendicular packing motif (see Section 6.2.1 for analysis of the energetics behind the different contact geometries). This is a noteworthy result because it runs counter to the expectation that a material with a strongly preferred packing arrangement is more likely to exhibit microstructural order.

Figure 5.11 shows the moieties that are involved in C16-IDTBT close contacts. The closest point of contact tends to involve the BT unit of one or both chains, corresponding with the 2D case (Section 5.2.1). In the microstructural models, BT-Th contacts occur most often (42%), followed by BT-BT (35%). This result suggests that the chemical-structural reason for the formation of perpendicular con-



(a) (b) (c)

Figure 5.12: Interchain contact occurrence statistics. (a) Distributions of the *total* number of close contacts made by each chain to any other chain. If multiple contacts are shared between a pair of chains, they are all counted. (b) Distributions of the number close contacts to *distinct* chains made by each chain. If multiple contacts are shared between a pair of chains only one count is recorded. (c) The number of close contacts *shared* between paired chains (with at least one contact between them). Contact statistics are gathered for backmapped systems of C16-IDTBT 24mers, C16-IDTBT 12mers, P3HT 48mers and PffBT4T-2OD 12mers. The distributions are normalised separately for each system, to account for the different numbers of chains in each.

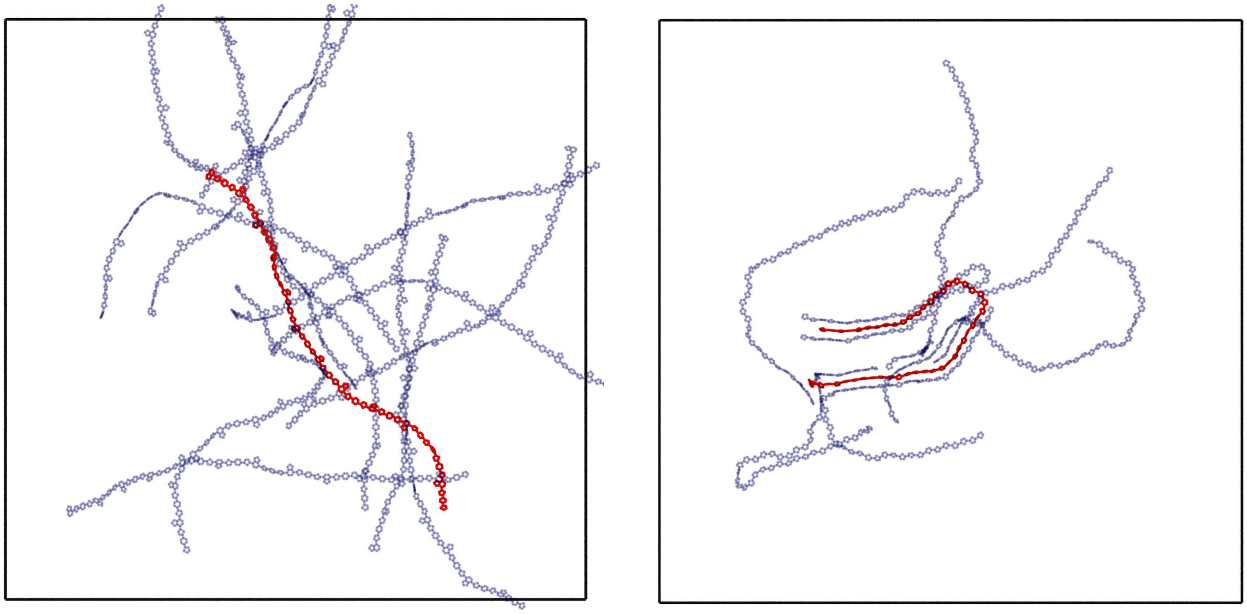
tacts is due to the presence of the four bulky side chains attached to the IDT unit, and the unadorned BT unit, as proposed in Section 5.2.1. In Section 6.2.1 I utilise quantum chemical calculations to further explore the chemical-structural origins of the different contact geometries in C16-IDTBT and P3HT.

The perpendicular θ at C16-IDTBT contacts decreases the degree of contact 'surface' between backbones compared to a parallel arrangement. This is likely to reduce the MO overlap at contacts, indicating that interchain coupling is likely to be lower in C16-IDTBT compared to the semicrystalline polymers. For transport considerations, this implies that strong interchain coupling is unlikely to be a factor contributing to the high bulk mobility of C16-IDTBT. However, the fact that the 1st NN r is so similar between C16-IDTBT and other systems (<0.2 Å difference) is noteworthy. It suggests that crystalline packing structures are not necessary for achieving tight packing at contacts. The crossing motif allows C16-IDTBT to achieve tight packing despite its lack of structural order, which may be sufficient to establish moderate interchain coupling. The relationship between the geometry of contacts and coupling strength is explored further in Section 6.2.1 and Section 6.2.2.

5.2.6 Interconnectivity

To understand how the different contact geometries influence broader microstructural trends, I assessed the occurrence of contacts in the microstructural models.

Figure 5.12 contains several results describing the occurrence of contacts. Considering Figure 5.12a, we see that, for all the systems with chains of comparable contour lengths, the total number of close contacts made by each chain tends to be similar, with a modal value of ∼12. This applies



(a) (b)

Figure 5.13: A visual depiction of interconnectivity in the (a) C16-IDTBT 12mer, and (b) P3HT systems. A single chain backbone is shown in red, with all chain backbones in close contact with this primary chain in semi-transparent blue. The simulation bounding box is shown as a black square. Only atoms that form part of the π-conjugated system are shown for clarity.

to C16-IDTBT 12mers, P3HT 48mers, and PffBT4T-2OD 12mers, which have contour lengths of ∼19.5 nm, ∼19.0 nm, and ∼25.0 nm, respectively. The chains are longer in the C16-IDTBT 24mer system (with contour length ∼39.0 nm), leading to a modal number of contacts of ∼23. The similar total numbers of contacts between the C16-IDTBT 12mers and the semicrystalline polymers is noteworthy if we consider the four bulky side chains attached to the IDTBT monomer. One might expect these to sterically block contact between backbones, so the fact that C16-IDTBT still achieves a similar number of contacts for a similar backbone length is surprising.

Figure 5.12b reveals a crucial difference between the C16-IDTBT and semicrystalline systems. In C16-IDTBT, chains tend to form close contacts with an unusually high number of *distinct* neighbours.

These two results (similar total number of contacts, and differing numbers of distinct contacts) can be understood by considering Figure 5.12c, which shows the number of close contacts that are shared between neighbouring chains. In the semicrystalline polymers, it is relatively common for any two chains with at least one contact to be arranged in such a way that they share multiple contacts along the length of their backbones. By contrast, in the C16-IDTBT systems, each pair of chains almost always shares a maximum of one contact. This indicates that the IDTBT backbones are arranged in such a way that they pass close to each other at one location before diverging.

I quantified the differences between the microstructures using a metric I term the *interconnectivity*. I defined this as the average number of close contacts with distinct chains divided by the contour length of the chains. In other words, this values gives the average number of distinct close contacts per unit of

backbone length. Calculating the interconnectivity of each of the systems, I found a value of $0.56\,\mathrm{nm}^{-1}$ for the C16-IDTBT 24mer system, $0.67\,\mathrm{nm}^{-1}$ for the C16-IDTBT 12mer system, $0.34\,\mathrm{nm}^{-1}$ for the P3HT system, and $0.37\,\mathrm{nm}^{-1}$ for the PffBT4T-2OD system. If we multiply the interconnectivity value of the C16-IDTBT 12mer system by the length of an IDTBT monomer (1.6 nm), we get a value of 1.1, meaning that the C16-IDTBT chains in this system participate in a close contact with a new chain slightly more often than once per monomer, on average. A visual depiction of the different levels of interconnectivity displayed by the C16-IDTBT and P3HT models can be seen in Figure 5.13.

The high interconnectivity values of the C16-IDTBT systems likely arises as a consequence of the perpendicular crossing motif, in combination with long and stiff backbones. With each contact in a crossed arrangement, many neighbouring chains can be positioned alongside each other, all making close contact with the same primary chain (e.g. the red chain in Figure 5.13). The stiff backbone (and crucially the lack of backbone folding) then allows each chain to extend through the microstructure to make contact with many neighbours. This is in contrast with polymer systems in which parallel contacts are favoured, where each neighbouring chain can sterically block a larger number of other potential neighbours from access to the primary chain. A simplified diagram contrasting these two cases can be seen in Figure 5.14.

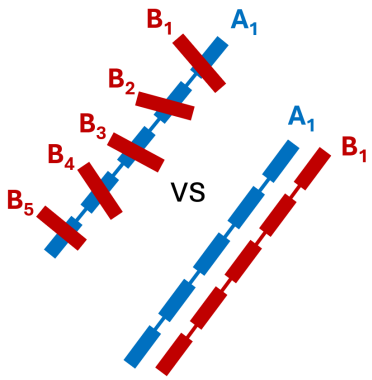


Figure 5.14: A perpendicular arrangement provides space for more distinct contacts.

For a charge being transported through the microstructure, the high interconnectivity of the C16-IDTBT systems means that each C16-IDTBT chain is accessible from, and provides access to, many of its neighbours. This is likely to benefit bulk mobility by opening up many different charge transport pathways. On the other hand, the low number of shared contacts between backbones implies a relatively low degree of contact, and therefore low coupling, between any two contacting chains, compared to the semicrystalline polymers P3HT and PffBT4T-2OD.

The highly interconnected microstructure of C16-IDTBT bares some similarities with cross-hatched crystallite structures describe by Takacs et al. and Schulz et al. in a series of semicrystalline materials [101, 102]. Although differing in the degree of long-range order present, these 2D crystallite structures demonstrate the benefits to transport that can be gained by moving away from a classical arrangement of parallel packed backbones. Takacs et al. proposed that the higher connectivity between chains in such microstructures, and the isotropy of locally accessible transport pathways, allows charges to navigate around blockages and traps [101]. The increased isotropy of accessible chains may also allow charges to more frequently transfer onto backbones orientated in-line with the field direction. This would increase mobility in a stiff, planar polymer such as C16-IDTBT, since each well-orientated backbone can act as a 'highway', rapidly transporting charges through the microstructure.

5.3 Conclusions

In conclusion, I have presented a series of computational investigations into the microstructure of the high-mobility conjugated polymer C16-IDTBT. I have focused on identifying and understanding those microstructural features which are relevant to the charge transport behaviour of C16-IDTBT. This has been aided by comparison with modelled microstructures of the semicrystalline polymers P3HT and PffBT4T-2OD.

My results indicate that C16-IDTBT chains make contact by adopting an unusual packing motif involving backbones crossing at perpendicular angles. This contact geometry allows C16-IDTBT backbones to pack as closely as semicrystalline polymer backbones. However, unlike these polymers, this close packing between immediate neighbours does not form part of a repeated packing structure. In fact, the strongly favoured crossing motif may be incompatible with long-range order.

The chemical-structural cause of the crossing motif in C16-IDTBT appears to involve the side chains of the polymer. In particular, the attachment point of the side chains on the IDT unit, and the unadorned BT unit. Crossing appears to be favoured even when side chains are short, although longer side chains appear to promote a narrower range of contact geometries around the perpendicular.

The perpendicular crossing motif promotes a highly interconnected microstructure, meaning that each C16-IDTBT chain is in close contact with many of its neighbours. This is achieved by allowing for a high density of close contacts along the backbone of each chain, with each contact being to a distinct neighbouring chain.

A high degree of interconnectivity is likely to benefit transport by increasing the number of easily accessible, (semi-)isotropic transport pathways, including intrachain pathways that are well-aligned with the field direction.

Based on these results, we can list some insights that may be useful when considering the design of new high-mobility polymers (see Section 6.3 for further discussion of design rules):

- Side chains can play a positive role in promoting useful packing arrangements.
- Crystallinity is not necessary for the close packing of backbones.
- Crystallinity can be detrimental to achieving other useful transport network topologies.

In this chapter, I have presented a microstructural picture of C16-IDTBT and stated some of the benefits to transport arising from this picture. To counterbalance these, it is also worth reiterating the potential drawbacks. In particular, the low number of shared contact locations between C16-IDTBT backbones, and the low degree of contact surface provided by a crossing arrangement, imply that the interchain coupling is likely to be relatively weak. In the traditional framework, used to explain the superior mobilities of semicrystalline polymers compared to older amorphous polymers, weak interchain

coupling is cited as the main reason why amorphous polymers perform worse, and therefore why long-range structural order is desirable [12].

To confirm whether the microstructural picture of C16-IDTBT presented in this chapter can rationalise the transport behaviour of the polymer, I carried out further analysis of the factors influencing transport, with a particular focus on the electronic coupling established at contacts. The results of this analysis are presented in the next chapter.

Chapter 6

Transport in C16-IDTBT

This chapter, and the previous, describe an investigation into the high-mobility, non-crystalline polymer C16-IDTBT. Developing on the microstructural insights detailed in Chapter 5, I explore the microstructure-transport relationship using quantum chemical calculations and simulations of charge transport through realistic microstructural models. Based on these analyses, I identify and compare the various factors contributing to the transport behaviour of C16-IDTBT, concluding that its high mobility arises from a combination of high intrachain mobility, close backbone packing, and a highly interconnected transport network. The majority of the work described here has been published in Proceedings of the National Academy of Sciences *[150].*

6.1 Introduction

The high-mobility conjugated polymer C16-IDTBT was introduced in Section 2.5. In the previous chapter, I formulated a picture of the microstructure of C16-IDTBT and proposed how features of the microstructure are likely to inform the transport behaviour of the polymer. In this chapter, I will describe my further investigation into the microstructure-transport link in C16-IDTBT. In particular, I will detail my exploration of the quantum chemical interactions established at interchain backbone contact points. This will be followed up by analysis of charge transport simulations. These simulations are used to consolidate information about the microstructure and electronic structure gathered over Chapters 5 and 6. The results allow me to test my propositions about the microstructure-transport link in C16-IDTBT.

Here, I provide a brief summary of insights relevant to this study, gained from past work and the results of the previous chapter. The C16-IDTBT backbone is linear and planar, indicating support for fast intrachain transport [86]. Bulk transport is likely to be limited by interchain charge transfer rates, as implied by the increase in experimentally measured mobilities with increasing chain lengths [91]. In the previous chapter, I identified a favoured interchain packing motif involving backbones crossing at perpendicular angles, with BT-BT or BT-Th moieties in contact between the backbones (Section 5.2.1

and Section 5.2.5). This motif enabled close packing between the backbones (Section 5.2.5). In the solid state, adopting the perpendicular motif allowed each backbone to make contact with a large number of neighbouring chains, producing a highly interconnected microstructure (Section 5.2.6). I proposed that a high interconnectivity would benefit transport by increasing the number of easily accessible, (semi-)isotropic transport pathways, including intrachain pathways well-aligned with the field direction.

With the above information in mind, several questions remain about the microstructure-transport link in C16-IDTBT, which I list here:

- What is the strength of interchain electronic coupling at contact points? Moreover, how does the preferred contact geometry influence the coupling strength?
- How do interchain coupling strength, intrachain transport, and microstructural interconnectivity combine to control the bulk mobility of C16-IDTBT?
- Do the above features and behaviours differ between C16-IDTBT and other conjugated polymers?

In seeking to answer these questions, I was aided by the work of my coauthors on [150]. In particular, I made use of data from experiments by Matthew J. Bird, and a computational study by Yucheng Xu. Matthew carried out pulse radiolysis time-resolved microwave conductivity (PR-TRMC) measurements on C16-IDTBT chains dispersed in solution. The data he gathered was used to estimate the mobility for holes confined to the backbones of single chains. Yucheng carried out a series of DFT simulations, from which he calculated a value for the reorganisation energy of C16-IDTBT. The results of both these investigations are given in Section 6.2.3, where they are used to inform the setup and analysis of my charge transport simulations.

My contributions to the investigation of the microstructure-transport link in C16-IDTBT are described in the remainder of this chapter. Here, I briefly outline the methods I employed, and how these were used to address the research questions listed above:

- In Section 6.2.1, I describe the construction of 'contact interaction maps' which relate the geometry of interchain contacts to the quantum chemical interactions established between polymer chains. Analysis of these maps provides insight into the chemical-structural reasons why certain contact arrangements are observed, and how these arrangements govern interchain coupling.
- In Section 6.2.2, I describe the calculation of coupling strength at interchain contact points in realistic microstructural models. Analysis of these results provides insight into the likely strength, and geometrical-dependency, of coupling in the solid state of real conjugated polymer materials.
- In Section 6.2.3, I describe the setup and running of charge transport simulations performed on realistic microstructural models, which consolidate much of the data gathered over this chapter

and the previous. Analysis of the simulation results allows us to identify factors contributing to the charge transport behaviour of C16-IDTBT, and weigh-up their relative importance.

Based on these results, I aim to rationalise the transport behaviour displayed by C16-IDTBT. In particular, I aim to unify the apparently contradictory characterisations of C16-IDTBT as both a structurally disordered, and high-mobility, material. In the concluding section of this chapter (Section 6.3), I will discuss how insights gained from this study can aid in the design of new conjugated polymers with even better transport properties.

6.2 Methods and Results

The result presented in Sections 6.2.1 and 6.2.2 are based on DFT calculations. All calculations were performed in `Gaussian 16` [157], at the `cam-b3lyp/cc-pVDZ` level of theory, with Grimme's D3 dispersion correction [111]. The systems evaluated by DFT consist of polymer chain segments that are approximately 3.2 nm long, corresponding to two monomers in C16-IDTBT and eight monomers in P3HT, which coincides with the segment lengths used for identifying locations of interchain contact in Section 5.2.4. I considered these as the maximum length of backbone for which thousands of DFT calculations could be performed within reasonable computational limits. In addition, I considered it desirable to use a C16-IDTBT segment length greater than one monomer, as there is evidence that holes delocalise across multiple monomers on the C16-IDTBT backbone [82, 86, 87]. Note that using a segment length shorter than the delocalisation length would likely lead to overestimated coupling strengths, since this would artificially increase the degree of MO overlap by overly localising the MOs on the shortened segments. The theoretical calculations reported in [87] implied that the delocalisation length is not significantly greater than two monomers, suggesting this segment length is sufficient. All side chains were replaced with methyl side groups before calculations were performed. Finally, all coupling calculations were performed with the projective method described in Section 3.1.5 [114].

6.2.1 Contact Interaction Maps

In this section I describe my exploration of the interaction energy (E) and interchain electronic coupling (J_{inter}) established between conjugate polymer backbones in contact. Analysing E can provide insight into why certain contact geometries are preferred based on the chemical structure of polymers. As seen in Section 5.2.5, the preferred contact geometry of a polymer has ramifications for larger scale microstructural trends in the solid state, which in turn affects the transport behaviour. Analysing J_{inter} can gives us another, more direct, view into how the contact geometry impacts transport, via its effect on charge transfer rates.

Strictly speaking, the number of DoFs defining the geometry of a contact is 3× the number of atoms in both segments. If the conformations of the individual segments are fixed, this may be reduced to the

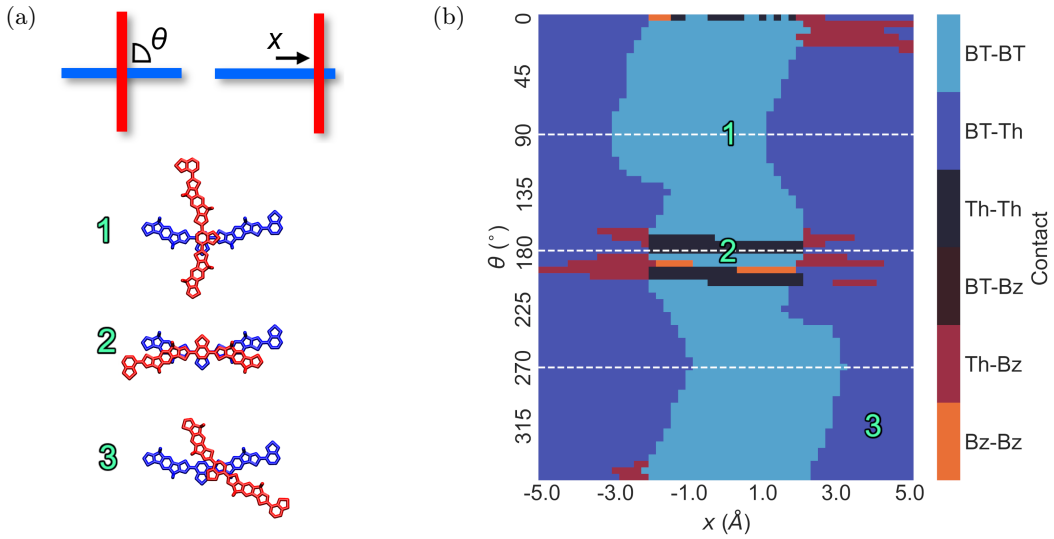


Figure 6.1: Diagrams illustrating the construction of contact interaction maps. (a) Demonstrates the DoFs explored to build maps. Three numbered examples of contact arrangements between IDTBT segments are shown below, with hydrogen atoms hidden for clarity. The upper segment is coloured red, while the static lower segment is coloured blue. (b) A contact map, revealing the combination of IDTBT moieties at the point of closest contact. This combination changes as the upper segment (red) is translated (x-axis) and rotated (y-axis) with respect to the static lower segment. The example arrangements in (a) correspond to specific pixels in (b), which have been annotated on the map. The horizontal dashed lines denote parallel and perpendicular arrangements of the segments. A version of (b) covering a broader range of x-shifts may be seen in Figure B.1.

six DoFs defining the relative positions of two rigid bodies. However I found that this still constituted too many dimensions to easily draw out meaningful insights into the relationship between contact geometry and interactions. I therefore chose to investigate an idealised model with a much reduced number of DoFs. This allowed me to generate 'maps' which can be used to describe and rationalise the contact geometry-interaction relationships.[1]

I constructed the maps by performing DFT calculations on pairs of IDTBT and P3HT backbone segments placed in various controlled geometries. All geometries featured the segments in a co-facial arrangement, at a fixed separation distance of 4 Å. This corresponds with the typical packing distance between 1st NNs observed in Section 5.2.5 and π-stacks in GIWAXS [29]. The effect of modifying separation distance was not explored, since the relationships between the separation of two cofacial molecules to E (Lennard-Jones potential, or similar), and J_{inter} (exponential decrease) are already familiar. One of the two segments, referred to as the lower segment, was held at a fixed position, while the other, the upper segment, was translated and rotated around its central moiety, as shown in Figure 6.1a (where they are coloured blue and red, respectively). Thus, using this approach, I was able to explore the effect on interactions of relative translations in the backbone direction of the lower chain (x), and changes in the crossing angle (θ). The range of x-shifts, from -5 Å to $+5$ Å, was chosen

[1]These maps are similar to those produced by Troisi et al. to explore the relationship between the arrangement of pentacene molecules and electronic coupling [95], although this similarity only came to my attention after I had performed this analysis.

to cover BT-Th and BT-BT contacts in C16-IDTBT, since these make up 77% of contacts observed in the solid-state MD models (see Section 5.2.5). Figure 6.1b shows a map of which moieties are in closest contact between a pair of C16-IDTBT segments. A version of Figure 6.1b covering a greater range of x-shifts may be seen in Figure B.1, revealing the onset of different moiety-contact combinations outside of $x \pm 5\,\text{Å}$.

I built the arranged contact structures from identical segments. Prior to being placed in contact structures, the individual segment geometries were fully optimised using DFT, except for the inter-monomer dihedral in P3HT. This dihedral was planarised, to ease comparison between the polymers by ensuring a more similar conformation between the C16-IDTBT and P3HT segments. The lowest energy conformation of the IDTBT segment has the BT unit orientated such that the S atom of the BT is directed opposite the S atom of the closest thiophene moiety on the IDT (see Section 7.2.2) [158]. The second monomer of the segment is therefore flipped by ∼180°, compared to the first, in order to achieve the correct orientation between the central BT and the two bonded IDTs. This conformation, which introduces a slight curve in the backbone of the 2mer segments[2], may be seen in Figure 6.1a.

Each pixel in the maps requires three single-point DFT calculations. These provide information that can be used to populate both the E and J_{inter} maps. E was calculated using $E = \epsilon_{AB} - \epsilon_A - \epsilon_B$, where ϵ_{AB}, ϵ_A, and ϵ_B are the energies of the segment pair, upper segment, and lower segment, respectively. Note that this only gives the enthalpic contribution to the free energy. In this model, with only two DoFs, we can expect the entropic contribution to the free energy to be small (i.e., the entropic penalty that opposes binding into a more restricted arrangement). Likely contact geometries are therefore expected to be dominated by the enthalpic contribution evaluated by our DFT calculations. In a more physical system, with more DoF, the entropic contribution will be larger, which may alter the likelihood of different contact geometries (this will be explored further below, when interpreting the E-maps). However, compared to other molecular systems, the rigidity of the conjugated units (and dihedral in case of IDTBT) will reduce overall contributions due to entropy, which suggests these maps are still useful for evaluating probable contact geometries. As stated, J_{inter} was calculated using the projective method described in Section 3.1.5 [114].

Figure 6.2 contains several interaction maps built using the method described above. The results shown in Figure 6.2a can rationalise why a perpendicular crossing motif is observed for C16-IDTBT contacts in simulations and experiments. Large areas of negative interaction energy are present surrounding the horizontal lines denoting $\theta = 90°$ and 270°. Outside of these stable regions, interaction energies rapidly rise above 0 eV. By inspecting the contact structures, we can deduce that this is caused by clashes involving atoms belonging to the side groups (with either the side groups or backbone of the opposing chain). These clashes occur because the side groups in C16-IDTBT are attached

[2]Note that this curve is only present on local scales, i.e. within each 2mer segment. For longer backbone lengths (in their minimum energy conformation) every other 2mer is 'flipped' in orientation, resulting in an overall linear conformation.

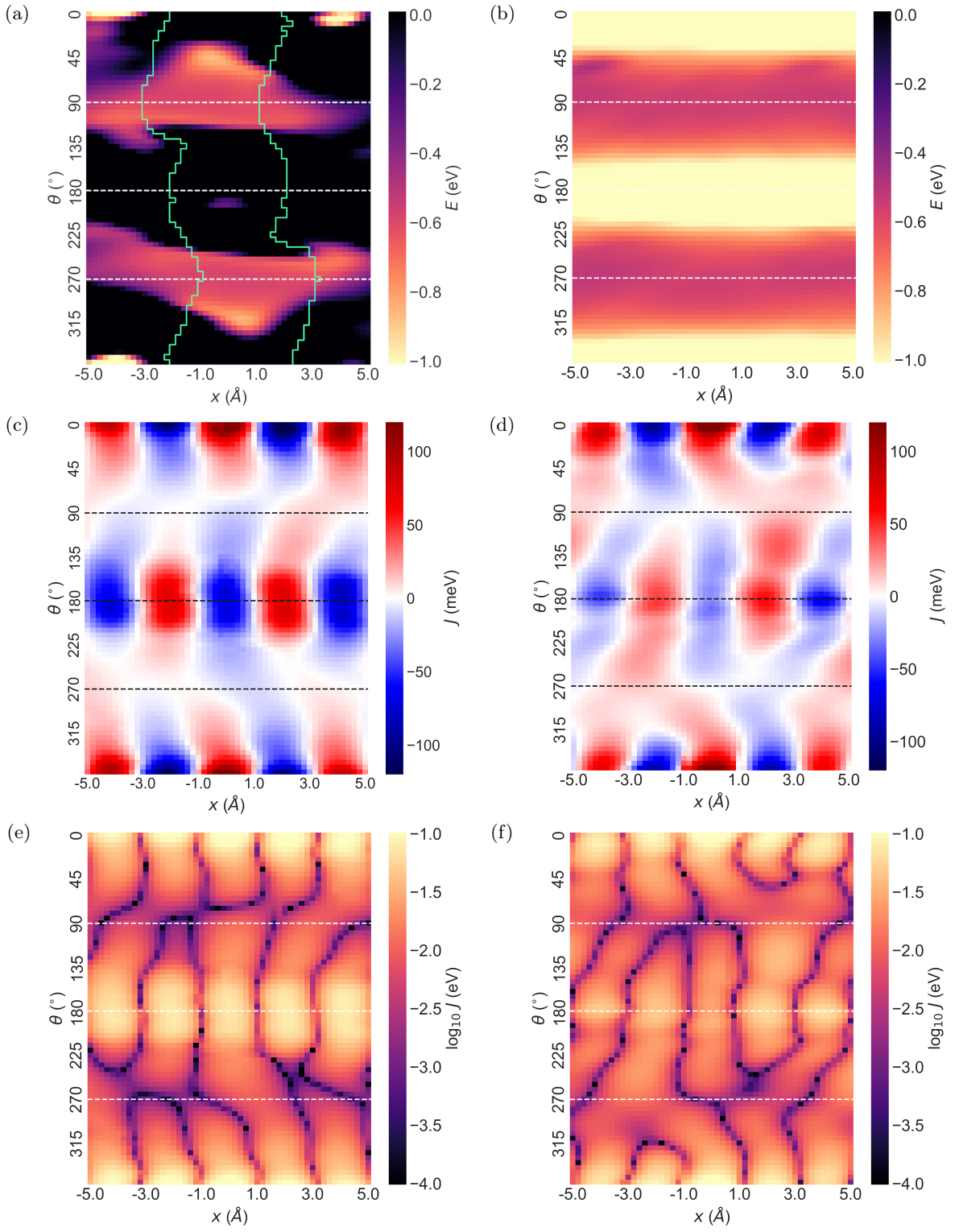


Figure 6.2: Maps displaying the enthalpic interaction energies (E) and hole transfer integrals (J_{inter}) between a pair of ∼3.2 nm segments with methyl side groups. Each pixel on the map represents a different arrangement, with the upper chain being shifted by x in the backbone direction of the lower chain and rotated in-plane by θ. A total of 3672 different arrangements are evaluated to construct each map. Dashed lines represent parallel and perpendicular arrangements of the segments. See Figure 6.1 for further explanation. The left column shows interactions between IDTBT segments, while the right column shows interactions between P3HT segments. The first row shows E maps. Overlaid green lines on the IDTBT map mark the boundary between BT-BT contact (inside the green lines) and BT-Th contact (outside the green lines). Small areas where other moieties are in contact have been neglected. The second row shows J_{inter} maps with a linear scale. The third row shows J_{inter} maps with a logarithmic scale.

to the backbone by an sp^3-hybridised bond, causing them to extend out of the plane of the backbone. Thus, during contact formation, contact geometries are repulsed away from a parallel arrangement and attracted towards a perpendicular arrangement of the backbones.

There are small regions of negative interaction energy corresponding to more parallel arrangements of the IDTBT backbones (e.g., in the top-right or bottom-left corners of Figure 6.2a). However, these regions are unlikely to be important for governing the types of contacts that form in physical microstructures. This is on the basis that these small regions of enthalpic stability are likely to be entropically disfavoured, due to the small range of contact geometries they encompass. With chains longer than the 2mers used here, it is likely to be even more difficult to access these geometry-regions, because a parallel arrangement at one location implies that nearby sections of both chains will also be parallel. Therefore, multiple segments of the two chains must all adopt a very specific contact geometry simultaneously, which is unlikely to occur during the contact formation process. In addition, E-maps constructed with the upper segment also translated in the y-direction (orthogonal to x and the conjugated planes) indicate that the enthalpically favourable regions become more restricted around perpendicular θ for non-zero y-shifts (these additional E-maps were computed using a forcefield approach, see Appendix B.2). For these reasons, we see a low occurrence of parallel contacts compared to perpendicular contacts in MD microstructural models of C16-IDTBT (see Section 5.2.5).

Comparing Figure 6.2a to Figure 6.1b (or considering the green lines overlaid on Figure 6.2a), we can understand why BT-BT and BT-Th contacts are prevalent in the MD microstructural models presented in Chapter 5. The bright regions, representing enthalpically stable contact geometries, extend to cover areas associated with both moiety combinations.

Figure 6.2b can be used to rationalise the contact geometries promoted by the chemical structure of P3HT. In P3HT, the side groups are attached such that they extend outwards in the same plane as the backbone. This means that, unlike IDTBT, clashes involving the side group atoms do not occur between chain segment pairs in the cofacial geometries evaluated here. None of the evaluated geometries are therefore enthalpically prohibited ($E > 0$), leading to the bright and relatively featureless E map in Figure 6.2b. With this in mind, parallel contacts are still clearly preferred, as we can discern from the bright horizontal bands centred on $\theta = 0°$ (wrapping round to 360°) and 180°. As raised in Section 5.2.5, it is noteworthy that the more strongly preferred contact arrangement in C16-IDTBT leads to a disordered microstructure, while the relatively ambivalent behaviour at P3HT contacts leads to a far more ordered microstructure.

Figures 6.2c to 6.2f show how the HOMO-HOMO coupling between IDTBT (left column) and P3HT (right column) chains varies with contact geometry. The complex nodal landscapes presented in these maps demonstrate the sensitivity of J_{inter} to small changes in the arrangement of backbones, arising from the highly nodal shape of the HOMOs. The key observation from these results comes from a comparison between the energetically stable geometries revealed by Figure 6.2a and Figure 6.2b, and

the strength of coupling established by these geometries. For both polymers, the strongest J_{inter} values are associated with parallel contact geometries, as shown by the brighter horizontal bands, and fewer nodes encountered, close to $\theta = 0°, 180°$ compared to $\theta = 90°, 270°$. This makes sense given the inherent increase in contact surface, and therefore MO overlap, achieved when backbones are parallel. For P3HT, an ideal situation results, in which the enthalpically favoured geometries also establish the strongest J_{inter} values. By contrast, for IDTBT, this leads to the unfortunate situation where the preferred contact geometries lead to relatively weak J_{inter} values.

While the HOMO in IDTBT is spread relatively evenly over the full segment, the LUMO is more localised on the central BT unit (shown later, in Figure 7.2b). Interestingly, this means that the LUMO-LUMO coupling tends to be stronger than the HOMO-HOMO coupling at IDTBT contacts, due to the π-stacked BT units. LUMO-LUMO coupling results may be seen in Appendix B.4.

Two more minor observations can also be gleaned from the J_{inter}-maps. Firstly, it is possible that the localisation of the HOMO and LUMO promoted by the donor-acceptor structure of the IDTBT backbone leads to a slightly less complex landscape in the J_{inter} maps compared to P3HT. This is based on purely visual inspection of the J_{inter} maps, as the degree of complexity is difficult to quantify. Secondly, the J_{inter} values established for anti-parallel contact geometries appear to be slightly stronger in IDTBT compared to P3HT, as indicated by the more saturated/brighter horizontal band around the $\theta = 180°$ line. This may be due to the slightly wider backbone of IDTBT, or other differences in the electronic structure due to differences in the chemical structures of IDTBT and P3HT.

To summarise, the results presented in this section correspond with those gathered from analysis of contact geometries in 2D (Section 5.2.1) and solid state (Section 5.2.5) MD models. Namely, that a perpendicular crossing motif, with BT-BT or BT-Th moieties at the point of contact, is promoted by the IDTBT chemical structure. Furthermore, analysis of these results gives us a direct insight into *why* this contact geometry is promoted; Because the attachment location and direction of the side groups repulse close packing between the IDT units. Since the backbones remain attracted to one another, to still converge, the IDT units must be rotated away from one another, opening up an avenue for the unadorned BT units to approach. This occurs even with the short methyl side groups used in this study.

The results also show that, despite their energetic favourability, perpendicular crossing contacts are not conducive to establishing strong J_{inter}. For transport considerations, this suggests that the high hole mobility displayed by C16-IDTBT is not explained by an ability to establish particularly fast rates of interchain charge transfer. However, it may be possible that, by circumscribing the the range of energetically allowed contact geometries, there may be some benefits to interchain transfer due to a moderating of interchain vibrational modes and their effect on dynamic disorder in J_{inter} [11, 57, 68, 69] (see Section 7.2.4 for further analysis relevant to this effect).

Beyond demonstrating the relatively low J_{inter} at contacts in C16-IDTBT, these results help us to

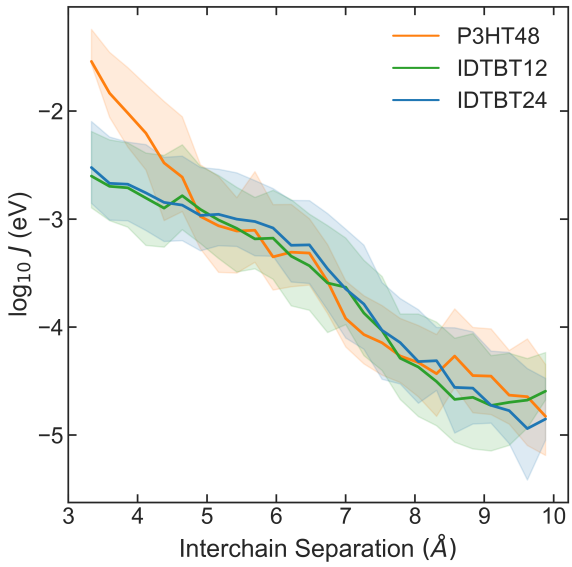


Figure 6.3: Distance dependence of coupling strength at contact locations. Shaded area represents interquartile range (i.e. middle 50% of values lie within shaded area).

identify the *causes* of these low J_{inter} values. This may prove useful for providing insight into potential pathways for further improving transport in materials similar to C16-IDTBT. An exploration of these pathways is provided in the concluding section of this chapter (Section 6.3).

6.2.2 Electronic Coupling at Contacts

In this section, I describe my exploration of interchain coupling at locations of backbone contact sampled directly from realistic models of conjugated polymer microstructures. In Sections 5.2.4 and 5.2.5 I described the identification of interchain contacts and the extraction of contact structures from backmapped thin film models of C16-IDTBT, P3HT, and PffBT4T-2OD. To briefly reiterate, contacts were identified between any pair of chain backbones with an intermolecular separation between π-system atoms $\leq$8 Å. Single or multiple contact structures were identified and extracted from each chain pair using a procedure described in Sections 5.2.4 and 5.2.5. 5787 contact structure were extracted from the C16-IDTBT 24mer model, 2821 from the C16-IDTBT 12mer model, 6062 from the P3HT model, and 4512 from the PffBT4T-2OD model. Contacts from the PffBT4T-2OD system were not used in the following analysis, due to time and computational constraints. However, we can expect PffBT4T-2OD to behave similarly to P3HT due to their similar semicrystalline microstructures and contact geometries (see Sections 5.2.5 and 5.2.6).

I performed coupling calculations on the full set of contacts from the C16-IDTBT and P3HT systems. Prior to calculation, a brief optimisation (3 steps) was performed using DFT. This was done to slightly fix the contact structures, since the geometry predicted by MD may be slightly inaccurate compared to that predicted by DFT. A small number of steps was used to ensure that the partial optimisation did not alter the geometries too greatly. This is necessary because the DFT calculations

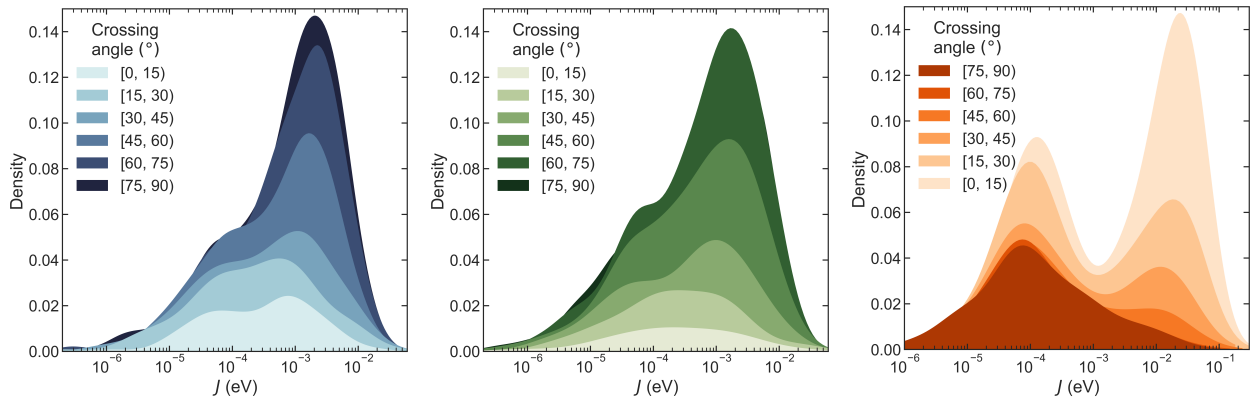


Figure 6.4: Distribution of J_{inter} for contacts extracted from the thin film models of (a) C16-IDTBT 24mers, (b) C16-IDTBT 12mers, and (c) P3HT 48mers. Distributions are binned according to the crossing angle between backbones. Darker shaded distributions represent more perpendicular crossing angles. Note that the distributions corresponding to larger crossing angles are drawn at the back for (a) and (b), but in front for (c).

are performed on short chain segments in vacuum, and we would like the geometries to remain informed by the solid state environment and extended chains from which they were extracted. To confirm this, I compared the bond lengths, dihedral angles and interchain separation distances (see Section 5.2.5 for definition) of the contact structures before and after the partial optimisation. Changes to the intrachain geometry were small, with bond lengths adjusting by 0.5±0.8 % and dihedral angles changing by $0.0 \pm 0.6°$ (where I have given the mean and standard deviation after fitting the changes in the relevant value to Gaussian distributions). The interchain distances tended to increase slightly with optimisation, likely due to the difference in the local environment (solid state versus vacuum). The changes in interchain separation conformed approximately to an exponential distribution with a scaling factor (i.e., mean) of 0.57 Å, corresponding to a typical increase of 15 %. After partially optimising, the contact structures were then subject to the procedure outlined in Section 3.1.5 [114], to calculate the coupling between the HOMOs of the two segments.

Figure 6.3 shows how the coupling strength (J_{inter}) varies with intermolecular separation (r), where r is the shortest distance between the CoGs of conjugated rings. As expected, J_{inter} falls exponentially with increasing r. The chemical structure does not have as strong an influence on the geometry of contacts when separation distances are large ($r > 5$ Å), leading to a wider array of backbone arrangements in both polymers (see Section 5.2.5). This results in the strength of J_{inter} displayed by both polymers becoming similar, and following a similar exponential relationship with r. However, for $r \leq 5$ Å, the trend levels out slightly for the C16-IDTBT systems, leading to lower J_{inter} strengths for the closest packed contacts, compared to P3HT. The wide error bars (representing the interquartile range), covering almost an order of magnitude, indicate the sensitivity of J_{inter} to small changes in the contact geometry, even at a fixed r.

The distributions shown in Figure 6.4 demonstrate how J_{inter} varies with crossing angle (θ), in each of the systems. For the C16-IDTBT systems, we observe a subtle positive correlation between larger θ and higher J_{inter}; The peaks of the crossing angle bins for $\theta \geq 45°$ are at a slightly stronger J_{inter} than the peaks for smaller angle contacts. Because of the established relationship between J_{inter} and r (see Section 3.1.5), these distributions resemble a mirrored version of those in Figure 5.10, indicating that this correlation is caused by the fact that the closest contacts involve perpendicular chains. In P3HT, the reverse trend is seen, with the strongest coupling achieved by parallel contacts. Furthermore, effectively no perpendicular contacts contribute to the 1$^{\text{st}}$ NN peak. As suggested in Section 5.2.5, this is because perpendicular contacts are not part of the ordered packing structure promoted by the chemical structure of P3HT.

The typical strength of J_{inter} is significantly different between the two polymers. In C16-IDTBT, we find a modal value of 2 meV. By contrast, the typical J_{inter} in P3HT is about an order of magnitude larger, with a modal value of 19 meV

For C16-IDTBT contacts, the deviation in J_{inter} from the trend of exponential increase with decreasing r (Figure 6.3, $r < 5$ Å) most likely results from the perpendicular crossing motif. While this arrangement does allow C16-IDTBT to make close contacts, it inherently limits the degree of contact surface, and thus the coupling that can be established. This can be demonstrated by considering the coupling heatmaps shown in Figure 6.2. For equal r, parallel contacts lead to higher J_{inter} in both C16-IDTBT and P3HT.

While the close packing of perpendicular contacts does lead to moderate J_{inter}, for transport considerations, these results imply that the high bulk mobility displayed by C16-IDTBT is unlikely to be caused by unexpectedly fast rates of interchain charge transfer.

6.2.3 Charge Transport Simulations

Using the microstructural models and calculated J_{inter} values, I simulated hole transport in C16-IDTBT and P3HT to directly evaluate which factors are most important for explaining the different hole mobilities (μ) of the two conjugated polymers. Because the contour lengths of C16-IDTBT 12mers and P3HT 48mers are similar (∼19.5 nm and ∼19.0 nm respectively), we can compare their predicted μ while neglecting the effects of chain length. On the other hand, comparing C16-IDTBT 12mers to C16-IDTBT 24mers (with a contour length of ∼39.0 nm) gives insight into the effects of chain length for this polymer. I ran transport simulations with a range of μ_{intra} values. This allowed me to separate out the main known advantage of C16-IDTBT, its high μ_{intra}, and thus isolate the influence of microstructure (including J_{inter}) on the bulk μ. In a similar vein, many of the transport-related parameters were set using experimentally informed values for C16-IDTBT, with the same values applied to P3HT to facilitate comparison between the microstructures.

I carried out all transport simulations using a KMC algorithm implemented via the program `ToFeT`

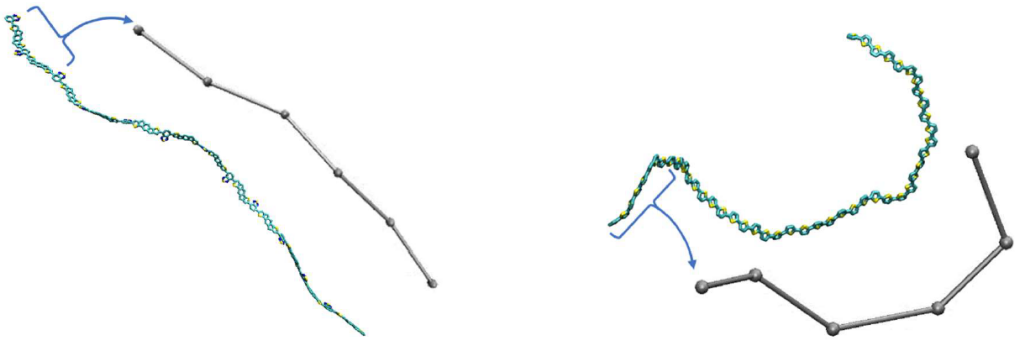


Figure 6.5: Conversion from atomistic representation to site representation based on coordinates of π-system atoms. (Left) C16-IDTBT, each 2mer segment is converted into a site. (Right) P3HT, each 8mer segment is converted into a site. Lines joining sites indicate intrachain transport pathways.

(see Section 3.3.1 and Section 4.3). Each polymer backbone in the systems was represented by a sequence of sites. Site coordinates were calculated from the CoG of π-system atoms belonging to backbone segments. As diagrammed in Figure 6.5, segments comprised two monomers in the C16-IDTBT systems and eight monomers in the P3HT system, representing approximately equal backbone lengths between the two polymers. These segments lengths were chosen to match the segment lengths used when identifying contact locations (Section 5.2.4) and when performing J_{inter} calculations (Section 6.2.2).

I introduced edges between site pairs that were electronically coupled. Intrachain edges were included between adjacent sites within the same chain. Interchain edges were included between any pair of sites when the location of the site pair corresponded to the location at which a contact was identified in the backmapped model. In other words, an interchain edge was placed wherever a J_{inter} calculation had been performed.

A hopping mechanism was used to model both intrachain and interchain transport within both systems. As discussed in Section 2.4.1, this may not be appropriate for modelling intrachain transport in conjugated polymers, due to the presence of high intrachain coupling. To justify this choice of transport model, we can consider the fact that previous calculations have suggested the delocalisation of charges on IDTBT backbone is typically not much larger than the 2mer segment lengths the backbones have been segmented into [82, 86, 87]. Furthermore, even if transport is more continuous in nature (e.g. band-like) along the backbone, it is not uncommon to represent continuous phenomena as a series of discrete steps. Ignoring temperature-dependent effects for the moment, a hopping model of intrachain transport should still yield valid behaviour, so long as, on average, charges move at the correct speed, and proportionally spend the correct amount of time in position for interchain hops. In other words, we can consider μ_{intra} as the single parameter defining intrachain transport. Of course, a different temperature-dependence of μ_{intra} would be expected from band-like or hopping intrachain transport. In this context, I justify the hopping mechanism by reference to the fact that the temperature-dependence of bulk mobility will be dominated by the increased temperature-dependence of the more weakly coupled interchain hops (see straight line on Arrhenius plot in Figure C.1b).

Nevertheless, in the context of intrachain transport, the assumptions and physical principles inherent to Marcus theory may no longer hold. The rate equation is still utilised, but plays a more abstract role, serving only as a means to parametrise the general intrachain transport behaviour of the model. Consequently, the intrachain electronic structure parameters (e.g. J_{intra}), should not be understood as aligning exactly with their standard physical interpretations. Partly for this reason, while simulations were conducted with various values for J_{intra}, results are presented here in terms of μ_{intra}.

As mentioned, aside from J_{inter}, all other electronic structure parameters (site energies (ϵ), J_{intra}, reorganisation energy (λ)) and simulation parameters (field strength (F), and temperature (T)) were kept equal between the polymer systems, or were varied across the same range of values. Parameter values were set as follows:

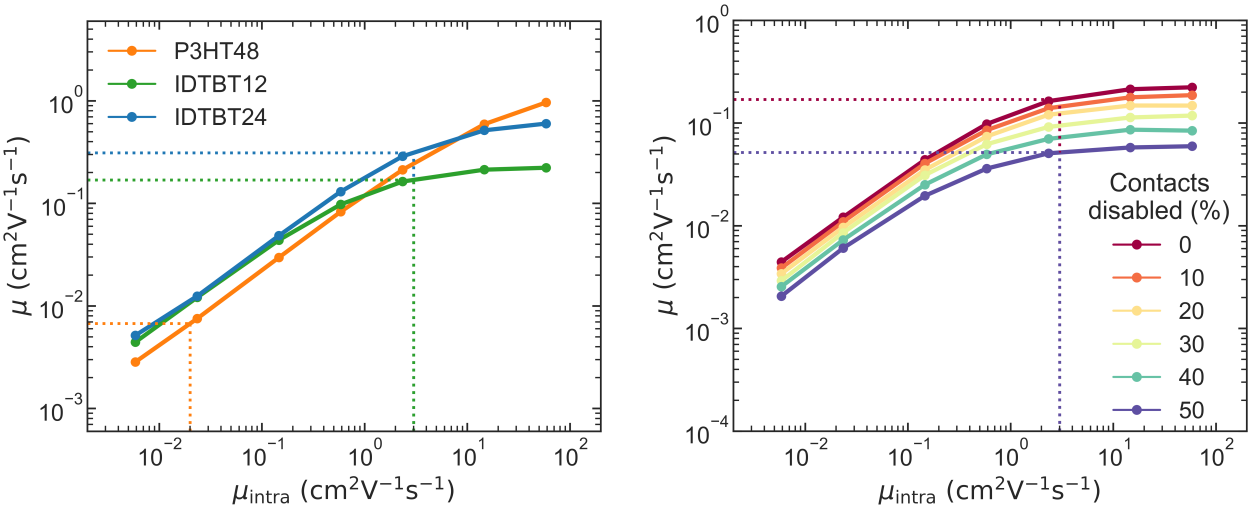
- ϵ was set to zero across all sites, representing a situation of negligible energetic disorder. This was chosen on the basis that C16-IDTBT has been found to display energetic disorder-free transport in experiments conducted by Venkateshvaran et al. [86].

- J_{intra} was generally varied across multiple transport simulations. During each simulation, a single value was used for all intrachain edges. For the presentation and interpretation of results, this value of J_{intra} was converted to a value of μ_{intra} using the relationship derived in Section 2.4.1. Values between 1 meV and 100 meV were chosen to represent a realistic range of μ_{intra} for both C16-IDTBT and P3HT.

- λ was set to 300 meV for all edges (see below for further details).

Calculations of inner-sphere λ for C16-IDTBT were performed by Yucheng Xu. Details may be found in the supporting information of [150]. To summarise here, he performed DFT calculations at the `cam-b3lyp/cc-pVDZ` level of theory. Using the four-point method (see Section 2.3.3), he compared IDTBT segments between their optimised ground and single-positively charged states. Testing at various segments lengths, he found that λ plateaued in the range 370 meV to 380 meV as length increased. As described, I used a slightly lower λ of 300 meV for the transport simulations. This was chosen as a compromise between Yucheng's calculated value and the activation energy (E_A) values typically extracted from temperature dependent transport experiments of C16-IDTBT. An E_A of 61 meV was reported by Zhang et al. [29], while E_A of 70 meV and 80 meV were reported by Ponder et al. [159]. These correspond to λ values of 244 meV, 280 meV and 320 meV respectively, when energetic disorder is neglected.

For the results shown here, system temperature and strength of the applied electric field were set to 300 K and 1×10^4 V cm^{-1} respectively. Experimental mobilities of OSCs are most commonly evaluated using FET devices, with charge transport being measured in the lateral, in-plane direction of the thin film. Because of this, for the results shown here, the field direction was aligned in one of the lateral



(a) (b)

Figure 6.6: In-plane bulk mobility (μ) estimates from KMC transport simulation, performed on realistic microstructural models. μ is shown to vary as a function of intrachain mobility (μ_{intra}). The dotted vertical lines indicate experimentally-informed μ_{intra} values. (a) μ of C16-IDTBT 24mers, C16-IDTBT 12mers, and P3HT 48mers are compared. (b) μ of C16-IDTBT 12mers. The different coloured lines show how μ changes as increasing proportions of interchain contacts are disabled at random.

directions of the models (the y-dimension of the MD models). This meant transport was measured in the same plane that most of the chain backbones were orientated in. Results for transport in different directions, and for a range of system temperatures and field strengths, may be seen in Appendix C.

A single mobile charge was propagated during each transport simulation, starting from a random initial location. PBCs were in place in all directions, allowing the charge to loop through the systems numerous times during each simulation run.

Figure 6.6a compares the simulated μ between the C16-IDTBT 24mer and 12mer systems, and the P3HT system. When μ_{intra} is low ($<1\,cm^2/Vs$), both C16-IDTBT systems outperform P3HT. This indicates a situation in which the higher interconnectivity of C16-IDTBT outweighs the order-of-magnitude larger J_{inter} values of P3HT; For transport, it is more advantageous to interact with many neighbouring chains via a relatively low J_{inter}, than a small number of chains with large J_{inter}. As μ_{intra} increases beyond $1\,cm^2/Vs$, the bulk μ of all systems begin to plateau. This starts earlier for the C16-IDTBT systems. At this point, chain length starts to influence μ, with C16-IDTBT 24mers saturating later and showing higher μ than 12mers. The higher J_{inter} values of P3HT mean that interchain charge transfer does not act as a limiting bottleneck to transport until much higher μ_{intra}. Thus, we observe only a slight deviation from the trend of linear growth in μ, at the highest μ_{intra} values.

The rapid increase of μ with μ_{intra} across all systems, up to the point of saturation, confirms the importance of fast intrachain transport for achieving high μ. The vertical dotted lines in Figure 6.6a indicate likely values of μ_{intra}. For C16-IDTBT, I chose a value of $3\,cm^2/Vs$. This is $3\times$ larger than the

value for the lower limit of μ_{intra} determined from PR-TRMC measurements by Matthew J. Bird [150]. I adopted a value 3× the lower limit following the precedent of a previous work by Bird et al., in which they found μ_{intra} for polyfluorene was 3× larger than the mobility measured by PR-TRMC, after accounting for defects, backbone curvature and finite chain length [160]. A value of $3\,\text{cm}^2/\text{Vs}$ also aligns with a previous theoretical prediction of μ_{intra} for C16-IDTBT [92]. For P3HT, I used a μ_{intra} value of $0.02\,\text{cm}^2/\text{Vs}$, based on PR-TRMC measurements [161]. With μ_{intra} set at these experimentally informed values, we can observe values of μ that correspond well with bulk transport experiments. The C16-IDTBT 24mer system shows a simulated μ of $0.3\,\text{cm}^2/\text{Vs}$, slightly lower than a value of $0.75\,\text{cm}^2/\text{Vs}$ measured by FET for samples with a molecular weight of $25.1\,\text{kg mol}^{-1}$ (corresponding to ∼19mer chains) [91]. The P3HT system shows a μ of $0.007\,\text{cm}^2/\text{Vs}$, well within the broad range of experimental μ values measured for P3HT thin films [162–164].[3]

The results shown in Figure 6.6b give an indication of the importance of interconnectivity for the high mobilities achieved by C16-IDTBT. To gather these results, I performed several transport simulations of the C16-IDTBT 12mer system, while disabling increasing proportions of randomly selected interchain contacts (setting hopping rates to zero). The bulk μ is seen to decrease across all values of μ_{intra}. At $\mu_{\text{intra}} = 3\,\text{cm}^2/\text{Vs}$, the bulk μ is reduced by a factor of ∼3 when 50% of contacts have been disabled.

Figure 6.7 shows how the mobilities of the C16-IDTBT 12mer and P3HT systems are affected by modifying J_{inter}. If we consider the difference in the curves when μ_{intra} is large, we can observe that increasing the J_{inter} prefactor causes the plateau in the relationship between μ and μ_{intra} to be lifted. This occurs because, with higher J_{inter} values, the rates of interchain transfer are no longer a limiting process to transport.

In contrast, it is interesting to examine the behaviour of the curves at low μ_{intra}. One might expect that bulk transport could also be limited by intrachain transport, in the same way it can be limited by the interchain transfer of charges. However, this does not appear to be the case. In both materials, even when μ_{intra} is at its lowest values ($\sim 0.01\,\text{cm}^2/\text{Vs}$), increasing the J_{inter} prefactor always benefits μ. This can be explained if we assume that there exist percolating interchain-only transport pathways through the materials. The existence of such pathways would also explain the small degree of plateauing seen at low μ_{intra} while applying the largest J_{inter} prefactors: Starting from the lowest μ_{intra} ($\sim 0.006\,\text{cm}^2/\text{Vs}$), and increasing it slightly, does not carry significant benefits to μ, because bulk charge transport is already progressing reasonably efficiently ($\sim 0.06\,\text{cm}^2/\text{Vs}$ for C16-IDTBT, at $\mu_{\text{intra}} = 0.01\,\text{cm}^2/\text{Vs}$, J_{inter} prefactor = 10) solely via interchain pathways. Therefore, making the slow intrachain pathways marginally less slow does not increase μ significantly, and thus we observe

[3] FET measurements of P3HT typically give μ in the $1 \times 10^{-3}\,\text{cm}^2/\text{Vs}$ to $1 \times 10^{-2}\,\text{cm}^2/\text{Vs}$ range. Although much higher values have been reported [165], these rely upon precise tuning of the processing conditions, and the elimination of backbone defects, in order to maximise the degree of crystallisation in films. Such high levels of microstructural order are generally not possible to replicate in MD simulations of film formation.

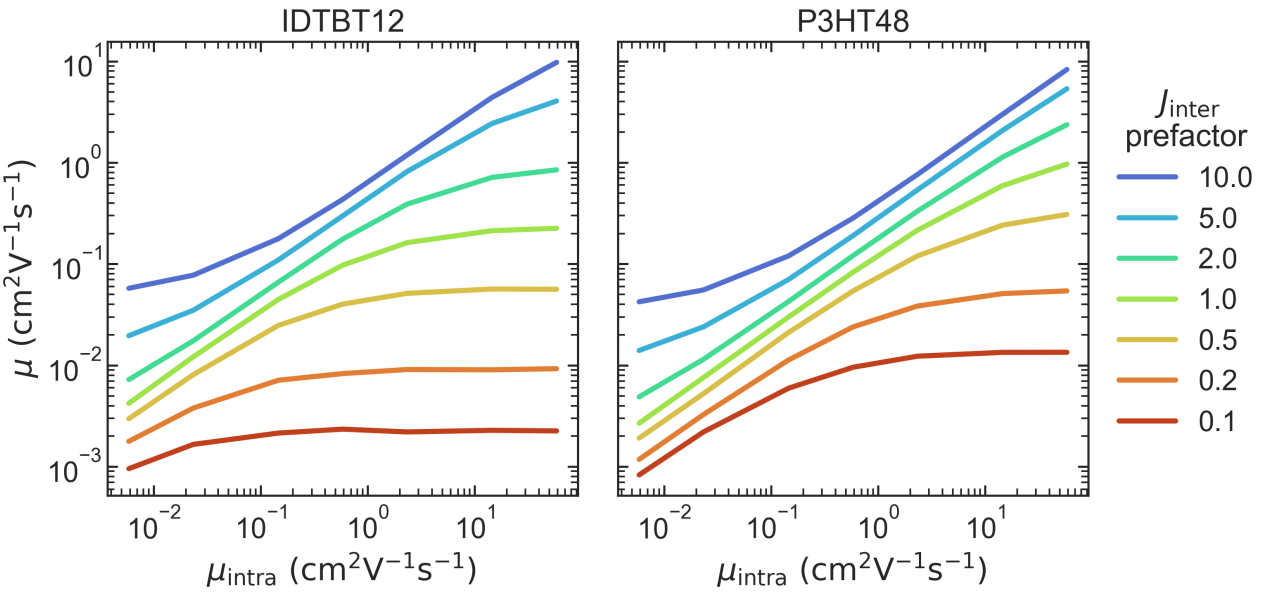


Figure 6.7: Mobilities predicted by KMC simulations after multiplying all J_{inter} strengths by a constant prefactor. (Left) C16-IDTBT 12mer system. (Right) P3HT 48mer system. Note that this prefactor is applied to the J_{inter} values calculated for both systems, meaning that, for the same prefactor, J_{inter} is typically 10× larger in P3HT.

a plateau in the relationship between μ and μ_{intra}. Conversely, there are no intrachain-only transport pathways that support percolation, so interchain charge transfer can limit bulk transport, leading to plateaus at high μ_{intra}.

The degree of separation between different J_{inter} prefactor curves tends to be larger for C16-IDTBT than P3HT (especially prominent at high μ_{intra}). This indicates that C16-IDTBT is more sensitive to changes in the typical strength of interchain coupling. With a J_{inter} prefactor of 10 for both systems, C16-IDTBT outperforms P3HT across the full span of μ_{intra}, despite the fact that typical J_{inter} values in P3HT remain an order-of-magnitude larger than those in C16-IDTBT.

The transport simulation results indicate that C16-IDTBT achieves its high μ by combining fast intrachain transport with a well-structured transport network. Linking to our results from Chapter 5, we can infer that the advantage of the C16-IDTBT transport network lies in its high interconnectivity. The benefits of interconnectivity are significant enough that C16-IDTBT can outperform P3HT, even when its main known advantage, namely its high μ_{intra}, is negated. This is despite the order-of-magnitude larger J_{inter} at P3HT contacts. However the simulation results also demonstrate how the low J_{inter} values of C16-IDTBT act as a limiting factor to transport. The J_{inter} prefactor results exemplify the importance of interchain processes, and therefore packing arrangements and microstructure, in governing the bulk transport behaviour of conjugated polymers. However, both inter- and intra-chain transport pathways must still be considered when designing new high-mobility polymers, as made clear by the contribution of a large μ_{intra} to C16-IDTBT's high bulk μ.

6.3 Conclusions

In conclusion, I have described a series of computational investigations aiming to rationalise the transport behaviour of the non-crystalline, high-mobility conjugated polymer C16-IDTBT.

The results presented in this chapter give clarification about why the perpendicular crossing contact motif, identified in Chapter 5, is promoted by the chemical structure of C16-IDTBT. As well as the attachment location of the side chains on the IDT unit, the direction of the side chain-backbone bond (which causes the side chains to protrude out of the backbone plane) appears to be crucial. Due to the steric effect of the side chains, the range of enthalpically favoured contact geometries is more narrowly bounded in C16-IDTBT, compared to P3HT (Section 6.2.1). Given that the crossing motif appears to be incompatible with traditional repeated packing structures, this leads to the interesting insight that a strongly preferred packing arrangement can actively prevent the establishment of long-range structural order.

The perpendicular crossing motif appears to reduce the strength of J_{inter} compared to a parallel contact geometry (Section 6.2.1). This is largely due to the inherently low degree of contact surface between backbones. For realistic contact geometries extracted from microstructural models, we observe a subtle increase in the strength of J_{inter} with increasing θ for C16-IDTBT (Section 6.2.2). This is because the backbones are able to pack closely in perpendicular contacts. Although we can presume that the close packing slightly mitigates the decrease in J_{inter}, the typical J_{inter} values established at contacts remain modest for C16-IDTBT. These were found to be $\sim$10$\times$ weaker than J_{inter} in P3HT, which features a more classical arrangement of closely packed, parallel backbones.

Despite the relatively low J_{inter} values in the C16-IDTBT system, transport simulations confirmed that the mobility of C16-IDTBT was still far higher than that of P3HT ($\sim$40$\times$ higher, when using experimentally-informed values of μ_{intra} for the two materials) (Section 6.2.3). Furthermore, the bulk mobility of C16-IDTBT remained higher even when its main known advantage, its high μ_{intra}, was negated by reducing μ_{intra} to match that of P3HT. The fact that C16-IDTBT outperforms P3HT in this modified scenario, despite its weaker J_{inter} strengths, demonstrates the value of C16-IDTBT's highly interconnected microstructure. This interconnectivity benefits transport by opening up a plethora of easily accessible transport pathways, including intrachain pathways well-aligned with the field direction.

Analysis of the the transport results indicate that the high experimental mobilities measured for C16-IDTBT arises due to a combination of chemical-structural factors. These include:

- A rigid and planar backbone, to enable a high μ_{intra}.
- Long chains, to effectively make use of its high μ_{intra}.
- An unadorned BT unit, to enable close packing at contacts necessary to somewhat mitigate the decrease in J_{inter} caused by the crossing motif.

- Long side chains, attached by an sp^3-hybridised bond to the backbone, to encourage perpendicular crossing at contacts. In combination with the stiff backbone, this promotes the formation of a highly interconnected, (semi-)isotropic transport network.

I note that each of the identified transport-influencing factors (μ_{intra}, J_{inter}, interconnectivity) has been linked to a chemical-, nano-, or micro-structural origin (backbone planarity, contact geometry, distinct contact density).

6.3.1 Design Rules

The plateauing of μ at high μ_{intra} indicates that transport in C16-IDTBT is limited by its low J_{inter} (Section 6.2.3). This is affirmed by the fact that μ increases dramatically when we artificially increase the J_{inter} values by multiplying them by a constant prefactor. The fact that C16-IDTBT appears to be more sensitive to modifications to J_{inter}, compared to P3HT, indicates that adopting a polymer with a C16-IDTBT-like interconnected microstructure as a 'baseline' would lead to better results when designing novel polymers for transport. Furthermore, the fact that we have identified the origin of the relatively low J_{inter} strengths in C16-IDTBT should make it easier for us to predict where improvements could come from i.e., to develop *design rules*.

Since the low J_{inter} values originate from the low degree of contact surface in the crossing arrangement, it is worth considering whether this contact surface could be increased while still promoting a high interconnectivity. A hypothetical alternative contact arrangement, enabled by a different backbone configuration, is shown in Figure 6.8. Although such an arrangement could hold some promise in this regard, it may be disqualified by the reduction in μ_{intra} implied by non-linear backbones.

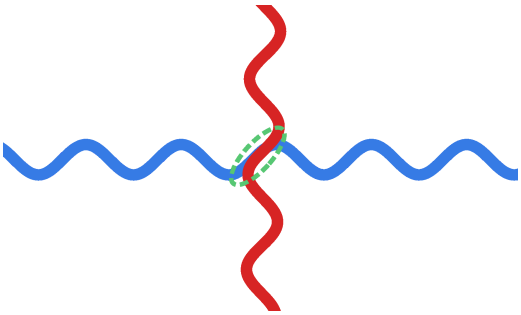


Figure 6.8: A 'wavy' backbone could increase the degree of contact surface (green circle) while maintaining perpendicular backbones.

A slight increase in contact surface could be achieved by a contact arrangement angled away from the perpendicular. As long as the angle is not too close to parallel, this could still avoid the steric contact-blocking effect linked to parallel contacts (Section 5.2.6). Such arrangements might be found in C16-IDTBT analogues with extended donor units. Lengthening the donor unit increases the spacing between side chain attachment locations on the backbone, which is likely to allow for a wider array of contact geometries, including a wider range of crossing angles. One example, TIFBT, has been demonstrated to show slightly higher μ than C16-IDTBT [166]. However, as proposed in [166], it is likely that the higher μ stems from an increased ability to form contacts (i.e., higher interconnectivity) afforded by the wider spacing between the side chain attachment locations and the BT unit. Other variants featuring minimally-, or maximally-extended donor units (IDTTBT and TBIDTBT) have also been synthesised, and showed similar μ to C16-IDTBT [158, 167, 168].

A similar effect to extending the donor unit may be achieved by including spacer-units between the IDT and BT. In [169], IDTBT analogues were synthesised containing thiophene spacers-units. Interestingly, the additional torsional degrees of freedom did not reduce the planarity of the backbone. However, these variants (also featuring shorter, branched side chains) displayed lower experimental μ than C16-IDTBT, likely because of the relatively low molecular weight (chain length) of the samples.

Another avenue to increasing contact surface, while maintaining a crossed contact geometry, may be to increase the size of the acceptor unit. This has been attempted by replacing the BT unit with a larger DTBT unit. However, this worsened the experimental μ, most likely because the non-linearity of the backbone introduced by the DTBT unit, as well as increased torsional disorder between the IDT and DTBT units, led to a decreased μ_{intra} [158, 170, 171]. Selecting a larger acceptor unit with collinear bonds to the donor unit may address this, if a similar torsional potential to that controlling the IDT-BT linkage can be established.

Rather than attempting to increase the contact surface, increased J_{inter} strengths could be sought by substituting heteroatoms onto the IDTBT backbone. Modification of this type will produce changes in the electronic structure of the backbone, which could potentially increase the degree of MO overlap at contacts. As well as potential effects on interchain interactions, changes to the electronic structure induced by heteroatoms will also affect the conformation of the backbone.

To explore the effect of substituting heteroatoms on the donor unit, I carried out an additional study of four donor-modified variants of C16-IDTBT. This investigation is detailed in Chapter 7. A discussion of previously-synthesised variants that were modified by heteroatom-substitution on the donor unit is provided in the introduction of that chapter (Section 7.1).

Fluorinating the acceptor unit has been shown to introduce an attractive electrostatic interaction between the F atoms on the acceptor and S atoms on IDT that further stabilises the backbone in a planar conformation [158, 172]. However, polymers synthesised with this modification produced lower experimental μ than C16-IDTBT [170]. Wadsworth et al. hypothesised that this could be due to the extreme rigidity of the backbone decreasing the solubility of the polymer, therefore restricting molecular weight (chain length) and negatively affecting film formation. The STM results in [150] also indicated that, even in a high μ_{intra} polymer such as C16-IDTBT, allowing for some degree of backbone flexibility was useful for facilitating higher amounts of contact formation. In terms of other changes to the acceptor, a possible future study examining the effect of substituting the chalcogen atom on the BT unit is discussed in Section 9.2.5.

A final, more drastic, approach to increasing J_{inter} would be to consider alternative donor-acceptor structures in which side chains are attached to the acceptor unit, while the donor is left unadorned. This suggestion is based on my results indicating that the LUMO-LUMO coupling is higher than the HOMO-HOMO coupling at IDTBT contacts, because of the increased localisation of the LUMO on the contacting BTs (see Section 6.2.1 and Appendix B.4). In light of this, switching the attachment

location of the side chains may lead to a better correspondence between the point of contact and the localisation of the HOMO, producing a stronger (hole) J_{inter}.

To summarise, I have laid out a number of suggested avenues (and associated complications) to increasing J_{inter} in a hypothetical C16-IDTBT-like conjugated polymer. Realising this increase, while maintaining the high μ_{intra} and interconnected microstructure of C16-IDTBT, may lead to new conjugated polymers with even better transport properties.

Chapter 7

Variants of C16-IDTBT

I describe an investigation into the electronic transport properties of variants of the high-mobility, non-crystalline polymer C16-IDTBT, featuring heteroatom-substituted donor units. I apply quantum chemical calculations to evaluate factors likely to influence charge transport, including the planarity of the backbone, interchain contact geometry, and interchain electronic coupling. From these analyses, I conclude that two variants, featuring thiazole moieties on the donor unit, may show higher hole mobilities than C16-IDTBT, due to enhanced backbone rigidity and a lower susceptibility to dynamic coupling disorder.

7.1 Introduction

The high-mobility conjugated polymer C16-IDTBT was introduced in Section 2.5. In the previous two chapters, I identified the chemical- and micro-structural features contributing to the high hole mobility of the polymer. Based on the results of this investigation, I discussed avenues to further improve transport behaviour by synthesising analogous of C16-IDTBT (Section 6.3.1).

Here, I extend the investigation to explore the potential effect on hole transport of substituting heteroatoms onto the donor unit of the IDTBT backbone. The structures considered in this chapter were proposed by Professor Iain McCulloch, following discussion of my findings on C16-IDTBT.

The donor unit of IDTBT could be modified by including F or N heteroatoms at various positions on the backbone. Four variants of IDTBT, arising from such substitutions, are shown in Figure 7.1. These have been labelled A, B, C, and D. The substitutions are designed to progressively deepen the frontier orbital energy levels as we move from IDTBT to A, and through the variants from A to D. Thus, selecting between the variants should allow for tuning of the polymer energy levels. This may be useful, for instance, in OPV applications, or when considering charge injection barriers at contacts. However, it is important to asses the impact of these substitutions on the charge transport properties of the variants, especially given that previous studies have demonstrated the extreme sensitivity of mobility to changes in the IDT unit [170].

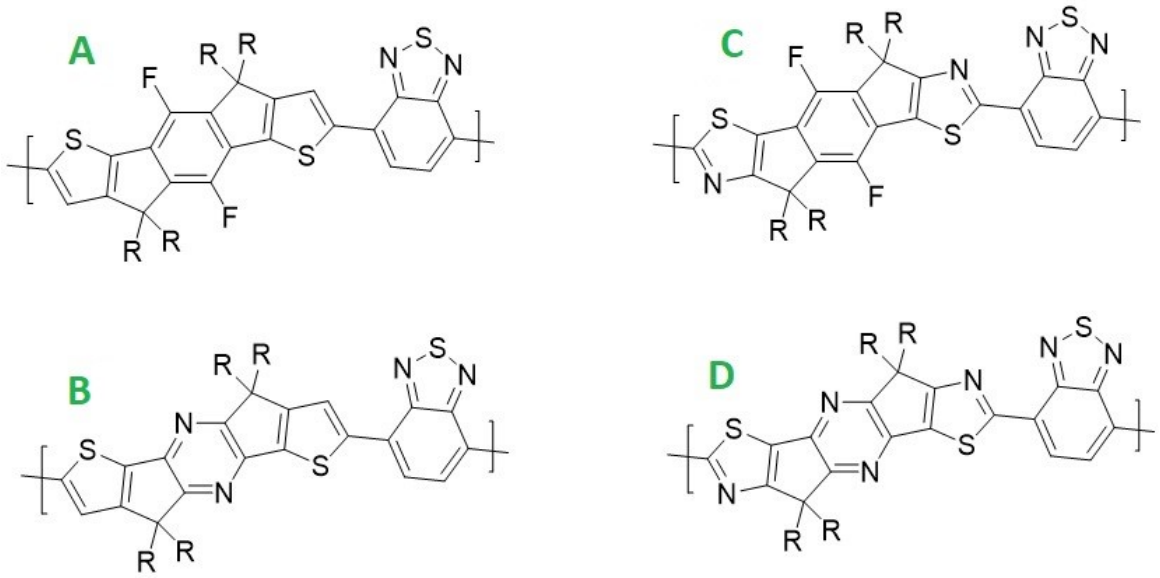


Figure 7.1: The chemical structure of four variants of IDTBT, arising from the inclusion of F or N heteroatoms at various positions on the donor unit. The variants have been labelled *A*, *B*, *C* and *D*. All chemical structures are displayed with the dihedral between donor and acceptor units in the 'upright' (0°) orientation. For microstructural considerations, C16 side chains (R) are assumed for all polymers. However, methyl groups were adopted for all quantum chemical calculations.

Aside from extending the length of the donor unit (see Section 6.3.1), other modifications to the donor that have been attempted generally involve substituting the sp^3-hybridised bridgehead carbons (to which the side chains are bonded) with heteroatoms [158]. Replacing the bridgehead carbons with heavier group 14 elements (such as Si [173], or Ge [174]) retains the general features of the IDTBT chemical structure, although the larger atomic radii of these atoms will lengthen the bond between the backbone and side chains. In Si- and Ge-substituted analogues of PCPDTBT, this enhanced the π-π stacking of backbones, leading to improved mobilities [175–177]. Replacing the bridgehead carbons with N atoms [178] causes a more dramatic change in the chemical and electronic structures of the polymer. The N atoms are sp^2-hybridised, and thus contribute to the π-conjugated system of the backbone. In addition, this means that only a single side chain may be bonded to each N bridgehead atom. These side chains protrude into the same plane as the backbone, eliminating the steric hindrance caused by the sp^3 attachment of the side chains in C16-IDTBT. In Section 6.2.1, the orientation of the P3HT side chains in the backbone plane allowed for a wider array of enthalpically-allowed packing arrangements at contacts, compared to the out-of-plane C16-IDTBT side chains, with a parallel arrangement of backbones preferred. This suggests that a parallel contact geometry may also be preferred by the N-substituted variant, potentially leading to stronger interchain coupling, at the possible cost of a less interconnected microstructure (see Section 5.2.6).

In all cases, substituting the bridgehead atoms resulted in lower average mobilities than C16-IDTBT in FET experiments ($8 \times 10^{-3}\,\mathrm{cm^2/Vs}$, $5 \times 10^{-3}\,\mathrm{cm^2/Vs}$, and $3 \times 10^{-2}\,\mathrm{cm^2/Vs}$, for Si-, Ge-, and N-substituted bridgeheads, respectively [158, 173, 174, 178]. Note that side chains were different from

C16 in all cases, which can affect mobilities [83]). For the N-substituted variant, this may partially be explained by the low molecular weight of the measured sample ($10\,\mathrm{kg\,mol^{-1}}$). This low molecular weight likely arose as an effect of poor solubility, due to the reduced number of side chains, more rigid backbone, and increased aggregation in the solution state [158, 178].

Although none of the variants investigated in this chapter have been previously synthesised (at time of writing), the chemical structures of variants *C* and *D* are similar to C16-IDTzBT. All feature thiazole moieties at either edge of the donor, replacing the thiophene moieties in IDTBT. In FET experiments, C16-IDTzBT was found to display a much lower hole mobility ($4 \times 10^{-5}\,\mathrm{cm^2/Vs}$) than C16-IDTBT [170]. Nikolka et al. considered this dramatic decrease in mobility surprising, since other thiazole-containing donor-acceptor polymers have been demonstrated without similarly poor mobilities [179, 180]. Rationalising the origin of this decreased mobility would therefore be a beneficial outcome of this study.

From the analysis of C16-IDTBT described in Chapters 5 and 6, and from past work (see Section 2.5.3), we have seen that the factors likely to govern hole mobilities in similar materials are 1) the rigidity and planarity of the backbone, 2) the packing geometry of interchain contacts, and 3) the strength of HOMO-HOMO coupling at contacts.

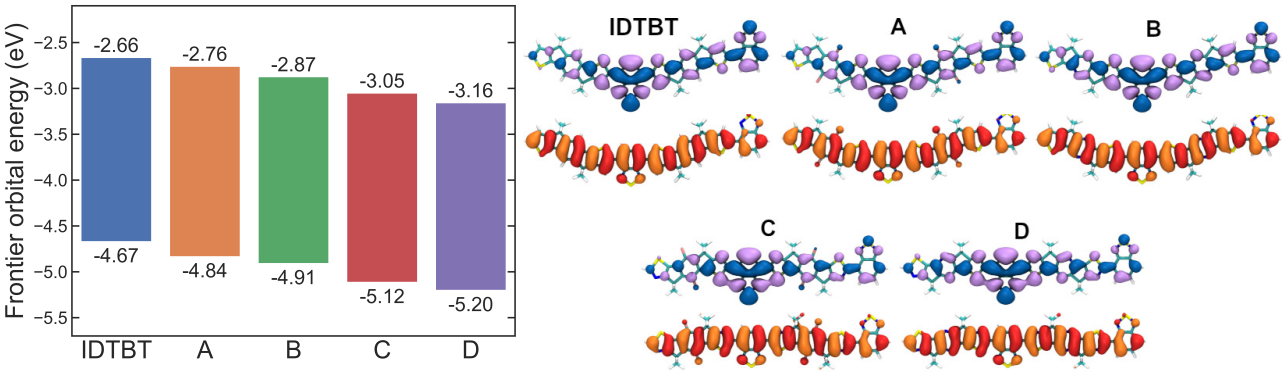
My assessment of these factors for each of the variants are described over the following sections, alongside comparisons to IDTBT.

7.2 Methods and Results

The results presented in the following subsections were derived from DFT calculations. All calculations were performed using `Gaussian 16` [157].

7.2.1 Frontier Orbitals

To confirm the effect of heteroatom substitution on the HOMO and LUMO levels, I performed single point DFT calculations on the optimised ground state geometries of each of the variants and IDTBT. The evaluated systems comprised 2mer segments with methyl side groups. This segment length was chosen because, as stated previously, past theoretical calculations have suggested that the frontier orbitals delocalise over backbone lengths greater than one monomer in IDTBT [86]. This choice of segment length also allowed for validation of my results by comparison with experimental and theoretical measurements (performed on 2mers) of the IDTBT HOMO energy reported by Kirkpatrick et al. [87]. The theoretical calculations in this work also indicated that the energy levels are negligibly affected by increasing the segment length beyond two repeat units. To facilitate comparison, I performed calculations at the same level of theory used in [87], namely `b3lyp/6-31g*`. Prior to the single point calculations, the relaxed geometries of IDTBT and the variants were located by optimising at the same



(a) (b)

Figure 7.2: (a) HOMO and LUMO energy levels of IDTBT and variants. (b) Visualisation of the HOMOs (red and orange) and LUMOs (blue and purple) for IDTBT and variants.

level theory, until convergence. As will be shown in Section 7.2.2, the minimum-energy conformations of variants C and D are somewhat distinct from those of IDTBT, A, and B. In particular, the angle of the dihedral connecting the donor and acceptor units is flipped by $\sim$180° in C and D, compared to the other polymers.

Figure 7.2a shows the computed HOMO and LUMO energies for each of the polymers. The HOMO level of IDTBT is in correspondence with the value found by Kirkpatrick et al. using the same functional[1] As expected, the HOMO and LUMO levels progressively deepen as we move from IDTBT to A, and through to D.

These calculations also allow us to visualise the frontier orbitals on each of the polymers, as shown in Figure 7.2b. In line with previous works, the IDTBT frontier orbitals are delocalised across the full length of the 2mer segment [86]. My calculations indicate that this degree of delocalisation carries over to all of the evaluated variants. This can be linked to the planarity of the backbones in their minimum energy conformations (see next section).

7.2.2 Torsional Potentials

To assess the capacity of the variants to support fast intrachain transport, I computed torsional potential surfaces for the donor-acceptor dihedral bond in each of the variants and IDTBT. The evaluated systems consisted of a single monomer, with methyl side groups. Calculations were performed using DFT at the `ωb97xd/6-311+G(d,p)` level of theory. This functional and basis set was chosen to align with previous calculations of the IDT-BT torsional potential carried out by Anders Gertsen (which was used to parameterise the IDTBT forcefield applied in Chapter 5 and [150]). Torsional scans were performed using the `opt=ModRedundant` function of `Gaussian`, which freezes the dihedral at specific angles while the remainder of the system is relaxed until convergence.

The donor-acceptor torsional potentials may be seen in Figure 7.3. All the polymers feature a global

[1] My value differs from that reported in [87] by 0.02 eV, possibly due a different treatment of the side groups. Methyl side groups were used for my calculations, while they appear to have substituted the side groups with H atoms

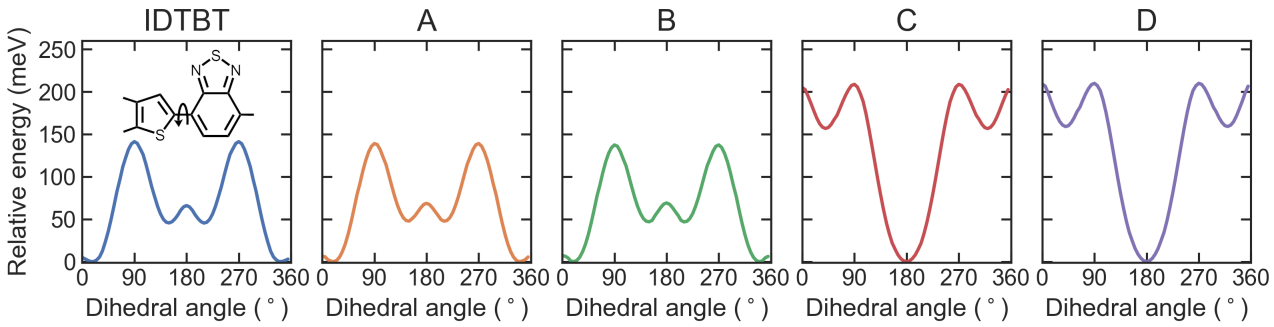


Figure 7.3: Torsional potentials controlling dihedral angle between donor and acceptor units of IDTBT and variants.

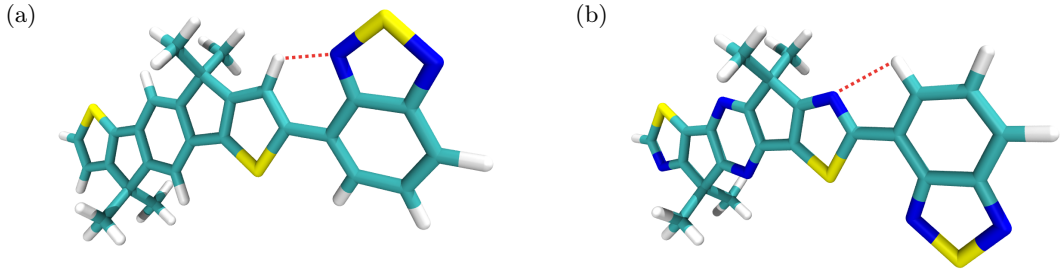


Figure 7.4: Geometry optimised monomers of a) IDTBT, and b) variant D. The donor-acceptor dihedral is in the 'upright' (0°) orientation for IDTBT, and the 'flipped' (180°) orientation for D. A dashed red line on (a) indicates the interaction between N-H atoms which stabilises the backbone in a planar conformation for IDTBT [158]. A dashed red line has also been included on (b), between a similar atom pairing on the D monomer, which may contribute to planarity of the backbone for this polymer.

minimum with the backbone in a planar conformation. Since, for IDTBT and all of the variants, there is a preference for each BT unit to adopt the same orientation with respect to both connected donor units, this leads to an alternating backbone conformation in which every other 2mer segment is 'flipped' in orientation. For IDTBT, A, and B, the global energy minimum occurs when the dihedral is orientated such that the S atom on the BT unit is directed opposite the S atom of the closest thiophene moiety of the donor (i.e., close to 0°, in the reference frame used here). The minimum energy conformation of IDTBT is depicted in Figure 7.4a. The stabilisation of the dihedral in this orientation is in line with previous reported calculations for IDTBT [150, 158]. In [158], this stabilisation, which helps to planarise the IDTBT backbone, was linked to electrostatic attraction between the electronegative N on the BT unit, and a nearby electropositive H on the IDT unit (joined by a dashed red line in Figure 7.4a). This interaction has been described as a non-traditional hydrogen bond [125, 158]. The same N-H atom pair is also present in A and B, which may explain why these variants show similar torsional potentials to IDTBT.

In variants C and D, replacing the thiophene moieties on the donor unit with thiazoles appears to have significantly altered the character of the dihedral torsional potential. In these variants, the 0° dihedral orientation is unstable. Instead, the minimum energy conformations are associated with dihedral angles of 180°, i.e., in a 'flipped' orientation compared to IDTBT. The minimum energy

conformation of D is depicted in Figure 7.4b. For backbones containing multiple monomers, this results in a more linear backbone shape, contrasting with the slight curve present for every 2mer segment of IDTBT, A, and B (this may be seen in Figure 7.2b, and later in Figure 7.6).[2] Notably, the potential well stabilising C and D in this flipped conformation is significantly more narrow close to the minimum, unlike IDTBT which features a region of somewhat flat potential close to 0°. This suggests that a planar conformation is more rigidly imposed in C and D than in IDTBT.

This is a surprising result, given that C and D lack the same N-H atom pairing which was identified as the main reason for the stiffly planar backbone of IDTBT [125, 158]. The minimum energy conformations of C and D do feature another, somewhat equivalent pair of atoms, this time involving an N on the donor and a H on the acceptor (joined by a dashed red line in Figure 7.4b). However, the distance between these atoms (2.48 Å) is greater than in IDTBT (2.38 Å), suggesting that the strength of the attractive force will be diminished. This implies that an alternative explanation may be required to understand the enhanced planarity of the C and D backbones. Notably, previous works have highlighted the importance of considering subtle increases in double bond character for explaining differences in the rigidity of certain donor-acceptor dihedral bonds with similarity to those discussed here. This effect has been proposed as contributing more to maintaining planarity across such dihedral bonds than the through-space electrostatic interaction described above [181, 182]. A potential future study on this topic is discussed in Section 9.2.5.

7.2.3 Contact Interaction Maps

To evaluate the effect of modifying the donor unit on the geometry of interchain contacts, and the strength of HOMO-HOMO coupling (J_{inter}), I computed interaction maps for each of the variants, using the procedure first described in Section 6.2.1. As before, a series of contact structures was generated for each variant by arranging pairs of 2mer chain segments in various face-on positions, all with a fixed separation distance of 4 Å. For each contact structure, the lower chain segment was held at a fixed position, while the upper chain segment was translated by x in the backbone direction of the lower segment, and rotated by θ around its central BT unit. The contact structures were then subject to DFT calculations, from which the enthalpic[3] interaction energy (E) and J_{inter} were computed.

To facilitate comparison with the IDTBT results, calculations were performed at the same level of theory as in Section 6.2.1 (`cam-b3lyp/cc-pVDZ`). Prior to being arranged as contact structures, the isolated segments were optimised at this level of theory, to locate their minimum energy conformations (featuring 'flipped' dihedrals in the case of C and D). As before, no further optimisation was performed after arranging the segments into contact structures.

The interaction maps constructed for variants A and D are shown in Figure 7.5. These were chosen

[2] For backbones containing multiple 2mer segments, the IDTBT, A, and B backbones are still linear on larger scales.
[3] A discussion of the expected contribution of entropy to the free energy is may be found in Section 6.2.1.

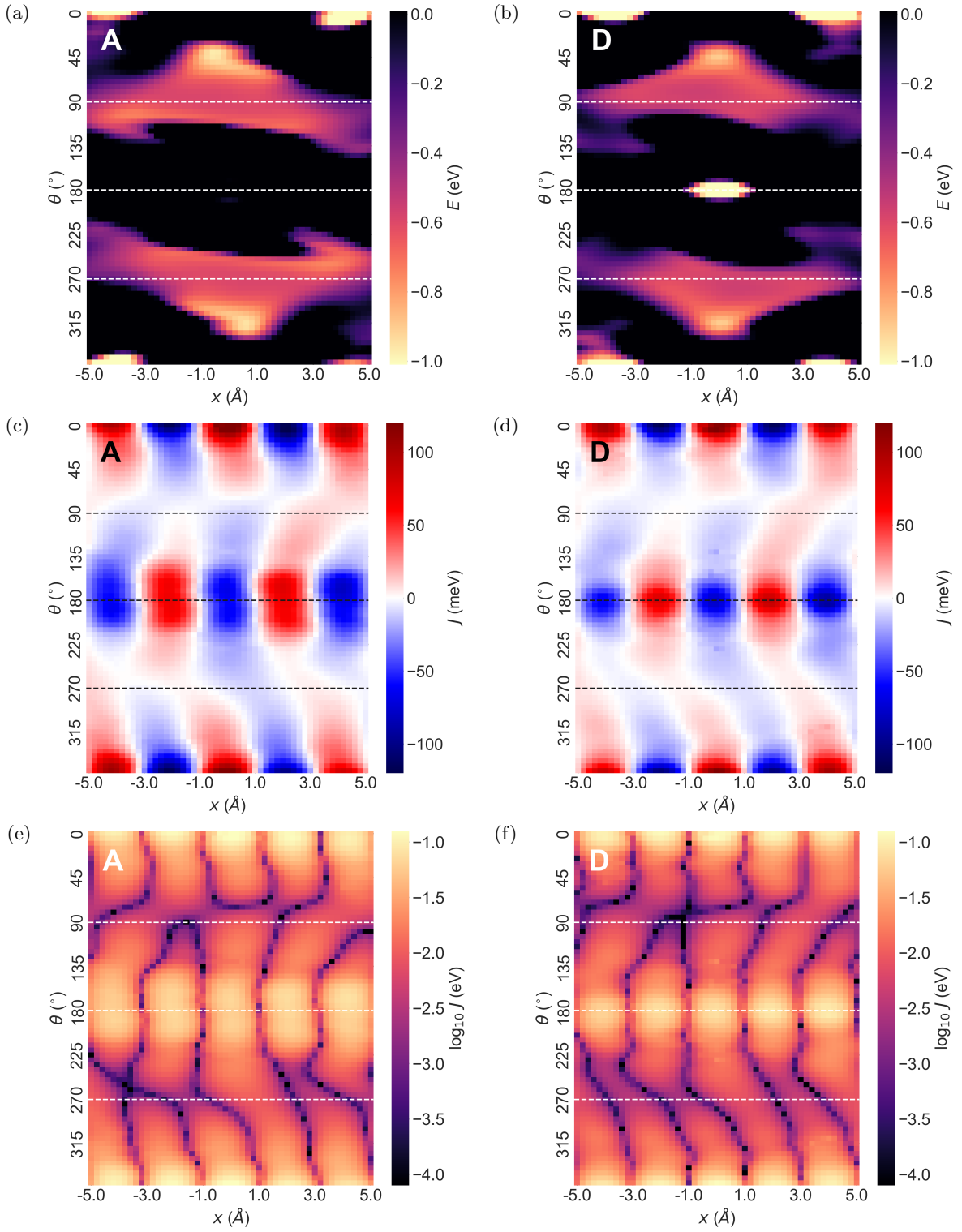


Figure 7.5: Maps displaying the enthalpic interaction energies (E) and hole transfer integrals (J_{inter}) between a pair of 2mer segments with methyl side groups. Each pixel on the map represents a different arrangement, with the upper chain being shifted by x in the backbone direction of the lower chain and rotated in-plane by θ. Dashed lines represent parallel and perpendicular arrangements of the segments. See Figure 6.1 for further explanation. The left column shows interactions between variant A segments, while the right column shows interactions between variant D segments. The first row shows E maps. The second row shows J_{inter} maps with a linear scale. The third row shows J_{inter} maps with a logarithmic scale.

as representatives since similar results were observed within the group featuring an 'upright' dihedral (IDTBT, A, B), and the group featuring a 'flipped' dihedral (C, D). Interaction maps for the other variants (except LUMO-LUMO coupling) may be found in Appendix B.3. All LUMO-LUMO coupling maps may be found in Appendix B.4.

The E maps for all variants are broadly similar to that of IDTBT (see Figure 6.2a), suggesting that the variants are also likely to display perpendicular crossing arrangements in the solid state. This shared behaviour is understandable based on my analysis indicating that the IDTBT crossing motif is promoted by the angle and position of the side groups on the donor, and the unadorned acceptor unit (Section 6.2.1). In these aspects of the chemical structure, the variants are unchanged from IDTBT. Combined with the rigidity of the backbones, suggested by the torsional potential results (Section 7.2.2), this preference for perpendicular contacts implies that the variants are likely to form microstructures with a high degree of interconnectivity, similar to IDTBT (see Section 5.2.6).

One feature present only on the the C and D interaction energy maps is a bright spot ($E < 0\,\text{eV}$) centred on $x = 0$, $\theta = 180°$. The presence of this spot indicates that the 'flipped dihedral' variants are able to pack in a stable antiparallel arrangement. This arrangement is shown on the right-hand side of Figure 7.6. The left-hand side of Figure 7.6 reveals how clashes between the side groups and backbones prevent the stable packing of IDTBT, and the other variants featuring an 'upright' dihedral, in a similar antiparallel arrangement.

Following the same argument given in Section 6.2.1, the small regions of negative interaction energy corresponding to parallel and antiparallel backbone arrangements are unlikely to be important for governing the types of contacts that form in physical microstructures. As before, this is on the basis that these small regions of enthalpic stability are likely to be entropically disfavoured, which will be more so the case for longer chain lengths. This argument was previously verified by the low occurrence of parallel contacts, compared to perpendicular contacts, in MD microstructural models of C16-IDTBT (see Section 5.2.5).

The coupling maps for all variants are broadly similar to that of IDTBT (see Figures 6.2c and 6.2d). One minor distinction is that the width of the bright horizontal bands (representing stronger coupling values), centred on 0° and 180°, are slightly reduced for C and D compared to the other variants

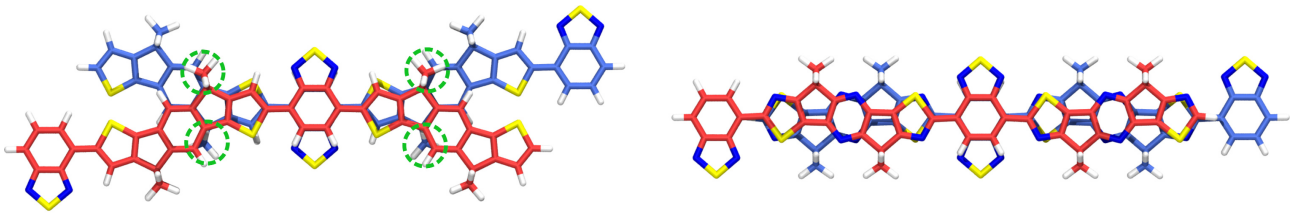


Figure 7.6: Top-down views of contacting segments of IDTBT (left) and variant D (right) in antiparallel arrangements ($x = 0$, $\theta = 180°$). Instances of clashes between the side groups and backbones for the IDTBT pair are circled in green. Carbon atoms in the upper and lower segments have been coloured red and blue respectively, to help distinguish them.

and IDTBT. This is likely related to the slight curve of the backbone present in the minimum energy conformation of IDTBT, A, and B, compared to the straight backbones of C and D. As stated, however, I do not expect these (anti)parallel arrangements, or their corresponding coupling strengths, to be common in physical or modelled microstructures of the polymers.

7.2.4 Thermal Distributions of Contact Arrangements

If we assume that the chain segments may only adjust their relative positions according to the degrees of freedom covered by the interaction maps (x and θ), then the E values can be used to assess the probability of finding a given contact in one of the evaluated geometries. For each polymer, I computed the probability of each contact geometry by inputting its associated E into a Boltzmann distribution, with system temperature set to 300 K. Before calculating the probabilities, I modified the interaction energies in order to neglect the energetic wells associated with some parallel and antiparallel backbone arrangements. This was done by locating all contact geometries with θ within $\pm 15°$ of $0°$ or $180°$, and setting any negative interaction energies to zero. I justified this on the basis that these arrangements rarely appeared in MD microstructural models of C16-IDTBT (see Section 5.2.5), implying that there is some effect preventing their formation in realistic microstructures (likely relating to the length of backbones or side chains). The calculated probabilities for different contact geometries of IDTBT, A, and D are visualised as maps in the left-hand column of Figure 7.7.

From Figures 7.7a, 7.7c, and 7.7e, we can observe that there is a high likelihood for contacts to be arranged in a relatively narrow range of geometries, indicated by deep red areas on the maps. Notably, these geometries tend to feature θ of $\sim 45°$ and $\sim 315°$, and are not, therefore, closely aligned with the perpendicular contacts that were most commonly represented in MD models of C16-IDTBT microstructures (see Section 5.2.5). This discrepancy may be related to the side groups used for these calculations versus those in the MD simulations. From the simulations of contacting pairs of IDTBT chains on substrate (Section 5.2.1), we saw how longer side chains tended to promote a narrower distribution of θ around the perpendicular. Shorter side chains appear to less tightly constrain the backbones in a perpendicular arrangement, which may allow contacts to locate energetically favourable geometries over a broader range of θ. Another contributing factor could relate to the limited degrees of freedom covered by these interaction maps. Additional E maps (computed using forcefields), representing IDTBT contact geometries with the upper chain segment also translated in the y-direction (orthogonal to x and the conjugated planes), may be viewed in Appendix B.2. These indicate that the regions of negative interaction energy tend to become more restricted around the perpendicular for contact geometries featuring non-zero translations in y.

The thermally-distributed probabilities assigned to each contact geometry can also be assigned to the J_{inter} values associated with those geometries. Figure 7.8 shows probability-weighted distributions of J_{inter} for each of the variants, plus IDTBT. A similar distribution of LUMO-LUMO coupling values

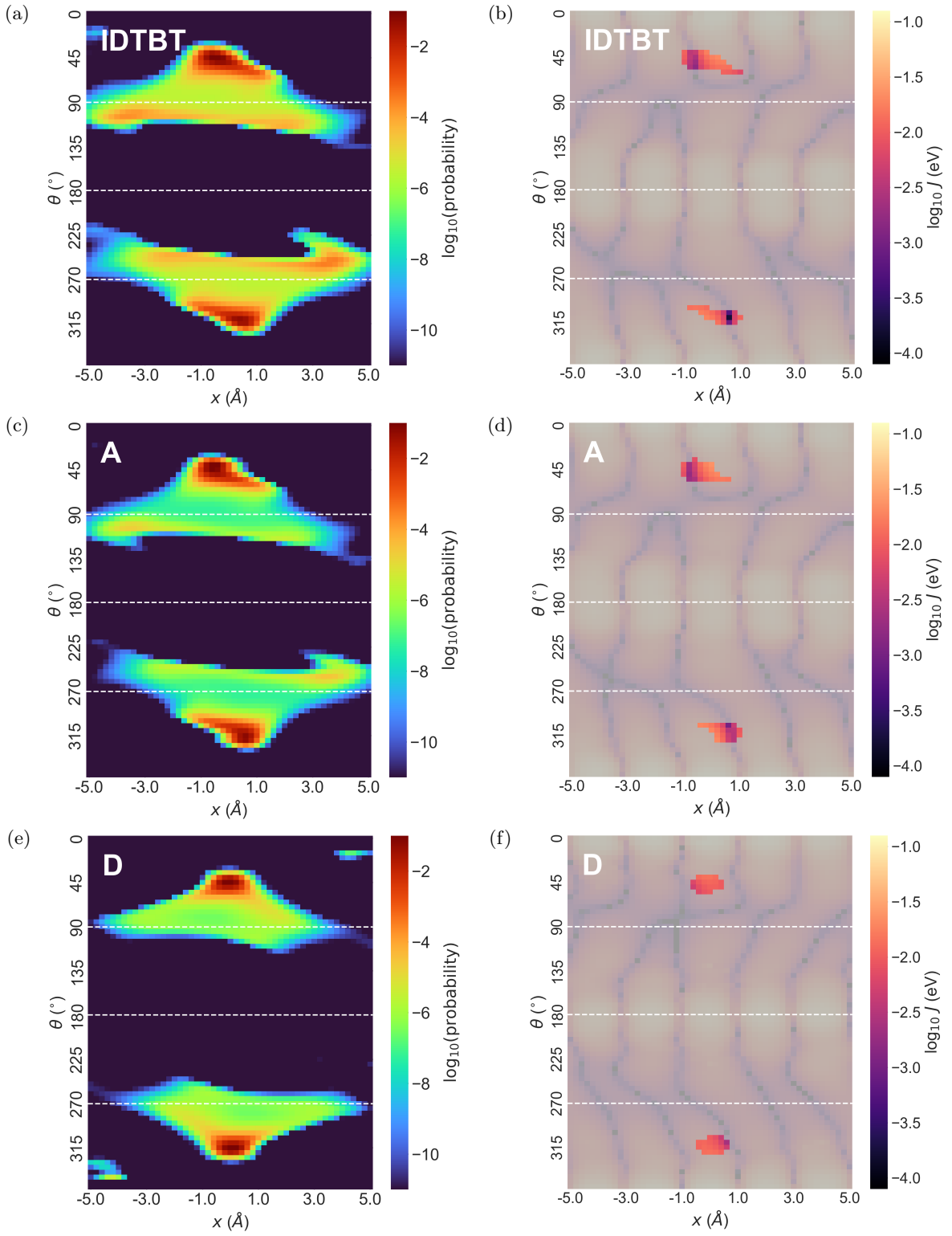


Figure 7.7: Maps displaying the thermally-distributed probability of contact geometries (left column) and hole transfer integrals (J_{inter}) (right column) between a pair of 2mer segments with methyl side groups. Each pixel on the map represents a different arrangement of the chain segments, with the upper segment being shifted by x in the backbone direction of the lower segment and rotated in-plane by θ. Dashed lines represent parallel and perpendicular arrangements of the segments. See Figure 6.1 for further explanation. The first row shows maps corresponding to IDTBT, while the second and third rows correspond to variants A and D, respectively. Pixels in the coupling maps are reduced in saturation ('greyed out') for contact arrangement with probabilities $< 0.1\%$. The probabilities of some parallel and antiparallel arrangements have been reduced, to focus on perpendicular arrangements.

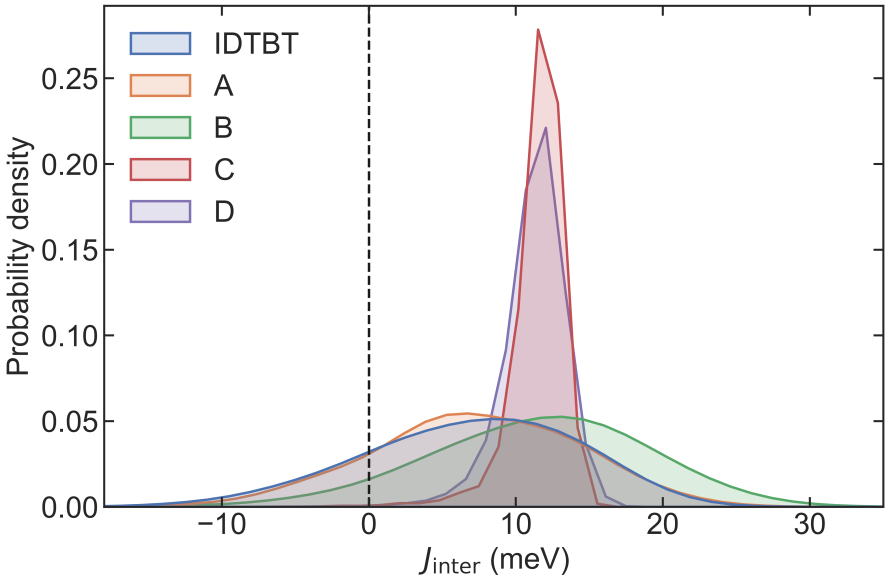


Figure 7.8: Distribution of HOMO-HOMO coupling strengths (J_{inter}) for pairs of contacting IDTBT segments, and variants. Contributions of different J_{inter} values are weighted according to the probability of finding the system in the arrangement which establishes that J_{inter}.

may be seen in Appendix B.9. We can observe that the distributions fall into two distinct groups, which align with whether the minimum energy conformation of the individual segments features the donor-acceptor dihedral in its 'upright' (IDTBT, A, and B), or 'flipped' orientation (C, D). The 'upright' group all show a relatively broad distribution of J_{inter}. Within this group, B appears to show higher J_{inter} values than IDTBT or A. The polymers in the 'flipped' group also show J_{inter} values distributed around a mean higher than that of IDTBT and A. However, the most distinct feature of this group is the far narrower range over which J_{inter} values are distributed.

We can identify the reason for this narrow range of J_{inter} by considering the coupling maps shown in the right-hand column of Figure 7.7. Here, I have plotted the coupling maps while reducing the saturation of (i.e., 'greying out') pixels representing contact geometries with probabilities $< 0.1\%$. In the case of IDTBT and A (Figures 7.7b and 7.7d, respectively), we observe that the saturated regions, representing the most probable contact geometries, are coincident with nodes in the J_{inter} values (dark lines). This may be contrasted with variant D (Figure 7.7f), for which we see that the saturated regions are located at positions of relatively constant, positive J_{inter}.

7.3 Conclusions

These results suggest that the heteroatom-substituted variants may exhibit similar microstructural features to C16-IDTBT, assuming the same choice of side chains. In particular, the torsional potentials calculations (Section 7.2.2) suggest that the variants will also have rigid and planar backbone conformations, while the interaction energy maps (Section 7.2.3) indicate that they are likely to adopt a similar perpendicular crossing motif at contacts. From my earlier analysis, this combination of fea-

tures was identified as one of the contributing factors to the high hole mobility (μ) of C16-IDTBT, since together they promote the formation of a highly interconnected transport network.

Compared to IDTBT, the variants *C* and *D* were found to have torsional potentials between the donor and acceptor units that even more strongly stabilised the backbones in a planar conformation. This may indicate support for faster intrachain transport in these polymers than IDTBT.

The results further suggested that, for a thermal distribution of contact geometries, the interchain coupling values established by variants *C* and *D* would be slightly higher on average, and fall within a much narrower range than those of IDTBT (Section 7.2.4). It is possible that this could translate into a lower susceptibility to the effects of dynamic coupling disorder, which may lead to improved interchain charge transport in these polymers [11, 57, 68, 69]. However, this latter point should be considered in light of the fact that the contact geometries associated with this narrow range of coupling values were somewhat distinct from the geometries typically observed in MD simulations of C16-IDTBT, which may be more representative of the those we can expect to be present in physical thin films (see Section 5.2.5). Furthermore, as discussed in Section 5.2.1, long side chains may also contribute to this 'contact locking' effect by sterically restricting the backbones in a perpendicular arrangement. Since the location and bond angle of the attached side chains is the same between all variants and C16-IDTBT, the contribution of side chains to this effect would likely be similar.

Nevertheless, these characteristics (a similar microstructure, higher intrachain mobility, and more stable interchain coupling) imply that the variants *C* and *D* could potentially achieve a higher hole μ than IDTBT.

This evaluation may be contrasted with the low experimental $\mu = 4 \times 10^{-5}\,\mathrm{cm}^2/\mathrm{Vs}$ displayed by C16-IDTzBT [170], which, as stated, features a similar chemical structure to variants *C* and *D*. Nikolka et al. hypothesised that the low μ of C16-IDTzBT could relate to a higher charge injection barrier in the measured FET device, caused by the deeper HOMO level of the polymer compared to C16-IDTBT (see Figure 7.2). However, they concluded that this could not be the only reason, since another analogue (IDTDTBT) showed a much less pronounced decrease in μ ($6 \times 10^{-2}\,\mathrm{cm}^2/\mathrm{Vs}$), despite having a similar HOMO level to C16-IDTzBT.

Another potential factor in the low μ of C16-IDTzBT may relate to the variant *C* and *D* results presented here. In particular, if C16-IDTzBT shares a similarly rigid backbone to *C* and *D* (see Section 7.2.2), this could potentially have an adverse effect on measurements of bulk μ, despite its likely benefits to intrachain transport The STM results in [150] indicated that allowing for some degree of backbone flexibility was useful for facilitating higher amounts of contact formation, which may therefore be reduced in C16-IDTzBT, as well as *C* and *D*. Furthermore, an overly rigid backbone may limit the solubility of these polymers, potentially restricting the chain lengths achievable during synthesis, and negatively affecting film formation. Wadsworth et al. hypothesised that low solubility could be the reason for the lower experimental mobilities [170] displayed by another IDTBT variant

(with a fluorinated acceptor unit), for which theoretical calculations also predicted a more rigidly planar backbone [158, 172]. For C16-IDTzBT, this effect on chain length may be evidenced by the low molecular weight (M_W) of the polymer sample used in [170] ($10\,\mathrm{kg\,mol^{-1}}$, corresponding to ∼8mers). By comparison, a $\mu = 0.75\,\mathrm{cm^2/Vs}$ was measured by Zhao et al. for a low M_W C16-IDTBT sample ($25.1\,\mathrm{kg\,mol^{-1}}$, ∼19mers) [91], while the charge transport simulations described in Section 6.2.3 predicted $\mu = 0.17\,\mathrm{cm^2/Vs}$ for C16-IDTBT 12mers. While these chain length are still longer than in the C16-IDTzBT sample, the fact that there remains a several order-of-magnitude difference between the μ values suggests that another explanation may be required to explain the dramatic decrease brought about by including thiazole moieties on the donor unit in this case. Investigating this, and assessing whether any of the same issues apply to variants C and D, would be an interesting topic for further study (see Section 9.2.5).

In contrast to variants C and D, the results of the analysis presented in this chapter suggest that the variants A and B would show similar transport behaviour to IDTBT.

Synthesising the variants, and subjecting them to experimental mobility measurements, would allow these evaluations to be tested.

Chapter 8

Disorder and Transport in O-IDTBR

I describe an investigation into the non-fullerene acceptor molecule O-IDTBR. I detail insights gained from my work, and that of collaborators, into the mechanisms and speed of electron transport, and how these are governed by material microstructure and energetic disorder. We find that transport proceeds via a transient delocalisation mechanism in crystalline structures, and via localised hopping in disordered thin film structures. We identify electrostatic-induced energetic disorder as the dominant factor governing transport in thin films, and link this to a chemical structural origin, namely the soft dihedral between acceptor and donor units making up the O-IDTBR core. This work has been published in Physical Review X *[60].*

8.1 Introduction

The development and use of NFA molecules led to a step-change in the performance of OPV devices [183, 184], with current devices able to achieve power conversion efficiencies > 19% [185]. This has been enabled by precise control over the photophysical properties of NFA molecules, such as their absorption spectra and MO energy levels. This control stems from the use of an alternating acceptor (A) and donor (D) unit molecular construction, typical to most NFAs. In this study, we investigated one of the first successful NFAs, O-IDTBR [186], which features an ADA core composed of the acceptor units BT and rhodanine, and an IDT donor unit.

Although highly beneficial to their optical properties, the effect of this ADA construction motif on charge transport properties is less well understood. Compared to other small molecule OSCs, NFAs often display higher levels of conformational and packing disorder that can hamper electron transport. This structural disorder is in turn thought to arise from chemical-structural features, in particular a relatively soft dihedral between the A and D units, which reduces the conformational rigidity of the molecules [121, 152]. Conformational and microstructural disorder is likely to produce electronic structural disorder, affecting transport in some systems. In particular, it is likely to effect the electronic coupling between molecules in the solid state, and may lead to energetic disorder arising from

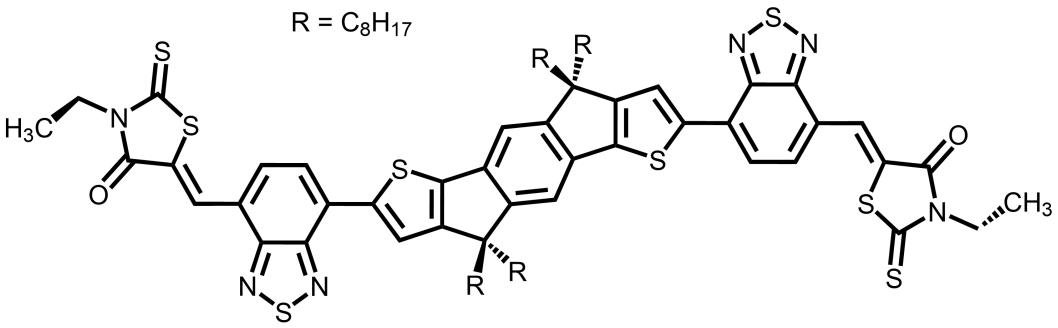


Figure 8.1: Chemical structure of O-IDTBR.

the different electrostatic potential experienced by an excess electron localised on each molecule [50].

The degree of electronic structural disorder not only affects the rate of electron transfer between molecules, but also determines the mechanism of electron transport. In Section 2.4.2, I introduced an intermediate transport regime in which charge transport proceeds via a transient (de)localisation mechanism. Past experiments and simulations have indicated that this transport mechanism is utilised in other, high-mobility, small molecule OSCs [57–59, 187]. However, in these examples, molecules tend to be more rigid, and display more crystalline microstructures, compared to NFAs such as O-IDTBR.

With the above in mind, the following questions remain about the relationship between chemical structure, microstructure and electron transport in O-IDTBR:

- Does transport in the crystalline regions of the O-IDTBR microstructure proceed via a transient delocalisation or localised-electron hopping mechanism? Does this mechanism carry over to the disordered regions?

- How does the transport mechanism, and other related factors such as energetic disorder, alter the electron mobilities predicted in the crystalline and disordered regions of the O-IDTBR microstructure?

- What is the chemical-structural origin of factors governing the mobility in O-IDTBR, and other similarly-constructed NFAs?

To address these questions, I carried out a series of KMC charge transport simulations on crystalline and disordered thin film models of O-IDTBR.

Here, I briefly outline the contributions of my coauthors to this study. A crystalline microstructural model of O-IDTBR was sourced from a previous study [188], while a thin film model was produced, using MD, by Anders S. Gertsen (using an atomistic version of the procedure summarised in Section 5.1 [121, 152]). My simulations, performed on these models, were compared against quantum-classical non-adiabatic MD transport simulations performed by Ljiljana Stojanović on the same models, using the code `FOB-SH` [74, 189, 190]. Both sets of simulation results were then compared against SCLC experiments carried out by Jun Yan. `FOB-SH` is able to simulate, and distinguish between, different

mechanisms of electron transport, but is limited in its ability to factor in intermolecular contributions to energetic disorder and reorganisation energy. Since we suspected that these effects could be significant in structurally disordered microstructures, my collaborators Samuele Giannini, Giacomo Londi, and Gabriele D'Avino evaluated the energetic landscape of the thin film system using the microelectrostatics model `MESCal` [50, 51]. Results from `MESCal` could then be used to parameterise the KMC simulations. Further methodological details and results from these contributions will be provided in Sections 8.2 and 8.3.

My contributions to this investigation are described over the remainder of this chapter. Here, I briefly outline my results and analysis, and how these were used to address the research questions listed above:

- In Section 8.3.1, I compare the results of KMC simulations performed on crystalline and disordered thin film structures, to understand the effect of microstructure on electron mobility. These results are further compared against `FOB-SH` simulations to probe the mechanism of transport in these systems, and understand the effect of transport mechanism on mobility.

- In Section 8.3.2, I compare the results of KMC simulations performed on thin film structures with, and without, intermolecular contributions to energetic disorder and reorganisation energy. Results are further compare against SCLC experiments. Analysis of these results is used to understand the factors governing mobility in realistic O-IDTBR microstructures, and to understand the chemical-structural origins of these factors.

Using these results, and those of my collaborators, we sought to provide a picture of the transport behaviour of electrons in O-IDTBR, and rationalise the transport characteristics displayed by this material and similar NFAs, based on their shared chemical- and micro-structural characteristics.

In the concluding section (Section 8.4), I discuss how insights gained from this study may aid in the development of new NFAs with superior electron transport properties, and thus more efficient OPV devices.

8.2 Method

A crystalline microstructural model of O-IDTBR was taken from [188], where the packing arrangement of molecules had been solved by X-ray crystallographic analysis. The crystal structure is shown in Figure 8.2. A thin film model was produced by Anders S. Gertsen, using the MD solution-evaporation deposition procedure introduced in Chapter 5. For this study, atomistic forcefields were used to represent the O-IDTBR and solvent (chloroform) molecules, as well as an explicit SiO2 substrate [121, 152]. Both systems were converted to a site representation by locating the CoGs of molecules.

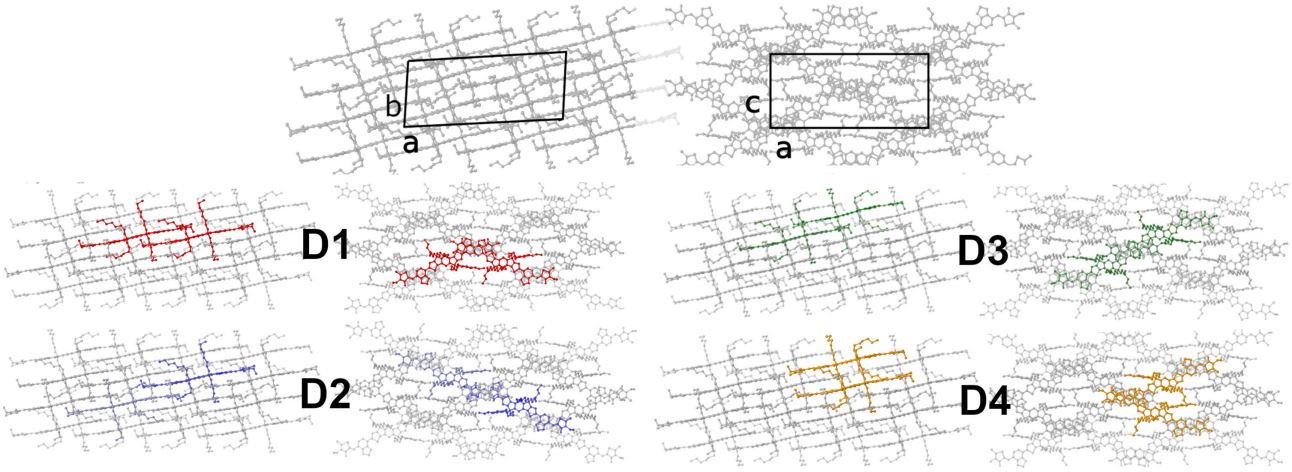


Figure 8.2: Crystal structure of O-IDTBR, shown from two projections. The unit cell is shown in the top row. In the following rows, molecule pairs (D) establishing the four largest electronic couplings are highlighted. With permission from Ljiljana Stojanović, this image has been adapted from [60], and is based on a structure from [188].

Electronic coupling strengths (J) in both systems were computed by my coauthors using the analytic overlap method and projector-operator-based diabatization method, as described in [60]. Instantaneous values ($J(t)$) were used in the `FOB-SH` simulations carried out by my coauthors. However, for the KMC simulations, I used thermally-averaged values, calculated by

$$J_{ij} = \sqrt{\langle J_{ij}(t)^2 \rangle},$$

for the electronic coupling between molecules i and j. Time-averaging was performed across multiple `FOB-SH` trajectories, which were themselves initiated from time-separated snapshots of an MD trajectory of the dry film (performed by Ljiljana, by continuing from the structure produced by Anders in the case of the thin film system). This averaging is appropriate for the hopping mode of transport, which assumes the thermal relaxation of molecules between hopping events, and, therefore, that the timescales of hopping are slower than the timescales of thermal fluctuations (and reorganisation, see [54] and Section 2.3.2). In this study, we validated this assumption for the thin film by comparing the timescales of hopping with the timescales of the intramolecular modes involved in reorganisation, which were calculate by BSc student George Su. This comparison is depicted in Figure 8.3, where we observe that the vast majority of hopping rates are indeed slower.

KMC transport simulations were performed using `ToFeT`. The J values indicated that the crystal system is relatively non-transporting in the c-crystallographic direction. As such, transport was only evaluated in the a and b directions (see Figure 8.2). These were aligned with the fixed field direction (z) imposed by `ToFeT` by rotating the system so that a or b coincided with z. During crystal simulations, PBCs were in place for all directions. For the thin film system, no couplings were computed for molecule pairs separated by the z-boundary of the MD model, so transport was only evaluated for the

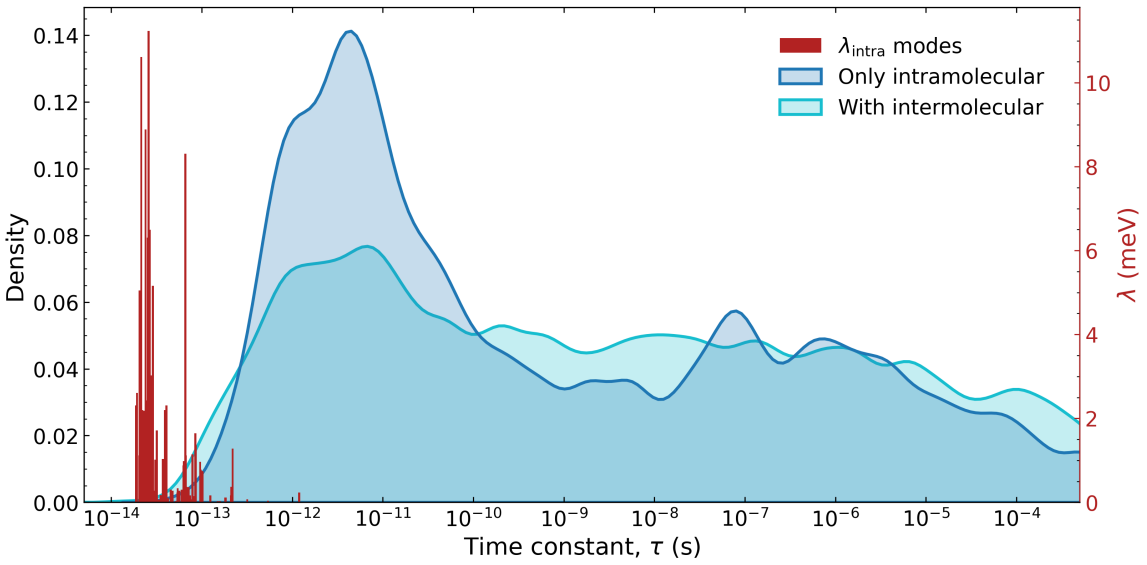


Figure 8.3: Comparison between timescales of hopping (smoothed distributions) and intramolecular reorganisation modes (red lines) in the O-IDTBR thin film system. Hopping timescales are shown with and without intermolecular contributions to site energies (ϵ) and reorganisation energy (λ).

in-plane x- and y-directions (corresponding with SCLC and FET experiments), again by rotating the system. During simulations, PBCs were in place for both x and y.

Site energies (ϵ) were set to zero for all sites in the crystal. This was on the basis that the electrostatic potential at all molecular sites was similar (verified by my collaborators using MD simulations with Ewald electrostatics applied), and contributions to ϵ from intramolecular vibrations thermally averaged to the same value for all molecules. In the disordered thin film, the electrostatic environment of molecules can vary significantly. For this reason, ϵ values were set based on calculations performed using the microelectrostatics model `MESCal`. The thermally-averaged contributions to ϵ form an approximate Gaussian distribution, with width $\sigma_\epsilon = 159\,\text{meV}$.

The reorganisation energy (λ) may be separated into intramolecular (λ_{intra}) and intermolecular (λ_{inter}) terms. λ_{intra} was found by my collaborators to have a value of 180 meV using the four-point method, aligning with the value of 182 meV found by normal mode analysis (see Figure 8.3). For the crystalline system, I neglected the λ_{inter} term in order to ease comparison between the KMC and `FOB-SH` simulations, which only include λ_{intra}. For the thin film, λ_{inter} can be significant. From the `MESCal` calculations, a value of $\lambda_{\text{inter}} = 80\,\text{meV}$ was found, representing the adaption of the environmental charge density when the conformation of a molecule changes from it's neutral geometry to charged geometry [60]. Combining the two contributions led to a total $\lambda = 260\,\text{meV}$. I ran transport simulations on the thin film both with and without the intermolecular electrostatic contributions to ϵ and λ, for comparison.

A single mobile electron was simulated at a time, initially generated on a random site for each run. The system temperature was set to 300 K, while the external field strength was set to $1 \times 10^4\,\text{V cm}^{-1}$. Simulation results for the crystalline and thin film systems are described below.

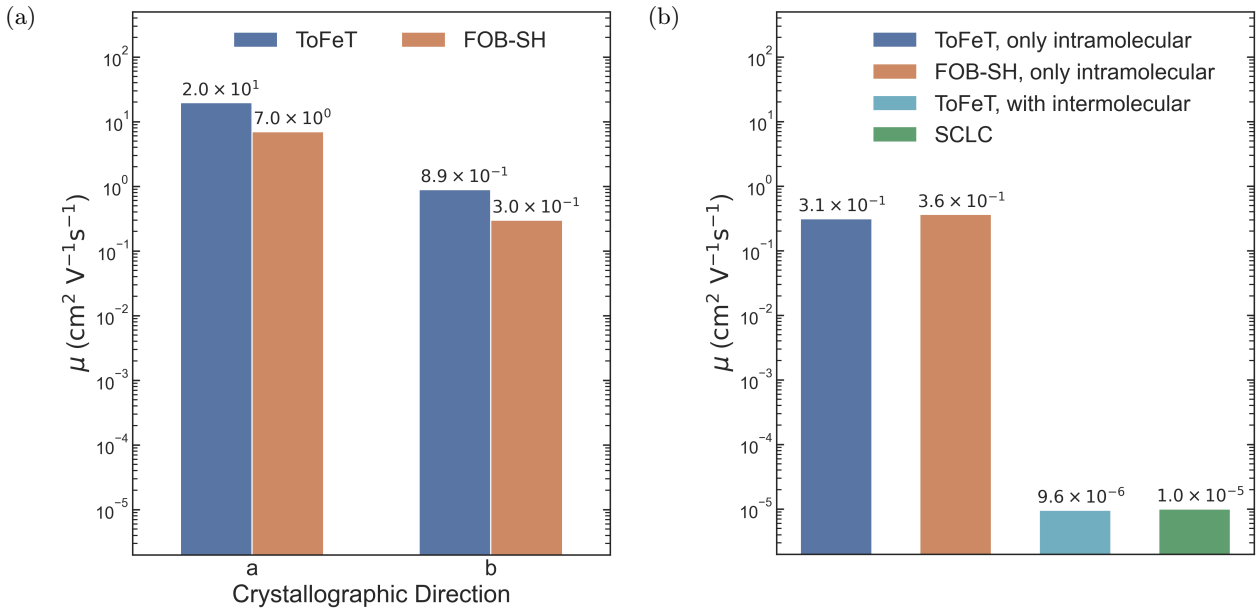


Figure 8.4: (a) Simulated electron mobilities for the crystalline O-IDTBR structure. (b) Simulated and experimental mobilities in disordered thin films of O-IDTBR.

8.3 Results

8.3.1 Effect of Microstructure on Transport

Figure 8.4a shows the mobilities (μ) calculated by `ToFeT` for the crystalline system, in comparison with those found by `FOB-SH`, while neglecting intermolecular contributions to ϵ and λ. Transport was found to be highly anisotropic, with `ToFeT` calculating $\mu = 20\,\mathrm{cm}^2/\mathrm{Vs}$ and $0.89\,\mathrm{cm}^2/\mathrm{Vs}$, for the a- and b-directions respectively. This is expected, given that two strongly coupled molecule pairs ($J = 96\,\mathrm{meV}$ and $46\,\mathrm{meV}$, labelled D1 and D2 on Figure 8.4a) form the transport pathway in a, while the b-pathway is periodically interrupted by a weakly coupled molecule pair ($J = 0.2\,\mathrm{meV}$, labelled D3 on Figure 8.4a).

There is some discrepancy between the μ values predicted by `ToFeT` and `FOB-SH` in the crystal, with `ToFeT` predicting values 3× larger than `FOB-SH`. At present, it is not possible to verify these experimentally, because fabricated samples of O-IDTBR do not generally form single crystals. However, we can assume that the `FOB-SH` results are more accurate in this instance. This is because the electronic structure parameter values place us outside the perturbative regime ($J \ll \lambda$) assumed by the Marcus model (see Section 2.3.2). The fact that `ToFeT` predicts higher μ than `FOB-SH` in this case is understandable in light of a previous study carried out by Spencer et. al, in which they showed that the Marcus equation tends to overestimate electron transfer rates when it is inappropriately applied in the adiabatic regime [75].

Figure 8.4b displays the μ computed by `ToFeT` for the thin film system. For now, I focus on the results computed without intermolecular contributions to ϵ and λ. Compared to the crystalline system,

μ in the thin film is predicted to be significantly lower, at $\mu = 0.31\,\mathrm{cm}^2/\mathrm{Vs}$. This is expected, since the J values were found to be lower than in the crystal. Although instances of high J exist between some molecule pairs, they are not widespread enough to form percolating pathways, so transport is limited by instances of lower J. My coauthors found that the average number of molecules in pathways connected by $J \geq \lambda/10$ (18 meV) was only 8, for a system of 234 molecules.

The relatively low J values suggest that we can have more confidence in the μ predicted by `ToFeT` for the thin film system than in the crystal. This is corroborated by the similarity between the μ values calculated using `ToFeT` ($0.36\,\mathrm{cm}^2/\mathrm{Vs}$) and `FOB-SH` ($0.31\,\mathrm{cm}^2/\mathrm{Vs}$). Unlike in the high-$J$ regime, electron transfer rates measured from `FOB-SH` simulations have been shown to converge with those calculated by the Marcus equation, when applied in the appropriate non-adiabatic regime [75]. In this case, my coauthors were able to provide further direct evidence justifying the hopping mechanism assumed by `ToFeT`. They calculated the inverse participation ratio of the electron wavefunction during `FOB-SH` simulations, finding that the electron rarely delocalises over more than 1 to 1.5 molecules.

In summary, I have described the results of KMC electron transport simulations carried out on crystalline and thin film structures of O-IDTBR (while neglecting intermolecular contributions to ϵ and λ, which is likely to affect transport in the thin film. See following section). Switching from a crystalline to a disordered microstructure results in a two order-of-magnitude drop in μ from the fastest transport direction in the crystal. Comparison with `FOB-SH` simulations indicated that one of the factors contributing to this large decrease was an overestimation of μ in the crystalline case, due to the inappropriate application of the Marcus rate equation in the the adiabatic regime. The lower J-values in the thin film meant we could be more confident that transport was in the non-adiabatic regime. This led to a good correspondence between the μ values calculated by `ToFeT` and `FOB-SH`.

8.3.2 Impact of Energetic Disorder on Transport

Figure 8.4b shows the results of `ToFeT` simulations performed on the thin film structure, with and without the inclusion of intermolecular contributions to ϵ and λ. μ is observed to fall dramatically, by five orders of magnitude, when intermolecular contributions are included.

With intermolecular contributions, the simulated μ ($9.6 \times 10^{-6}\,\mathrm{cm}^2/\mathrm{Vs}$) corresponds closely with the experimental μ (between $1 \times 10^{-5}\,\mathrm{cm}^2/\mathrm{Vs}$ and $2 \times 10^{-5}\,\mathrm{cm}^2/\mathrm{Vs}$), measured by SCLC. The SCLC μ was evaluated by fitting a drift-diffusion model with a distribution of site energies to the experimental J-V data. In this regard, the best fit was found by applying a Gaussian distribution of energies, with a width of 150 meV, which may be compared with $\sigma_\epsilon = 159$ meV calculated by `MESCal`. To add to this, SCLC experiments are operated under a low charge injection regime, relative to the more commonly applied FET method. This aligns with the low charge density regime of the simulations, meaning that transport in both cases is highly sensitive to the energetic landscape presented by the LUMO energy levels of molecules. On this basis, the close alignment between the simulated and experimental

μ is therefore understandable; In both situations, transport appears to be dominated by the effect of energetic disorder. For the KMC model, this was confirmed by running simulations with only the intermolecular electrostatic contribution to λ included, which resulted in μ decreasing by a factor of three, a much smaller effect than the several order-of-magnitude drop caused by the introduction of energetic disorder.

It is worth noting that, in previous studies, reported μ values from SCLC measurements of O-IDTBR have been slightly larger [191], corresponding less precisely with the μ computed here. These higher experimental μ values likely result from measurements performed on films that have undergone thermal annealing. This is a common processing technique applied following film deposition, and is intended to enhance the μ of films by increasing their crystallinity. In the study described here, the SCLC measurements were performed on deliberately non-annealed thin films, so that their microstructures would better match the MD model.

In our model, the energetic disorder arose from the different strength of collective electrostatic (i.e. Coulombic) interactions experienced by an excess electron, when it is localised on each of the molecules in the material. Variations in the electrostatic potential originate from variations in the local charge density throughout the material. How charge density is distributed through the system depends on 1) the position and conformation of neutral molecules (treating them in isolation i.e., in their gas phase), 2) rearrangement of the charge density (polarisation) due to the interactions between neutral molecules, and 3) a further rearrangement due to the inclusion of an excess charge (induction). In the O-IDTBR thin film system, significant variations in the local charge density originated from structural disorder in the position, orientation and conformation of molecules. The degree of conformational disorder was assessed by my collaborators, by calculating the torsional angles between IDT and BT units, which were found to adopt a broad bimodal distribution. The effect this had on local charge density is exacerbated by the presence of several heteroatoms on the IDT, BT, and rhodanine units of the molecule.

In summary, I have described the results of KMC electron transport simulations carried out on a thin film model of O-IDTBR, with the inclusion of energetic disorder and λ_{inter} calculated using the microelectrostatics model `MESCal` [51]. I compared these with results from simulations without the intermolecular electrostatic interactions, showing that, in the more realistic system, charge transport is dominated by the effect of the disordered energetic landscape. This premise was validated by comparing the computed μ against SCLC experiments, performed on a similar disordered microstructure, and operating in a similar low charge density regime. With respect to more sophisticated transport simulation techniques such as `FOB-SH`, the utility of the KMC approach was demonstrated by the capacity to easily include information provided by other methods, such as microelectrostatics calculations.

8.4 Conclusions

In conclusion, I carried out KMC charge transport simulations to evaluate electron transport in the non-fullerene acceptor material O-IDTBR. Results were compared against quantum-classical non-adiabatic MD transport simulations and experimental measurements of mobility. I found that electron mobilities decrease significantly when switching from a crystalline to a disordered thin film microstructure, due to the decreased in coupling between molecule pairs that this entails. Comparison with `FOB-SH` simulations further indicated that this decrease in coupling led to a change in the mechanism of electron transport between the two systems. Transport in the crystal occurred via a transient delocalisation mechanism, while transport in the thin film occurred via localised-electron hopping. The KMC simulations were well suited to capturing transport behaviour in the latter case, but were limited in their ability to capture the former, leading to an overestimation of the electron mobility. Thus, we provided a case study demonstrating the circumstances under which it is appropriate to model transport using Marcus-rate parametrised KMC, and the consequences of applying it incorrectly.

Confounding the lower coupling strengths and consequent change in transport mechanism, my results indicated that the largest factor governing electron mobility in thin films was the presence of significant electrostatic-induced energetic disorder. This originates from the different electrostatic potential experienced by an excess electron localised on each molecular site, which is in turn established by variation in the charge density throughout the material due to disorder in the conformation, location and orientation of molecules. Introducing energetic disorder into the KMC model caused a dramatic five order-of-magnitude drop in the electron mobility.

The dominating effect of energetic disorder was supported by the agreement between the simulated mobilities and experimental mobilities, extracted from SCLC measurements. Both the simulations and experiments operated under the low charge density regime, and were therefore sensitive to the influence of the energetic landscape. In both cases, the electron mobilities were found by applying a similar degree of energetic disorder, with a Gaussian width of $\sim$150 meV.

A significant degree of the electrostatic-induced energetic disorder in the thin film was linked to conformational disorder arising from the soft dihedral between the acceptor (A) and donor (D) units of the molecule. It is therefore likely that insights gained from this study, namely the transport-limiting effect of electrostatic-induced energetic disorder, could apply to other NFAs featuring an A-D-A or A-DAD-A core. Greater rigidity between the A and D units and/or greater crystallinity would therefore be expected to reduce energetic disorder and improve electron mobilities in these materials. This may be one reason why other NFAs, such as Y6, exhibit higher mobilities than O-IDTBR.

Although it serves a very different role as a donor polymer, it is worth highlighting that the conjugated polymer C16-IDTBT, discussed in Chapters 5 and 6, is composed of two of the same A and D units as O-IDTBR. Unlike O-IDTBR, however, the dihedral linking these units is notably more rigid

in C16-IDTBT. This has been linked to the fact that the polymer displays near energetic-disorder free hole transport [86]. In Chapter 6, the effect this had, particularly on intrachain transport, was identified as one of the reasons for the high hole-mobility displayed by C16-IDTBT. A comparison between these two materials further exemplifies the crucial importance of conformational control (alongside the coupled parameter of microstructural control) when it comes to designing new high-mobility OSCs.

Chapter 9

Conclusions and Outlook

In this thesis, I have described a series of computational investigations exploring the relationship between microstructure and charge transport in organic semiconductor materials. Where relevant, I additionally connected these to the performance exhibited in specific device applications. I focussed on materials showing a divergence from the usual correlation between increased microstructural order, higher charge mobilities, and improved device performance. In each material case, I sought to explore and rationalise the role played by the typically high degrees of microstructural disorder in determining transport behaviour and performance.

I employed a multiscale modelling approach that included the use of molecular dynamics (MD), density functional theory (DFT) and charge transport simulation methods. I showed how the chemical structure of polymers and small molecules determines their packing arrangements, how this impacts the strength of electronic coupling and broader microstructural trends, and how these factors govern the bulk transport properties of materials.

9.1 Chemical Structure, Microstructure, and Charge Transport

In Chapter 4, I described the development of two charge transport simulation codes, `ToFeT` and `MESol`, which respectively employ the kinetic Monte Carlo (KMC) and master equation (ME) approaches. These modelling tool were then applied in two case studies to demonstrate their capability.

In the first case study (Section 4.5.1), I used `ToFeT` to probe the impact of electron density and mobility on the performance of an interfacial photocatalytic polymer system for hydrogen production. I compared simulation results from two model systems to explain the different hydrogen production efficiencies of photocatalysis based on the sulfone polymers FS-Hex and FS-TEG. The glycol side chains attached to FS-TEG led to increased water permeation in experimental systems, which was replicated *in silico* by decreasing the electronic coupling between polymer sites in the FS-TEG model, with respect to FS-Hex. From the simulation and experimental results, we found that, in the high charge density regime, the higher mobility of FS-Hex was likely to decrease the performance of devices

compared to FS-TEG. This was linked to a 'queuing' effect, established by the rate-limiting proton reduction reaction occurring on residual co-catalytic palladium sites, which greatly increased the time taken for electrons to exit the polymer region when electron densities were high. In experiments, the presence of this effect was indicated by an unusual trend of electron lifetimes in the polymer increasing with higher light intensity, and therefore with higher densities of generated electrons. Based on the hypothesis that electrons 'waiting' in the polymer region may suffer from increased recombination rates for higher mobility polymers, we were able to rationalise the high performance of sulfone polymers in this application, in light of their low mobilities compared to alternative photocatalytic polymers [128, 138].

In the second case study described in Chapter 4 (Section 4.5.2), I used `MESol` to evaluate electron transport in bis-adduct isomers of PCBM. The different isomers had been shown by my collaborators to favour different crystalline packing arrangements, which were linked to the differing degrees of symmetry displayed by the isolated molecules. From the results of charge transport simulations, I found that trends in the experimental mobilities of the isomers could be rationalised by considering the dimensionality of transport supported by the different crystal structures. These result were used to explain a noteworthy trend in the experimental results, namely that molecules with higher symmetry generally showed higher crystallinity, but worse mobilities. This was explained by the fact that the more amorphous microstructures were able to facilitate increasingly isotropic charge transport pathways [129].

In Chapter 5, I described an investigation into the microstructure of the high-mobility, structurally-disordered conjugated polymer C16-IDTBT. Using MD simulations and comparisons with STM experiments, I identified an unusual packing arrangement between polymer chains on surfaces and in the bulk. My results indicated that chains make contact via a packing motif involving backbones crossing over one another at near-perpendicular angles. The chemical-structural origin of this arrangement was linked to the attachment location of the four bulk side chains on the IDT donor unit, and the unadorned BT acceptor unit. In the 2D case, longer side chains were shown to promote a tighter distribution of backbone crossing angles around the perpendicular. This motif enables pairs of chains to pack as closely as semicrystalline polymers. When combined with the rigid, linear backbones of C16-IDTBT, the crossing motif was also shown to promote the formation of a highly interconnected microstructure. By quantifying the degree of interconnectivity, I was able to demonstrate the distinctiveness of the C16-IDTBT microstructure compared to the other polymers (P3HT and PffBT4T-2OD) analysed in this study [150].

In Chapter 6, I described my continued investigation of C16-IDTBT, here extending the study to explicitly evaluate the effect of microstructure on charge transport. I used DFT calculations to construct maps relating the interaction energy and electronic coupling between chain segments to their spatial arrangement. Analysis of these maps indicated that the perpendicular contact motif of

C16-IDTBT (identified in Chapter 5) is promoted not only by the attachment location of the side chains on the IDT unit, but, in particular, by the angle at which the side chains are bonded to the backbone. Although analysis of the maps and contacts sampled from realistic microstructural models demonstrated that the crossing motif inherently limits interchain hole coupling, I was able to show that the hole mobility of C16-IDTBT remains high in charge transport simulations. In line with experiments, C16-IDTBT was shown to outperform the semicrystalline polymer P3HT, despite the stronger interchain coupling of the latter. Analysis of the simulation results revealed that the high mobility of C16-IDTBT arises from a combination of 1) a high intrachain mobility, 2) an interconnected microstructure, and 3) modest (i.e. not too low) interchain coupling. These features were, in turn, linked to chemical-structural origins, namely, a linear and rigidly planar backbone, with side chains attached via sp^3-hybridised bonds to the IDT unit, and an unadorned BT unit [150].

Building on this analysis, I demonstrated that a slight improvement in the strength of interchain coupling would likely result in significantly higher bulk mobilities for C16-IDTBT, with a responsiveness greatly exceeding that of P3HT. Thus, the results of this study indicated that a promising pathway towards realising even higher mobility conjugated polymers would involve designing polymers for increased interchain coupling strengths, while maintaining similar microstructures to C16-IDTBT. I suggested some chemical design proposals for achieving this in Section 6.3.

In Chapter 7, I extended the analysis of C16-IDTBT to consider variants of the polymer featuring heteroatom-substituted donor units. Based on my findings in Chapters 5 and 6, I evaluated the factors likely to influence charge transport in these materials, including the rigidity and planarity of the backbones, the packing geometry at interchain contacts, and the strength of coupling at contacts. My results indicated that, assuming the same choice of side chains, two of the variants (labelled A and B, featuring a modified benzene moiety at the centre of the donor unit) would likely show similar hole mobilities to C16-IDTBT. The results further suggested that the remaining two variants (labelled C and D, featuring similarly modified benzene moieties to A and B respectively, plus thiazole moieties, on the donor) could show higher hole mobilities than C16-IDTBT. This was based on my assessment that, compared to C16-IDTBT, C and D featured enhanced backbone rigidity, and potentially a lower susceptibility to dynamic coupling disorder

In Chapter 8, I described an investigation into the charge transport behaviour of the NFA molecule O-IDTBR. I used `ToFeT` to perform KMC charge transport simulations on crystalline and disordered thin film models. For the thin film model, I ran simulations with and without the inclusion of intermolecular contributions to the energetic landscape and reorganisation energy. When these contributions were neglected, I found that the lower electronic coupling strengths in the thin film caused the mobility to decreased by two orders of magnitude compared to the crystal. A similar decrease was predicted by NAMD transport simulations performed by my collaborators. Their method further revealed that transport in the crystal proceeded via transient delocalisation, while transport in the

thin film occurred via localised hopping. For the thin film, the corresponding transport mechanism in the KMC and NAMD simulations led to similar mobilities, whereas the KMC approach was shown to overestimate mobilities in the crystal. Thus, we were able to demonstrate the circumstances under which it is appropriate to model transport using Marcus-rate parametrised KMC, and the consequences of misapplying it in a situation where the low-coupling assumption no longer holds [60].

The degree of energetic disorder in the thin film system was evaluated by my collaborators using a microelectrostatics model that accounts for charge polarisation and electrostatic interactions between molecules [51]. Introducing energetic disorder into the thin film KMC simulations caused the predicted mobility to drop by five orders of magnitude. An experimental mobility of similar magnitude to this lower value was measured by my collaborators by fitting data from the SCLC method to a drift-diffusion model with a DoSs closely matching the distribution of molecular site energies input into the KMC simulations. Therefore, by comparing with experiments, we were able to validate our finding that transport in O-IDTBR thin films is dominated by energetic disorder, and by contributions from electrostatic effects in particular. A significant degree of the energetic disorder was linked to conformational disorder arising from the soft dihedral between the acceptor (A) and donor (D) units of the molecule. Thus, this study revealed the chemical-structural origin of the relatively low mobilities exhibited by O-IDTBR and other A-D-A molecules, and indicated a pathway to improving the electron mobility of these materials by increasing the rigidity of the molecular core [60].

Overall, my work has reaffirmed the importance of understanding the role of microstructure – and particularly microstructural disorder – in determining the charge transport properties of OSC materials and their performance in device applications, and demonstrated how computational techniques may be applied to deepening this understanding.

9.2 Future Work

Several avenues of research could be pursued to expand upon the results presented in this thesis. Since my work heavily involved studying C16-IDTBT, most of my thoughts and considerations concerning further research have focused on this polymer, or on what this polymer can tell us about the structure-transport link in conjugated polymers more broadly. I list several suggestions for future research in the following subsections.

9.2.1 Experimental Assessment of the Geometry and Density of Interchain Contact Points by Solid-State Nuclear Magnetic Resonance

Techniques such as dynamic nuclear polarisation-enhanced solid-state nuclear magnetic resonance (SS-NMR) [192–194] can be used to assess the geometry and density of interchain contact points in disordered polymer microstructures. This could allow for experimental verification, in the solid

state, of the C16-IDTBT perpendicular crossing structures identified by STM and MD [150] (Chapter 5). Spectral data provided by SS-NMR can be decoded to provide information about the pairwise distances between atoms within a ∼1 nm range. Such data could be compared with simulated contact structures extracted from MD models (Section 5.2.4) or from controlled arrangements of polymer segments (Section 6.2.1).

Decoding the SS-NMR spectra associated with carbon and hydrogen atoms is made substantially more difficult by the abundance of these atoms in the backbone and side chains. This could be addressed by also analysing heteroatom-substituted variants of C16-IDTBT (see Section 6.3.1 and Chapter 7). In particular, evaluating pairwise separations between F atoms in fluorinated-BT variants may provide the means for a more straightforward insight into the geometry and density of contact points. Such results could be linked to C16-IDTBT under the assumption (or evaluation) of similar microstructures. An investigation of this nature has been proposed during discussions with Professor Hugo Bronstein, Dr Craig Yu, and Dr Yao Fu.

9.2.2 Further Analysis of Contact Locking

In Sections 5.2.1, 6.2.1, and 7.3, I hypothesised that certain interactions (mostly involving the side chains) in C16-IDTBT, and variants, may enhance interchain charge transfer by 'locking' contacts into a narrow range of geometries, and thus moderating dynamic coupling disorder [11, 57, 68, 69].

This effect could be explored further, perhaps by computing coupling distributions based on MD trajectories of pairs of contacting IDTBT chains with various side chain lengths. The use of MD trajectories would enable entropic contributions to the free energy of contact geometries to be evaluated, complementing the enthalpic interaction energy calculations presented in Sections 6.2.1 and 7.2.3.

A low susceptibility to dynamic coupling disorder has been identified as particularly important for enabling high mobilities in crystalline small molecule OSCs, since it facilitates the transient (de)localised transport mechanism [58–60] (see Chapter 8). Disordered polymers, on the other hand, do not feature the extended π-π stacking arrangements that host the delocalised charge states used by this mechanism. Therefore, when considering the thermal distribution of interchain coupling values at each given contact in a polymer microstructure, it would be interesting to clarify which of the following two options leads to better bulk transport: 1) a broad distribution, which may allow occasional access to high instantaneous coupling values, or 2) a narrow distribution, which would align with the preferred scenario in small molecule crystals. Exploring this idea would likely require the adoption of more sophisticated models beyond standard high-temperature Marcus theory (Section 2.3.2), such as NAMD simulations (Section 2.4.3).

9.2.3 Analysis of Contact Formation (Aggregation) during the Solution State-Solid State Transition

To establish a clearer link between the packing arrangements of pairs of C16-IDTBT chains on surfaces (Section 5.2.1) and contacts in solid state models (Section 5.2.5), it may be useful to explore the aggregation behaviour of chains in solution. This could be used to inform our understanding of how contacts form during the transition between the solution state and dry films [38, 40, 123–125]. As stated in Section 9.2.2, the use of MD would allow entropic contributions to the contact free energy to be assessed, alongside enthalpic contributions.

Such a study could draw upon models and theories developed for biological systems (e.g., protein-ligand binding [195]) to understand the analogous 'binding' process as it applies to conjugated polymers during the initial stages of film formation. Metadynamics MD simulations [196] could be particularly relevant in this regard.

9.2.4 Network Analysis of Conjugated Polymer Microstructures

The interconnectivity metric I defined in Section 5.2.6 was sufficient for rationalising the high mobility of C16-IDTBT compared to P3HT, but I suspect that it could be improved.

Jackson et al. demonstrated an approach for characterising the influence of microstructure on charge transport in small molecule OSC systems derived from the Kirchoff index (i.e., network resistivity) [197, 198]. While appealing, my preliminary testing of this graph-based approach indicated that it did not produce sensible results when applied to the conjugated polymers systems described in Chapter 5.

It would therefore be useful to develop an alternative graph-based method for characterising polymers. In particular, this would be useful in light of my assessment that higher mobility polymers could best be sought by maintaining a C16-IDTBT-like microstructure, while enhancing interchain coupling (Section 6.3.1). An example of a graph-based assessment of a polymer system has been described in a work by Pokuri et al. [199]. Here, they assessed the resiliency of transport through a particular conjugated polymer microstructure to physical or chemical damage (modelled by deactivating monomeric nodes). It would be worthwhile to extend upon methods such as this to allow for simple and robust comparisons between different polymer microstructures.

As well as qualitatively aligning with mobility trends between different polymers (and thus having predictive power), an ideal metric would be calculated from microstructural information alone[1], in order to keep computational costs low.

[1] i.e., without the need to perform expensive electronic structure calculations, perhaps by relying upon separation-dependent estimations of the coupling strength (Equation 3.28).

9.2.5 Further Analysis of IDTxBx Variants

In light of my results in Section 7.2.2, it would be interesting to explore why the thiazole-containing variants of IDTBT (variants *C* and *D*) appeared to feature a more rigidly planar backbone, despite lacking the same N-H through-space interaction shown to stabilise the IDT-BT dihedral [125, 158]. This study could involve applying the analysis described in [125] to the variants *C* and *D*. Since other works, such as those by Karunasena et al. [181] and Duke et al. [182], have highlighted the importance of considering subtle increases in double bond character for controlling the rigidity of donor-acceptor dihedrals in similar chemical systems, it would also be worthwhile exploring this as a factor influencing the planarity of *C* and *D* compared to IDTBT. In their work, Karunasena et al. presented bond ellipticity as a useful measure for quantifying the π-character of bonds and assessing the degree of single- or double-bondedness [181, 200].

A further unanswered question raised in Chapter 7 relates to the low experimental mobility of C16-IDTzBT [170], which features a largely similar chemical structure to variants *C* and *D*. It would be useful to better understand the reasons behind this low mobility, given the implications of my analysis that variants *C* and *D* could display higher mobilities than IDTBT (Chapter 7). A natural starting point would be to synthesise samples of C16-IDTzBT, *C*, and *D* and subject them to experimental mobility measurements (to check for other unaccounted for causes of the previous low μ measurement, such as impurities, in the case of C16-IDTzBT). These results could be complemented by analysing the polymers using the multiscale modelling procedure described over Chapters 5 and 6. This could be applied to 8mer chains, matching the low molecular weight of the previously-measured C16-IDTzBT sample [170].

As well as further analysis of the donor-variants, the effect on transport of modifying the acceptor unit could be explored. Based on suggestions by Professor Iain McCulloch, substitution of the chalcogen (S) atom on the BT unit could be used to alter the bond lengths between the chalcogen atom and the two bonded N atoms. This may affect the planarity of the polymer by varying the strength of the electrostatic interaction between each N atom and the neighbouring H atom on the IDT unit [125, 158]. Further changes may also be found in the preferred geometry and coupling at interchain contacts, which would be worth exploring.

9.2.6 Light-Matter Interactions in IDTBT

As discussed in Section 2.5.2, although OPV devices using IDTBT (with relatively short, branched side chains) as a donor have been reported to achieve moderate efficiencies, up to 5.5% [83, 87, 88], it remains relatively unexplored in this application. For instance, it has thus far only been paired with fullerene acceptors, and could be tested with a broader range of NFA components.

Recently, there has been much interest shown in the possibility of free (mobile) charge generation

in single-component devices. Most famously this has related to the Y6 molecule [201, 202], although other donor-acceptor small molecules [203], and donor-acceptor block copolymers [204], have also been identified as possible candidates for single-component devices. In Y6 and other small molecules, charge generation has been suggested to occur via pathways involving intramolecular charge-transfer states, while in block copolymers the process is likely to involve packing between neighbouring donor and acceptor blocks.

Based on time-resolved infrared spectroscopic data gathered by Professor Sophia C. Hayes, and supported by excited state calculations by Dr Mohammed Azzouzi, a similar process may occur in IDTBT. As mentioned in Section 2.5.2, C16-IDTBT was previously rejected as a component in OPV devices because its long side chains were thought to inhibit mixing with acceptor molecules, leading to poor efficiencies. Naturally, a hypothetical intrachain pathway to free charge generation would not be negatively impacted by this. An interchain pathway may also be possible in C16-IDTBT. While the long side chains could certainly inhibit packing with other molecules, the results presented in Chapter 5 show that C16-IDTBT chains can still pack closely with other C16-IDTBT chains.

Based on these considerations, it may therefore be worthwhile to explore the possibility of intra- and inter-chain free charge generation pathways (e.g., using time-dependent DFT calculations, or excited state NAMD simulations), as well as to measure the performance of single-component OPV devices based on IDTBT.

Bibliography

[1] J. Rockström *et al.*, "A safe operating space for humanity," *Nature*, vol. 461, no. 7263, pp. 472–475, Sep. 2009, ISSN: 1476-4687. DOI: 10.1038/461472a.

[2] J. Rockström *et al.*, "Safe and just Earth system boundaries," *Nature*, vol. 619, no. 7968, pp. 102–111, Jul. 2023, ISSN: 1476-4687. DOI: 10.1038/s41586-023-06083-8.

[3] K. Calvin *et al.*, "IPCC, 2023: Climate Change 2023: Synthesis Report. Contribution of Working Groups I, II and III to the Sixth Assessment Report of the Intergovernmental Panel on Climate Change [Core Writing Team, H. Lee and J. Romero (eds.)]. IPCC, Geneva, Switzerland.," Intergovernmental Panel on Climate Change (IPCC), Tech. Rep., Jul. 2023. DOI: 10.59327/IPCC/AR6-9789291691647.

[4] A. Köhler and H. Bässler, "The Electronic Structure of Organic Semiconductors," in *Electronic Processes in Organic Semiconductors*, John Wiley & Sons, Ltd, 2015, pp. 1–86, ISBN: 978-3-527-68517-2.

[5] S. R. Forrest, "Bulk and thin film organic crystal structures," in *Organic Electronics: Foundations to Applications*, S. R. Forrest, Ed., Oxford University Press, Aug. 2020, ISBN: 978-0-19-852972-9. DOI: 10.1093/oso/9780198529729.003.0002.

[6] O. Inganäs, "Organic Photovoltaics over Three Decades," *Advanced Materials*, vol. 30, no. 35, p. 1 800 388, 2018, ISSN: 1521-4095. DOI: 10.1002/adma.201800388.

[7] S. Poncé, W. Li, S. Reichardt, and F. Giustino, "First-principles calculations of charge carrier mobility and conductivity in bulk semiconductors and two-dimensional materials," *Reports on Progress in Physics*, vol. 83, no. 3, p. 036 501, Feb. 2020, ISSN: 0034-4885. DOI: 10.1088/1361-6633/ab6a43.

[8] G. G. Malliaras and J. C. Scott, "The roles of injection and mobility in organic light emitting diodes," *Journal of Applied Physics*, vol. 83, no. 10, pp. 5399–5403, May 1998, ISSN: 0021-8979, 1089-7550. DOI: 10.1063/1.367369.

[9] F. Zhao and D. Ma, "Approaches to high performance white organic light-emitting diodes for general lighting," *Materials Chemistry Frontiers*, vol. 1, no. 10, pp. 1933–1950, Sep. 2017, ISSN: 2052-1537. DOI: 10.1039/C6QM00365F.

[10] R. A. K. Yadav, D. K. Dubey, S.-Z. Chen, T.-W. Liang, and J.-H. Jou, "Role of Molecular Orbital Energy Levels in OLED Performance," *Scientific Reports*, vol. 10, no. 1, p. 9915, Jun. 2020, ISSN: 2045-2322. DOI: 10.1038/s41598-020-66946-2.

[11] S. Fratini, M. Nikolka, A. Salleo, G. Schweicher, and H. Sirringhaus, "Charge transport in high-mobility conjugated polymers and molecular semiconductors," *Nature Materials*, vol. 19, no. 5, pp. 491–502, May 2020, ISSN: 1476-1122, 1476-4660. DOI: 10.1038/s41563-020-0647-2.

[12] H. Sirringhaus, "25th Anniversary Article: Organic Field-Effect Transistors: The Path Beyond Amorphous Silicon," *Advanced Materials*, vol. 26, no. 9, pp. 1319–1335, 2014, ISSN: 1521-4095. DOI: 10.1002/adma.201304346.

[13] A. M. Levine, G. Bu, S. Biswas, E. H. R. Tsai, A. B. Braunschweig, and B. L. Nannenga, "Crystal structure and orientation of organic semiconductor thin films by microcrystal electron diffraction and grazing-incidence wide-angle X-ray scattering," *Chemical Communications*, vol. 56, no. 30, pp. 4204–4207, Apr. 2020, ISSN: 1364-548X. DOI: 10.1039/D0CC00119H.

[14] O. Panova *et al.*, "Diffraction imaging of nanocrystalline structures in organic semiconductor molecular thin films," *Nature Materials*, vol. 18, no. 8, pp. 860–865, Aug. 2019, ISSN: 1476-4660. DOI: 10.1038/s41563-019-0387-3.

[15] A. R. Aiyar, J.-I. Hong, R. Nambiar, D. M. Collard, and E. Reichmanis, "Tunable Crystallinity in Regioregular Poly(3-Hexylthiophene) Thin Films and Its Impact on Field Effect Mobility," *Advanced Functional Materials*, vol. 21, no. 14, pp. 2652–2659, 2011, ISSN: 1616-3028. DOI: 10.1002/adfm.201002729.

[16] Z. Peng, L. Ye, and H. Ade, "Understanding, quantifying, and controlling the molecular ordering of semiconducting polymers: From novices to experts and amorphous to perfect crystals," *Materials Horizons*, vol. 9, no. 2, pp. 577–606, Feb. 2022, ISSN: 2051-6355. DOI: 10.1039/D0MH00837K.

[17] C. Groves, "Simulating charge transport in organic semiconductors and devices: A review," *Reports on Progress in Physics*, vol. 80, no. 2, p. 026 502, Dec. 2016, ISSN: 0034-4885. DOI: 10.1088/1361-6633/80/2/026502.

[18] B. Baumeier, F. May, C. Lennartz, and D. Andrienko, "Challenges for in silico design of organic semiconductors," *Journal of Materials Chemistry*, vol. 22, no. 22, pp. 10 971–10 976, May 2012, ISSN: 1364-5501. DOI: 10.1039/C2JM30182B.

[19] I. Y. Kanal, S. G. Owens, J. S. Bechtel, and G. R. Hutchison, "Efficient Computational Screening of Organic Polymer Photovoltaics," *The Journal of Physical Chemistry Letters*, vol. 4, no. 10, pp. 1613–1623, May 2013. DOI: 10.1021/jz400215j.

[20] J. A. Schmidt *et al.*, "Computational Screening of Chiral Organic Semiconductors: Exploring Side-Group Functionalization and Assembly to Optimize Charge Transport," *Crystal Growth & Design*, vol. 21, no. 9, pp. 5036–5049, Sep. 2021, ISSN: 1528-7483. DOI: 10.1021/acs.cgd.1c00473.

[21] K. M. Katubi *et al.*, "Machine learning assisted designing of organic semiconductors for organic solar cells: High-throughput screening and reorganization energy prediction," *Inorganic Chemistry Communications*, vol. 151, p. 110 610, May 2023, ISSN: 1387-7003. DOI: 10.1016/j.inoche.2023.110610.

[22] C. Kunkel, J. T. Margraf, K. Chen, H. Oberhofer, and K. Reuter, "Active discovery of organic semiconductors," *Nature Communications*, vol. 12, no. 1, p. 2422, Apr. 2021, ISSN: 2041-1723. DOI: 10.1038/s41467-021-22611-4.

[23] L. D. Site, "What is a Multiscale Problem in Molecular Dynamics?" *Entropy*, vol. 16, no. 1, pp. 23–40, Jan. 2014, ISSN: 1099-4300. DOI: 10.3390/e16010023.

[24] J. Lenhard, S. Stephan, and H. Hasse, "On the History of the Lennard-Jones Potential," *Annalen der Physik*, vol. 536, no. 6, p. 2 400 115, 2024, ISSN: 1521-3889. DOI: 10.1002/andp.202400115.

[25] V. Coropceanu, J. Cornil, D. A. da Silva Filho, Y. Olivier, R. Silbey, and J.-L. Brédas, "Charge Transport in Organic Semiconductors," *Chemical Reviews*, vol. 107, no. 4, pp. 926–952, Apr. 2007, ISSN: 0009-2665. DOI: 10.1021/cr050140x.

[26] S. Wang, "Emerging efficient charge-transport landscape based on short-range order in conjugated polymers," *Synthetic Metals*, vol. 251, pp. 104–119, May 2019, ISSN: 0379-6779. DOI: 10.1016/j.synthmet.2019.03.021.

[27] S. Himmelberger and A. Salleo, "Engineering semiconducting polymers for efficient charge transport," *MRS Communications*, vol. 5, no. 3, pp. 383–395, Sep. 2015, ISSN: 2159-6859, 2159-6867. DOI: 10.1557/mrc.2015.44.

[28] S. Holliday, J. E. Donaghey, and I. McCulloch, "Advances in Charge Carrier Mobilities of Semiconducting Polymers Used in Organic Transistors," *Chemistry of Materials*, vol. 26, no. 1, pp. 647–663, Jan. 2014, ISSN: 0897-4756. DOI: 10.1021/cm402421p.

[29] X. Zhang *et al.*, "Molecular origin of high field-effect mobility in an indacenodithiophene–benzothiadiazole copolymer," *Nature Communications*, vol. 4, no. 1, p. 2238, Oct. 2013, ISSN: 2041-1723. DOI: 10.1038/ncomms3238.

[30] R. Noriega, "Efficient Charge Transport in Disordered Conjugated Polymer Microstructures," *Macromolecular Rapid Communications*, vol. 39, no. 14, p. 1 800 096, 2018, ISSN: 1521-3927. DOI: 10.1002/marc.201800096.

[31] R. Noriega *et al.*, "A general relationship between disorder, aggregation and charge transport in conjugated polymers," *Nature Materials*, vol. 12, no. 11, pp. 1038–1044, Nov. 2013, ISSN: 1476-1122, 1476-4660. DOI: 10.1038/nmat3722.

[32] M. Kim *et al.*, "Donor–Acceptor-Conjugated Polymer for High-Performance Organic Field-Effect Transistors: A Progress Report," *Advanced Functional Materials*, vol. 30, no. 20, p. 1 904 545, 2020, ISSN: 1616-3028. DOI: 10.1002/adfm.201904545.

[33] Y. Yang, Z. Liu, G. Zhang, X. Zhang, and D. Zhang, "The Effects of Side Chains on the Charge Mobilities and Functionalities of Semiconducting Conjugated Polymers beyond Solubilities," *Advanced Materials*, vol. 31, no. 46, p. 1 903 104, 2019, ISSN: 1521-4095. DOI: 10.1002/adma.201903104.

[34] G. Ma, Z. Li, W. Xia, L. Fang, and X. Gu, "Effect of solvent quality and sidechain architecture on the conjugated polymer chain conformation in solution," *Nanoscale*, Jan. 2024, ISSN: 2040-3372. DOI: 10.1039/D3NR05721F.

[35] L. Yang, H. Zhou, and W. You, "Quantitatively Analyzing the Influence of Side Chains on Photovoltaic Properties of Polymer-Fullerene Solar Cells," *The Journal of Physical Chemistry C*, vol. 114, no. 39, pp. 16 793–16 800, Oct. 2010, ISSN: 1932-7447, 1932-7455. DOI: 10.1021/jp106640r.

[36] B. Kuei and E. D. Gomez, "Chain conformations and phase behavior of conjugated polymers," *Soft Matter*, vol. 13, no. 1, pp. 49–67, Dec. 2016, ISSN: 1744-6848. DOI: 10.1039/C6SM00979D.

[37] Z. Cao, M. Leng, Y. Cao, X. Gu, and L. Fang, "How rigid are conjugated non-ladder and ladder polymers?" *Journal of Polymer Science*, vol. 60, no. 3, pp. 298–310, 2022, ISSN: 2642-4169. DOI: 10.1002/pol.20210550.

[38] D. T. Duong, M. F. Toney, and A. Salleo, "Role of confinement and aggregation in charge transport in semicrystalline polythiophene thin films," *Physical Review B*, vol. 86, no. 20, p. 205 205, Nov. 2012. DOI: 10.1103/PhysRevB.86.205205.

[39] M. Brinkmann, "Structure and morphology control in thin films of regioregular poly(3-hexylthiophene)," *Journal of Polymer Science Part B: Polymer Physics*, vol. 49, no. 17, pp. 1218–1233, 2011, ISSN: 1099-0488. DOI: 10.1002/polb.22310.

[40] C. Scharsich *et al.*, "Control of aggregate formation in poly(3-hexylthiophene) by solvent, molecular weight, and synthetic method," *Journal of Polymer Science Part B: Polymer Physics*, vol. 50, no. 6, pp. 442–453, 2012, ISSN: 1099-0488. DOI: 10.1002/polb.23022.

[41] Z.-D. Yu, Y. Lu, J.-Y. Wang, and J. Pei, "Conformation Control of Conjugated Polymers," *Chemistry – A European Journal*, vol. 26, no. 69, pp. 16 194–16 205, 2020, ISSN: 1521-3765. DOI: 10.1002/chem.202000220.

[42] R. A. Marcus, "On the Theory of Oxidation-Reduction Reactions Involving Electron Transfer. I," *The Journal of Chemical Physics*, vol. 24, no. 5, pp. 966–978, May 1956, ISSN: 0021-9606, 1089-7690. DOI: 10.1063/1.1742723.

[43] R. A. Marcus, "On the Theory of Oxidation-Reduction Reactions Involving Electron Transfer. II. Applications to Data on the Rates of Isotopic Exchange Reactions," *The Journal of Chemical Physics*, vol. 26, no. 4, pp. 867–871, Apr. 1957, ISSN: 0021-9606, 1089-7690. DOI: 10.1063/1.1743423.

[44] R. A. Marcus, "Nonadiabatic processes involving quantum-like and classical-like coordinates with applications to nonadiabatic electron transfers," *The Journal of Chemical Physics*, vol. 81, no. 10, pp. 4494–4500, Nov. 1984, ISSN: 0021-9606, 1089-7690. DOI: 10.1063/1.447418.

[45] R. A. Marcus, "Electron transfer reactions in chemistry. Theory and experiment," *Reviews of Modern Physics*, vol. 65, no. 3, pp. 599–610, Jul. 1993, ISSN: 0034-6861, 1539-0756. DOI: 10.1103/RevModPhys.65.599.

[46] E. R. Heller and J. O. Richardson, "Semiclassical instanton formulation of Marcus–Levich–Jortner theory," *The Journal of Chemical Physics*, vol. 152, no. 24, p. 244 117, Jun. 2020, ISSN: 0021-9606, 1089-7690. DOI: 10.1063/5.0013521.

[47] J. Kirkpatrick, "An Approximate Method for Calculating Transfer Integrals Based on the ZINDO Hamiltonian," *International Journal of Quantum Chemistry*, vol. 108, no. 1, pp. 51–56, 2008, ISSN: 00207608, 1097461X. DOI: 10.1002/qua.21378.

[48] F. Gajdos *et al.*, "Ultrafast Estimation of Electronic Couplings for Electron Transfer between π-Conjugated Organic Molecules," *Journal of Chemical Theory and Computation*, vol. 10, no. 10, pp. 4653–4660, Oct. 2014, ISSN: 1549-9618. DOI: 10.1021/ct500527v.

[49] J.-L. Brédas, D. Beljonne, V. Coropceanu, and J. Cornil, "Charge-Transfer and Energy-Transfer Processes in π-Conjugated Oligomers and Polymers: A Molecular Picture," *Chemical Reviews*, vol. 104, no. 11, pp. 4971–5004, Nov. 2004, ISSN: 0009-2665. DOI: 10.1021/cr040084k.

[50] G. D'Avino *et al.*, "Electrostatic phenomena in organic semiconductors: Fundamentals and implications for photovoltaics," *Journal of Physics: Condensed Matter*, vol. 28, no. 43, p. 433 002, Sep. 2016, ISSN: 0953-8984. DOI: 10.1088/0953-8984/28/43/433002.

[51] G. D'Avino, L. Muccioli, C. Zannoni, D. Beljonne, and Z. G. Soos, "Electronic Polarization in Organic Crystals: A Comparative Study of Induced Dipoles and Intramolecular Charge Redistribution Schemes," *Journal of Chemical Theory and Computation*, vol. 10, no. 11, pp. 4959–4971, Nov. 2014, ISSN: 1549-9618. DOI: 10.1021/ct500618w.

[52] V. Nádaždy, F. Schauer, and K. Gmucová, "Energy resolved electrochemical impedance spectroscopy for electronic structure mapping in organic semiconductors," *Applied Physics Letters*, vol. 105, no. 14, p. 142 109, Oct. 2014, ISSN: 0003-6951. DOI: 10.1063/1.4898068.

[53] H. Bässler, "Charge Transport in Disordered Organic Photoconductors a Monte Carlo Simulation Study," *physica status solidi (b)*, vol. 175, no. 1, pp. 15–56, Jan. 1993, ISSN: 03701972, 15213951. DOI: 10.1002/pssb.2221750102.

[54] A. Troisi, "The speed limit for sequential charge hopping in molecular materials," *Organic Electronics*, vol. 12, no. 12, pp. 1988–1991, Dec. 2011, ISSN: 15661199. DOI: 10.1016/j.orgel.2011.08.020.

[55] N. Karl *et al.*, "Fast electronic transport in organic molecular solids?" *Journal of Vacuum Science & Technology A*, vol. 17, no. 4, pp. 2318–2328, Jul. 1999, ISSN: 0734-2101. DOI: 10.1116/1.581767.

[56] T. Sakanoue and H. Sirringhaus, "Band-like temperature dependence of mobility in a solution-processed organic semiconductor," *Nature Materials*, vol. 9, no. 9, pp. 736–740, Sep. 2010, ISSN: 1476-4660. DOI: 10.1038/nmat2825.

[57] S. Fratini, D. Mayou, and S. Ciuchi, "The Transient Localization Scenario for Charge Transport in Crystalline Organic Materials," *Advanced Functional Materials*, vol. 26, no. 14, pp. 2292–2315, Apr. 2016, ISSN: 1616301X. DOI: 10.1002/adfm.201502386.

[58] S. Giannini *et al.*, "Quantum localization and delocalization of charge carriers in organic semiconducting crystals," *Nature Communications*, vol. 10, no. 1, p. 3843, Dec. 2019, ISSN: 2041-1723. DOI: 10.1038/s41467-019-11775-9.

[59] S. Giannini, O. G. Ziogos, A. Carof, M. Ellis, and J. Blumberger, "Flickering Polarons Extending over Ten Nanometres Mediate Charge Transport in High-Mobility Organic Crystals," *Advanced Theory and Simulations*, vol. 3, no. 9, p. 2 000 093, 2020, ISSN: 2513-0390. DOI: 10.1002/adts.202000093.

[60] L. Stojanović *et al.*, "Disorder-Induced Transition from Transient Quantum Delocalization to Charge Carrier Hopping Conduction in a Nonfullerene Acceptor Material," *Physical Review X*, vol. 14, no. 2, p. 021 021, Apr. 2024. DOI: 10.1103/PhysRevX.14.021021.

[61] M. Casalegno, A. Bernardi, and G. Raos, "Numerical simulation of photocurrent generation in bilayer organic solar cells: Comparison of master equation and kinetic Monte Carlo approaches," *The Journal of Chemical Physics*, vol. 139, no. 2, p. 024 706, Jul. 2013, ISSN: 0021-9606. DOI: 10.1063/1.4812826.

[62] W. F. Pasveer, J. Cottaar, P. A. Bobbert, and M. A. J. Michels, "Temperature, charge carrier density, and electric field dependence of mobilities in disordered conjugated polymers: Simulation results," *Synthetic Metals*, Proceedings of the International Conference on Science and Technology of Synthetic Metals, vol. 152, no. 1, pp. 157–160, Sep. 2005, ISSN: 0379-6779. DOI: 10.1016/j.synthmet.2005.07.164.

[63] Z. G. Yu, D. L. Smith, A. Saxena, R. L. Martin, and A. R. Bishop, "Molecular Geometry Fluctuation Model for the Mobility of Conjugated Polymers," *Physical Review Letters*, vol. 84, no. 4, pp. 721–724, Jan. 2000, ISSN: 0031-9007, 1079-7114. DOI: 10.1103/PhysRevLett.84.721.

[64] Z. G. Yu, D. L. Smith, A. Saxena, R. L. Martin, and A. R. Bishop, "Molecular geometry fluctuations and field-dependent mobility in conjugated polymers," *Physical Review B*, vol. 63, no. 8, p. 085 202, Feb. 2001. DOI: 10.1103/PhysRevB.63.085202.

[65] J. J. Kwiatkowski, J. M. Frost, and J. Nelson, "The Effect of Morphology on Electron Field-Effect Mobility in Disordered C60 Thin Films," *Nano Letters*, vol. 9, no. 3, pp. 1085–1090, Mar. 2009, ISSN: 1530-6984. DOI: 10.1021/nl803504q.

[66] J. Nelson, J. J. Kwiatkowski, J. Kirkpatrick, and J. M. Frost, "Modeling Charge Transport in Organic Photovoltaic Materials," *Accounts of Chemical Research*, vol. 42, no. 11, pp. 1768–1778, Nov. 2009, ISSN: 0001-4842, 1520-4898. DOI: 10.1021/ar900119f.

[67] D. Balzer, T. J. A. M. Smolders, D. Blyth, S. N. Hood, and I. Kassal, "Delocalised kinetic Monte Carlo for simulating delocalisation-enhanced charge and exciton transport in disordered materials," *Chemical Science*, vol. 12, no. 6, pp. 2276–2285, Feb. 2021, ISSN: 2041-6539. DOI: 10.1039/D0SC04116E.

[68] H. Sirringhaus, T. Sakanoue, and J.-F. Chang, "Charge-transport physics of high-mobility molecular semiconductors," *physica status solidi (b)*, vol. 249, no. 9, pp. 1655–1676, 2012, ISSN: 1521-3951. DOI: 10.1002/pssb.201248143.

[69] T. Nematiaram and A. Troisi, "Strategies to reduce the dynamic disorder in molecular semiconductors," *Materials Horizons*, vol. 7, no. 11, pp. 2922–2928, Nov. 2020, ISSN: 2051-6355. DOI: 10.1039/D0MH01159B.

[70] T. R. Nelson *et al.*, "Non-adiabatic Excited-State Molecular Dynamics: Theory and Applications for Modeling Photophysics in Extended Molecular Materials," *Chemical Reviews*, vol. 120, no. 4, pp. 2215–2287, Feb. 2020, ISSN: 0009-2665. DOI: 10.1021/acs.chemrev.9b00447.

[71] E. Tapavicza, G. D. Bellchambers, J. C. Vincent, and F. Furche, "Ab initio non-adiabatic molecular dynamics," *Physical Chemistry Chemical Physics*, vol. 15, no. 42, pp. 18 336–18 348, Oct. 2013, ISSN: 1463-9084. DOI: 10.1039/C3CP51514A.

[72] J. C. Tully, "Molecular dynamics with electronic transitions," *The Journal of Chemical Physics*, vol. 93, no. 2, pp. 1061–1071, Jul. 1990, ISSN: 0021-9606. DOI: 10.1063/1.459170.

[73] H. Oberhofer, K. Reuter, and J. Blumberger, "Charge Transport in Molecular Materials: An Assessment of Computational Methods," *Chemical Reviews*, vol. 117, no. 15, pp. 10 319–10 357, Aug. 2017, ISSN: 0009-2665. DOI: 10.1021/acs.chemrev.7b00086.

[74] J. Spencer, F. Gajdos, and J. Blumberger, "FOB-SH: Fragment orbital-based surface hopping for charge carrier transport in organic and biological molecules and materials," *The Journal of Chemical Physics*, vol. 145, no. 6, p. 064 102, Aug. 2016, ISSN: 0021-9606, 1089-7690. DOI: 10.1063/1.4960144.

[75] J. Spencer, L. Scalfi, A. Carof, and J. Blumberger, "Confronting surface hopping molecular dynamics with Marcus theory for a molecular donor–acceptor system," *Faraday Discussions*, vol. 195, pp. 215–236, 2016, ISSN: 1359-6640, 1364-5498. DOI: 10.1039/C6FD00107F.

[76] Y. Olivier *et al.*, "25th Anniversary Article: High-Mobility Hole and Electron Transport Conjugated Polymers: How Structure Defines Function," *Advanced Materials*, vol. 26, no. 14, pp. 2119–2136, 2014, ISSN: 1521-4095. DOI: 10.1002/adma.201305809.

[77] A. Zen *et al.*, "Effect of Molecular Weight on the Structure and Crystallinity of Poly(3-hexylthiophene)," *Macromolecules*, vol. 39, no. 6, pp. 2162–2171, Mar. 2006, ISSN: 0024-9297, 1520-5835. DOI: 10.1021/ma0521349.

[78] K. Gu, C. R. Snyder, J. Onorato, C. K. Luscombe, A. W. Bosse, and Y.-L. Loo, "Assessing the Huang–Brown Description of Tie Chains for Charge Transport in Conjugated Polymers," *ACS Macro Letters*, vol. 7, no. 11, pp. 1333–1338, Nov. 2018. DOI: 10.1021/acsmacrolett.8b00626.

[79] Y.-Y. Zhou *et al.*, "Visualizing the multi-level assembly structures of conjugated molecular systems with chain-length dependent behavior," *Nature Communications*, vol. 14, no. 1, p. 3340, Jun. 2023, ISSN: 2041-1723. DOI: 10.1038/s41467-023-39133-w.

[80] S. Himmelberger, K. Vandewal, Z. Fei, M. Heeney, and A. Salleo, "Role of Molecular Weight Distribution on Charge Transport in Semiconducting Polymers," *Macromolecules*, vol. 47, no. 20, pp. 7151–7157, Oct. 2014, ISSN: 0024-9297. DOI: 10.1021/ma501508j.

[81] I. McCulloch *et al.*, "Semiconducting Thienothiophene Copolymers: Design, Synthesis, Morphology, and Performance in Thin-Film Organic Transistors," *Advanced Materials*, vol. 21, no. 10-11, pp. 1091–1109, 2009, ISSN: 1521-4095. DOI: 10.1002/adma.200801650.

[82] W. Zhang *et al.*, "Indacenodithiophene Semiconducting Polymers for High-Performance, Air-Stable Transistors," *Journal of the American Chemical Society*, vol. 132, no. 33, pp. 11 437–11 439, Aug. 2010, ISSN: 0002-7863. DOI: 10.1021/ja1049324.

[83] H. Bronstein *et al.*, "Indacenodithiophene- *co* -benzothiadiazole Copolymers for High Performance Solar Cells or Transistors via Alkyl Chain Optimization," *Macromolecules*, vol. 44, no. 17, pp. 6649–6652, Sep. 2011, ISSN: 0024-9297, 1520-5835. DOI: 10.1021/ma201158d.

[84] D. Mühlbacher *et al.*, "High Photovoltaic Performance of a Low-Bandgap Polymer," *Advanced Materials*, vol. 18, no. 21, pp. 2884–2889, 2006, ISSN: 1521-4095. DOI: 10.1002/adma.200600160.

[85] R. P. Fornari and A. Troisi, "Narrower Bands with Better Charge Transport: The Counterintuitive Behavior of Semiconducting Copolymers," *Advanced Materials*, vol. 26, no. 45, pp. 7627–7631, 2014, ISSN: 1521-4095. DOI: 10.1002/adma.201402941.

[86] D. Venkateshvaran *et al.*, "Approaching disorder-free transport in high-mobility conjugated polymers," *Nature*, vol. 515, no. 7527, pp. 384–388, Nov. 2014, ISSN: 1476-4687. DOI: 10.1038/nature13854.

[87] J. Kirkpatrick *et al.*, "A Systematic Approach to the Design Optimization of Light-Absorbing Indenofluorene Polymers for Organic Photovoltaics," *Advanced Energy Materials*, vol. 2, no. 2, pp. 260–265, 2012, ISSN: 1614-6840. DOI: 10.1002/aenm.201100622.

[88] Y. W. Soon *et al.*, "Energy versus electron transfer in organic solar cells: A comparison of the photophysics of two indenofluorene: Fullerene blend films," *Chemical Science*, vol. 2, no. 6, pp. 1111–1120, Jun. 2011, ISSN: 2041-6539. DOI: 10.1039/C0SC00606H.

[89] Y. Li, W. K. Tatum, J. W. Onorato, Y. Zhang, and C. K. Luscombe, "Low Elastic Modulus and High Charge Mobility of Low-Crystallinity Indacenodithiophene-Based Semiconducting Polymers for Potential Applications in Stretchable Electronics," *Macromolecules*, vol. 51, no. 16, pp. 6352–6358, Aug. 2018, ISSN: 0024-9297. DOI: 10.1021/acs.macromol.8b00898.

[90] Y. Zheng *et al.*, "An Intrinsically Stretchable High-Performance Polymer Semiconductor with Low Crystallinity," *Advanced Functional Materials*, vol. 29, no. 46, p. 1 905 340, 2019, ISSN: 1616-3028. DOI: 10.1002/adfm.201905340.

[91] B. Zhao *et al.*, "Simultaneous Enhancement of Stretchability, Strength, and Mobility in Ultrahigh-Molecular-Weight Poly(indacenodithiophene-co-benzothiadiazole)," *Macromolecules*, vol. 54, no. 21, pp. 9896–9905, Nov. 2021, ISSN: 0024-9297. DOI: 10.1021/acs.macromol.1c01513.

[92] R. Dilmurat, S. Prodhan, L. Wang, and D. Beljonne, "Thermally activated intra-chain charge transport in high charge-carrier mobility copolymers," *The Journal of Chemical Physics*, vol. 156, no. 8, p. 084 115, Feb. 2022, ISSN: 0021-9606, 1089-7690. DOI: 10.1063/5.0082569.

[93] C. Cendra *et al.*, "Unraveling the Unconventional Order of a High-Mobility Indacenodithiophene–Benzothiadiazole Copolymer," *ACS Macro Letters*, vol. 10, no. 10, pp. 1306–1314, Oct. 2021. DOI: 10.1021/acsmacrolett.1c00547.

[94] I. Dobryden *et al.*, "Dynamic self-stabilization in the electronic and nanomechanical properties of an organic polymer semiconductor," *Nature Communications*, vol. 13, no. 1, p. 3076, Jun. 2022, ISSN: 2041-1723. DOI: 10.1038/s41467-022-30801-x.

[95] A. Troisi, G. Orlandi, and J. E. Anthony, "Electronic Interactions and Thermal Disorder in Molecular Crystals Containing Cofacial Pentacene Units," *Chemistry of Materials*, vol. 17, no. 20, pp. 5024–5031, Oct. 2005, ISSN: 0897-4756. DOI: 10.1021/cm051150h.

[96] X. Feng *et al.*, "Towards high charge-carrier mobilities by rational design of the shape and periphery of discotics," *Nature Materials*, vol. 8, no. 5, pp. 421–426, May 2009, ISSN: 1476-1122, 1476-4660. DOI: 10.1038/nmat2427.

[97] T. H. Thomas *et al.*, "Short contacts between chains enhancing luminescence quantum yields and carrier mobilities in conjugated copolymers," *Nature Communications*, vol. 10, no. 1, p. 2614, Jun. 2019, ISSN: 2041-1723. DOI: 10.1038/s41467-019-10277-y.

[98] T. H. Thomas *et al.*, "Chain Coupling and Luminescence in High-Mobility, Low-Disorder Conjugated Polymers," *ACS Nano*, vol. 13, no. 12, pp. 13 716–13 727, Dec. 2019, ISSN: 1936-0851, 1936-086X. DOI: 10.1021/acsnano.9b07147.

[99] H. N. Tsao *et al.*, "Ultrahigh Mobility in Polymer Field-Effect Transistors by Design," *Journal of the American Chemical Society*, vol. 133, no. 8, pp. 2605–2612, Mar. 2011, ISSN: 0002-7863. DOI: 10.1021/ja108861q.

[100] H. Makki, C. A. Burke, and A. Troisi, "Microstructural Model of Indacenodithiophene-co-benzothiadiazole Polymer: π-Crossing Interactions and Their Potential Impact on Charge Transport," *The Journal of Physical Chemistry Letters*, pp. 8867–8873, Sep. 2023. DOI: 10.1021/acs.jpclett.3c02305.

[101] C. J. Takacs, M. A. Brady, N. D. Treat, E. J. Kramer, and M. L. Chabinyc, "Quadrites and Crossed-Chain Crystal Structures in Polymer Semiconductors," *Nano Letters*, vol. 14, no. 6, pp. 3096–3101, Jun. 2014, ISSN: 1530-6984. DOI: 10.1021/nl500150t.

[102] G. L. Schulz *et al.*, "The PCPDTBT Family: Correlations between Chemical Structure, Polymorphism, and Device Performance," *Macromolecules*, vol. 50, no. 4, pp. 1402–1414, Feb. 2017, ISSN: 0024-9297. DOI: 10.1021/acs.macromol.6b01698.

[103] N. M. Harrison, *An Introduction to Density Functional Theory*, Imperial College London Computational Material Science Teaching Resources, https://www.imperial.ac.uk/media/imperial-college/research-centres-and-groups/computational-materials-science/teaching/DFT_NATO.pdf, [Online, accessed Jul. 2024].

[104] J. J. Kwiatkowski, "From Molecules to Mobilities: Modelling Charge Transport in Organic Semiconductors," Ph.D. Thesis, Imperial College London, London, United Kingdom, Dec. 2008.

[105] E. Rice, "Computational Modelling of Electronic States, Charge Transfer and Charge Transport in Organic Semiconductors," Ph.D. Thesis, Imperial College London, London, United Kingdom, Nov. 2017.

[106] W. Kohn and L. J. Sham, "Self-Consistent Equations Including Exchange and Correlation Effects," *Physical Review*, vol. 140, no. 4A, A1133–A1138, Nov. 1965. DOI: 10.1103/PhysRev.140.A1133.

[107] T. Yanai, D. P. Tew, and N. C. Handy, "A new hybrid exchange–correlation functional using the Coulomb-attenuating method (CAM-B3LYP)," *Chemical Physics Letters*, vol. 393, no. 1, pp. 51–57, Jul. 2004, ISSN: 0009-2614. DOI: 10.1016/j.cplett.2004.06.011.

[108] P. J. Stephens, F. J. Devlin, C. F. Chabalowski, and M. J. Frisch, "Ab Initio Calculation of Vibrational Absorption and Circular Dichroism Spectra Using Density Functional Force Fields," *The Journal of Physical Chemistry*, vol. 98, no. 45, pp. 11 623–11 627, Nov. 1994, ISSN: 0022-3654. DOI: 10.1021/j100096a001.

[109] J. Tirado-Rives and W. L. Jorgensen, "Performance of B3LYP Density Functional Methods for a Large Set of Organic Molecules," *Journal of Chemical Theory and Computation*, vol. 4, no. 2, pp. 297–306, Feb. 2008, ISSN: 1549-9618. DOI: 10.1021/ct700248k.

[110] T. Tsuneda and K. Hirao, "Long-range correction for density functional theory," *WIREs Computational Molecular Science*, vol. 4, no. 4, pp. 375–390, 2014, ISSN: 1759-0884. DOI: 10.1002/wcms.1178.

[111] S. Grimme, J. Antony, S. Ehrlich, and H. Krieg, "A consistent and accurate ab initio parametrization of density functional dispersion correction (DFT-D) for the 94 elements H-Pu," *The Journal of Chemical Physics*, vol. 132, no. 15, p. 154 104, Apr. 2010, ISSN: 0021-9606. DOI: 10.1063/1.3382344.

[112] J.-D. Chai and M. Head-Gordon, "Long-range corrected hybrid density functionals with damped atom–atom dispersion corrections," *Physical Chemistry Chemical Physics*, vol. 10, no. 44, pp. 6615–6620, Nov. 2008, ISSN: 1463-9084. DOI: 10.1039/B810189B.

[113] T. H. Dunning Jr., "Gaussian basis sets for use in correlated molecular calculations. I. The atoms boron through neon and hydrogen," *The Journal of Chemical Physics*, vol. 90, no. 2, pp. 1007–1023, Jan. 1989, ISSN: 0021-9606. DOI: 10.1063/1.456153.

[114] B. Baumeier, J. Kirkpatrick, and D. Andrienko, "Density-functional based determination of intermolecular charge transfer properties for large-scale morphologies," *Physical Chemistry Chemical Physics*, vol. 12, no. 36, p. 11 103, 2010, ISSN: 1463-9076, 1463-9084. DOI: 10.1039/c002337j.

[115] E. F. Valeev, V. Coropceanu, D. A. da Silva Filho, S. Salman, and J.-L. Brédas, "Effect of Electronic Polarization on Charge-Transport Parameters in Molecular Organic Semiconductors," *Journal of the American Chemical Society*, vol. 128, no. 30, pp. 9882–9886, Aug. 2006, ISSN: 0002-7863. DOI: 10.1021/ja061827h.

[116] F. Steiner *et al.*, "Distinguishing the influence of structural and energetic disorder on electron transport in fullerene multi-adducts," *Materials Horizons*, vol. 2, no. 1, pp. 113–119, 2015, ISSN: 2051-6347, 2051-6355. DOI: 10.1039/C4MH00173G.

[117] V. Rühle *et al.*, "Microscopic Simulations of Charge Transport in Disordered Organic Semiconductors," *Journal of Chemical Theory and Computation*, vol. 7, no. 10, pp. 3335–3345, Oct. 2011, ISSN: 1549-9618. DOI: 10.1021/ct200388s.

[118] C. C. Moser, S. E. Chobot, C. C. Page, and P. L. Dutton, "Distance metrics for heme protein electron tunneling," *Biochimica et Biophysica Acta (BBA) - Bioenergetics*, 15th European Bioenergetics Conference 2008, vol. 1777, no. 7, pp. 1032–1037, Jul. 2008, ISSN: 0005-2728. DOI: 10.1016/j.bbabio.2008.04.021.

[119] I. Bertini, H. B. Gray, S. J. Lippard, and J. S. Valentine, "6.6: Long-range Electron Transfer in Proteins (Part 1)," in *Bioinorganic Chemistry*, (public version), University Science Books, 1994, ISBN: 0-935702-57-1.

[120] M. J. Abraham, D. van der Spoel, E. Lindahl, and B. Hess, *GROMACS User Manual version 2018*, 2018.

[121] A. S. Gertsen, "Multiscale Modelling of Organic Solar Cell Materials," Ph.D. Thesis, Technical University of Denmark, DTU, Department of Energy Conversion and Storage, Fysikvej, Building 310, 2800 Kgs. Lyngby Denmark, Dec. 2020.

[122] R. W. Hockney, S. P. Goel, and J. W. Eastwood, "Quiet high-resolution computer models of a plasma," *Journal of Computational Physics*, vol. 14, no. 2, pp. 148–158, Feb. 1974, ISSN: 0021-9991. DOI: 10.1016/0021-9991(74)90010-2.

[123] A. Khasbaatar *et al.*, "Solution Aggregate Structures of Donor Polymers Determine the Morphology and Processing Resiliency of Non-Fullerene Organic Solar Cells," *Chemistry of Materials*, vol. 35, no. 7, pp. 2713–2729, Apr. 2023, ISSN: 0897-4756. DOI: 10.1021/acs.chemmater.2c02141.

[124] Y.-Q. Zheng *et al.*, "Unraveling the Solution-State Supramolecular Structures of Donor–Acceptor Polymers and their Influence on Solid-State Morphology and Charge-Transport Properties," *Advanced Materials*, vol. 29, no. 42, p. 1 701 072, 2017, ISSN: 1521-4095. DOI: 10.1002/adma.201701072.

[125] N. E. Jackson *et al.*, "Controlling Conformations of Conjugated Polymers and Small Molecules: The Role of Nonbonding Interactions," *Journal of the American Chemical Society*, vol. 135, no. 28, pp. 10 475–10 483, Jul. 2013, ISSN: 0002-7863. DOI: 10.1021/ja403667s.

[126] P. C. T. Souza *et al.*, "Martini 3: A general purpose force field for coarse-grained molecular dynamics," *Nature Methods*, pp. 1–7, Mar. 2021, ISSN: 1548-7105. DOI: 10.1038/s41592-021-01098-3.

[127] S. J. Marrink, H. J. Risselada, S. Yefimov, D. P. Tieleman, and A. H. de Vries, "The MARTINI Force Field: Coarse Grained Model for Biomolecular Simulations," *The Journal of Physical Chemistry B*, vol. 111, no. 27, pp. 7812–7824, Jul. 2007, ISSN: 1520-6106. DOI: 10.1021/jp071097f.

[128] S. A. J. Hillman *et al.*, "Large Particles, Poor Transport, High Performance: The Importance of Solvent Permeation in Hydrogen-Evolving Polymer Photocatalysts," *in preparation*, 2025 (Expected).

[129] X. Hou *et al.*, "Structure–Property Relationships for the Electronic Applications of Bis-Adduct Isomers of Phenyl-C61 Butyric Acid Methyl Ester," *Chemistry of Materials*, vol. 36, no. 1, pp. 425–438, Jan. 2024, ISSN: 0897-4756. DOI: 10.1021/acs.chemmater.3c02353.

[130] J. J. Kwiatkowski and J. F. Coker, *Jfcoker/tofet*, Jul. 2021.

[131] J. F. Coker, *Jfcoker/MESol*, Sep. 2024.

[132] A. J. Chatten, S. M. Tuladhar, S. A. Choulis, D. D. C. Bradley, and J. Nelson, "Monte Carlo modelling of hole transport in MDMO-PPV: PCBM blends," *Journal of Materials Science*, vol. 40, no. 6, pp. 1393–1398, Mar. 2005, ISSN: 1573-4803. DOI: 10.1007/s10853-005-0572-4.

[133] Y. V. Burdakov and V. Nikitenko, "Monte-Carlo study of drift mobility in ultrathin organic layers: Miller-Abrahams and Marcus models," *Journal of Physics: Conference Series*, vol. 938, p. 012 067, Dec. 2017, ISSN: 1742-6588, 1742-6596. DOI: 10.1088/1742-6596/938/1/012067.

[134] A. Kokil, K. Yang, and J. Kumar, "Techniques for characterization of charge carrier mobility in organic semiconductors," *Journal of Polymer Science Part B: Polymer Physics*, vol. 50, no. 15, pp. 1130–1144, 2012, ISSN: 1099-0488. DOI: 10.1002/polb.23103.

[135] W. E. Spear, "Drift mobility techniques for the study of electrical transport properties in insulating solids," *Journal of Non-Crystalline Solids*, vol. 1, no. 3, pp. 197–214, Apr. 1969, ISSN: 0022-3093. DOI: 10.1016/0022-3093(69)90001-5.

[136] U. K. Deiters, "Efficient Coding of the Minimum Image Convention," *Zeitschrift für Physikalische Chemie*, vol. 227, no. 2-3, pp. 345–352, Mar. 2013, ISSN: 0942-9352. DOI: 10.1524/zpch.2013.0311.

[137] B. Gough, *GNU Scientific Library Reference Manual - Third Edition*, 3rd. Network Theory Ltd., 2009, ISBN: 978-0-9546120-7-8.

[138] S. A. J. Hillman *et al.*, "Why Do Sulfone-Containing Polymer Photocatalysts Work So Well for Sacrificial Hydrogen Evolution from Water?" *Journal of the American Chemical Society*, vol. 144, no. 42, pp. 19 382–19 395, Oct. 2022, ISSN: 0002-7863. DOI: 10.1021/jacs.2c07103.

[139] D. J. Woods *et al.*, "Side-chain tuning in conjugated polymer photocatalysts for improved hydrogen production from water," *Energy & Environmental Science*, vol. 13, no. 6, pp. 1843–1855, Jun. 2020, ISSN: 1754-5706. DOI: 10.1039/D0EE01213K.

[140] N. Siemons *et al.*, "Controlling swelling in mixed transport polymers through alkyl side-chain physical cross-linking," *Proceedings of the National Academy of Sciences*, vol. 120, no. 35, e2306272120, Aug. 2023. DOI: 10.1073/pnas.2306272120.

[141] J. Nelson, S. A. Haque, D. R. Klug, and J. R. Durrant, "Trap-limited recombination in dye-sensitized nanocrystalline metal oxide electrodes," *Physical Review B*, vol. 63, no. 20, p. 205 321, May 2001, ISSN: 0163-1829, 1095-3795. DOI: 10.1103/PhysRevB.63.205321.

[142] J. Nelson and R. E. Chandler, "Random walk models of charge transfer and transport in dye sensitized systems," *Coordination Chemistry Reviews*, Michael Graetzel Festschrift, a tribute for his 60th Birthday, Dye Sensitized Solar Cells, vol. 248, no. 13, pp. 1181–1194, Jul. 2004, ISSN: 0010-8545. DOI: 10.1016/j.ccr.2004.04.001.

[143] T. M. Clarke, F. C. Jamieson, and J. R. Durrant, "Transient Absorption Studies of Bimolecular Recombination Dynamics in Polythiophene/Fullerene Blend Films," *The Journal of Physical Chemistry C*, vol. 113, no. 49, pp. 20 934–20 941, Dec. 2009, ISSN: 1932-7447. DOI: 10.1021/jp909442s.

[144] C. Li and J.-B. Baek, "Recent Advances in Noble Metal (Pt, Ru, and Ir)-Based Electrocatalysts for Efficient Hydrogen Evolution Reaction," *ACS Omega*, vol. 5, no. 1, pp. 31–40, Jan. 2020. DOI: 10.1021/acsomega.9b03550.

[145] G. Zwaschka, Y. Tong, M. Wolf, and R. Kramer Campen, "Probing the Hydrogen Evolution Reaction and Charge Transfer on Platinum Electrodes on Femtosecond Timescales," *ChemElectroChem*, vol. 6, no. 10, pp. 2675–2682, 2019, ISSN: 2196-0216. DOI: 10.1002/celc.201900336.

[146] G. Zuo, M. Linares, T. Upreti, and M. Kemerink, "General rule for the energy of water-induced traps in organic semiconductors," *Nature Materials*, vol. 18, no. 6, pp. 588–593, Jun. 2019, ISSN: 1476-4660. DOI: 10.1038/s41563-019-0347-y.

[147] W. Shi *et al.*, "Purification and electronic characterisation of 18 isomers of the OPV acceptor material bis-[60]PCBM," *Chemical Communications*, vol. 53, no. 5, pp. 975–978, Jan. 2017, ISSN: 1364-548X. DOI: 10.1039/C6CC07820F.

[148] T. Liu, I. Abrahams, and T. J. S. Dennis, "Structural Identification of 19 Purified Isomers of the OPV Acceptor Material bisPCBM by 13C NMR and UV–Vis Absorption Spectroscopy and High-Performance Liquid Chromatography," *The Journal of Physical Chemistry A*, vol. 122, no. 16, pp. 4138–4152, Apr. 2018, ISSN: 1089-5639. DOI: 10.1021/acs.jpca.8b00713.

[149] B. Rice, A. A. Y. Guilbert, J. M. Frost, and J. Nelson, "Polaron States in Fullerene Adducts Modeled by Coarse-Grained Molecular Dynamics and Tight Binding," *The Journal of Physical Chemistry Letters*, vol. 9, no. 22, pp. 6616–6623, Nov. 2018. DOI: 10.1021/acs.jpclett.8b02320.

[150] J. F. Coker *et al.*, "Perpendicular crossing chains enable high mobility in a noncrystalline conjugated polymer," *Proceedings of the National Academy of Sciences*, vol. 121, no. 37, e2403879121, Sep. 2024. DOI: 10.1073/pnas.2403879121.

[151] A. S. Gertsen, *Molecular dynamics force fields for organic solar cell materials*, Technical University of Denmark, Jan. 2021. DOI: 10.11583/DTU.c.5254236.v1.

[152] A. S. Gertsen, M. K. Sørensen, and J. W. Andreasen, "Nanostructure of organic semiconductor thin films: Molecular dynamics modeling with solvent evaporation," *Physical Review Materials*, vol. 4, no. 7, p. 075 405, Jul. 2020. DOI: 10.1103/PhysRevMaterials.4.075405.

[153] S. Moro *et al.*, "The Effect of Glycol Side Chains on the Assembly and Microstructure of Conjugated Polymers," *ACS Nano*, vol. 16, no. 12, pp. 21 303–21 314, Dec. 2022, ISSN: 1936-0851. DOI: 10.1021/acsnano.2c09464.

[154] T. A. Wassenaar, K. Pluhackova, R. A. Böckmann, S. J. Marrink, and D. P. Tieleman, "Going Backward: A Flexible Geometric Approach to Reverse Transformation from Coarse Grained to Atomistic Models," *Journal of Chemical Theory and Computation*, vol. 10, no. 2, pp. 676–690, Feb. 2014, ISSN: 1549-9618. DOI: 10.1021/ct400617g.

[155] N. Michaud-Agrawal, E. J. Denning, T. B. Woolf, and O. Beckstein, "MDAnalysis: A toolkit for the analysis of molecular dynamics simulations," *Journal of Computational Chemistry*, vol. 32, no. 10, pp. 2319–2327, 2011, ISSN: 1096-987X. DOI: 10.1002/jcc.21787.

[156] R. J. Gowers *et al.*, "MDAnalysis: A Python Package for the Rapid Analysis of Molecular Dynamics Simulations," *Proceedings of the 15th Python in Science Conference*, pp. 98–105, 2016. DOI: 10.25080/Majora-629e541a-00e.

[157] M. J. Frisch *et al.*, *Gaussian 16 Revision C.01*, Wallingford, CT, USA, 2016.

[158] A. Wadsworth *et al.*, "Modification of Indacenodithiophene-Based Polymers and Its Impact on Charge Carrier Mobility in Organic Thin-Film Transistors," *Journal of the American Chemical Society*, vol. 142, no. 2, pp. 652–664, Jan. 2020, ISSN: 0002-7863. DOI: 10.1021/jacs.9b09374.

[159] J. F. Ponder Jr *et al.*, "Low-Defect, High Molecular Weight Indacenodithiophene (IDT) Polymers Via a C–H Activation: Evaluation of a Simpler and Greener Approach to Organic Electronic Materials," *ACS Materials Letters*, vol. 3, no. 10, pp. 1503–1512, Oct. 2021. DOI: 10.1021/acsmaterialslett.1c00478.

[160] M. J. Bird *et al.*, "Mobility of Holes in Oligo- and Polyfluorenes of Defined Lengths," *The Journal of Physical Chemistry C*, vol. 118, no. 12, pp. 6100–6109, Mar. 2014, ISSN: 1932-7447, 1932-7455. DOI: 10.1021/jp5010874.

[161] F. Grozema, L. Siebbeles, J. Warman, S. Seki, S. Tagawa, and U. Scherf, "Hole Conduction along Molecular Wires: σ-Bonded Silicon Versus π-Bond-Conjugated Carbon," *Advanced Materials*, vol. 14, no. 3, pp. 228–231, 2002, ISSN: 1521-4095. DOI: 10.1002/1521-4095(20020205)14:3<228::AID-ADMA228>3.0.CO;2-3.

[162] H. Sirringhaus *et al.*, "Two-dimensional charge transport in self-organized, high-mobility conjugated polymers," *Nature*, vol. 401, no. 6754, pp. 685–688, Oct. 1999, ISSN: 1476-4687. DOI: 10.1038/44359.

[163] S. A. Choulis *et al.*, "High ambipolar and balanced carrier mobility in regioregular poly(3-hexylthiophene)," *Applied Physics Letters*, vol. 85, no. 17, pp. 3890–3892, Oct. 2004, ISSN: 0003-6951. DOI: 10.1063/1.1805175.

[164] A. Nawaz *et al.*, "High mobility organic field-effect transistors based on defect-free regioregular poly(3-hexylthiophene-2,5-diyl)," *Organic Electronics*, vol. 38, pp. 89–96, Nov. 2016, ISSN: 1566-1199. DOI: 10.1016/j.orgel.2016.08.002.

[165] A. Nawaz, A. Kumar, and I. A. Hümmelgen, "Ultra-high mobility in defect-free poly(3-hexylthiophene-2,5-diyl) field-effect transistors through supra-molecular alignment," *Organic Electronics*, vol. 51, pp. 94–102, Dec. 2017, ISSN: 1566-1199. DOI: 10.1016/j.orgel.2017.08.032.

[166] H. Chen *et al.*, "Dithiopheneindenofluorene (TIF) Semiconducting Polymers with Very High Mobility in Field-Effect Transistors," *Advanced Materials*, vol. 29, no. 36, p. 1 702 523, 2017, ISSN: 1521-4095. DOI: 10.1002/adma.201702523.

[167] W. Zhang *et al.*, "A Novel Alkylated Indacenodithieno[3,2-b]thiophene-Based Polymer for High-Performance Field-Effect Transistors," *Advanced Materials*, vol. 28, no. 20, pp. 3922–3927, 2016, ISSN: 1521-4095. DOI: 10.1002/adma.201504092.

[168] H. Chen *et al.*, "The Effect of Ring Expansion in Thienobenzo[*b*]indacenodithiophene Polymers for Organic Field-Effect Transistors," *Journal of the American Chemical Society*, vol. 141, no. 47, pp. 18 806–18 813, Nov. 2019, ISSN: 0002-7863, 1520-5126. DOI: 10.1021/jacs.9b09367.

[169] H. Bronstein *et al.*, "Effect of Fluorination on the Properties of a Donor–Acceptor Copolymer for Use in Photovoltaic Cells and Transistors," *Chemistry of Materials*, vol. 25, no. 3, pp. 277–285, Feb. 2013, ISSN: 0897-4756, 1520-5002. DOI: 10.1021/cm301910t.

[170] M. Nikolka, M. Hurhangee, A. Sadhanala, H. Chen, I. McCulloch, and H. Sirringhaus, "Correlation of Disorder and Charge Transport in a Range of Indacenodithiophene-Based Semiconducting Polymers," *Advanced Electronic Materials*, vol. 4, no. 10, p. 1 700 410, 2018, ISSN: 2199-160X. DOI: 10.1002/aelm.201700410.

[171] M. Planells *et al.*, "The effect of thiadiazole out-backbone displacement in indacenodithiophene semiconductor polymers," *Journal of Materials Chemistry C*, vol. 2, no. 41, pp. 8789–8795, Oct. 2014, ISSN: 2050-7534. DOI: 10.1039/C4TC01500B.

[172] C. B. Nielsen, A. J. P. White, and I. McCulloch, "Effect of Fluorination of 2,1,3-Benzothiadiazole," *The Journal of Organic Chemistry*, vol. 80, no. 10, pp. 5045–5048, May 2015, ISSN: 0022-3263. DOI: 10.1021/acs.joc.5b00430.

[173] B. C. Schroeder *et al.*, "Silaindacenodithiophene-Based Low Band Gap Polymers – The Effect of Fluorine Substitution on Device Performances and Film Morphologies," *Advanced Functional Materials*, vol. 22, no. 8, pp. 1663–1670, 2012, ISSN: 1616-3028. DOI: 10.1002/adfm.201102941.

[174] Z. Fei *et al.*, "Germaindacenodithiophene based low band gap polymers for organic solar cells," *Chemical Communications*, vol. 48, no. 24, pp. 2955–2957, Feb. 2012, ISSN: 1364-548X. DOI: 10.1039/C2CC17996B.

[175] H.-Y. Chen, J. Hou, A. E. Hayden, H. Yang, K. N. Houk, and Y. Yang, "Silicon Atom Substitution Enhances Interchain Packing in a Thiophene-Based Polymer System," *Advanced Materials*, vol. 22, no. 3, pp. 371–375, 2010, ISSN: 1521-4095. DOI: 10.1002/adma.200902469.

[176] M. C. Scharber *et al.*, "Influence of the Bridging Atom on the Performance of a Low-Bandgap Bulk Heterojunction Solar Cell," *Advanced Materials*, vol. 22, no. 3, pp. 367–370, 2010, ISSN: 1521-4095. DOI: 10.1002/adma.200900529.

[177] Z. Fei *et al.*, "A low band gap co-polymer of dithienogermole and 2,1,3-benzothiadiazole by Suzuki polycondensation and its application in transistor and photovoltaic cells," *Journal of Materials Chemistry*, vol. 21, no. 40, pp. 16 257–16 263, Oct. 2011, ISSN: 1364-5501. DOI: 10.1039/C1JM13628C.

[178] J. E. Donaghey *et al.*, "Pyrroloindacenodithiophene containing polymers for organic field effect transistors and organic photovoltaics," *Journal of Materials Chemistry*, vol. 21, no. 46, pp. 18 744–18 752, Nov. 2011, ISSN: 1364-5501. DOI: 10.1039/C1JM13428K.

[179] D. H. Kim *et al.*, "Liquid-Crystalline Semiconducting Copolymers with Intramolecular Donor-Acceptor Building Blocks for High-Stability Polymer Transistors," *Journal of the American Chemical Society*, vol. 131, no. 17, pp. 6124–6132, May 2009, ISSN: 0002-7863. DOI: 10.1021/ja8095569.

[180] I. Osaka, G. Sauvé, R. Zhang, T. Kowalewski, and R. D. McCullough, "Novel Thiophene-Thiazolothiazole Copolymers for Organic Field-Effect Transistors," *Advanced Materials*, vol. 19, no. 23, pp. 4160–4165, 2007, ISSN: 1521-4095. DOI: 10.1002/adma.200701058.

[181] C. Karunasena, S. Li, M. C. Heifner, S. M. Ryno, and C. Risko, "Reconsidering the Roles of Noncovalent Intramolecular "Locks" in π-Conjugated Molecules," *Chemistry of Materials*, vol. 33, no. 23, pp. 9139–9151, Dec. 2021, ISSN: 0897-4756. DOI: 10.1021/acs.chemmater.1c02335.

[182] R. Duke, V. Bhat, A. Smith, S. Goodlett, S. Tretiak, and C. Risko, "Factors Impacting Dihedral Angle Rotation and Classification in π-Conjugated Systems," *Macromolecules*, vol. 56, no. 14, pp. 5259–5267, Jul. 2023, ISSN: 0024-9297. DOI: 10.1021/acs.macromol.3c00824.

[183] J. Hou, O. Inganäs, R. H. Friend, and F. Gao, "Organic solar cells based on non-fullerene acceptors," *Nature Materials*, vol. 17, no. 2, pp. 119–128, Feb. 2018, ISSN: 1476-4660. DOI: 10.1038/nmat5063.

[184] A. Karki, A. J. Gillett, R. H. Friend, and T.-Q. Nguyen, "The Path to 20% Power Conversion Efficiencies in Nonfullerene Acceptor Organic Solar Cells," *Advanced Energy Materials*, vol. 11, no. 15, p. 2 003 441, 2021, ISSN: 1614-6840. DOI: 10.1002/aenm.202003441.

[185] L. Zhu *et al.*, "Single-junction organic solar cells with over 19% efficiency enabled by a refined double-fibril network morphology," *Nature Materials*, vol. 21, no. 6, pp. 656–663, Jun. 2022, ISSN: 1476-4660. DOI: 10.1038/s41563-022-01244-y.

[186] S. Holliday *et al.*, "High-efficiency and air-stable P3HT-based polymer solar cells with a new non-fullerene acceptor," *Nature Communications*, vol. 7, no. 1, p. 11 585, Jun. 2016, ISSN: 2041-1723. DOI: 10.1038/ncomms11585.

[187] A. Troisi, "Charge transport in high mobility molecular semiconductors: Classical models and new theories," *Chemical Society Reviews*, vol. 40, no. 5, p. 2347, 2011, ISSN: 0306-0012, 1460-4744. DOI: 10.1039/c0cs00198h.

[188] H. Bristow *et al.*, "Impact of Nonfullerene Acceptor Side Chain Variation on Transistor Mobility," *Advanced Electronic Materials*, vol. 5, no. 10, p. 1 900 344, 2019, ISSN: 2199-160X. DOI: 10.1002/aelm.201900344.

[189] S. Giannini and J. Blumberger, "Charge Transport in Organic Semiconductors: The Perspective from Nonadiabatic Molecular Dynamics," *Accounts of Chemical Research*, vol. 55, no. 6, pp. 819–830, Mar. 2022, ISSN: 0001-4842. DOI: 10.1021/acs.accounts.1c00675.

[190] S. Giannini, A. Carof, M. Ellis, O. G. Ziogos, and J. Blumberger, "Chapter 6. From Atomic Orbitals to Nano-scale Charge Transport with Mixed Quantum/Classical Non-adiabatic Dynamics: Method, Implementation and Application," in *Theoretical and Computational Chemistry Series*, D. R. Salahub and D. Wei, Eds., Cambridge: Royal Society of Chemistry, 2021, pp. 172–202, ISBN: 978-1-83916-178-0. DOI: 10.1039/9781839164668-00172.

[191] D. Baran *et al.*, "Reducing the efficiency–stability–cost gap of organic photovoltaics with highly efficient and stable small molecule acceptor ternary solar cells," *Nature Materials*, vol. 16, no. 3, pp. 363–369, Mar. 2017, ISSN: 1476-4660. DOI: 10.1038/nmat4797.

[192] A. J. Rossini *et al.*, "Dynamic Nuclear Polarization Enhanced Solid-State NMR Spectroscopy of Functionalized Metal–Organic Frameworks," *Angewandte Chemie International Edition*, vol. 51, no. 1, pp. 123–127, 2012, ISSN: 1521-3773. DOI: 10.1002/anie.201106030.

[193] A. J. Rossini *et al.*, "Dynamic Nuclear Polarization Enhanced NMR Spectroscopy for Pharmaceutical Formulations," *Journal of the American Chemical Society*, vol. 136, no. 6, pp. 2324–2334, Feb. 2014, ISSN: 0002-7863. DOI: 10.1021/ja4092038.

[194] P. Murto *et al.*, "Steric Control of Luminescence in Phenyl-Substituted Trityl Radicals," *Journal of the American Chemical Society*, vol. 146, no. 19, pp. 13 133–13 141, May 2024, ISSN: 0002-7863. DOI: 10.1021/jacs.4c00292.

[195] H. Fu *et al.*, "Accurate determination of protein:ligand standard binding free energies from molecular dynamics simulations," *Nature Protocols*, vol. 17, no. 4, pp. 1114–1141, Apr. 2022, ISSN: 1750-2799. DOI: 10.1038/s41596-021-00676-1.

[196] A. J. Clark *et al.*, "Prediction of Protein–Ligand Binding Poses via a Combination of Induced Fit Docking and Metadynamics Simulations," *Journal of Chemical Theory and Computation*, vol. 12, no. 6, pp. 2990–2998, Jun. 2016, ISSN: 1549-9618. DOI: 10.1021/acs.jctc.6b00201.

[197] N. E. Jackson, B. M. Savoie, L. X. Chen, and M. A. Ratner, "A Simple Index for Characterizing Charge Transport in Molecular Materials," *The Journal of Physical Chemistry Letters*, vol. 6, no. 6, pp. 1018–1021, Mar. 2015. DOI: 10.1021/acs.jpclett.5b00135.

[198] N. E. Jackson, L. X. Chen, and M. A. Ratner, "Charge transport network dynamics in molecular aggregates," *Proceedings of the National Academy of Sciences*, vol. 113, no. 31, pp. 8595–8600, Aug. 2016. DOI: 10.1073/pnas.1601915113.

[199] B. S. Sarath Pokuri, S. M. Ryno, R. Noruzi, C. Risko, and B. Ganapathysubramanian, "Computational characterization of charge transport resiliency in molecular solids," *Molecular Systems Design & Engineering*, 2022. DOI: 10.1039/D1ME00163A.

[200] T. O. Lopes, D. F. S. Machado, C. Risko, J.-L. Brédas, and H. C. B. de Oliveira, "Bond Ellipticity Alternation: An Accurate Descriptor of the Nonlinear Optical Properties of π-Conjugated Chromophores," *The Journal of Physical Chemistry Letters*, vol. 9, no. 6, pp. 1377–1383, Mar. 2018. DOI: 10.1021/acs.jpclett.8b00478.

[201] M. B. Price *et al.*, "Free charge photogeneration in a single component high photovoltaic efficiency organic semiconductor," *Nature Communications*, vol. 13, no. 1, p. 2827, May 2022, ISSN: 2041-1723. DOI: 10.1038/s41467-022-30127-8.

[202] E. Sağlamkaya *et al.*, "What is special about Y6; the working mechanism of neat Y6 organic solar cells," *Materials Horizons*, vol. 10, no. 5, pp. 1825–1834, May 2023, ISSN: 2051-6355. DOI: 10.1039/D2MH01411D.

[203] K.-i. Nakayama *et al.*, "Single-Component Organic Solar Cells Based on Intramolecular Charge Transfer Photoabsorption," *Materials*, vol. 14, no. 5, p. 1200, Jan. 2021, ISSN: 1996-1944. DOI: 10.3390/ma14051200.

[204] D. Theunissen, S. Smeets, and W. Maes, "Single-component organic solar cells—Perspective on the importance of chemical precision in conjugated block copolymers," *Frontiers in Chemistry*, vol. 11, Dec. 2023, ISSN: 2296-2646. DOI: 10.3389/fchem.2023.1326131.

Appendix A

Microstructure

A.1 IDTBT Chains on Substrate: S and T stacks

Figure A.1c shows the orientation between IDTBT backbone planes for simulations of chains deposited on substrate. We can observe that larger angles are more common when side chain lengths are longer, especially at C8 and above. This demonstrates a discrepancy with the STM results, in which only S-stacked backbones were observed [1].

Figure A.2a shows that, at longer side chain lengths, contributions to the enthalpic interaction energy (E) are dominated by interactions between side chains and the substrate. This occurs even though the side chain-substrate E values have been divided by 12 (the number of monomers in each chain), to roughly account for the fact that the side chains are in contact with the substrate across the full length of both chains, while the chains can typically only interact with one-another within a $\sim$1 monomer range (due to their perpendicular crossing arrangement).

Figure A.2c shows that, if only interactions between the backbones of two C16-IDTBT chains are considered, we recover the expected relationship between E and the relative orientation of the backbones. Namely, that it is energetically favourable for backbones to be in and S-stacked (π-stacked) arrangement. Figure A.2c shows the relationship between the relative orientation of the backbones and the contribution to E from interactions between side chains and the substrate. Here, we see that there is a large degree of noise in the E values, and that there is no obvious trend. Because the rigid backbones are much less influenced by entropic effects than the flexible side chains, it may be that, at long timescales, the preference for an S-stacked arrangement between the backbones will eventually lead to most contact points adopting this configuration, thus explaining why this is the case in the physical contacts probed by STM. However, on the shorter timescales accessible by MD, contact arrangements will be dominated by the interactions between side chains and substrate, which show no preference for S-stacked backbones, and the random entropic motion of the side chains. Thus, we see a wider variety in the angles between the planes of the backbones at the conclusion of the MD simulations. In addition, the discrepancy between the simulated and experimental observations may

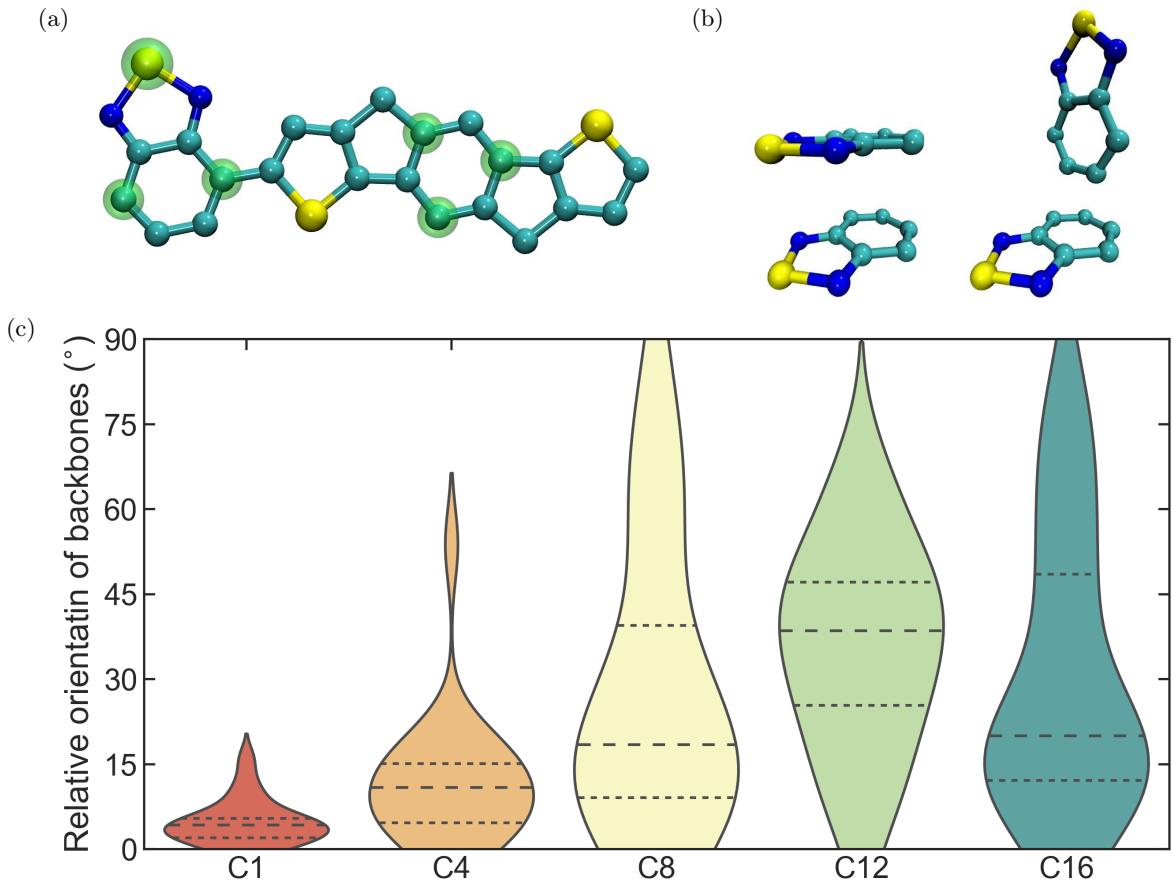


Figure A.1: Relative orientation between IDTBT backbone planes for simulations of chains deposited on substrate. (a) An IDTBT monomer, with side chains and hydrogen atoms hidden. The orientation of the BT and IDT units are defined using the vector orthogonal to the plane of these units, where the plane is chosen to intersect through the three atoms highlighted in green. The relative angle between two backbones is calculated from the difference between the orientation of the closest BT or IDT units (based on their CoGs). (b) Diagrams illustrating S (left) and T (right) orientations of BT units, corresponding to relative angles of 0° and 90°, respectively. (c) Distributions of the relative orientation between backbones, calculated from simulations with different side chain lengths (20 repeats each).

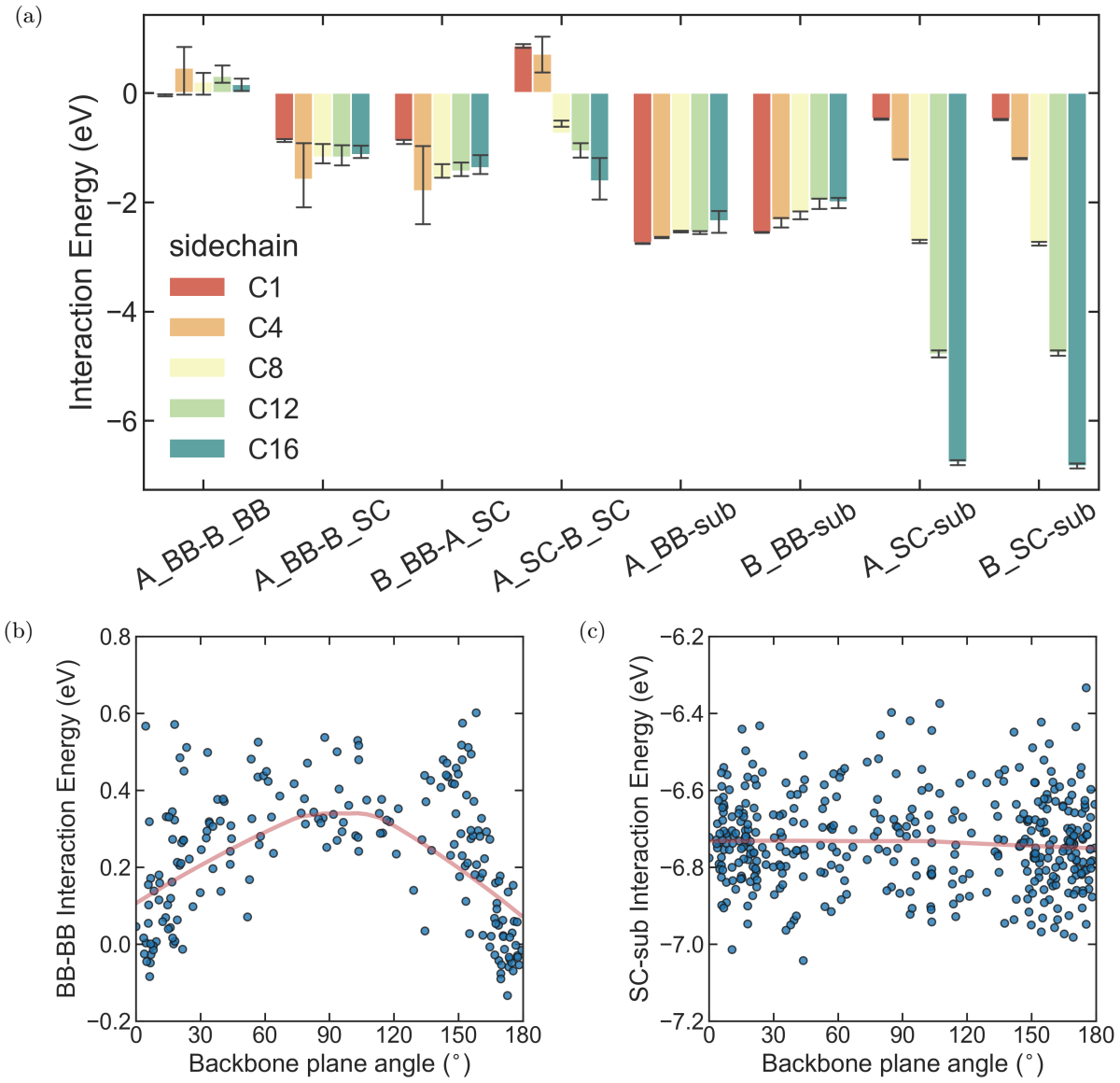


Figure A.2: Enthalpic interaction energy (E) trends for pairs of IDTBT chains on substrate. A and B refer to the two polymer chains, BB to backbone atoms, SC to side chain atoms, and sub to the substrate. Interaction energies involving the substrate are divided by 12, the number of monomers in each chain. All interaction energies are calculated using single point calculations based on an empirical forcefield (adopting the same atomistic forcefield as the MD simulations described in Chapter 5). (a) Contributions to E from interactions between different components of the system. Multiple bars are shown for each contribution, which correspond to simulations with different side chain lengths (20 repeats each). Error bars indicate the interquartile range. (b) and (c) show the relationship of E between different components and the angle between the planes of the backbone units in contact (i.e. their relative rotation). Calculated values were derived from 200 repeats simulation using C16 side chains. The red lines are LOWESS functions which serve as a guide to the eye.

be related to the inability of MD forcefields to fully capture π-π interactions that would be enhanced in an S-stacked arrangement.

A.2 Backmapping Details

Here, I provide details of the backmapping procedure applied during the investigation described in Chapters 5 and 6. Backmapping is a technique used to convert CG microstructural models to an atomistic representation. This retains the orientation and conformation of chains, while providing access to atomic-scale information.

My implementation of the backmapping technique was based on the procedure `backwards`, developed by Tsjerk Wassenaar [2]. A notable feature of `backwards` is the inclusion of an initial projection step; Taking the positions of CG beads as input, a mapping file is employed, customised for each species, to project a reasonable first guess for the positions of atoms. This is an improvement over other backmapping procedures, which tend to randomly place atoms near their respective beads, often leading to a poor initial guess of the atomistic structure and thus to larger changes in the conformation of molecules, or to numerical instabilities in subsequent simulations. By default, `backwards` performs the following steps:

1) Projection

2) Optimise with non-bonded interactions disabled.

3) Optimise with all interactions enabled.

4–7) Run a series of very short MD simulations. The simulation timestep at is initially small (0.2 fs), and with each simulation gradually increases, until reaching a standard timestep for atomistic MD (2.0 fs).

Because of the subsequent optimisation steps, the initial projection does not need to be highly precise. Note that, for the two optimisation steps, bonded interactions are prioritised first as they are stiffer than non-bonded interactions, and so more likely to cause numerical issues when stretched into non-realistic arrangements. For the final series of MD steps, shorter timesteps are initially used because they are more numerically stable. The mentioned numerical issues refers to the tendency of MD simulations to crash when there are extremely steep potentials in the system, usually due to unrealistic structures. These steep potentials cause large forces to be established on atoms, which prevents the MD algorithm from propagating the system, since it cannot unambiguously calculate the next position of the atoms.

To suit the `backwards` procedure to my purposes, I made a number of modifications. These included:

- Converting `backwards.py` to `python 3`. This was done so that I could integrate it with my other scripts.

- Introducing a collision avoidance step between steps 3 and 2, which detects atoms positioned too close to one another and pushes them apart. This improved the stability of the procedure for large solid state structures with lots of closely packed molecules.

- Introducing a monomer index group. This was necessary to ensure that the polymers I was backmapping were recognised by the script (the original script is designed for biological systems and only recognises proteins, membranes and solvents).

- Introduced an option to specify a mapping file. This allows multiple projection schemes to exist for a given species and forcefield, from which one can be selected unambiguously.

- Introduced an option to halt backmapping after the initial projection step. This was useful for checking the quality of the applied projection scheme.

To use the backwards procedure on the CG models described in Chapter 5, I needed to create mapping files for each of the polymers: C16-IDTBT, P3HT, and PffBT4T-2OD. Within each file, I created separate mapping schemes for the start, internal, and end monomers of the chains, to account for terminal groups. As a general principle, I found it best to project the atoms such that, where possible, each atom was given a unique position, and atoms were placed reasonably far apart.

Some details of the projection maps are provided here. For the polymer backbones, I used the average positions of beads, including virtual beads, to try and place atoms in reasonable arrangements with respect to other atoms. This was helped by the fact that `Martini` beads are slightly more fine grained than in other CG models [3]. Combining this with the CG modelling principles for organic systems developed by Anders Gertsen and Riccardo Alessandri [4], the result is that each π-conjugated ring is usually defining using a few beads, which can make positioning atoms easier. The 'trans' and 'cis' functions provided by `backwards` were employed to arrange atoms when there was no selection of beads whose average position would give an appropriate position. The 'out' function was used to place hydrogen atoms outside of the heavy backbone atoms.

Developing a projection map for the side chains was slightly more tricky, because the relatively simple chemical structure of the alkane side chains means that they are usually represented by a low number of `Martini` beads. For the linear portions of the side chains, I used a rolling average applied to the bead locations to space carbons evenly. The hydrogen atoms were generally placed at the same location as their bonded carbon. For PffBT4T-2OD, the branched side chains were difficult to deal with. My early projection attempts often produced overlapping atoms near the branching point, causing crashes. To address this, I used the 'trans' and 'cis' functions to try and separate atoms where possible. However, in the end, I only managed to consistently avoid crashes by introducing an

additional step into the backmapping scheme, placed between the bonded-only optimisation (step 3) and non-bonded optimisation (step 2). It consisted of a simple collision avoidance check. This involved searching through the partially-optimised model to locate any atom pairs that were within a short-cutoff distance. Any pairs of colliding atoms were then automatically pushed apart by a small distance. After implementing this step, I was able to backmap large and dense systems without issue.

I ran `backwards` on the CG models with the following parameters modified from their default values: `from Martini`, `to OPLS-AA`, `kick 0.1`, `em 100`, `nb 1000`.

`from Martini` and `to OPLS-AA` were used to select the forcefields I was converting between. `kick` was increased from its default value of 0.05 Å to make collisions less likely after projection, especially in the side chains, where I could not always separate hydrogen atoms from carbons. `em` was changed to reduce the number of iterations made during the bonded-only optimisation step from its default value of 500. This was done to to prevent chain conformations optimising too much before non-bonded interactions are introduced, which can lead to overlapping atoms, especially between stiff backbones that will gradually straighten during optimisation. `nb` was increased from its default value of 500 to reduce the forces in the system before running MD simulations, and therefore improve numerical stability.

A.3 Chain Orientation in C16-IDTBT Microstructural Models

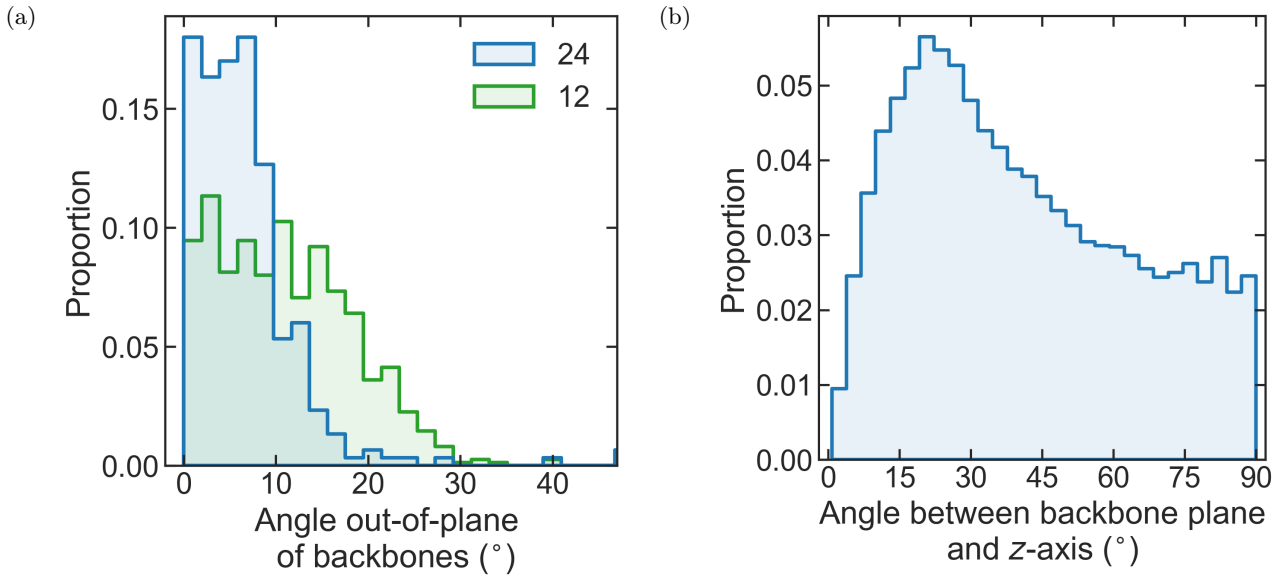


Figure A.3: Orientation of C16-IDTBT chains in the microstructural model. (a) Distribution of angles between chain end-to-end vectors and the xy-plane of the model for the C16-IDTBT 24mer and 12mer systems. This reveals the proportion of chains angled out-of-plane. (b) Distribution of angles between the conjugated plane of backbone moieties and the z-axis of the model. Calculated for the C16-IDTBT 24mer model. This reveals the proportion of backbone moities that are face-on to the upper and lower (i.e., substrate) interfaces.

Appendix B

Contact Geometry and Electronic Coupling

B.1 Extended Moiety Contact Maps

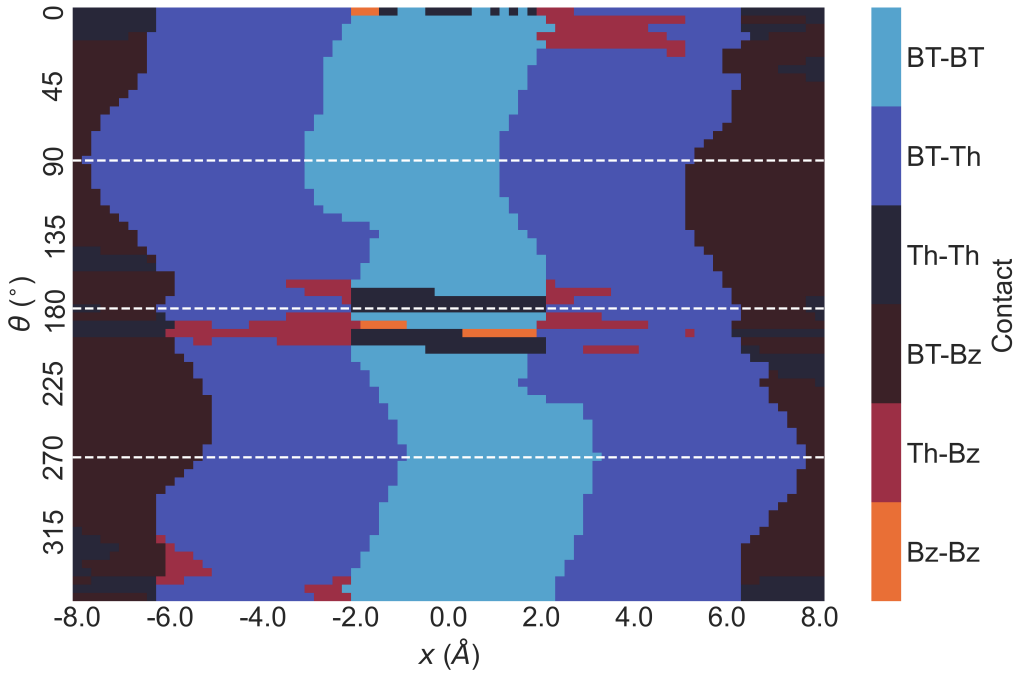


Figure B.1: A contact map, showing the combination of IDTBT moieties at the point of closest contact. This combination changes as the upper segment is translated (x-axis) and rotated (y-axis) with respect to the static lower segment. The horizontal dashed lines denote parallel and perpendicular arrangements of the segments.

B.2 Interaction Maps with y-Shift

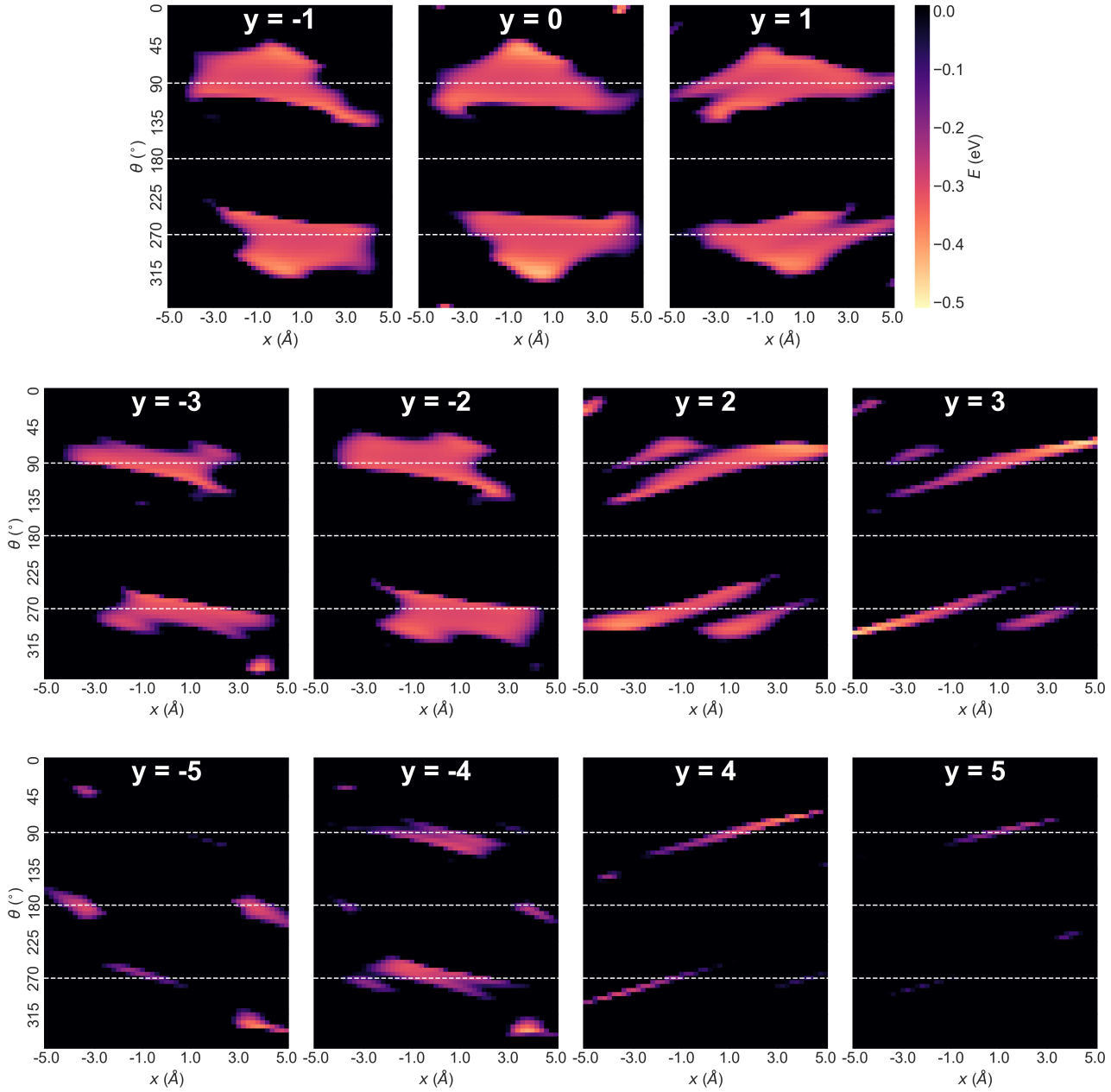


Figure B.2: Maps displaying the enthalpic interaction energies (E) between a pair of IDTBT 2mer segments with methyl side groups. Different maps are shown for translations of the upper chain segment in the y-direction, i.e., orthogonal to the backbone direction of the static lower chain (x) and the conjugated plane of both segments. The translation in y is shown on the maps (in Å). Dashed lines represent parallel and perpendicular arrangements of the segments. Interaction energies were calculated using single point calculations based on an empirical forcefield (adopting the same atomistic forcefield as the MD simulations described in Chapter 5). Note that the scale of the colour range has been reduced compared to the DFT-based E maps shown in Figures 6.2 and 7.5.

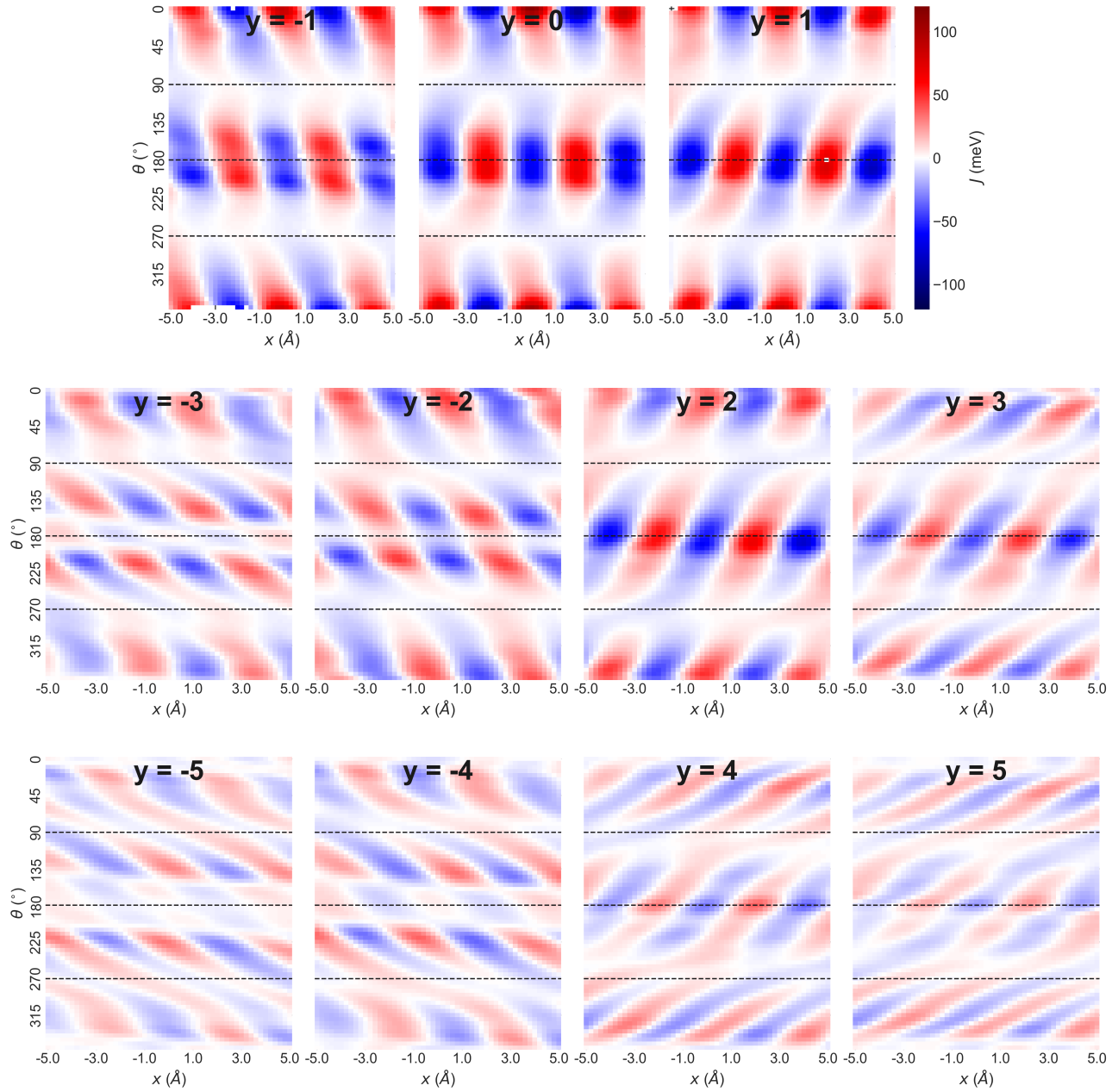


Figure B.3: Maps displaying the HOMO-HOMO coupling (J) between a pair of IDTBT 2mer segments with methyl side groups, on a linear scale. Different maps are shown for translations of the upper chain segment in the y-direction, i.e., orthogonal to the backbone direction of the static lower chain (x) and the conjugated plane of both segments. The translation in y is shown on the maps (in Å). Dashed lines represent parallel and perpendicular arrangements of the segments. Coupling values were calculated using the molecular orbital overlap (MOO) method described in [5]. Making use of the ZINDO Hamiltonian, this method requires only a single self-consistent field calculation, performed on an isolated molecule, to estimate the electronic coupling between a pair of identical molecules in multiple contact geometries.

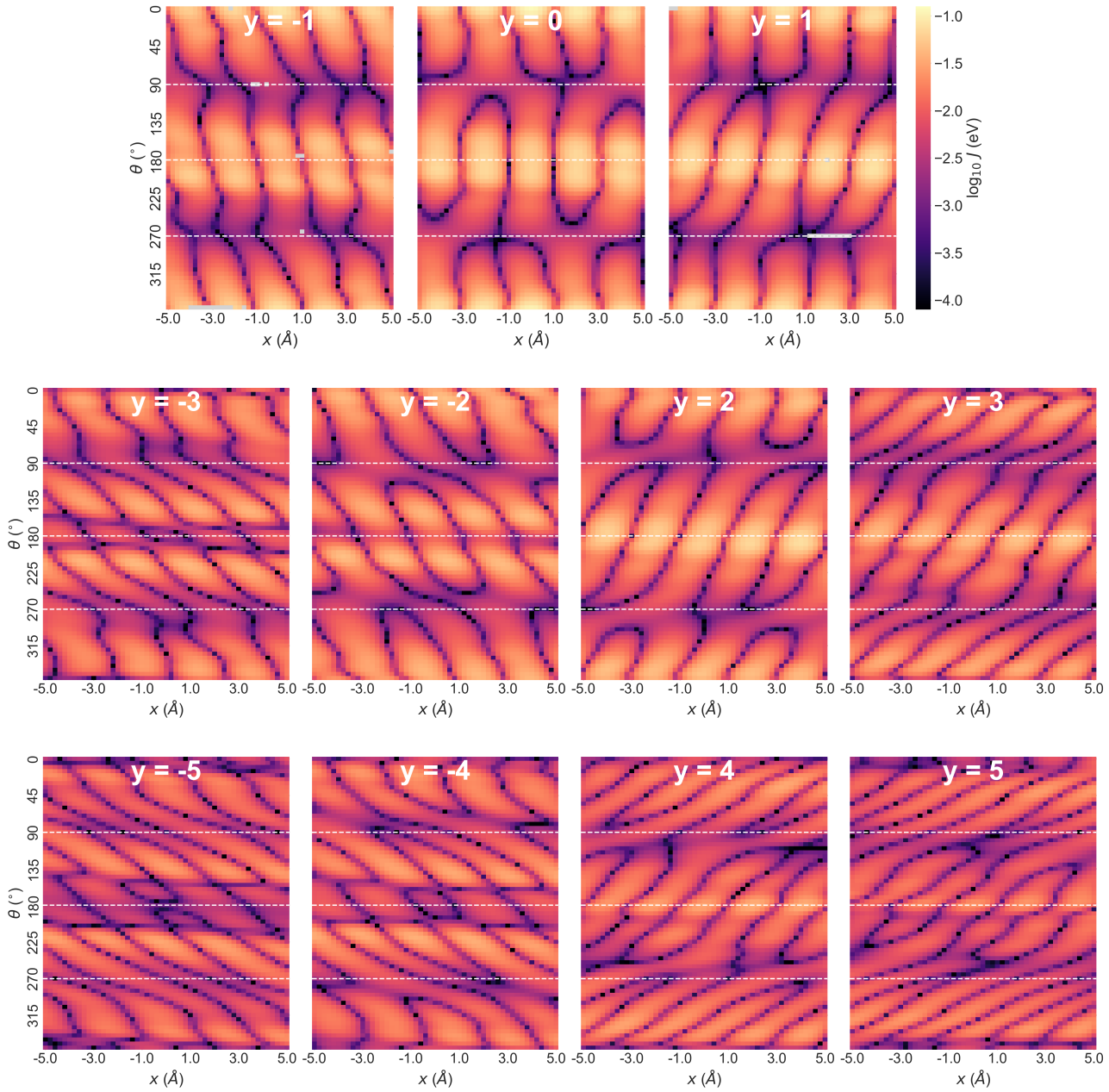


Figure B.4: Maps displaying the hole coupling (E) between a pair of IDTBT 2mer segments with methyl side groups, on a logarithmic scale. Different maps are shown for translations of the upper chain segment in the y-direction, i.e., orthogonal to the backbone direction of the static lower chain (x) and the conjugated plane of both segments. The translation in y is shown on the maps (in Å). Dashed lines represent parallel and perpendicular arrangements of the segments. Coupling values were calculated using the molecular orbital overlap (MOO) method described in [5]. Making use of the ZINDO Hamiltonian, this method requires only a single self-consistent field calculation, performed on an isolated molecule, to estimate the electronic coupling between a pair of identical molecules in multiple contact geometries.

B.3 Variants B and C Interaction maps

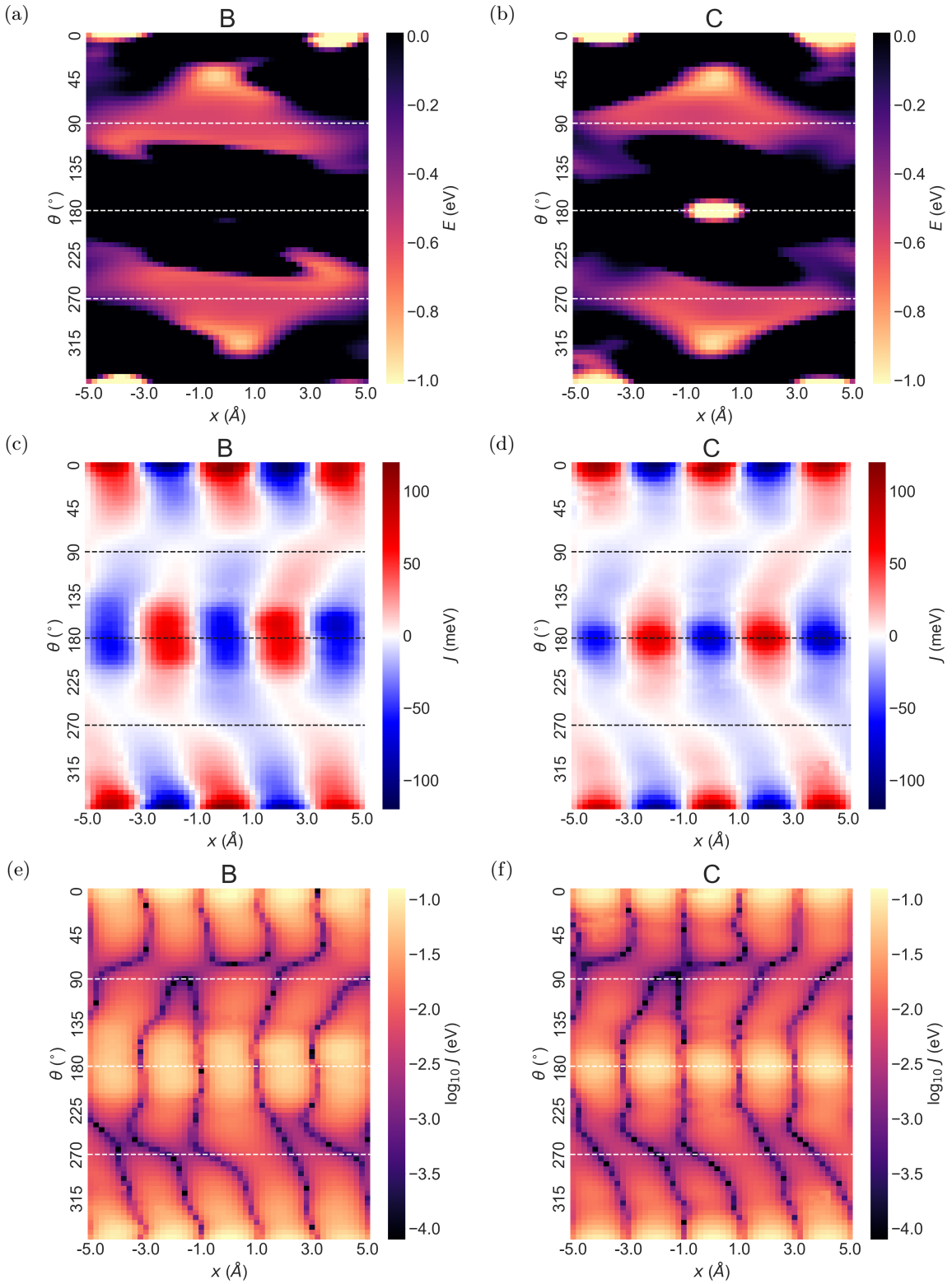


Figure B.5: Maps displaying the enthalpic interaction energies (E) and hole transfer integrals (J_{inter}) between a pair of 2mer segments with methyl side groups. Dashed lines represent parallel and perpendicular arrangements of the segments. The left column shows interactions between variant B segments, while the right column shows interactions between variant C segments. The first row shows E maps. The second row shows J_{inter} maps with a linear scale. The third row shows J_{inter} maps with a logarithmic scale.

B.4 LUMO-LUMO Coupling

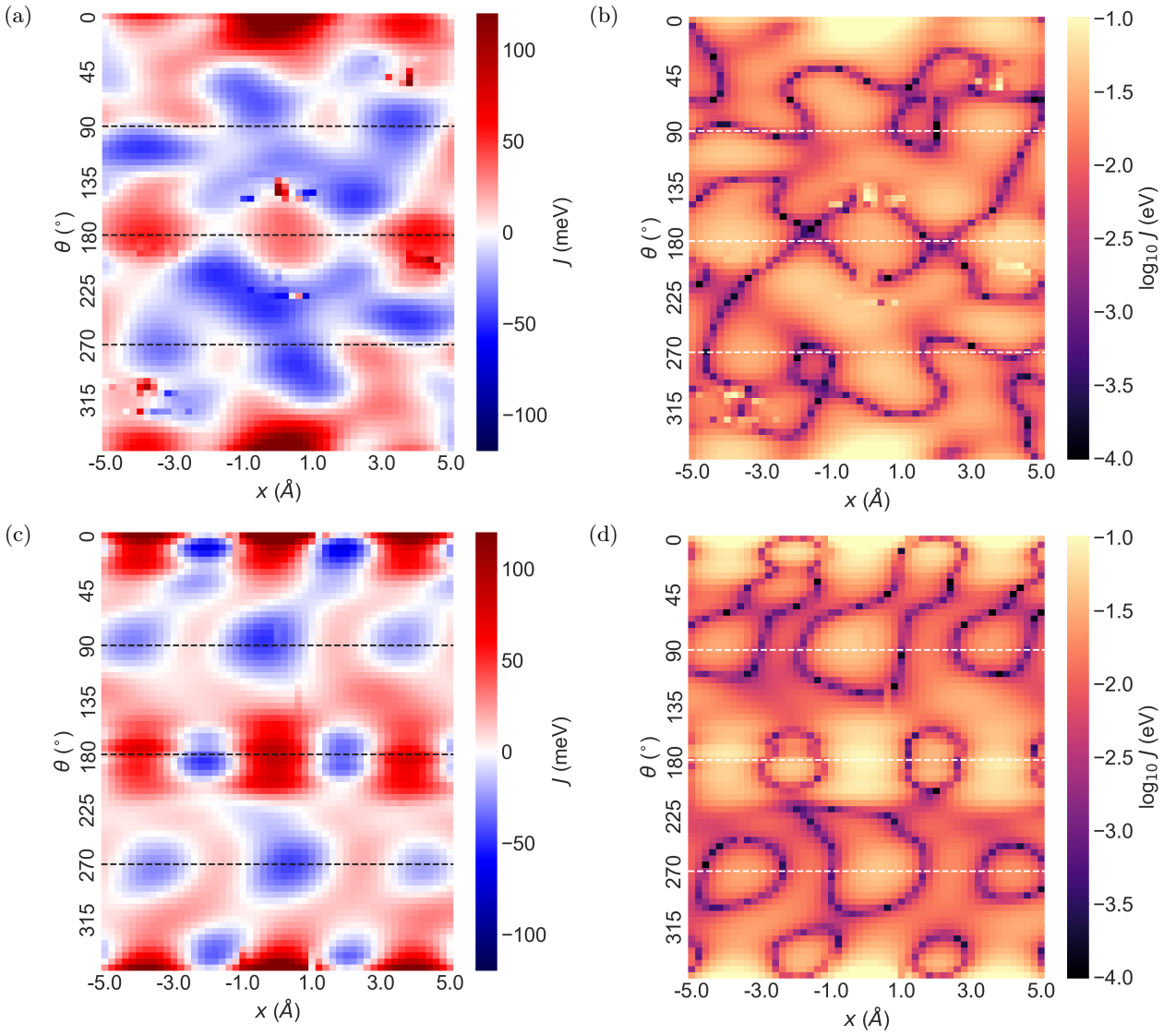


Figure B.6: Maps displaying the LUMO-LUMO coupling (J) between a pair of ∼3.2 nm segments with methyl side groups. Dashed lines represent parallel and perpendicular arrangements of the segments. The first row shows J between IDTBT 2mer segments, on a) linear, and b) logarithmic scales. The second row shows J between P3HT 8mer segments, on a) linear, and b) logarithmic scales. Coupling values are derived from the same calculations described in Section 6.2.1. The LUMO-LUMO couplings tend to show some artefacts for certain arrangements, for unknown reasons.

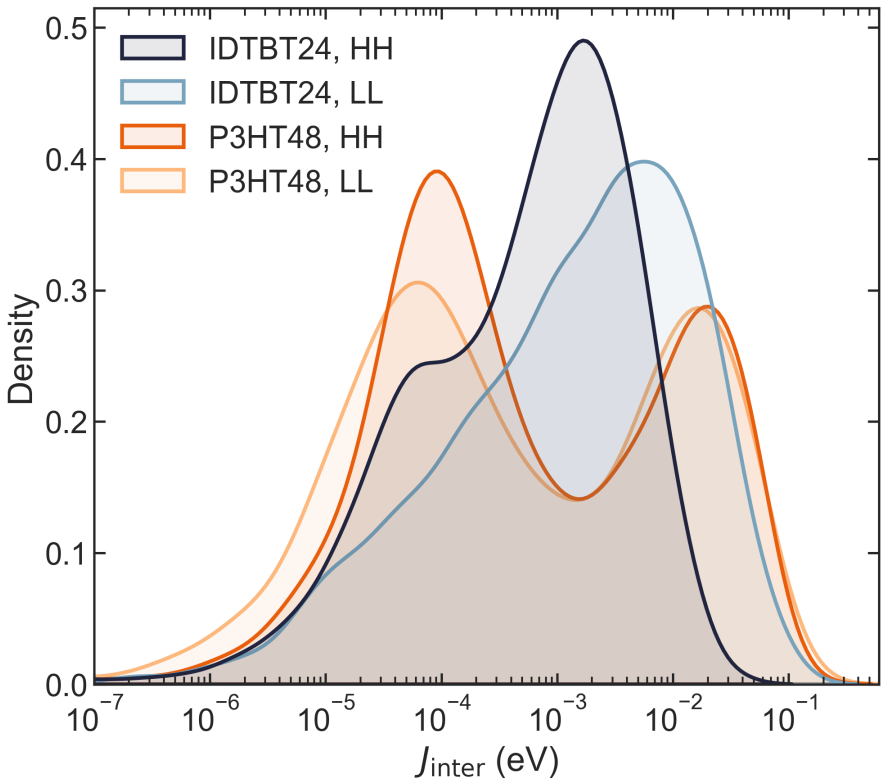


Figure B.7: Distribution of J_{inter} for contacts extracted from the thin film models of C16-IDTBT 24mers, and P3HT 48mers. Both HOMO-HOMO (HH) and LUMO-LUMO (LL) coupling values are shown, for comparison. Coupling values are derived from the same calculations described in Section 6.2.2.

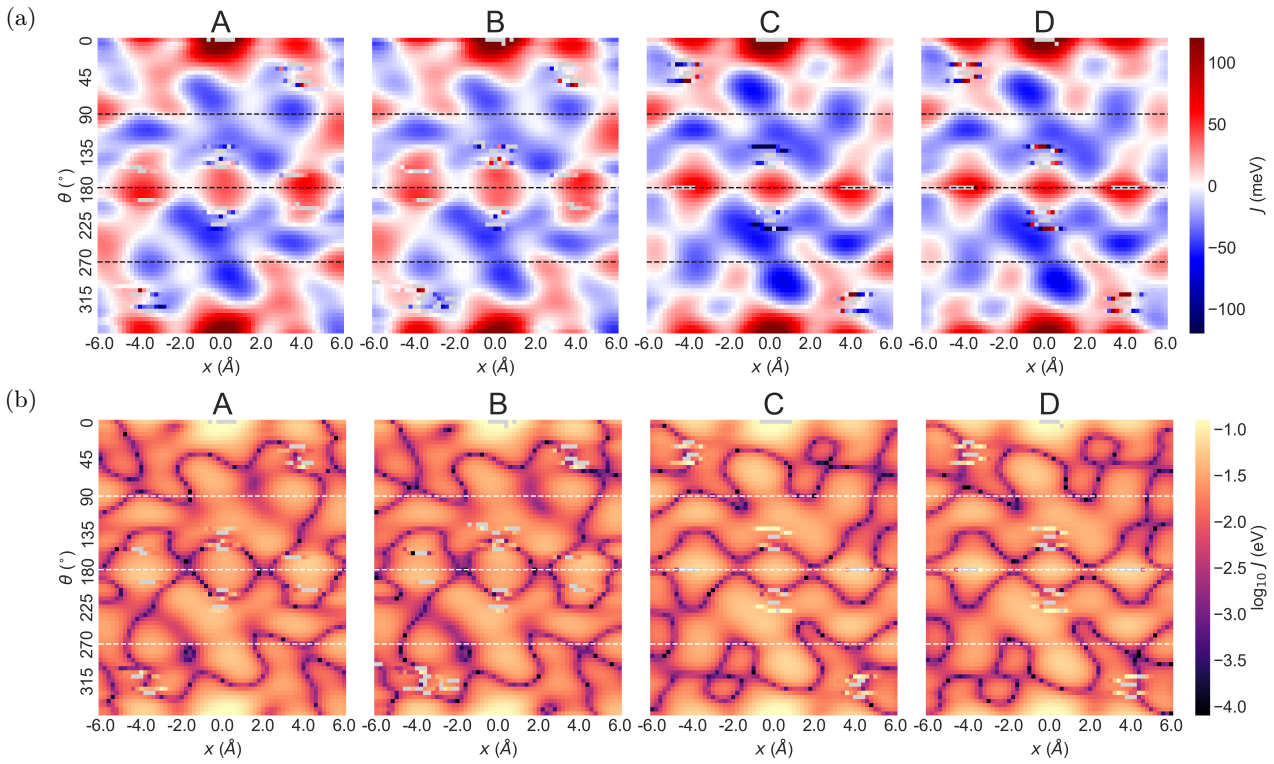


Figure B.8: Maps displaying the LUMO-LUMO coupling (J) between a pair of IDTBT variant 2mer segments with methyl side groups. Dashed lines represent parallel and perpendicular arrangements of the segments. Values are shown on a) a linear scale, and b) a logarithmic scale. Coupling values are derived from the same calculations described in Section 7.2.3. The LUMO-LUMO couplings tend to show some artefacts for certain arrangements, for unknown reasons.

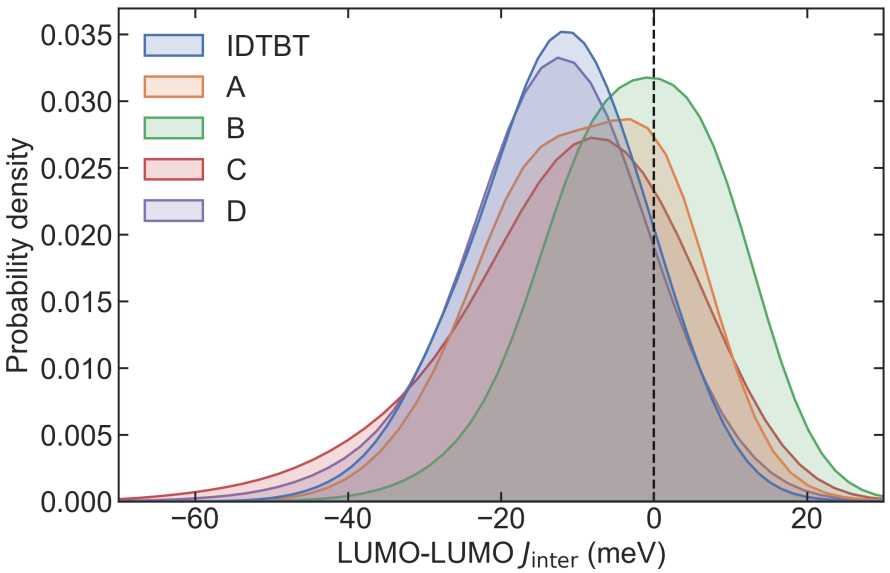


Figure B.9: Distribution of LUMO-LUMO coupling strengths (J_{inter}) for pairs of contacting IDTBT segments, and variants. Contributions of different J_{inter} values are weighted according to the probability of finding the system in the arrangement which establishes that J_{inter}. Coupling values are derived from the same calculations described in Sections 7.2.3 and 7.2.4.

Appendix C

Temperature and Field Dependence of Mobility.

The temperature and field dependence of mobility in C16-IDTBT and P3HT were evaluated using KMC simulations (see Chapter 6). Transport was simulated in the different axis-directions of the microstructural models. μ_{intra} values for C16-IDTBT and P3HT are set to the experimentally-informed values discussed in Section 6.2.3 ($3\,\text{cm}^2/\text{Vs}$ and $0.02\,\text{cm}^2/\text{Vs}$ respectively).

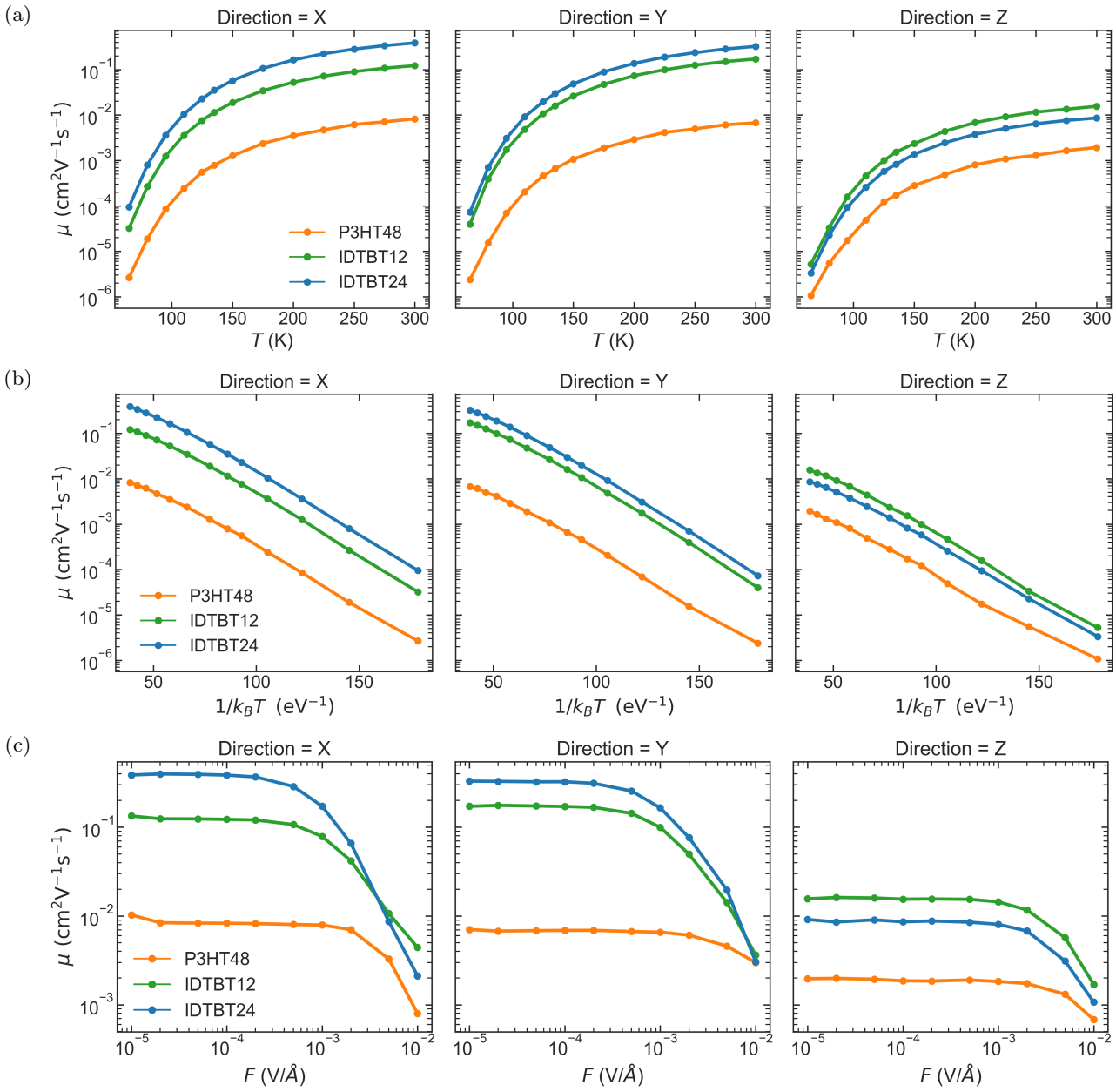


Figure C.1: Mobility calculations for C16-IDTBT and P3HT, from KMC simulations. a) Temperature dependence of hole mobility b) Temperature dependence of hole mobility, shown on an Arrhenius plot. c) Field strength dependence of hole mobility.

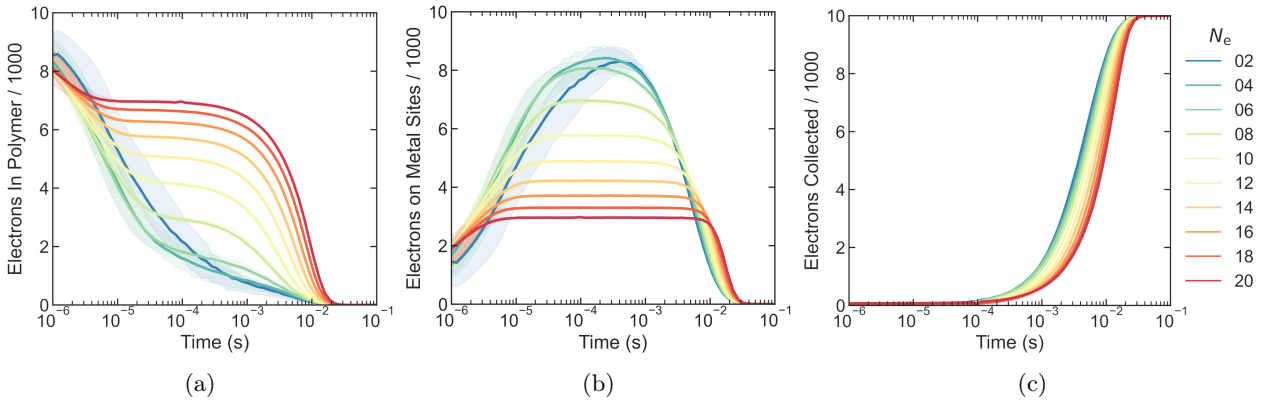
Appendix D

Parameter Exploration for Polymer Photocatalyst Model

Default Parameter Values

Parameter	Value
N_{metal}	6
J_{polymer}	0.6 meV
J_{metal}	0.1 meV
$J_{\text{reduction}}$	3×10^{-4} meV
$\epsilon_{\text{polymer}}$	0 meV
ϵ_{metal}	−300 meV
$\epsilon_{\text{reduction}}$	−300 meV
ξ	0
β_{polymer}	0
β_{metal}	0
$\beta_{\text{reduction}}$	0
λ	300 meV
T	300 K
F	1×10^4 V cm^{-1}

Table D.1: Default parameter values for the polymer photocatalyst model. For the parameter exploration results shown here, all model parameters were set to their default values, unless stated otherwise. When implementing disorder, all polymer site energy values ($\epsilon_{\text{polymer}}$) were sampled from an exponential distribution with scaling factor ξ (see Equation 4.1). Disordered coupling values (J) were computed by first sampling from an exponential distribution with scaling factor β, and then inputting each sampled value (x) into the function $J = J_0 \exp(-x)$, where J_0 is either J_{polymer}, J_{metal}, or $J_{\text{reduction}}$, depending on where coupling disorder is being implemented. This method was chosen in order to model a exponential distribution of packing distances between sites (and assuming an exponential decrease of J with packing distance). The resulting distribution has the shape of a conventional exponential distribution when plotted on a logarithmic scale (see Figure D.7d). When disorder was present, 10 repeats of each system were created and simulated to gather results, with ϵ or J values resampled from the distribution for each repeat.



(a) (b) (c)

Figure D.1: Transient populations in a) polymer, b) metal, and c) collected.

Varying Singular Parameter Values

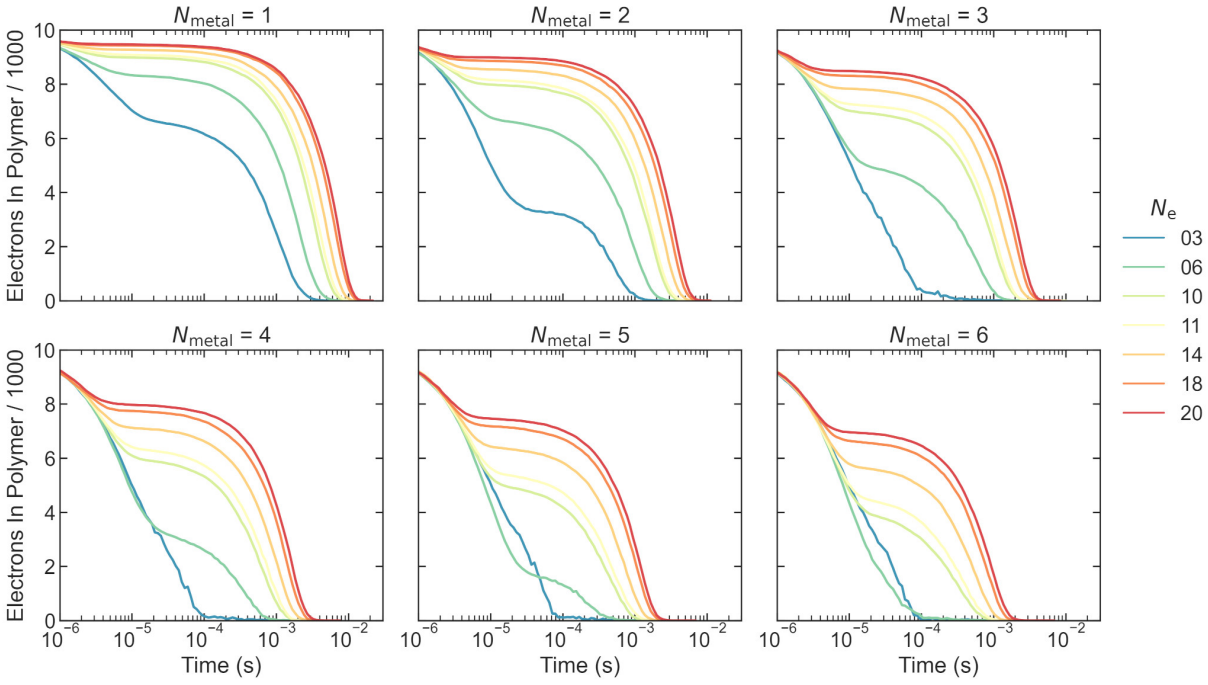


Figure D.2: Varying N_{metal}.

Varying N_{metal} (Figure D.2) affects the length of the initial phase in the transient population kinetics (when electrons have yet to fully occupy the metal sites), as well as governing at which N_e the second (queuing) phase is present at all. For higher N_{metal}, the different N_e-curves diverge at later times, and when there are fewer electrons still remaining in the polymer region.

Varying J_{polymer} (Figure D.3) also impacts the length of the initial phase, shifting the divergence point of the N_e-curves to different times, but without affecting the population threshold at which queuing begins. This reflects the speed at which charges can travel through the polymer region, to begin occupying the metal sites (i.e., the polymer's mobility).

J_{metal} has a relatively minor influence (Figure D.4), unless it is decreased significantly below J_{polymer}

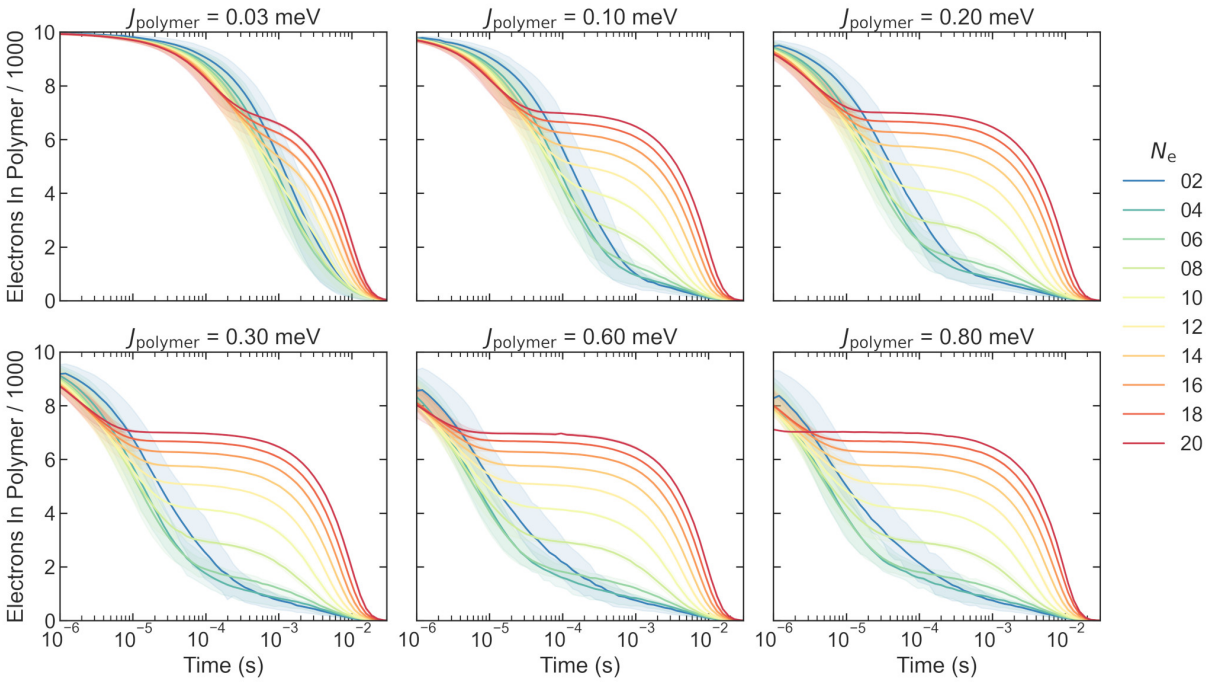


Figure D.3: Varying J_{polymer}.

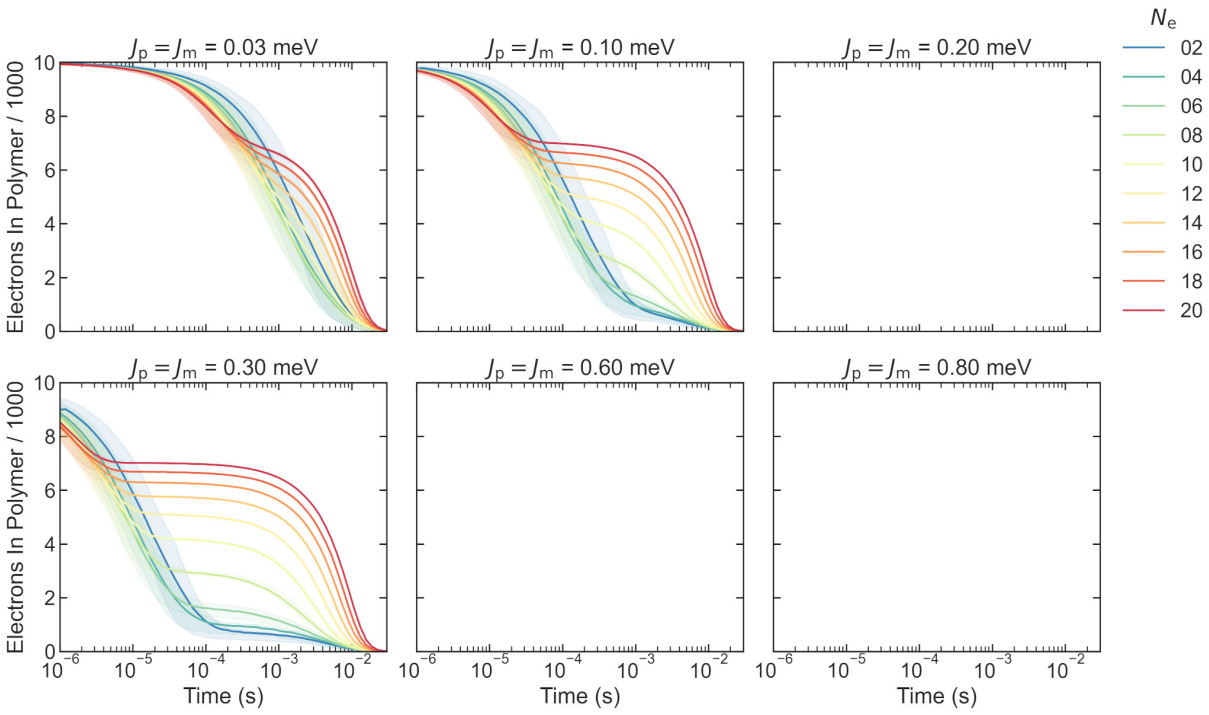


Figure D.4: Varying J_{polymer} and J_{metal} (equal values). Some plots are left blank in order to ease visual comparison with Figure D.3.

(Figure D.5), in which case the queuing effect will be reduced, leading to less separation between the different N_e-curves.

$J_{\text{reduction}}$ is a critical parameter, since it determines the rate of the (typically) limiting proton reduction step (Figure D.6). The queuing effect is only observed when $J_{\text{reduction}} < J_{\text{polymer}}$ and $J_{\text{reduction}} < J_{\text{metal}}$. Tuning this model parameter in particular was used to ensure that the time at

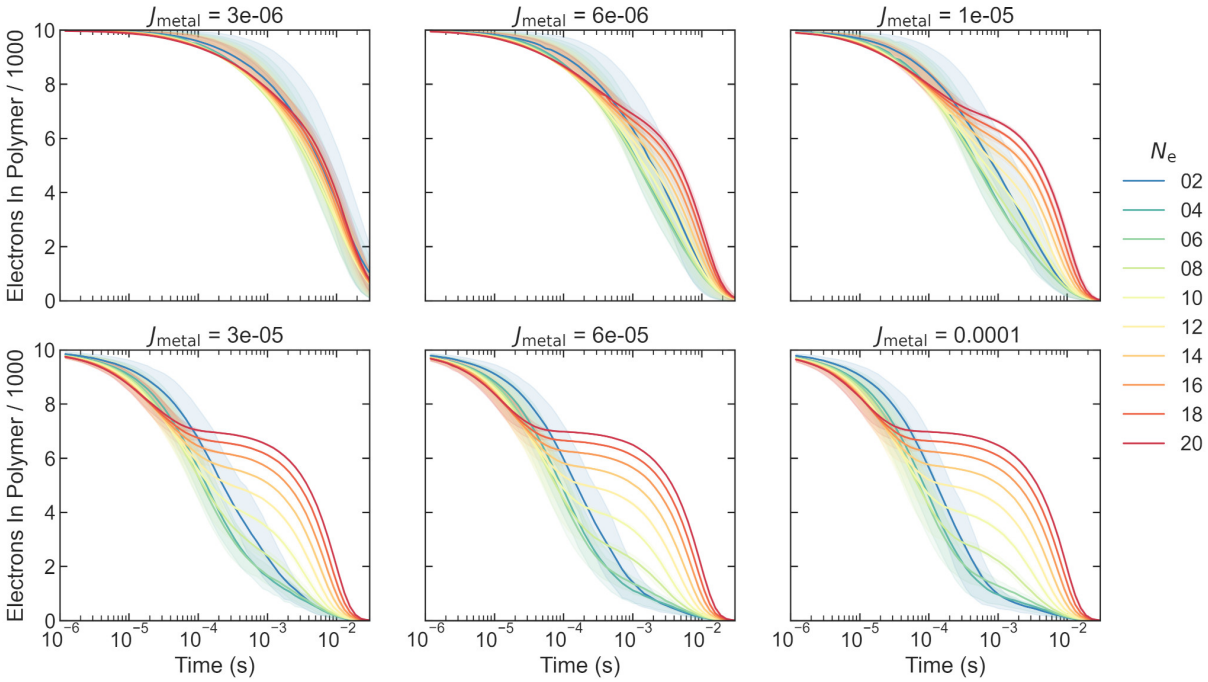


Figure D.5: Varying J_{metal}. J_{polymer} was set to 0.1 meV. Values in the title of each plot are in eV.

which all electrons have exited the polymer region was in correspondence with the experimental data (∼10 ms, see Figure 4.2).

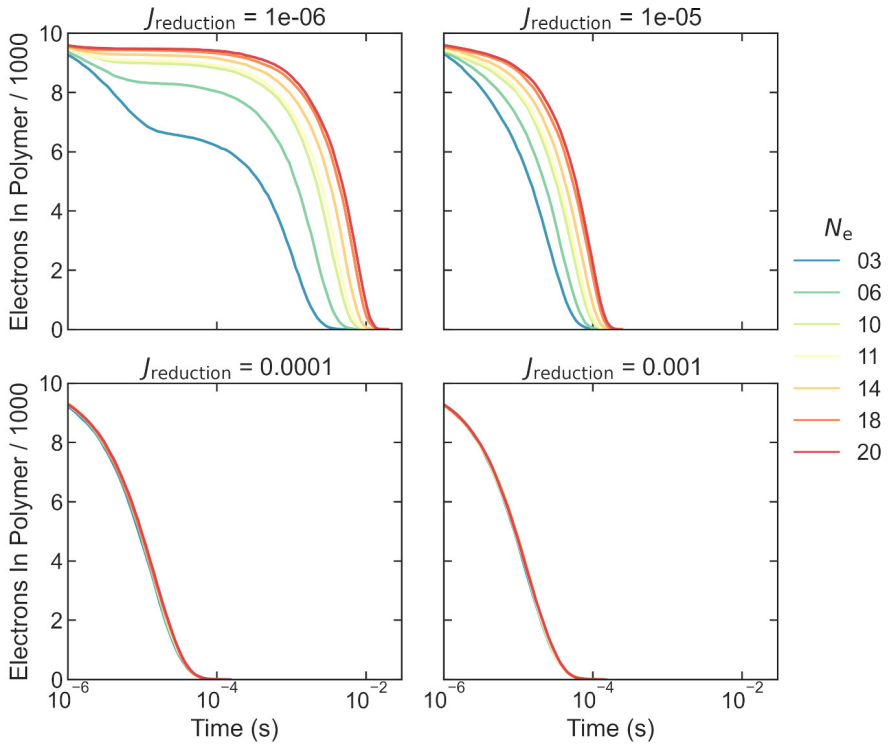


Figure D.6: Varying $J_{\text{reduction}}$. N_{metal} was set to 1, while J_{polymer} was set to 0.1 meV. Values given in the title of each plot are in eV.

Varying Disorder Scales

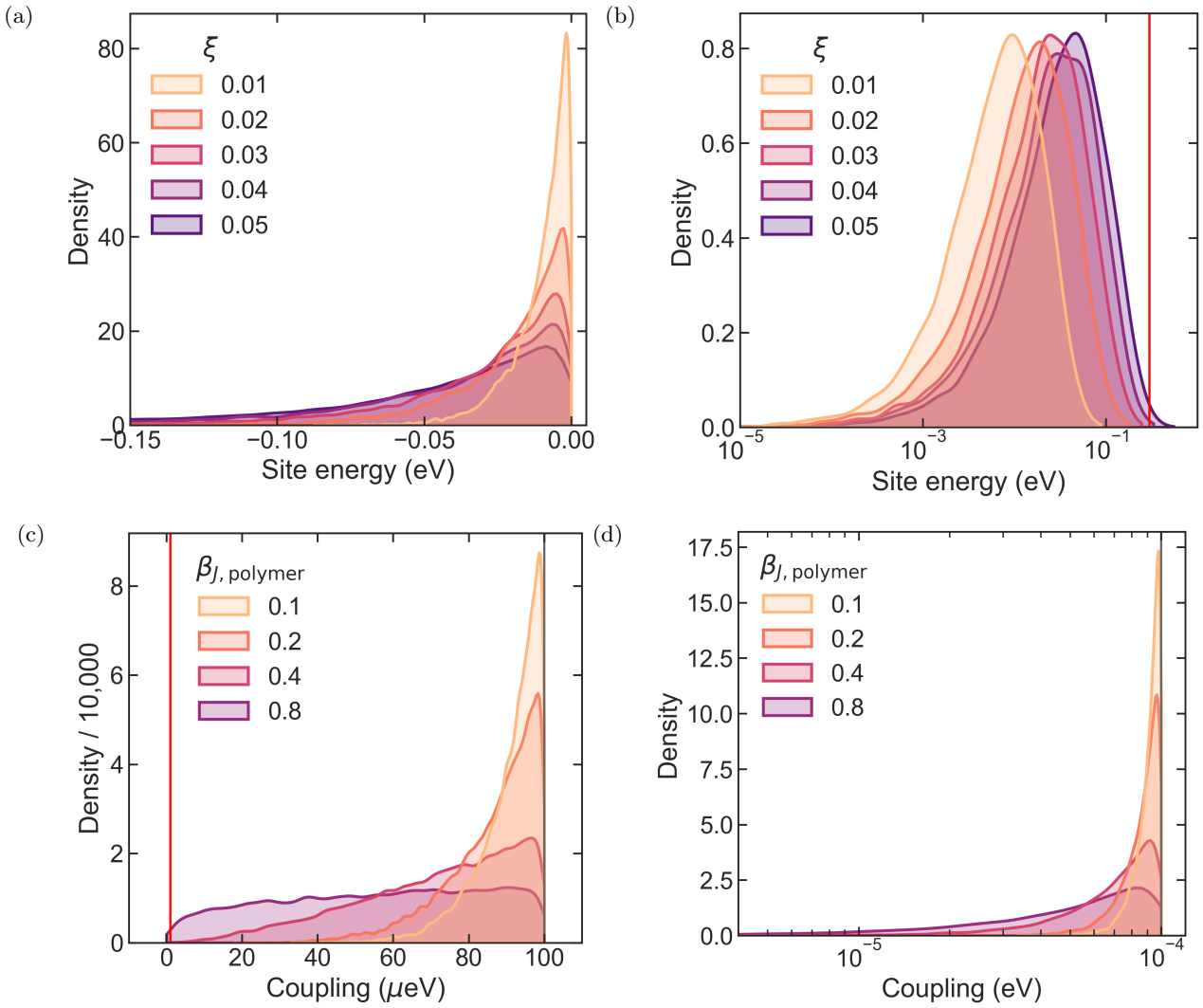


Figure D.7: Distributions in site energy (first row) and coupling (second row), when disorder is introduced into the model. Distributions are shown on a linear scale (first column) and a logarithmic scale (second column). The vertical grey line present on some plots indicates the site energy or coupling value associated with the metal sites (hops from polymer to metal, in the case of coupling), while the red line indicates values associated with the collection site (hops from metal to collection site, in the case of coupling).

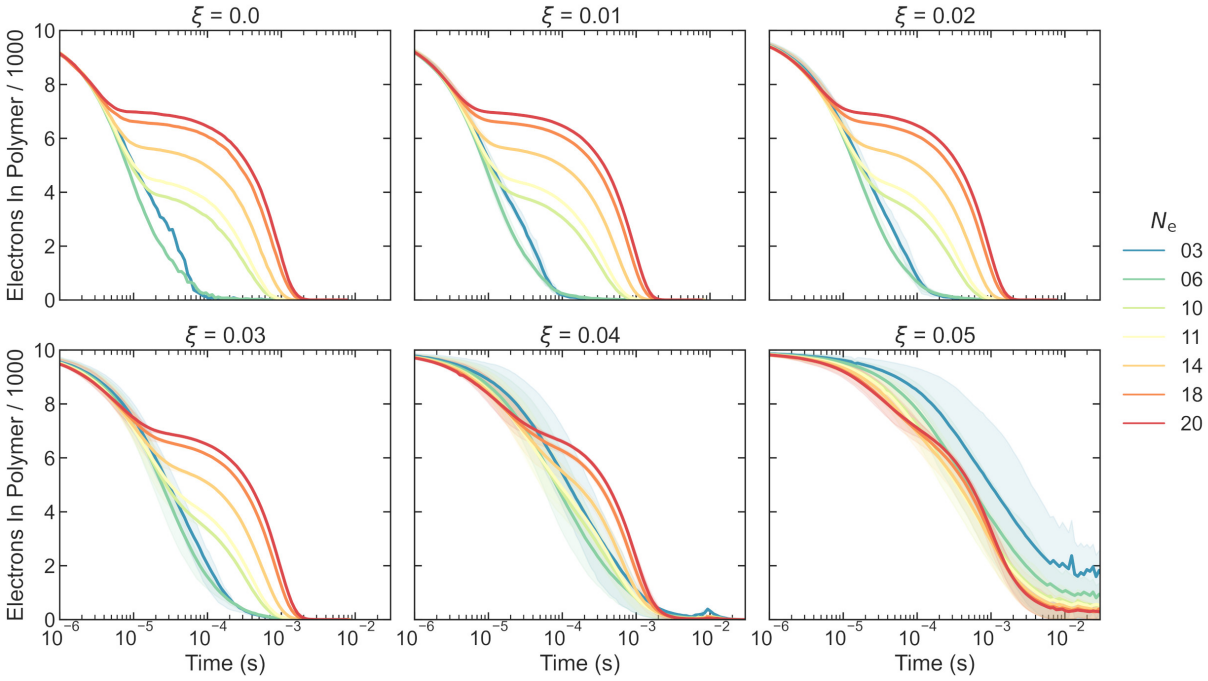


Figure D.8: Varying ξ. J_{polymer} was set to 0.1 meV.

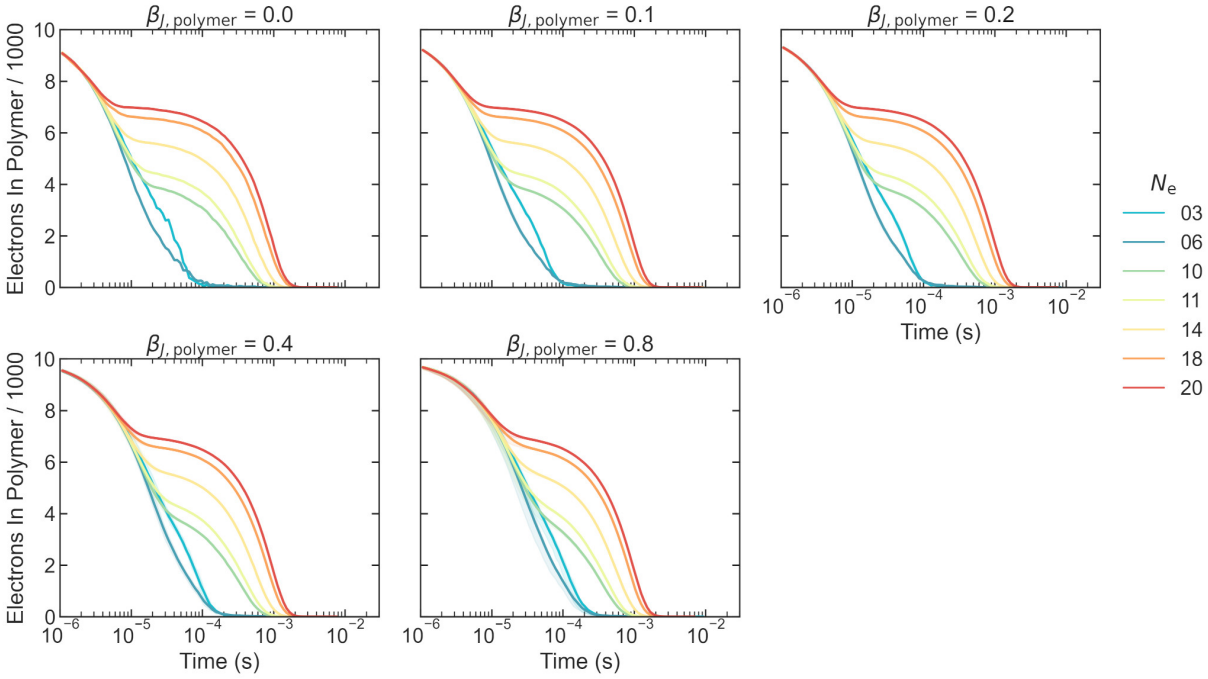


Figure D.9: Varying β_{polymer}. J_{polymer} was set to 0.1 meV.

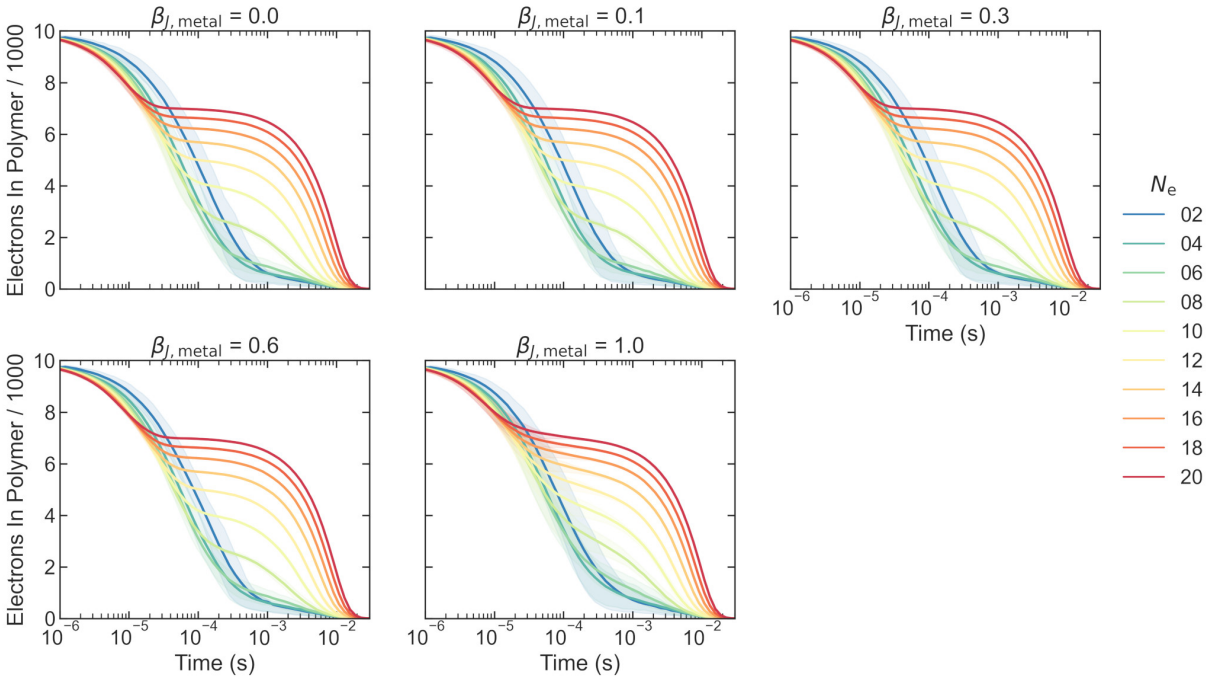


Figure D.10: Varying β_{metal}. J_{polymer} was set to 0.1 meV.

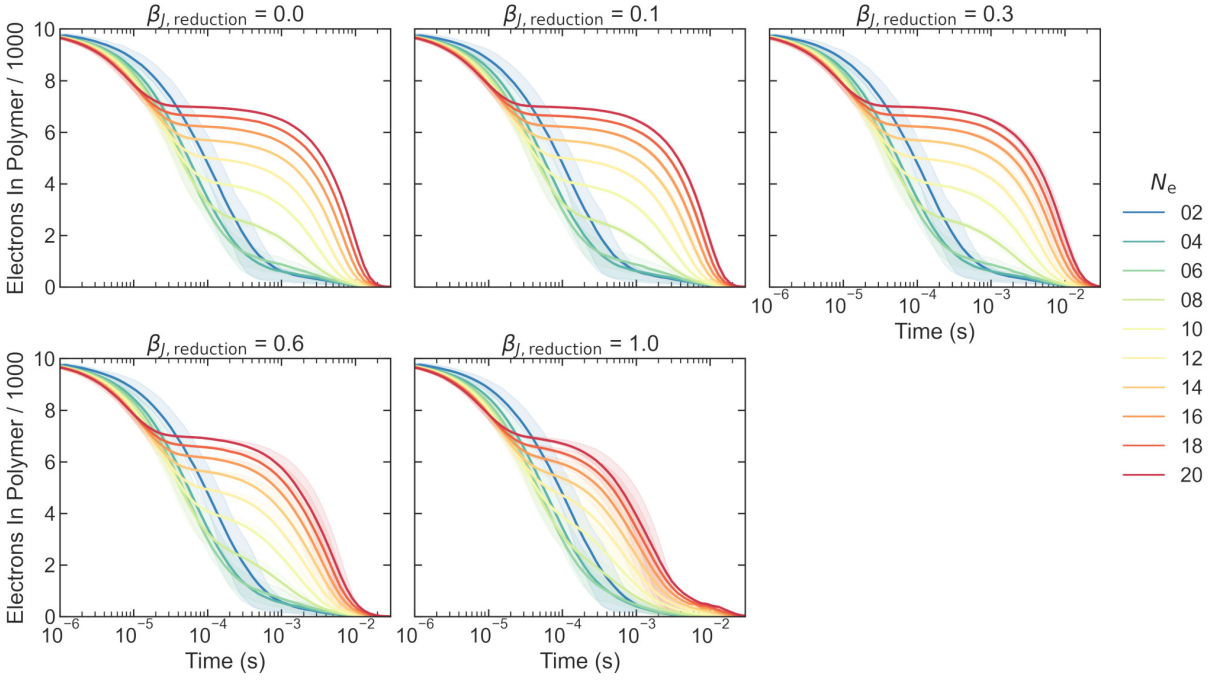


Figure D.11: Varying $\beta_{\mathrm{reduction}}$. J_{polymer} was set to 0.1 meV.

Fluctuating Transient Populations

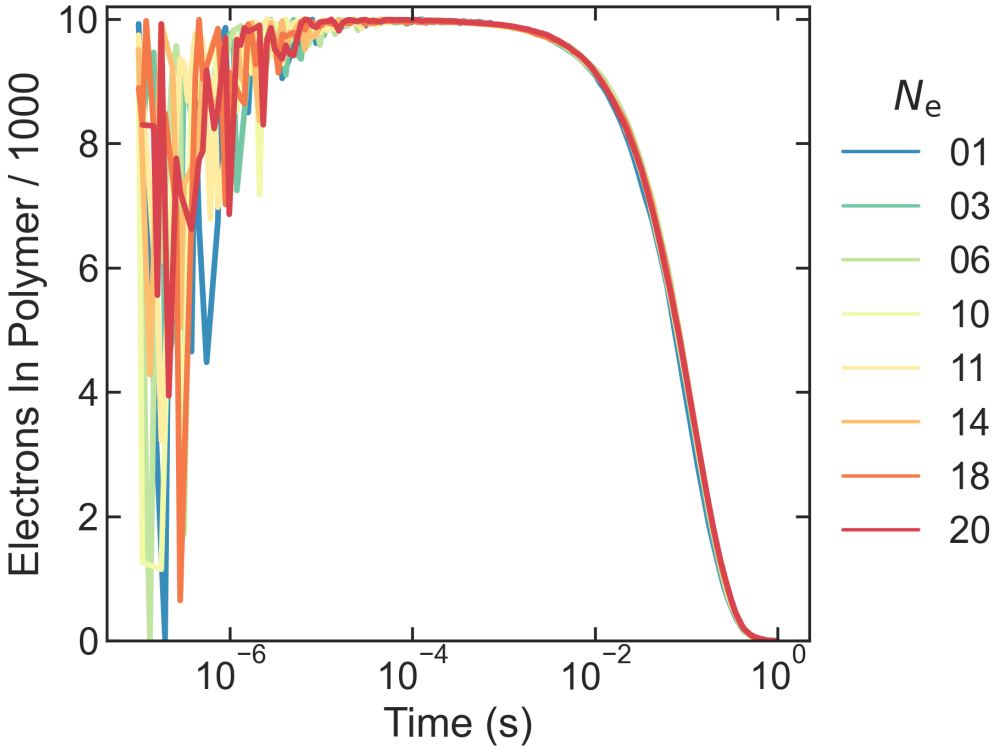


Figure D.12: Populations in the polymer region are shown to erroneously fluctuate at early times, indicating an issue with the way that populations are tracked. This occurs for two reasons: 1) because the time-bins are more narrow for early times in the simulation, and 2) because J_{polymer} was set to a low value of 1×10^{-6} eV. Therefore, in some runs, no hops occurred within the early time-bins. Since the program can only record populations when a hop occurs, this leads to fluctuations in the populations when they are summed over all runs.

Appendix Bibliography

[1] J. F. Coker *et al.*, "Perpendicular crossing chains enable high mobility in a noncrystalline conjugated polymer," *Proceedings of the National Academy of Sciences*, vol. 121, no. 37, e2403879121, Sep. 2024. DOI: 10.1073/pnas.2403879121.

[2] T. A. Wassenaar, K. Pluhackova, R. A. Böckmann, S. J. Marrink, and D. P. Tieleman, "Going Backward: A Flexible Geometric Approach to Reverse Transformation from Coarse Grained to Atomistic Models," *Journal of Chemical Theory and Computation*, vol. 10, no. 2, pp. 676–690, Feb. 2014, ISSN: 1549-9618. DOI: 10.1021/ct400617g.

[3] P. C. T. Souza *et al.*, "Martini 3: A general purpose force field for coarse-grained molecular dynamics," *Nature Methods*, pp. 1–7, Mar. 2021, ISSN: 1548-7105. DOI: 10.1038/s41592-021-01098-3.

[4] R. Alessandri, F. Grünewald, and S. J. Marrink, "The Martini Model in Materials Science," *Advanced Materials*, vol. 33, no. 24, p. 2 008 635, 2021, ISSN: 1521-4095. DOI: 10.1002/adma.202008635.

[5] J. J. Kwiatkowski, J. M. Frost, and J. Nelson, "The Effect of Morphology on Electron Field-Effect Mobility in Disordered C60 Thin Films," *Nano Letters*, vol. 9, no. 3, pp. 1085–1090, Mar. 2009, ISSN: 1530-6984. DOI: 10.1021/nl803504q.